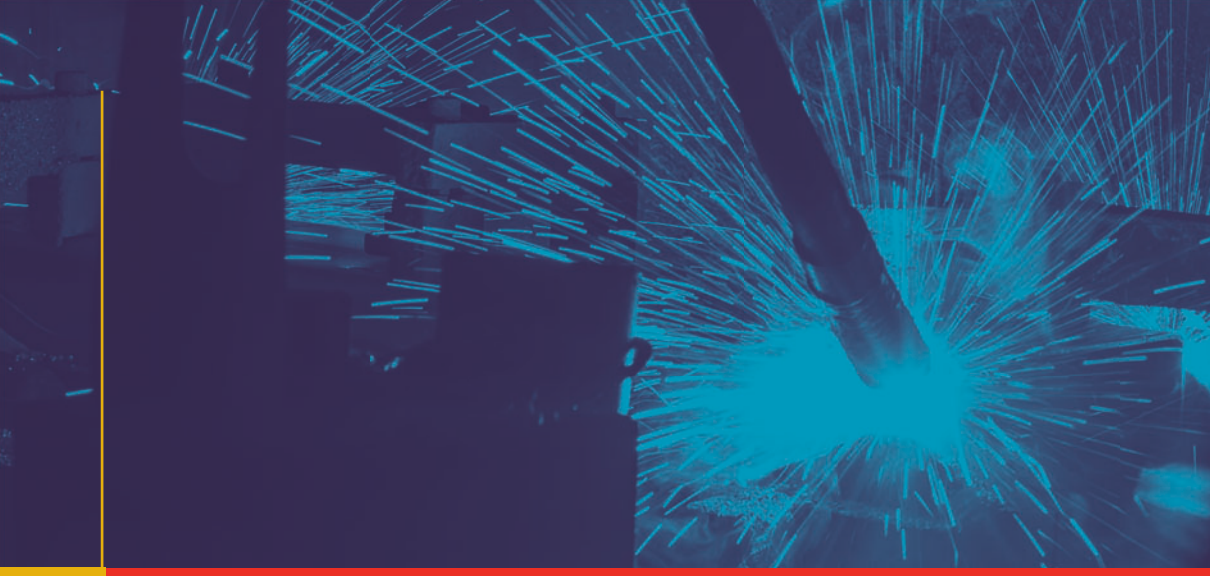

Transactions on Intelligent Welding Manufacturing

Volume I No. 2 2017

Springer

Transactions on Intelligent Welding Manufacturing

More information about this series at http://www.springer.com/series/15698

Shanben Chen · Yuming Zhang
Zhili Feng
Editors

Transactions on Intelligent Welding Manufacturing

Volume I No. 2 2017

Springer

Editors
Shanben Chen
Shanghai Jiao Tong University
Shanghai
China

Zhili Feng
Oak Ridge National Laboratory
Oak Ridge, TN
USA

Yuming Zhang
Department of Electrical and Computer Engineering
University of Kentucky
Lexington, KY
USA

ISSN 2520-8519 ISSN 2520-8527 (electronic)
Transactions on Intelligent Welding Manufacturing
ISBN 978-981-10-7042-6 ISBN 978-981-10-7043-3 (eBook)
https://doi.org/10.1007/978-981-10-7043-3

Library of Congress Control Number: 2017943844

Printed on acid-free paper

This Springer imprint is published by Springer Nature
The registered company is Springer Nature Singapore Pte Ltd.
The registered company address is: 152 Beach Road, #21-01/04 Gateway East, Singapore 189721, Singapore

Editorials

Research and development of intelligent welding technology are a vital part of intelligent manufacturing, and have continuously attracted researchers' attention recently. This second issue of the Transactions on Intelligentized Welding Manufacturing (TIWM) provides a sample on recent developments in methods and technologies that lead to innovative intelligent welding applications. It includes a feature article and other 15 papers selected from 2017 International Workshop on Intelligentized Welding Manufacturing (IWIWM2017) contributing to intelligent welding manufacturing through understanding, sensing, and control of welding manufacturing processes.

The featured article in this volume "Intelligent Weld Manufacturing Role of Computational Welding Engineering" is contributed by S. A. DAVID, Jian CHEN, Brian T. GIBSON, and Zhili FENG from Oak Ridge National Laboratory, Oak Ridge, Tennessee, USA. This feature article discusses the progress in process modeling, microstructure, properties, and process control and automation and the importance of ICWE. Also, control and automation strategies for friction stir welding will be discussed.

The first paper of research papers "A Reinforcement Learning Based Approach for Welding Sequence Optimization" is contributed by a group of researchers from Mexico. They develop and implement a Q-learning based Reinforcement Learning (RL) algorithm for Welding Sequence Optimization (WSO) where structural deformation is used to compute reward function. It is shown that RL-based welding optimization technique not only allows the reduction of structural deformation up to 66% but also substantially speeds up the computational time over the exhaustive search.

For the second paper, "Time-Optimal Path Planning for Dual-Welding Robots Based on Intelligent Optimization Strategy", the subject of study is path planning for dual-welding robots. It is contributed by researchers from East China University of Science and Technology. An intelligent optimization strategy, i.e., GC-PSO

algorithm is proposed to realize time-optimal path planning for dual-welding robots. Simulation results show that the intelligent path planning strategy is effective and can be used for welding robot path optimization.

The third paper "Improving Stability of Welding Model with ME-ELM" is contributed by a joint research team from Nanchang Institute of Technology, Jiangxi Aeronautical Institute, and East China Jiaotong University. A new algorithm named ME-ELM is developed and results show that such algorithm works more effective than BP and other variants of ELM in reducing influence and has the highest accuracy in predicting the welding shape.

The fourth selected paper "Study on the Cracks of NiTiNb/TC4 Lap Joints Welded by Micro Laser Welding" is a contribution from a group of researchers associated with Nanchang Hangkong University, China. In this paper, the microstructure and crack in the weld are studied by optical microscope (OM) and scanning electron microscope (SEM). Results show that the cracks are easy to generate during the laser lap welding of NiTiNb alloy and TC4 alloy due to plenty of brittle intermetallic compound of Ti_2Ni.

The fifth paper is titled "Research on the Ultrasonic Welding of Titanium Alloy after Embedding Fiber Bragg Grating Sensor". The authors are from School of Mechanical & Electrical Engineering, Nanchang University. In this paper, the electroplated nickel FBG is embedded in a direct or indirect way and welded by ultrasonic welding to research the rapid prototyping and sensing properties of the titanium alloy intelligent structural parts. The experiment of embedding electroplated nickel FBG into titanium alloy in the direct way shows that titanium alloy is not suitable for embedding matrix. On the other hand, the experiment of indirect way shows that the figure of FBG temperature sensitivity is 2.13 times larger than that of original bare fiber grating, and is 1.11 times larger than that of direct way.

The sixth paper will be "Analysis of Vacuum Chamber Structure based on Visual Environment", in which the feasibility of improving the vacuum chamber structure of vacuum packaging machine is discussed.

The seventh paper, "Single Channel Blind Source Separation based on EEMD and Its Application on Arc Sound Signal Processing", is contributed from Xi'an Jiao Tong University. A single channel blind source separation (BSS) algorithm based on the ensemble empirical mode decomposition (EEMD) is proposed to purify and de-noise the arc sound signals. Principal component analysis (PCA) is used to reduce the multi-dimensional IMFs to low-dimensional IMFs, and independent component analysis (ICA) separates the virtual multichannel signals into target sources. Experiment results indicated that the source signals of arc sound were effectively separated despite the environmental noise signals.

Wire and arc additive manufacturing (WAAM) has gained popularity in recent years due to its unique efficiency and cost advantages. The eighth paper, "Investigation on Surface Quality in a Hybrid Manufacturing System Combining Wire and Arc Additive Manufacturing and Machining", is contributed from a group

of researchers from Beijing University of Technology. In this paper, the dependence of the machined surface quality (characterized by surface roughness) on the influencing factors mentioned above is investigated based on quadratic general rotary unitized design (QGRUD). To reduce the number of experiments, a comprehensive factor, namely material removal area (MRA), is introduced to characterize the deposition width, deposition height, and surface waviness. The analysis results show that spindle speed is the most influential factor, followed by MRA and feed rate. Furthermore, a high spindle speed and a moderate feed rate are preferred, which contribute to not only improving the surface quality and the efficiency but also reducing the demand of geometric accuracy for WAAM.

The ninth paper, "Preliminary Research on Intelligent Mobile Tool Cart for Industrial Manufacturing in a Factory Environment", is also contributed from College of Mechanical Engineering and Applied Electronics Technology, Beijing University of Technology. This paper presents a preliminary research on intelligent mobile tool cart (IMTC) for working alongside workers in manufacturing process.

The tenth paper is titled "Microstructure and Mechanical Properties of Friction Stir Weld of Dissimilar Ti6Al4V Titanium Alloy to AA2024 Aluminum Alloy". Dissimilar Ti6Al4V titanium alloy and AA2024 aluminum alloy sheets with a thickness of 3mm are friction stir welded successfully, and the microstructure and mechanical properties of the butt joints are investigated. The eleventh paper is from School of Mechanical and Automotive Engineering, South China University of Technology. In this paper "Control of Current Waveform for Pulsed MIG Welding of Aluminum Alloy Sheets", a simplified model of pulsed MIG welding is established and simulated using MATLAB.

The first paper of short papers on "Study of Ultrasonic Phased Array in Underwater Welding" is contributed by a group of researchers and engineers from Nanchang Institute of Technology and East China Jiaotong University. Interference principle of acoustic beam is first analyzed, and the relationship of focusing precision, phased array (PA) shape, and gap distance between adjacent units, sensor element number as well as time resolution is revealed with simulation.

In recent years, intelligent robotic welding has been an active research area. Vision sensors have been widely used in robotic welding systems for information collection and processing. In the second paper, "Type Identification and Feature Extraction of Weld Joint for Adaptive Robotic Welding", an algorithm is proposed to identify joint type and extract relevant feature values by extracting three feature lines and two key turning points. Three types of weld joints are inspected and the results indicate that the algorithm is of high efficiency and robustness.

The last (third) paper, "Kinematic Model Analysis of an 8-DOF Photographic Robot", develops a kinematic model and verifies it using MATLAB.

Welding is often served as the final assembly of high value-added product in critical applications. Continued research effort is needed to establish the foundation for intelligent welding processes and systems to promise better quality and higher

productivity. To this end, innovative methods are needed to better understand and more effectively sense and control welding manufacturing processes.

Yukang LIU, Ph.D., TIWM Regional Editor of Americas
Senior Engineer, Control Design Automation, MathWorks Inc.
yukang.liu@mathworks.com

YuMing ZHANG, Ph.D., TIWM Editor-in-Chief
James R. Boyd Professor of Electrical Engineering, University of Kentucky
Fellow, American Welding Society (AWS)
Fellow, American Society of Mechanical Engineers (ASME)
Fellow, Society of Manufacturing Engineers (SME)
yuming.zhang@uky.edu

Contents

Part I
Feature Articles

Intelligent Weld Manufacturing: Role of Integrated Computational Welding Engineering

S. A. David, Jian Chen, Brian T. Gibson and Zhili Feng

Abstract A master welder uses his sensory perceptions to evaluate the process and connect them with his/her knowledge base to take the necessary corrective measures with his/her acquired skills to make a good weld. All these actions must take place in real time. Success depends on intuition and skills, and the procedure is labor-intensive and frequently unreliable. The solution is intelligent weld manufacturing. The ultimate goal of intelligent weld manufacturing would involve sensing and control of heat source position, weld temperature, weld penetration, defect formation and ultimately control of microstructure and properties. This involves a solution to a problem (welding) with many highly coupled and nonlinear variables. The trend is to use an emerging tool known as intelligent control. This approach enables the user to choose a desirable end factor such as properties, defect control, or productivity to derive the selection of process parameters such as current, voltage, or speed to provide for appropriate control of the process. Important elements of intelligent manufacturing are sensing and control theory and design, process modeling, and artificial intelligence. Significant progress has been made in all these areas. Integrated computational welding engineering (ICWE) is an emerging field that will aid in the realization of intelligent weld manufacturing. The paper will discuss the progress in process modeling, microstructure, properties, and process control and automation and the importance of ICWE. Also, control and automation strategies for friction stir welding will be discussed.

Keywords Intelligent · Weld manufacturing · Sensing · Control
Automation · Weld pool · Geometry · Convection · Solidification
Integration · Modeling · Friction stir welding

S. A. David (✉) · J. Chen (✉) · B. T. Gibson · Z. Feng (✉)
Oak Ridge National Laboratory, Oak Ridge, TN, USA
e-mail: standavid@charter.net

J. Chen
e-mail: chenj2@ornl.gov

Z. Feng
e-mail: fengz@ornl.gov

S. Chen et al. (eds.), *Transactions on Intelligent Welding Manufacturing*,
Transactions on Intelligent Welding Manufacturing,
https://doi.org/10.1007/978-981-10-7043-3_1

1 Introduction

Welding is a multibillion dollar industry used extensively in the construction of buildings, bridges, aircraft, ships, automobiles, and electronics. In recent years welding has emerged as a multidisciplinary activity that involves a large number of variables and that requires knowledge of basic science and engineering. In the last four decades, significant advances have been made in taking welding from a job shop technology to a highly automated, computer-oriented technology [1–7]. To meet the demands of quality and productivity is a continuing challenge. This is where intelligent weld manufacturing comes into play. Worldwide significant amount of work is being done in intelligent weld manufacturing [8].

"Intelligent manufacturing is real-time-based optimization through the entire value chain." Welding is ideally suited for intelligent manufacturing. It involves sensing and control of the heat source, position, weld defect formation, and ultimately microstructure and properties. This involves solution to a problem with many highly coupled and nonlinear variables in welding. The trend is to use intelligent control. This enables the user to choose a desired end factor such as penetration and productivity to drive the selection of process parameters such as current, voltage, and speed to provide for appropriate control of the process. In other words, intelligent welding aims at controlling for microstructure properties and performance of the welded parts. Chen has discussed the frame work for the science and technology for intelligent weld manufacturing [9]. Important elements of intelligent weld manufacturing are sensing and control design, process modeling, and artificial intelligence. The ultimate goal of intelligent weld manufacturing is to produce high-quality welds with increased productivity. To achieve this, it is necessary to have a thorough knowledge and understanding of four key elements: (1) process and process modeling, (2) microstructure, (3) properties, and (4) process control and automation. Mathematical modeling and simulation are integral parts of these elements. Details about the four elements are found in the published literature [10, 11]. Figure 1 shows the importance and integration of these elements. A wealth of information is available about these four elements in the Proceedings of a series of two International Conferences, namely, Trends in Welding Research and Mathematical Modeling of Weldability, held in recent years [10, 11]. The proceedings of these conferences contain a wealth of knowledge and information on intelligent control and automation. Although significant advances are being made in all these four areas, to integrate them successfully for a process that is highly coupled with a large number of variables is a major challenge. An approach to solving this problem is integrated computational welding engineering (ICWE). ICWE is an approach to design and produce welds in materials and by methods linking process models. ICWE is a major part of intelligent weld manufacturing. Another emerging field is integrated computational materials engineering (ICME). Both ICWE and ICME are engineering disciplines that speed up process development by integrating materials design, fabrication, and performance using computational process.

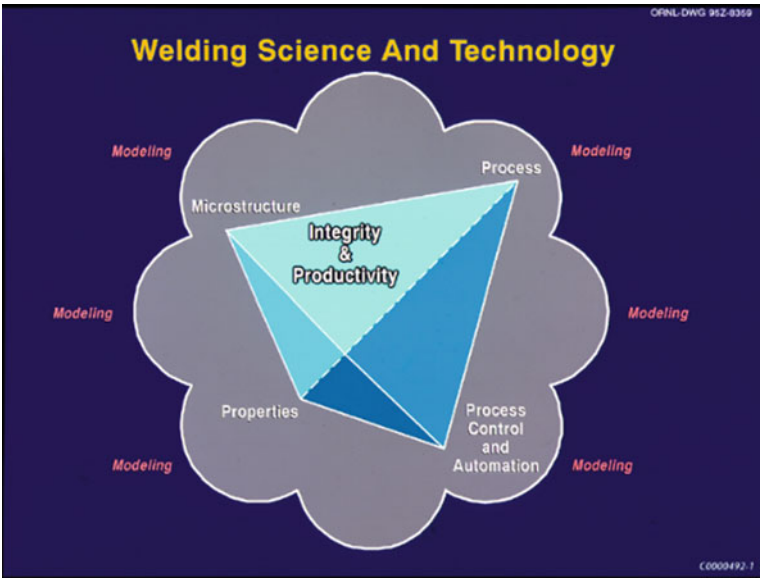

Fig. 1 Integration of process, microstructure, properties and process control and automation [10]

The paper will address the role of ICWE and ICME models in advanced intelligent weld manufacturing. It will address the progress made in various aspects of ICWE and ICME, most importantly in welding processes, microstructure and properties, and process control and automation. Current state-of-the-art of process modeling, microstructure and properties modeling, integration of various models, and sensing and control will be discussed. The paper will also address control and automation strategies for friction stir welding.

2 Process Modeling

In this section, recent advances in processes and process modeling will be described.

2.1 Weld Pool Dynamics and Geometry

Two of the most important parameters to control in automation are penetration and weld geometry. During welding, as the heat source interacts with the metal, several physical processes occur (e.g., melting, evaporation of elements, solution of gases, solidification, phase transformation residual stresses). It is important to understand

the physical processes and their interactions to develop ICWE and intelligent weld manufacturing. Direct observation of the process is difficult, time consuming, and expensive because of the complexities, the large number of variables, and the presence of plasma. A solution is to model and simulate the process using equations of conservation of mass, momentum, and energy with appropriate boundary conditions.

Significant advances have been made in calculating the weld pool geometry [12–27] since the earlier Rosenthal analysis of heat flow in welds [28, 29], which was an analytical and a conduction model. Weld pool heat flow and fluid flow are recognized to be critical in the development of the shape and size of the weld pool and the macrostructure and microstructure of the weld. Current models address coupled conduction and convection problems to predict weld pool geometry. Of the various heat transfer models, the ones with convection play a major role in determining weld pool geometry and penetration. Convection in the weld pool is driven by surface tension, buoyancy, and electromagnetic forces [15, 17, 18, 30–36]. In addition, aerodynamic drag force due to plasma stream is also thought to be a factor [36]. Various forces are shown schematically in Fig. 2 [36]; convection due to surface tension is the dominant force contributing to fluid flow in the weld pool. The presence of a significant temperature gradient on the weld pool surface leads to spatial gradient of surface tension, also known as Marangoni stress, which contributes to convection in the weld pool. Buoyancy effects due to spatial variation of

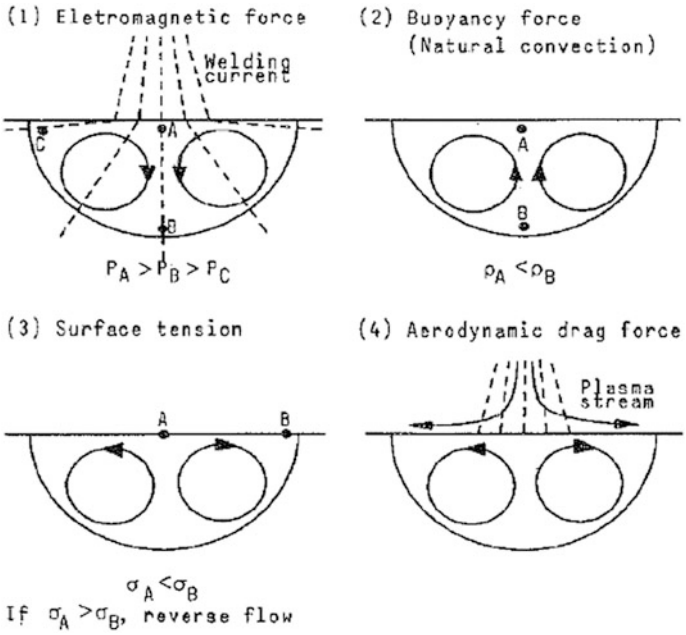

Fig. 2 Flow filed in the liquid pool induced by the four forces during arc welding (P_A, P_B and P_C are electromagnetic force induced pressure; ρ_A and ρ_B are buoyancy force; σ_A and σ_B are surface tension) [36]

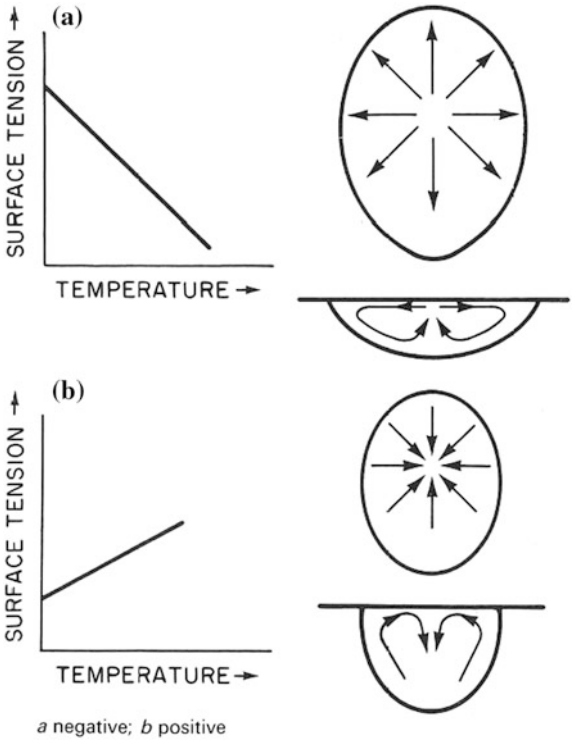

Fig. 3 Different convective flow pattern produced by different temperature coefficient of surface tension [62]

density of the liquid as a function of temperature and composition can provide convective flow. Electromagnetic forces are due to the divergent path of the current and the magnetic field that the current generates.

The reason that a shallow or deep penetration weld forms depends on the temperature coefficient of surface tension ($d\gamma/dT$). For pure metals and alloys, $d\gamma/dT$ is negative (Fig. 3). In a stationary arc weld, the highest temperature is in the middle of the weld pool. Therefore, the hot liquid flows outward, resulting in a shallow weld pool (Fig. 3). In the presence of surface-active elements such as phosphorous and sulfur and sometimes oxygen, the $d\gamma/dT$ is positive, resulting in the flow of the hot liquid inward, driving the hot liquid downward, and resulting in a deep weld pool. Figure 4 shows flow fields for pure iron resulting in a shallow weld pool and a deeper penetration with addition of oxygen. Depending on the interplay between various forms of driving force, the convective flow can be simple recirculation or a complex pattern with several convective cells (Fig. 4) [28, 36–38].

In the past three decades, most of the studies have concentrated on convective heat transfer, in particular, on the effect of spatial variation of surface tension on

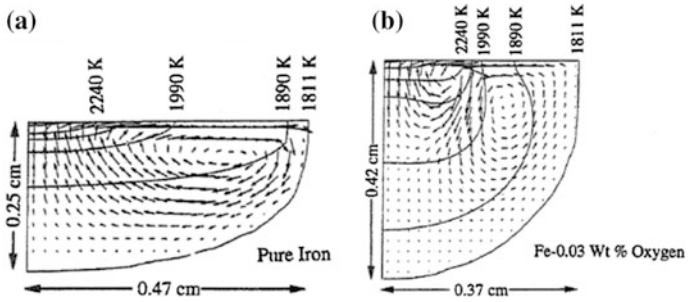

Fig. 4 Velocity and temperature fields for two different cases: **a** for pure iron and **b** for Fe-0.03 wt% oxygen [38]

weld penetration. For simplicity, most of the earlier models assumed stationary arc with a rigid weld pool surface. Recently, the models have been refined to incorporate realistic welding conditions such as deformable weld pool surface and moving heat source. In the last two decades, we have seen an enormous growth in understanding the physical process of welding. This is in part due to the speed and availability of computers. The introduction of massively parallel computers is expected to solve complex problems posed by intelligent weld manufacturing.

DebRoy et al. [39] have developed a computerized analysis for predicting heat transfer, phase changes, and fluid flow. They describe the use of modeling of the mushy zone using an ethology-porosity technique [39]. Figure 5 shows the computed convective flow of the weld part during arc welding. The color represents the temperature (in degrees kelvin), and the dotted lines show the liquid flow field. The two large loops shown near the surface of the pool are from Marangoni flow; the other loops below are due to electromagnetic effects [40].

The variable penetration during welding of different batches of a commercial alloy within a prescribed range has received considerable attention. Studies [39] have shown that knowledge of the interfacial phenomenon is the key for understanding and controlling weld penetration [17, 18, 28, 35–40]. Often the penetration

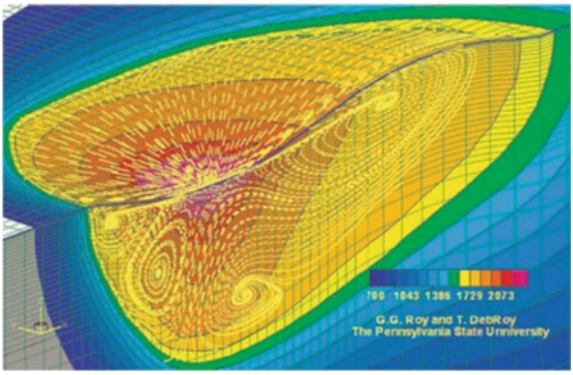

Fig. 5 Computed flow fields in a GTA weld pool. The color represents the temperature in the weld pool, and the dotted lines represent the liquid flow pattern. Two loops on the surface are from Marangoni flow (courtesy of Prof. DebRoy, Penn State University) (Color figure online)

is determined by the concentration of surface-active elements in the alloy [41–43]. This can affect the temperature/coefficient of surface tension and the resulting direction of fluid flow [34].

Weld penetration is an important consideration for weld automation. It is one of the parameters that need to be incorporated in the models. Weld penetration has been determined extensively by the physical feature of the weld pool such as weld pool oscillation and geometry [44–46].

2.2 Vaporization and Solution of Gas

During welding, the surface temperature of the weld pool is higher than the liquidus temperature of the alloy. In a high-energy-density process such as laser and electron beam welding, the temperature would exceed the boiling point of the alloy [47, 48]. Consequently, vaporization of the alloying elements can occur, changing the composition and hence changing the microstructure and the properties of the weld. DebRoy et al. have developed a computer model to describe the vaporization of the elements in a weld [49–51].

During welding, gases such as hydrogen, oxygen, and nitrogen dissolve in the liquid pool, causing pinholes and porosity. They also react with elements in the weld pool to form oxide and nitride inclusions [52]. Hydrogen causes hydrogen embrittlement, and nitrogen increases the yield strength and reduces ductility. Realistic modeling of hydrogen absorption and diffusion and their effects on hydrogen embrittlement is a challenge.

2.3 Artificial Neural Network Modeling

Two of the most important weld features in automated welding are weld pool geometry and penetration. Over the past three decades, several computational models have been developed for weld pool shape and penetration. The models have become more complex and sophisticated and require greater computational power. Although they are excellent tools for understanding the physical processes in welding, they are not available for the end users. An alternate process is the use of artificial neural network (ANN) [53]. A publication by Bhadeshia highlights the application of neural network in materials science [54]. Neural network models can be sophisticated, but they are limited to the experimental datasets on which they are based.

ANN has been used to solve problems in many areas of science and technology. The neural networks are modeled after the learning process in the human brain. Such models are empirically based and are capable of providing results rapidly. An example is the prediction of weld pool shape in a hybrid laser/arc process for which the physics of the process is not well known. Numerical models exist for laser or arc

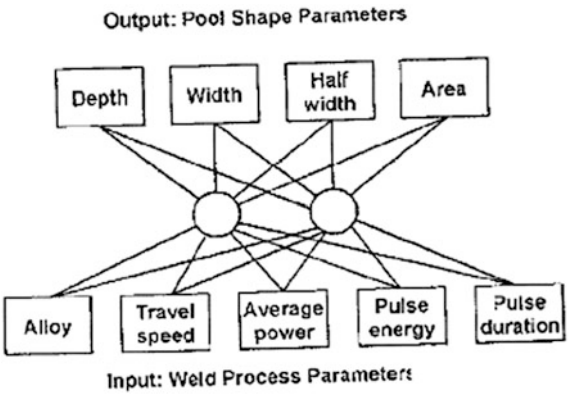

Fig. 6 Neural network architecture for predicting weld pool shape and penetration [53]

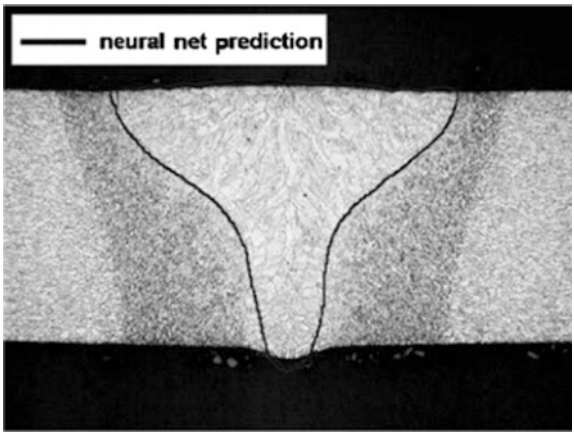

Fig. 7 Comparison of weld cross section predicted by neural network model and the actual weld pool [53]

welding processes. Other examples include prediction of the weld joint penetration based on the shape of the weld pool geometry [55] and real-time control of weld penetration based on real-time measurement of the weld pool geometry [56]. It is difficult to accurately model the hybrid process without knowing the physics of the process [53]. Figure 6 shows neural network architecture for laser/arc hybrid process; Fig. 7 shows prediction of an ANN model and the weld metal. The agreement is excellent. ANN modeling has been used for a wide variety of investigations [54, 57–60]. Sterjovski et al. have used ANNs for modeling the mechanical properties of steels in various applications [58] and for predicting diffusible hydrogen control and cracking susceptible in flux-covered arc welds [59]. Vitek et al. [60] have developed the Oak Ridge Ferrite Number (ORFN), a new model for predicting ferrite content in stainless steel welds. For the first time, ferrite content is predicted quantitatively as a function of alloy composition and cooling rate. The model is based on a neural network analysis of existing data supplemented with newly generated data.

3 Microstructure

As a welding heat source interacts with metal, three distinct regions can be identified, namely, fusion zone (FZ), heat affected zone (HAZ), and the base material (BM) (Fig. 8). The microstructural characteristics of the three regions control the properties and performance of the weld. A weldment is often the weakest link in the structure. During welding, various physical processes such as thermochemical reactions in the liquid, solidification, and solid-state transformation that occur in the weld metal control the microstructural development in the weld. Some fundamental knowledge of the effect of these physical processes on the microstructural development in the weld metal already exists. A review by Babu [61] examines various models for the development of microstructure in weldments. He analyzes the phase transformation in metals and alloys due to the weld thermal cycle experience during welding. The first event to occur when the weld pool cools is liquid transforming to solid and solid subsequently transforming to single-phase or multiple-phase structures through a solid-state reaction. The same is true of the HAZ except there is no melting in the HAZ. All these events are analyzed using computational thermodynamics (CT) models and computational kinetics (CK) models that relate to free energy of phases. The stability of the phases depends on the free energy of phases. Phases with high free energy are unstable; phases with low free energy are stable. The rate of phase change is related to diffusion and nucleation rate within the parent phase that leads to the product phase. However, a generalized integrated model encompassing our current understanding of the evaluation of microstructure is just emerging. Such models are needed in the design and successful development of intelligent weld manufacturing.

Most of our knowledge about weld metal solidification is derived from the extension of the knowledge of freezing of castings and single crystals in lower thermal gradients and at slower growth rates [62]. However, various physical processes that occur during the interaction of the heat source with the metal add a

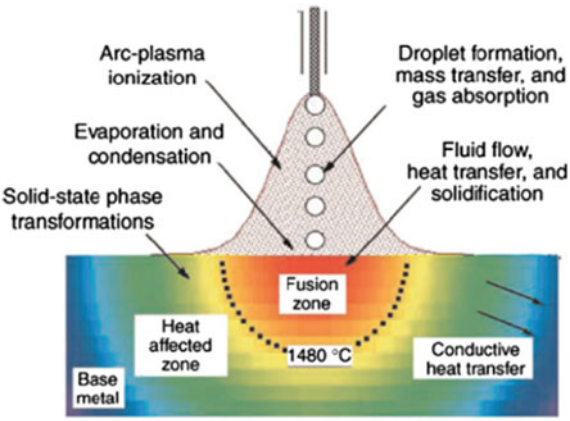

Fig. 8 Schematic illustration of interaction of heat source with metal and three regions of the weldment, namely FZ, HAZ and BM

new dimension to our understanding of weld metal solidification. Conventional theories of solidification over a broad range of conditions can be extended to understand weld pool solidification. In certain cases, because of rapid cooling rate effects, it is not unusual to observe nonequilibrium phases. Recent developments in the application of computational thermodynamics and kinetic models, studies of single-crystal welds and advanced characterization techniques have enhanced our understanding of weld pool solidification behavior. Advanced in situ characterization techniques such as synchrotron and neutron sources have enhanced our understanding of phase formation and formation of nonequilibrium phases [63, 64]. Other important factors are the dynamics of weld pool development and steady state geometry. Weld pool shape is important in the development of grain structure and the dendrite grain selection process [62].

Several fundamental aspects of solidification processes (nucleation, epitaxial growth, the growth selection process, growth kinetics, and microsegregation) must be understood to develop a basic model for solidification microstructure. In the FZ, the liquid metal transforms to solid. The size and shape of the grains, the distribution of inclusions, and the presence of defects such as hot cracks are controlled by the solidification behavior. Unlike the solidification of ingots and casting, solidification of a weld occurs without a nucleation barrier. No significant undercooling is required for the formation of the solid. Solidification occurs spontaneously by epitaxial growth on the partially melted grains.

Solidification microstructures in welds are often difficult to interpret and are commonly analyzed with the help of classical theories of nucleation and growth [62]. The development of microstructural features (morphology) of the solid in the weld is controlled by the shape of the solid/liquid interface and its stability. Stability of the interface is determined by the constitution and thermal conditions that exist at the interface. Theories have been developed for interface stability for equilibrium conditions at the interface for normal solidification or under extreme nonequilibrium conditions prevalent during rapid solidification [65, 66]. These theories can be extended to weld pool solidification. The parameters that determine the solidification microstructures in contrast are growth rate (R), thermal gradient (G) and undercooling (ΔT). It is well known that temperature gradient and growth rate are important in the combined form $G \bullet R$ or G/R. Depending on the conditions, growth of the solid can be planar, cellular, or dendritic. A dendrite isolated from the liquid is shown in Fig. 9 [67]. Weld metal grain structure is predominantly determined by the base metal grain structure [68]. Crystallographic effects and welding conditions have been found to influence this grain structure. Often the grains during the weld pool solidification tend to grow along a crystallographic direction that is easy growth direction. For cubic metals the easy growth directions are <100>. Conditions for growth are optimal when one of the easy growth directions coincides with the heat flow direction. Therefore, during welding among the randomly oriented grains in the polycrystalline base metal, those that are favorably oriented will continue to grow. Unfortunately for the unfavorably oriented grains, the growth will terminate, thus leading to a grain growth selection process. This grain anisotropy

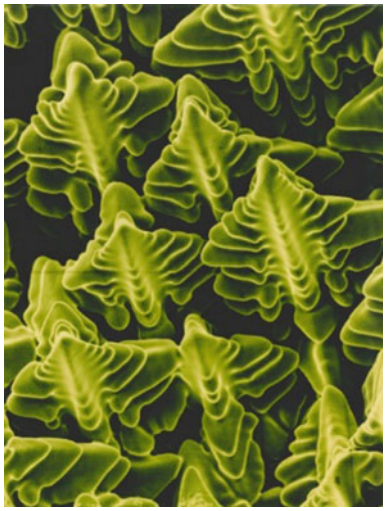

Fig. 9 Scanning electron micrograph showing the features of dendrite structure that develops in a nickel-based superalloy [67]

was clearly demonstrated by the work of Rappaz and David using a Fe-Ni-Cr single-crystal weld [69].

Another significant aspect of weld pool solidification is solute redistribution. During welding, the extensive solute redistribution that occurs in the weld pool results in segregation that can adversely affect weldability, microstructure, and properties. Only recently some attention is being given to this important aspect of weld pool solidification [70–73]. A great deal of work needs to be done in this area. Availability of software packages to calculate multicomponent phase diagrams will make it easier to determine models for solute redistribution in multicomponent alloys.

In most of the cases, both the weld metal and the HAZ go through a solid-state transformation. The transformation and the resulting microstructures control the properties. Hence modeling of solid-state transformations in the weld is important to developing an integrated model [61]. In addition to phase transformation in the weldment, an integrated model should address grain growth, precipitations, coarsening, and solute redistribution. The transformations can be grouped in four classes: (1) phase changes involving diffusional processes, (2) solid-state processes involving grain growth, (3) phase changes involving displacement transformation, and (4) phase changes such as spinodal decompositions. The driving force for grain growth and coarsening relates to minimization of interfacial energy. Analytical models and Monte-Carlo simulations are routinely carried out to analyze these phenomena [62, 72, 73].

In most of the alloy systems, the development of microstructure depends on a series of events. In the case of low-alloy steels, the sequences of events that occur are shown in Fig. 10 [74]. The model for microstructure development in low-alloy steel has a number of sub-models recorded on the sequences of events that the weld metal goes through. In low-alloy steel welds the properties of steel are improved by maximizing acicular ferrite phase constituent in the microstructure. Although

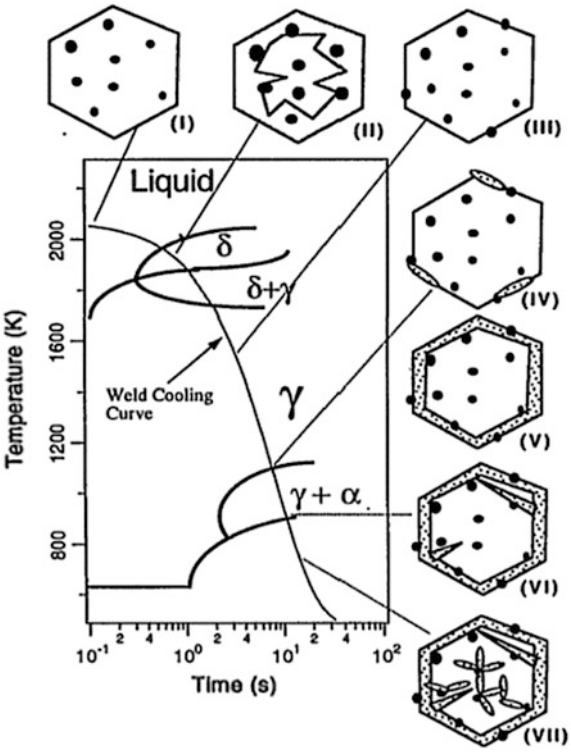

Fig. 10 The sequential formation of various phase changes that occur during cooling of the low-alloy steel weldment [74]

acicular ferrite forms from austenite, the feasibility of acicular ferrite formation depends on the presence of inclusions and austenite grain size. The microstructure evolution is controlled by the sequential formation of various phases as shown in Fig. 10.

4 Sensors, Intelligent Control, and Automation

Intelligent control and automation are critical elements of ICWE and intelligent weld manufacturing. As welding technology matures, there will be a steady decrease in manual welding. For increased accuracy and productivity, future welding operations will require welding systems with effective adaptive control [75]. Adaptive weld control is a closed loop approach that relies on measurements of relevant physical characteristics of the weld pool as the feedback and feedback control algorithms that decide how to respond to the feedback. Chen has discussed the framework for research and technology for intelligent weld manufacturing [76, 77]. This includes computer vision systems for visual feedback sensing, and control, neural network modeling of the process dynamics, and fuzzy logic and neurons self-leaving learning for control algorithms of arc welding. The machinery, controls, and materials needed

for ICWE are becoming more sophisticated, and the industry to produce them is growing. The needed sensors, controls, and control software, robots, and automatic machines are constantly being invented and integrated.

Zhang [78] has provided a comprehensive analysis on why a welding process should be monitored and how they can be effectively monitored for control. In his analysis, welding process is treated as a system, argued as a complex system, analyzed for its uncertainty and the necessity for monitoring and control, and is artificially decomposed for effective monitoring for control.

Naidu et al. [79] have conducted a survey of automatic control strategies for gas metal arc welding (GMAW) process. His results provide the status of feedback control techniques as applied to the GMAW process. Naidu's report describes the current state of sensing and control techniques involved such as classical control, neutral network, fuzzy logic control, adaptive control, and expert systems.

One of the critical elements of adaptive control is sensors. The function of the sensors is to provide information to the control system to face the necessary changes to the process to produce parts with highest integrity or at least meeting the specification despite variations in manufacturing conditions. Significant advances are being made in the development of sensors [44, 45, 80–86]. The sensors that are available currently are optical, arc, infrared, acoustic, and ultrasonic. For example, novel optical sensors have been used for observing welding operations and processes. Some have the resolution to view the weld puddle and to clearly see the solidification substructure (dendrites) formed on the pool surface [84].

For weld penetration, den Ouden [44] was able to correlate the weld pool oscillation frequency to the weld penetration, and Zhang [45] was able to correlate the weld pool geometry to the weld penetration. Zhang and his group have developed a real-time sensing and control device to predict weld penetration based on weld pool surface reflectivity [85]. In that system, the intensity of the weld pool surface reflectivity increases as the weld penetration increases. That correlation has been used to control the quality of the weld.

Seam tracking is a critical element in adaptive welding. Dilthey [84] developed a "through the arc" sensing device for seam tracking. Cook et al. [86] developed a seam-tracking control system based on fuzzy logic that tracks seams during pulsed GMAW. To produce welds with good quality and specified geometry, it is necessary to control the positioning of the welding torch. The method of using the arc itself as a sensor to sense and control the process is called "through the arc" tracking. Dilthey designed and implemented a fuzzy logic through-the-arc control system. The system provides an excellent real-time feedback control system for welding machine R&D.

Lv et al. [87] have developed a real-time arc length control and weld pool surface height prediction method by acoustic sensing and segmented self-adaptive proportional–integral–derivative (PID) controller during pulsed gas tungsten arc welding (GTAW). The experimental validation has demonstrated the feasibility of weld process control through the acoustic signals from the welding arc.

Recent developments using infrared sensing have demonstrated its potential for seam tracking [88]. Although these types of sensors are critical for ultimate process

control, significant emphasis should be placed on sensors for microstructure and properties [89]. The ultimate goal of the adaptive control is to regulate the process to make welds with desired quality, performance, and productivity. The current trend is to use an emerging tool known as "intelligent control." This will enable one to choose a desirable end factor such as property, defect control, or productivity instead of process parameters such as current, voltage, or speed to provide for appropriate control of the process.

Another intelligent welding approach is automated pass planning. Welders often take a fairly long time when they use multipass welding to weld large joints. With appropriate automated pass planning, the sequence and number of passes can be optimized, and a welding robot can complete the welding process in a much shorter time [90].

Significant advances are being made to produce parts intelligently through the development of sensors and feedback control systems. Neural networks are being applied for seam tracking. Cook et al. have developed neural network fuzzy logic control system [75].

Tight coupling of the welding variables imposes limitations on the extent of control that can be exercised. Cook et al. [86] discuss decoupling of welding variables for improved automatic control. The process considered includes GTAW, and GMAW. From the point of view of control, the process or the process variant that gives the most decoupling of the control parameters is desired because it would make it easier for control system design and would increase the range of control over the variable parameters.

Sadek and Drews [91] have investigated intelligent systems for welding process automation. They evaluated the idea and the implementation of two distinct multiserver systems for automated manufacturing based on a parallel computing architecture. They have shown that multiserver systems with distributed architectures offer considerable advantages over standard bus-based systems.

5 Friction Stir Welding

The four key elements to intelligent weld manufacturing that enable the production of high-quality welds with increased productivity, which again are process and process modeling, microstructure, properties, and process control and automation, are not unique to arc welding. Other forms of welding, including welding that occurs in the solid-state, are guided by these principles as well. One form of solid-state welding, Friction Stir Welding (FSW), in particular, has garnered attention from researchers in recent years as a highly dynamic, thermomechanical process with a rich potential for research endeavors into process modeling, control, and intelligent welding. FSW is relatively a new welding process developed by Wayne Thomas at The Welding Institute (TWI), Cambridge, UK [92, 93]. It is a solid-state process and involves plunging and rotating a tool at the joint to be made between two plates and traversing along the joint line. Heat generated due to

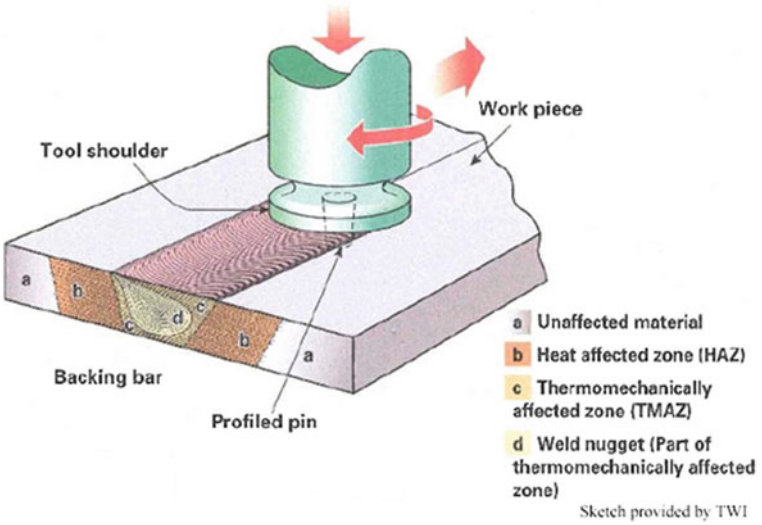

Fig. 11 Schematic of friction stir welding process showing the interaction of the tool with the material (courtesy of TWI)

friction and plastic deformation softens the workpiece, and flow of the metal brings about a metallurgical bond. A schematic of the process is shown in Fig. 11. It has great potential for applications in automotive, aerospace, transportation, and energy industries. While the fundamental underlying theories and methods for modeling of the weld process, conducting process development, and performing analysis of weld properties and microstructure are perhaps not significantly different, specific techniques are tailored to meet the unique details, conditions, and constraints of the FSW process. With respect to process modeling, researchers have approached FSW from both analytical and numerical modeling perspectives. DebRoy and his group [94–97] have carried out extensive modeling and simulation studies of FSW processes related to 3D heat and material flow, torque and power, tool durability, and dissimilar materials joining. Nunes developed a widely utilized analytical model [98].

5.1 Control and Automation of FSW

In order to achieve high-quality FSW, a well-understood framework for control and automation is imperative, and the variables to control and automate the process are different from that of commercial fusion welding processes. Cook [99, 100] and Smith [101, 102] were among the first to document the challenges and opportunities associated with robotic FSW. One of the most important relationships to control is relative tool-workpiece positioning, i.e. the tool plunge depth. This relationship can

impact weld penetration, defect formation, tool wear, heat generation, and resulting weld properties. Position control alone can be inadequate due to inconsistent workpiece dimensions, thermal expansion, robot deflection due to high process forces, or the welding of complex geometries. For these reasons, force or torque control in FSW has become important for researchers and manufacturers, with Longhurst et al. [103–107] contributing significantly in this area, along with many others [108–110]. Force sensing is thus an important capability as well, with sensing typically accomplished via load cell [111–114], but Smith et al. [115] demonstrated that axial force can also be sensed via measurement of robot motor currents and use of the Jacobian [116] relationship.

5.2 Advanced Sensing and Intelligent FSW

Given the success of 'through-the-arc' sensing techniques, 'through-the-tool' sensing has been explored in FSW as a means of similarly improving process characteristics. Smith et al. [117] and De Backer et al. [118] documented problems in robotic FSW, such as planned-path deviations caused by high forces. While, Soron et al. [119] and Fleming et al. [120] showed that it is possible to compensate for deviations based on force sensing (and the use of vision systems is an option too [118, 121]), novel 'through-the-tool' joint tracking capabilities have been successfully demonstrated [122–124]. Intelligent FSW describes the correlation of process output data to welding outcomes to augment the knowledge of researchers and to improve process efficiency. Boldsaikhan et al. have been significant contributors in this area, with a focus on defect detection and with the use of artificial neural networks [125–128]. Both Fleming et al. [129] and Gibson et al. [130] used dimensional reduction techniques to classify weld quality, and defect formation caused by tool wear has been detected as well [131]. Additional efforts in intelligent FSW by Bhowmick [132], Jene et al. [133], Britos et al. [134–136], and Burford et al. [137] have included successful attempts to map process input parameters to welding outcomes and to correlate force signatures with weld features.

6 Integration of Weld Models

To develop an intelligent weld manufacturing, all the four principal elements defined by various sub-models must be integrated. Integration of all the four principal elements mentioned early with sub-models is a very challenging and a monumental task. This can be achieved but it would be costly and time consuming. Such integration is essential to the development of intelligent weld manufacturing. Microstructural evolution in low-alloy steel welds is described as an example. Evolution of microstructures in a low-alloy weld is not defined by a single event. It occurs over a range of temperatures. First, as the liquid metal cools, the oxygen in

the liquid steel reacts with the deoxidizing element in the liquid to form an oxide inclusion that acts as a nucleating agent for solid δ-ferrite. This occurs over a range of temperatures. Figure 9 shows schematic of continuous cooling transformation showing the development of weld metal microstructure in low-alloy steels. Upon cooling, δ-ferrite forms and with further cooling the δ-ferrite transforms to austenite and austenite transforms to γ-ferrite with different morphologies [84]. These changes occur sequentially. Physical processes that occur at elevated temperatures, such as plasma–liquid metal interaction, also affect the ultimate microstructure obtained. Vaporization and dissolution of gases change the composition of the liquid. This change in composition that occurs at elevated temperatures affects the microstructural evolution at lower temperatures. Therefore, an integrated model is necessary to predict the evolution of microstructure in the low-alloy steel welds.

Integrated process models (thermal models) and microstructure models were developed in the nineties [89, 91, 138, 139]. However, integration of the integrated process models with the microstructure models has been achieved only recently [39, 89]. The ability to predict microstructural evolution in weld metal is critical to the development of intelligent manufacturing. Using a CT and CK framework, Babu [61] describes the phase stability and rates of change during phase transformation during a weld thermal cycle. The work carried out at universities, national laboratories, and industrial research organizations in the United States, Europe, and Asia laid the foundation for developing an integrated thermomechanical and microstructure models. These developments were summarized by Kirkaldy [138] in a block diagram (Fig. 12). First the thermal model simulates three-dimensional (3D) temperature distribution as a function of process parameters and time [61]. The materials model uses thermal cycle data to predict the microstructure evolution and its effect on transient mechanical properties. The transient change in thermal and mechanical properties is fed into a finite-element structural model to predict plastic stress distribution. That information is used for prediction of final properties, residual stress, and distortion.

Pavlyk et al. [140] modeled the coupling of simulated weld-solidification microstructure with a macroscopic fluid flow model. Several microstructural simulation techniques have been developed. Pavlyk et al. used a coupled CA-FDM technique to simulate weld dendrite structure. They determined solidification conditions during weld pool solidification. As in the case of accurate physical models, calculations are carried out at microstructural spatial resolution.

DebRoy et al. [39] carried out weld microstructure calculations from the fundamentals of transport phenomena in the arc welding of low-alloy steel welds. A 3D transient heat and fluid flow model was used to calculate the cooling rates in a manual GTA weld of different compositions of low-alloy steel welds. The weld metal composition was used to calculate the time temperature and transformation (TTT) diagram. These TTT diagrams were converted to continuous cooling transformation (CCT) diagrams. Cooling rates were coupled to TTT diagram to obtain CCT diagrams, using which the various microstructural constituents were determined.

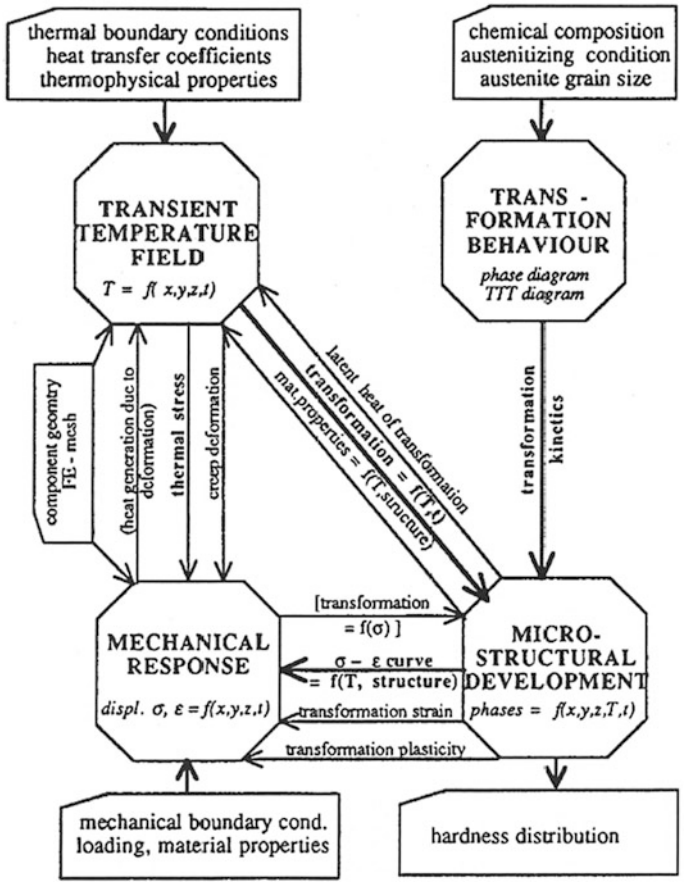

Fig. 12 Block diagram describing integrated weld modeling methodology by Kirkaldy [138]

Feng et al. [141, 142] developed modeling approach based on ICWE to predict the mechanical behavior of resistance spot welds. They devised an incrementally coupled electric-thermal-mechanical-metallurgical model to predict weld microstructure and properties as a function of steel chemistry and welding conditions. The resulting microstructure and property distribution in a spot weld is then used in a damage-mechanics-based structural model to predict the strength and failure of resistance spot welds of advanced high-strength steels for automotive applications. With such an ICWE-based model, it is possible to realistically simulate the effects of welding conditions and steel chemistry on the highly heterogeneous microstructure distribution (Fig. 13) as well as the deformation, strength, and failure of the weld as function of microstructure and property distributions (Fig. 14).

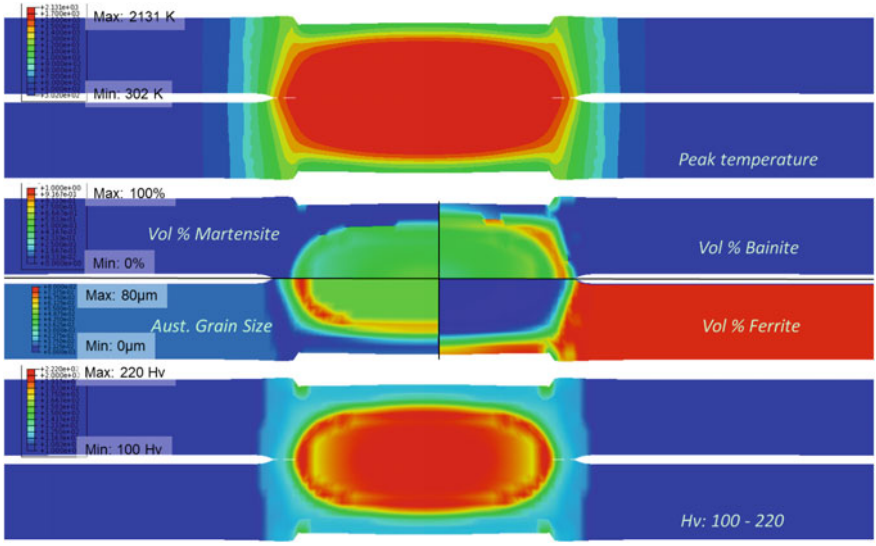

Fig. 13 Prediction of weld nugget formation, grain growth, microstructural constituents and resulting microhardness distribution of a DQSK steel during resistance spot welding [142]

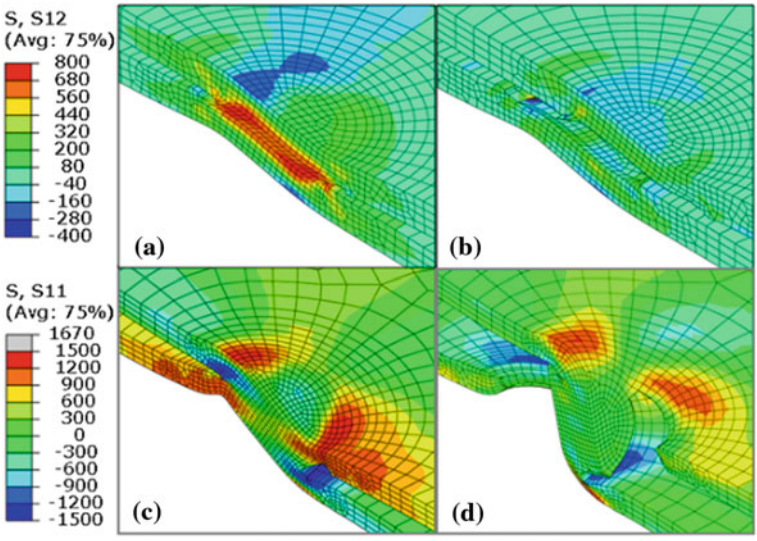

Fig. 14 Predicted failure mode changes of resistance spot weld of a boron steel [142]

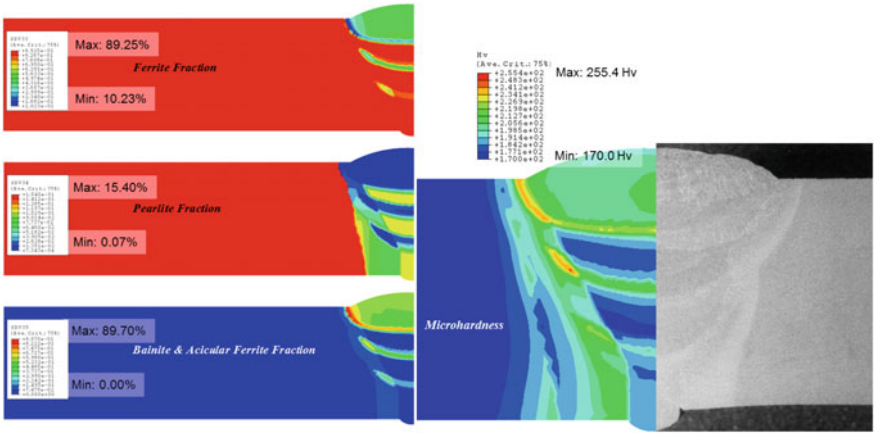

Fig. 15 Prediction of microstructure constituents and resulting microhardness distribution in a X65 pipeline steel [143]

The ICWE modeling approach taken by Feng et al. is also applicable to arc welding processes and friction stir welding of steels and aluminum alloys [143, 144]. In the case of a multipass X65 pipeline steel, the coarse grain HAZ exhibited elevated hardness due to formation of different microstructure constituents in solid-state phase transformation as a result of grain growth in the coarse grain heat affected zone (CGHAZ) (Fig. 15). The effect of multiple welding thermal cycles on the microstructure is also faithfully simulated. Such a model has been used to optimize the welding process conditions and weld filler metal chemistry to tailor the weld microstructure and weld residual stress in high-strength steel to eliminate hydrogen-induced cracking, improve weld fatigue life, and minimize weld distortions [145].

Feng et al. [144] demonstrated that the ICWE model is capable of predicting the effect of welding process conditions on the microstructure, strength, and deformation and failure of friction stir welded Al6061 alloys. The effect of welding speed on the temperature, microstructure, strength, and residual stress can be predicted with high fidelity (Fig. 16). Such a model has been used to guide the welding process development to improve the properties of friction stir welds.

Doyle and Conrady describe a program for the design, construction, and demonstration of a prototype programmable automated welding system [146]. The program, known as the programmable automated welding system (PAWS), was sponsored by the US Naval Surface Warfare Center. Doyle and Conrady developed a system with control capabilities to accept, arbitrate, and reach its inputs from multiple sensors.

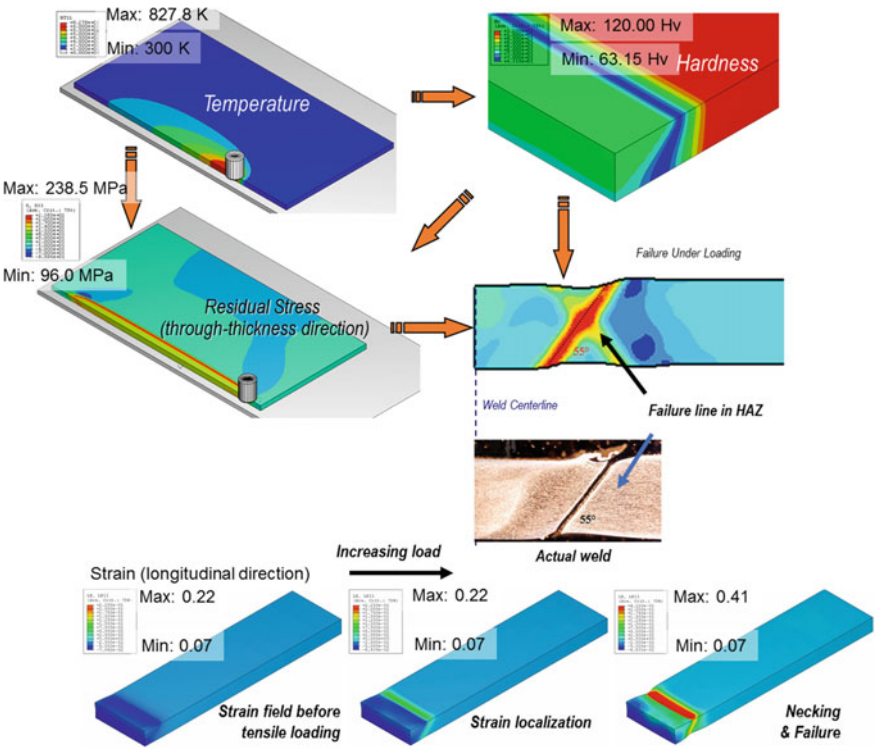

Fig. 16 Integrated multiphysics simulations provide realistic predictions of performance and failure of Al 6061 friction stir welds [144]

7 Conclusion

Intelligent weld manufacturing involves sensing and control of the heat source, position, weld defect formation, and ultimately microstructure and properties. The ultimate goal of intelligent weld manufacturing is to produce high-quality welds with increased productivity. Computational modeling and simulation are key parts of intelligent weld manufacturing. Computational modeling of weld manufacturing involves solution to a problem with many highly coupled and nonlinear variables. It requires a multidisciplinary ICWE modeling approach to cover and connect four major elements—processes, control and automation, microstructure, and properties—for intelligent weld manufacturing.

Intelligent weld manufacturing is at a crossroads. We are at a point in the research at which major breakthroughs are possible to enable us to attain the ultimate goal of intelligent weld manufacturing. Yet significant challenges remain. In ICWE, it is now possible to perform a detailed simulation with sufficient fidelity to achieve design and manufacturing optimization of structural welding of vehicles or welding of nuclear reactor components. However, this type of weld simulation is

very time consuming with today's computers. It often takes weeks or months to perform such a detailed simulation. Research and development to utilize high-performance computing systems would be a potential direction to drastically reduce the computational time (by 103 or more) for intelligent weld manufacturing. Artificial intelligence and deep machine learning would be another potential solution to integrate ICWE into intelligent weld manufacturing.

Acknowledgements The authors would like to acknowledge Ms. Shirin Badlani for her help in preparing the manuscript. We would also like to acknowledge Prof. Yuming Zhang (University of Kentucky) and Prof. G.E. Cook (Vanderbilt University) for their review and valuable comments. This material is based upon work supported by the U.S. Department of Energy, Office of Science, Office of Basic Energy Sciences, Office of Nuclear Energy, and Office of Energy Efficiency and Renewable Energy under a prime contract with Oak Ridge National Laboratory (ORNL). ORNL is managed by UT-Battelle, LLC for the U.S. Department of Energy under Contract DE-AC05-00OR22725.

References

1. Drews P, Starke G (1994) Welding in the century of information technology. Weld. World 34:1–20
2. Dilthey U, Stein L (1992) Robot system for arc welding-current position and future trends. Weld. Cutting 8:E150–E152
3. Pan JL (1999) A survey of welding sciences in 21st century. In: Proceedings of 9th Chinese Welding Conference, vol 1, CWC, Tianjin, China, p D001-D017
4. Trailer (1995) Manufacturer depends on robotic welding to boost production. Weld J 74(7): 49–51
5. Tarn TJ, Chen SB, Zhou CJ (2004) Robotic welding, intelligence and automation. Springer, Berlin
6. Tarn TJ, Chen SB, Zhou CJ (2007) Robotic welding, intelligence and automation. Springer, Berlin
7. Tarn TJ, Chen SB, Fang G (2011) Robotic welding, intelligence and automation. Springer, Berlin
8. Chen SB (2015) Robotic welding, intelligence and automation, advances in intelligent systems and computing. Springer, Singapore
9. Chen SB, Lou YJ, Wu L et al (2000) Intelligent methodology for sensing, modeling and control of pulsed GTAW: Part l, bead-on-plate welding. Weld. J. 79(6):151s–163s
10. David SA, Vitek JM. International trends in welding research (1986, 1989, 1992, 1995, 1998, 2001, 2004, 2008, 2010), ASM Intl, Material Park, OH
11. Cerjak H, Bhadesha HKDH. Mathematical modeling of weld phenomenon (1993, 1995, 1997, 1998, 2000, 2002), Springer, Berlin
12. Friedman E (1978) Analysis of weld puddle distortion and its effect on penetration. Weld. J. 57(6):161s–166s
13. Jhaveri P, Moffat WG, Adams CM (1962) The effect of plate thickness and radiation on heat flow in welding and cutting. Weld. J. 41(1):12s–16s

14. Nippes EF, Merrill LL, Savage WF (1949) Cooling rates in arc welds in ½ plates. Weld. J. 28(12):556s–564s
15. Oreper GM, Szekely J (1984) Heat-flow and fluid-flow phenomena in weld pools. Fluid. Mech. 147:53–79
16. Tsai NS, Eagar TW (1984) The distribution of heat source in arc welding. In: Proceedings of the international conference modeling of casting and welding process II, AIME, New York, p 317
17. Kou S, Sun DK (1985) Fluid flow and weld penetration in stationary arc welds. Metall. Trans. A 16:203–213
18. Kou S, Wang YH (1986) Weld pool convection and its effects. Weld. J. 65:63s–70s
19. Sundell RE, Correa SM, Harris LP, et al (1986) GE Report 86SRD013
20. Zacharia T, Eraslan AH, Aidun DK (1988) Modeling of non-autogenous welding. Weld. J. 67(1):18s–27s
21. Zacharia T, Eraslan AH, Aidun DK et al (1989) Three-dimensional transient model for arc welding process. Metall. Trans. B 20:645–659
22. Zacharia T, David SA, Vitek JM et al (1989) Weld pool development during GTA and laser beam welding of type 304 stainless steel, Part I—theoretical analysis. Weld. J. 68(2):499s–509s
23. Zacharia T, David SA, Vitek JM et al (1991) Computational modeling of stationary gas-tungsten-arc weld pools and comparison to stainless steel 304 experimental results. Metall Trans B 22B:243–257
24. Choo RT, Szekely J (1991) The effect of gas shear stress on Marangoni flows in arc welding. Weld. J. 70:223s–233s
25. David SA, DebRoy T (1992) Current issues and problems in welding science. Science 257:497–502
26. Zacharia T, Bjeria MA, Tmorovic SC (1993) International conference on modeling and control of joining processes. MCJP, Orlando, FL
27. Miller R, DebRoy T (1990) Energy absorption by metal-vapour-dominated plasma during carbon dioxide laser welding of steels. J. Appl. Phys. 68:2045–2050
28. Rosenthal D (1941) Mathematical theory of heat distribution during welding. Weld. J. 20 (5):220s–234s
29. Rosenthal D (1946) The theory of moving sources of heat and its application to metal treatments. Trans. ASME 68:849–866
30. Zacharia T, Vitek JM, Goldak JA et al (1995) Modeling of fundamental phenomena in welds. Model. Simul. Mater. Sci. Eng. 2:265–288
31. Kou S, Le Y (1983) Three-dimensional heat flow and solidification during the autogenous GTA welding of aluminum plate. Metall. Trans. A 14A:2243–2253
32. Chan C, Mazumder J, Chen MM (1984) A two-dimensional transient model for convection in laser melted pool. Metall. Trans. A 15A:2175–2184
33. Paul A, DebRoy T (1988) Free surface flow and heat transfer in conduction mode laser welding. Metall. Trans. B 19B:851–858
34. Zacharia T, David SA, Vitek JM et al (1989) Heat transfer during Nd-YAG pulsed laser welding and its effect on solidification structure of austenitic stainless-steels. Metall. Trans. A 20A:957–967
35. Zacharia T, David SA, Vitek JM (1991) Effect of convection in weld pool development. In: Proceedings of symposium on the metals science and joining, Cincinnati, OH, pp 257–263
36. Matsunawa A (1992) Modeling of heat and fluid flow in arc welding. International Trends in Welding Research, ASM International, Materials Park, OH
37. Kou S, Le Y (1988) Welding parameters and the grain-structure of weld metal—a thermodynamic consideration. Metall. Trans. 19(4):1075–1082
38. Zacharia T, David SA, Vitek JM et al (1991) Effect of evaporation and temperature-dependent material properties on weld pool development. Metall. Trans. B 22B:233–241

39. Mundra K, DebRoy T, Keller KM (1996) Numerical prediction of fluid flow and heat transfer in welding with a moving heat source. Numer. Heat Transfer Part A 29(2):115–129
40. DebRoy T (1995) Role of interfacial phenomena in numerical analysis of weldability, mathematical modelling of weld phenomena II. Dissertation, The Institute of Materials, London, pp 3–21
41. Heiple CR, Roper JR (1982) Mechanism for minor element effect on GTA fusion zone geometry. Weld. J. 61(4):97s–102s
42. Heiple CR, Burgardt P (1985) Effects of SO_2 shielding gas additions on GTA weld shape. Weld. J. 64(6):159s–162s
43. Szekely J, Preper GM, McKelliget J (1986) Proceedings of the engineering foundation conference on the modeling and control of welding and casting processes. Springer, Santa Barbara, CA, USA
44. Hu B, den Ouden G (1999) Weld penetration sensing and control during GTA welding using weld pool oscillation. Trends in Welding Research, ASM International, Materials Park, OH
45. Zhang YM, Li L (1999) Controlling joint penetration based on weld pool geometry. Trends in Welding Research, ASM International, Materials Park, OH
46. Zhang YM, Wu L, Walcott BL et al (1993) Determining joint penetration in GTAW with vision sensing of weld face geometry. Weld. J. 72(10):463s–469s
47. Batanov VA, Bunkin FV, Prokhorov AM et al (1973) Evaporation of metallic targets caused by intense optical radiation. Sov. Phys. 36:311–322
48. Chan CL, Mazumder J (1987) One-dimensional steady-state model for damage by vaporization and liquid expulsion due to laser-material interaction. J. Appl. Phys. 62 (11):4576–4586
49. Khan PA, DebRoy T (1984) Alloying element vaporization and weld pool temperature during laser-welding of ANSI 202 stainless-steel. Metall. Trans. B 15(4):641–644
50. Mundra K, DebRoy T (1993) Calculation of weld metal composition change in high-power conduction mode carbon-dioxide laser-welded stainless-steels. Metall. Trans. B 24(1): 145–155
51. Mundra K, DebRoy T (1993) Role of thermophysical properties in weld pool modeling. Weld. J. 72(1):1s–9s
52. Banerjee A, Onneby C, DebRoy T, et al (1993) Nitrogen dissolution in the weld pool. Trends in Welding Research, ASM International, Materials Park, OH
53. Vitek JM, Iskander YS, Oblow EM, et al (1999) Neural network modeling of pulsed-laser weld pool shape in aluminum alloy welds. Trends in Welding Research, ASM International, Materials Park, OH
54. Bhadeshia HKDH (2009) Neural networks and information in materials science. Stat. Anal. Data Min. 1:296–305
55. Kovacevic R, Zhang YM (1997) Neurofuzzy model-based weld fusion state estimation. IEEE Control Syst. Mag. 17(2):30–42
56. Zhang YM, Kovacevic R (1998) Neurofuzzy model-based predictive control of weld fusion zone geometry. IEEE Trans. Fuzzy Syst. 6(3):389–401
57. Vitek JM, Iskander YS, Oblow EM, et al (1999) Neural network model for predicting ferrite number in stainless steel welds. In: Trends in Weld Research, ASM International, Material Park, OH
58. Sterjovski Z, Nolan D, Carpenter MR et al (2005) Artificial neural networks for modeling the mechanical properties of steels in various applications. J. Mater. Process. Technol. 170:536–544
59. Sterjovski Z, Pitrun MD, Nolan D et al (2007) Artificial neural networks for predicting diffusible hydrogen content and cracking susceptibility in rutile flux-cored arc welds. J. Mater. Process. Technol. 184(1–3):420–427
60. Vitek JM, David SA, Hinman CR (2003) Improved ferrite number prediction model that accounts for cooling rate effects—part 1: model development—details of a prediction model based on a neural network system of analysis are described. Weld. J. 82(1):10s–17s

61. Babu SS (2009) Thermodynamic and kinetic models for describing microstructure evolution during joining of metals and alloys. Int. Mater. Rev. 54(6):333–367
62. David SA, Vitek JM (1989) Correlation between solidification parameters and weld microstructures. Int. Mater. Rev. 34(5):213–245
63. Elmer JW, Wong J, Ressler T (2000) In-situ observations of phase transformations during solidification and cooling of austenitic stainless-steel welds using time-resolved X-ray diffraction. Scr. Mater. 43(8):751–757
64. Elmer JW, Wong J, Ressler T (2001) Spatially resolved X-ray diffraction mapping of phase transformations in the heat-affected zone of carbon-manganese steel arc welds. Metall. Mater. Trans. A 32(5):1175–1187
65. Flemingo MC (1974) Solidification processing. McGraw Hill, NY
66. Kurz W, Fisher DJ (1986) Fundamentals of solidification. Trans SEM Publication, Acdemana Dort, Switzerland
67. David SA, Siefert JA, DuPont JN et al (2015) Weldability and weld performance of candidate nickel base super-alloys for advanced ultra-supercritical fossil power plants part I: fundamentals. Sci. Technol. Weld. Joining 20(7):532–552
68. Savage WF, Lundin CD, Aronson A (1965) Weld metal solidifications mechanics. Weld. J. 44(4):s175
69. Rappaz M, David SA, Vitek JM et al (1990) Analysis of solidification microstructures in Fe-Ni-Cr single-crystal welds. Metall. Trans. A 21A:1767–1782
70. Brooks JA, Baskes NT, Grelich FA (1991) Solidification modeling and solid-state transformations in high-energy density stainless-steel welds. Metall. Trans. A 22(4):915–926
71. Lippold JC, Savage W (1980) Modeling of casting and welding processes. Warrendale, PA
72. David SA, Vitek JM (1993) Mathematical modeling of weld Phenomena. The Institute of Materials, London, pp 41–59
73. Radhakrishnan B, Zacharia T (1995) Simulation of curvature-driven grain-growth by using a modified Monte-Carlo algorithm. Metall. Mater. Trans. 26:167–180
74. Babu SS, David SA (2002) Inclusion formation and microstructure evolution in low alloy steel welds. ISIJ Int. 42(12):1344–1353
75. Cook GE, Andersen K, Barrathe KJ (1990) Feedback and adaptive control in welding. In: Proceedings of Recent Trends in Welding Technology, ASM Intl, Materials Park, OH
76. Chen SB, Lou YJ, Wu L et al (2000) Intelligent methodology for sensing, modeling and control of pulsed GTAW: part I—bead-on-plate welding. Weld. J. 79(6):151s–163s
77. Chen SB, Lou YJ, Wu L et al (2000) Intelligent methodology for sensing, modeling and control of pulsed GTAW: part II—Butt joint welding. Weld. J. 79(6):164s–174s
78. Zhang YM (2008) An analysis of welding process monitoring and control. Real-Time Weld Process Monitoring, Cambridge, England, pp. 1–11
79. Naidu DS, Moore KL (1999) Automatic control strategies for gas metal arc welding: a status survey. Trends in Welding Research, ASM International Materials Park, OH
80. Richardson RW, Gutow DA, Anderson RA et al (1984) Coaxial arc weld pool viewing for process monitoring and control. Weld. J. 63(3):43–49
81. Bolstad J (1987) Advances in automation for precision arc welding. In: Proceedings of Edison Welding Institute, EWI, Columbus, OH
82. Bolikel C, Mazumder J (1992) Optical diagnostics of laser weld pool free surface. In: 3rd International Conference on Trends in Welding Research, ASM International, Materials Park, OH
83. Nagarajan S, Banderjee P, Chen WH et al (1991) Control of the welding process using infrared sensors. IEEE Trans. Robot. Autom. 8(1):86–93
84. Dilthey U, Gollnick J (1999) Through-the-arc sensing in GMA-welding with high speed rotating torch. In: Proceedings of Trends in Welding Research, ASM International, Materials Park, OH
85. Chen J, Chen J, Feng Z, et al (2016) Dynamic evolution of the weld pool reflection during weld penetration development. In: IEEE International Conference on Advanced Intelligent Mechatronics, IEEE, Banff, Albert, Canada

86. Barnett RJ, Cook GE, Damrongsak D et al (1999) Through-the-arc sensing and control in pulsed gas tungsten metal arc welding. Trends in Welding Research, ASM International, Material Park, OH
87. Lv N, Zhong J, Chen H et al (2014) Real-time control of welding penetration during robotic GTAW dynamical process by audio sensing of arc length. Int. J. Adv. Manuf. Technol. 74 (1–4):235–249
88. Chin BA, Madsen NH, Goodling JS (1983) Infrared thermography for sensing the weld process. Weld. J. 62(9):227s–234s
89. Babu SS, David SA, Vitek JM et al (1995) Phase transformations and microstructure development in low alloy steel welds. In: Proceedings of International Symposium in Phase Transformation during Thermomechanical Processing of Steels, Vancouver, Canada
90. Yan SJ, Ong SK, Nee AYC (2016) Optimal pass planning for robotic welding of large-dimension joints with deep grooves. Procedia CIRP 56:188–192
91. Sadek Alfredo CA, Drews P (2006) Intelligent systems for welding process automation. Braz. Soc. Sci. Eng. 26(1):25–29
92. Thomas WM (1991) Friction stir butt welding. International Patent Application No PCT/GB92 Patent Application No. 9125978.8
93. Thomas WM, Nicholas ED (1997) Friction stir welding and friction extrusion of aluminium and its alloys. In: 3rd World Congress on Aluminium, Limassol, Cyprus
94. DebRoy T, De A, Bhadeshia HKDH et al (2012) Tool durability maps for friction stir welding of an aluminum alloy. In: Proceedings of the Royal Society A—Mathematical Physical and Engineering Sciences, vol. 468, pp. 3552–3570
95. Manvatkar VD, Arora A, De A et al (2012) Neural network models of peak temperature, torque, traverse force, bending stress and maximum shear stress during friction stir welding. Sci. Technol. Weld. Joining 17(6):460–466
96. Nandan R, Roy GG, Lienert TJ et al (2007) Three-dimensional heat and material flow during friction stir welding of mild steel. Acta Mater. 55:883–895
97. Nandan R, Prabu B, De A et al (2007) Improving reliability of heat transfer and fluid flow calculations during friction stir welding of dissimilar aluminum alloys. Weld. J. 86 (10):313s–322s
98. Nunes AC, Bernstein EI, McClure JC (2000) A rotating plug model for friction stir welding. In: Proceedings of the 81st American Welding Society Convention, AWSC, Chicago, IL
99. Cook GE, Smartt H, Mitchell J et al (2003) Controlling robotic friction stir welding. Weld. J. 8:28–34
100. Cook GE, Crawford R, Clark D et al (2004) Robotic friction stir welding. Ind. Robot 31 (1):55–63
101. Smith C (2007) Robots and machines for friction stir welding/processing. Friction Stir Weld. Process. 11:219–233
102. Smith C (2000) Robotic friction stir welding using a standard industrial robot. In: Proceedings of the 2nd International Symposium on Friction Stir Welding, TWI, Cambridge, UK
103. Longhurst WR (2009) Force control of friction stir welding. Dissertation, Vanderbilt University
104. Longhurst WR, Strauss AM, Cook GE et al (2010) Investigation of force controlled friction stir welding for manufacturing and automation. Proc. Inst. Mech. Eng. Part B: J Eng Manuf. 224(6):937–949
105. Longhurst WR, Strauss AM, Cook GE (2011) Identification of the key enablers for force control of robotic friction stir welding. J. Manuf. Sci. Eng. 133(3):31008–31019
106. Longhurst WR, Strauss AM, Cook GE et al (2010) Torque control of friction stir welding for manufacturing and automation. Int. J. Adv. Manuf. Technol. 51:905–913
107. Longhurst WR, Cox CD, Gibson BT et al (2014) Applied torque control of friction stir welding using motor current as feedback. Proc. Inst. Mech. Eng. Part B: J. Eng. Manuf. 228 (8):947–958

108. Gibson BT, Lammlein DH, Prater TJ et al (2014) Friction stir welding: process, automation, and control. J. Manuf. Process. 16(1):56–73
109. Fehrenbacher A, Duffie NA, Ferrier NJ et al (2011) Toward automation of friction stir welding through temperature measurement and closed-loop control. J. Manuf. Sci. Eng. 133 (5):1–12
110. Cederqvist L, Garpinger O, Oberg T (2012) Control of temperature, power input, and tool depth during FSW of copper canisters. In: Proceedings of the 9th International Symposium on Friction Stir Welding, TWI, Cambridge, UK
111. Blignault C, Hattingh DG, Kruger GH et al (2008) Friction stir weld process evaluation by multi-axial transducer. Measurement 41:32–43
112. Gibson BT (2011) Custom low-cost force measurement methods in friction stir welding. Dissertation, Vanderbilt University
113. Gibson BT, Cox CD, Longhurst WR et al (2012) Exploiting robotic link deflection for low-cost force measurement in manufacturing. Measurement 45:140–142
114. Gibson BT, Cox CD, Aguilar JR et al (2012) Low-cost wireless force sensor design with applications in friction stir welding. In: Proceedings of 9th International Trends in Welding Research Conference, RTWRC, Chicago, IL
115. Smith C, Hinrichs J, Crusan W (2003) Robotic friction stir welding: state-of-the-art. In: Proceedings of the 4th International Symposium on Friction Stir Welding, TWI, Cambridge, UK
116. Craig J (2005) Introduction to Robotics Mechanics and Control. Pearson Prentice Hall
117. Smith CB, Schroeder K, Fehrenbacher A (2012) An automated path planning and programming system with real-time adaptive control for friction stir processing of cast surfaces. In: Proceedings of the 9th International Symposium on Friction Stir Welding, TWI, Cambridge, UK
118. De Backer J, Christiansson AK, Oqueka J et al (2012) Investigation of path compensation methods for robotic friction stir welding. Ind. Robot Int. J. 39(6):601–608
119. Soron M, De Backer J, Christiansson AK et al (2010) A local model for online path corrections in friction stir welding. In Proceedings of Friction Stir Welding and Processing Conference, FSWPC, Lille, France
120. Fleming PA, Lammlein DH, Wilkes DM et al (2009) Misalignment detection and enabling of seam tracking for friction stir welding. Sci. Technol. Weld. Joining 14(1):93–96
121. Christner B, Hansen M, Skinner M et al (2003) Friction stir welding system development for thin gauge aerospace structures. In: Proceedings of the 4th International Symposium on Friction Stir Welding, TWI, Cambridge, UK
122. Fleming PA, Hendricks CE, Wilkes DM et al (2009) Automatic seam-tracking of friction stir welded T-joints. Int. J. Adv. Manuf. Technol. 45:490–495
123. Fleming PA, Hendricks CE, Cook GE et al (2010) Seam-tracking for friction stir welded lap joints. J. Mater. Eng. Perform. 19(8):1128–1132
124. Gibson BT, Cox CD, Ballun MC et al (2014) Automatic tracking of blind sealant paths in friction stir lap joining. J. Aircr. 51(3):824–832
125. Boldsaikhan E, Corwin E, Logar A et al (2006) Neural network evaluation of weld quality using FSW feedback data. In: Proceedings of the 6th International Symposium on FSW, FSW, Saint-Sauver, Canada
126. Boldsaikhan E (2008) The use of feedback forces for non-destructive evaluation of friction stir welding. Dissertation, South Dakota School of Mines and Technology
127. Boldsaikhan E, Corwin E, Logar A et al (2011) The use of neural network and discrete Fourier transform for real-time evaluation of friction stir welding. Appl. Soft Comput. 11:4839–4846
128. Boldsaikhan E, Bharat J, Logar A (2010) A phase space approach to detecting volumetric defects in friction stir welding. In: Proceedings of the 8th International Symposium on Friction Stir Welding, TWI, Cambridge, UK
129. Fleming PA, Lammlein DH, Wilkes DM et al (2008) In-process gap detection in friction stir welding. Sens. Rev. 28(1):62–67

130. Gibson BT, Wilkes DM, Cook GE et al (2013) In-Process detection of faying surface sealant application flaws in friction stir welding. J. Aircr. 50(2):567–575
131. Gibson BT, Tang W, Peterson AG et al (2017) Evaluating the potential for remote in-process monitoring of tool wear in friction stir welding of stainless steel. J. Manuf. Sci. Eng. Accepted manuscript published online, July 13
132. Bhowmick A (2010) Prediction of friction stir weld quality using self-organized maps. Dissertation, Aukland University of Technology, Aukland, New Zealand
133. Jene T, Dobman G, Wagner G (2008) Monitoring of the friction stir welding process to describe parameter effects on joint quality. Weld. World 52(9–10):47–53
134. Britos P, Widener C, Brown J et al (2009) Correlation between ultrasonic phased array and feedback force analysis of friction stir welds. Friction Stir Welding and Processing V, Springer, Berlin
135. Britos P, Widener C, Boldsaikhan E et al (2010) Probability of detection analysis of NDT methods for friction stir welded panels. In: Proceedings of the 8th International Symposium on Friction Stir Welding, TWI, Cambridge, UK
136. Britos P (2010) Probability of detection in friction stir welding using non-destructive evaluation techniques. Dissertation, Wichita State University
137. Burford D, Britos P, Boldsaikhan E (2010) Evaluation of friction stir weld process and properties for aerospace application: e-NDE for friction stir processes. In: Proceedings of FAA Joint Advanced Materials & Structures (JAMS) 6th Annual Technical Review Meeting, JAMS, Seattle, USA
138. Kirkaldy JS (1991) Diffusion-controlled phase-transformations in steels—theory and applications. Scand. J. Metall. 20:50–61
139. Mundra BK, DebRoy T, Babu SS et al (1997) Weld metal microstructure calculations from fundamentals of transport phenomena in the arc welding of low-alloy steels. Weld. J. 76(4): s163–s171
140. Pavlyk V, Dithey U (2004) Simulation of weld solidification microstructure and its coupling to the macroscopic heat and fluid flow modelling. Model. Simul. Mate. Sci. Eng. 12: S33–S45
141. Feng Z, Babu SS, Riemer BW et al (2001) Modeling of resistance spot welds: process and performance. Weld. World 45:18–24
142. Zheng L, Feng Z, Simunovic S et al (2013) Integrated computational model for resistance spot welds in auto-body crashworthiness CAE: process, properties, and performance. In: Proceedings of 2nd World Congress on Integrated Computational Materials Engineering, WCICME, Salt Lake City, Utah, USA
143. Chauhan V, Feng Z (2002) Gas transmission pipeline girth weld residual stresses and the effects of hydrotesting. In: Proceedings of 4th International Pipeline Conference, ASME, Calgary, Canada, pp. 381–388
144. Feng Z, Wang XL, David SA et al (2007) Modelling of residual stresses and property distributions in friction stir welds of aluminum alloy 6061-T6. Sci. Technol. Weld. Joining 12:348–356
145. Feng Z, David SA, Tzelepis DA et al (2015) US Patent Application Pub No 2016/0228998A1
146. Manly TD, Doyle TE (1993) Arc hydrogen monitoring for synergic GMAW. In: Proceedings of International Trends in Welding Science and Technology, ASM International Materials Park, OH

Part II
Research Papers

A Reinforcement Learning Based Approach for Welding Sequence Optimization

Jesus Romero-Hdz, Baidya Saha, Gengis Toledo-Ramirez and Ismael Lopez-Juarez

Abstract We develop and implement a Q-learning based Reinforcement Learning (RL) algorithm for Welding Sequence Optimization (WSO) where structural deformation is used to compute reward function. We utilize a thermomechanical Finite Element Analysis (FEA) method to predict deformation. We run welding simulation experiment using well-known Simufact® software on a typical widely used mounting bracket which contains eight welding beads. RL based welding optimization technique allows the reduction of structural deformation up to $\sim 66\%$. RL based approach substantially speeds up the computational time over exhaustive search.

Keywords Reinforcement learning (RL) · Welding sequence optimization Structural deformation · Finite element analysis (FEA) · Simufact software

1 Introduction

Welding is the most common fabrication process typically used for joining metals [1]. It is widely used in various industries such as automotive, shipbuilding, aerospace, construction, gas and oil trucking, nuclear, pressure vessels, and heavy and earth-moving equipment [2, 3]. Structural deformation of welded structures is a natural outcome of internal stresses produced while welding due to intrinsic nonuniform heating and cooling of the joint. Nevertheless, welding deformation plays a negative role in the process having high impacts in several ways, such as

J. Romero-Hdz (✉) · G. Toledo-Ramirez
Centro de Ingeniería Y Desarrollo Industrial (CIDESI), Santiago de Querétaro, Mexico
e-mail: jaromero@cidesi.edu.mx

B. Saha
Centro de Investigación En Matemáticas (CIMAT), Guanajuato, Mexico
e-mail: baidya.saha@cimat.mx

I. Lopez-Juarez
Centro de Investigación Y de Estudios Avanzados (CINVESTAV), Mexico City, Mexico

S. Chen et al. (eds.), *Transactions on Intelligent Welding Manufacturing*,
Transactions on Intelligent Welding Manufacturing,
https://doi.org/10.1007/978-981-10-7043-3_2

constraints in the design phase, reworks, quality cost, and overall capital expenditure. Selection of welding sequence could substantially reduce structural deformation. The common industrial practice is to select a sequence by experience using a simplified design of experiments which does not guarantee an optimal sequence [4]. Welding deformation can be numerically computed through Finite Element Analysis (FEA) using thermomechanical models. FEA can provide reasonable solutions for various welding conditions and geometric configurations. However, it can be computationally very expensive and time consuming.

The optimal welding sequence can be achieved by using a full factorial design procedure. The total number of welding configurations (N) is counted by, $N = n^r \times r!$, where n and r are the number of welding directions and seams (beads) respectively. This is an *NP*-hard problem and these possible configurations grow exponentially with the number of welding beads. As an example, the mounting bracket used in this study has eight weld seams that can be welded in two directions; hence the number of welding configurations for exhaustive search is 10,321,920. In real-life application, a complex weldment like an aero-engine assembly might have between 52 and 64 weld segments [5]. Therefore, full factorial design is practically infeasible even for simulation experiment using FEA.

Here, we develop and implement a Q-Learning based RL algorithm [6] for WSO. The technical contributions of this paper are as follows. First, a deformation based reinforcement learning significantly reduces the computational complexity over extensive search. In this experiment, we achieve the optimal solution through RL after executing 2 iterations. Second, we exploit a novel reward function for RL consisting of the inverse of the maximum structural deformation for WSO. Third, we compare our RL algorithm with both single objective [7] and multi-objective [8] Genetic Algorithm (GA) and we demonstrate that RL finds a pseudo optimal solution which is much faster than GA, in both cases.

We conduct simulation experiments for Gas Metal Arc Welding (GMAW) process through the simulation software Simufact®. The scope of this study is limited to GMAW process. The average execution time for each simulation (welding configuration) is 30 min using a workstation with two Intel Xeon® @2.40 GHz processors, 48 GB of RAM and 4 GB of dedicated video memory. We conduct our experiment on a mounting bracket which is usually used in telescopic jib [9] and automotive industries [10, 11].

The organization of this paper is as follows. Section 2 presents literature review. Section 3 demonstrates reinforcement learning based welding sequence optimization method. Section 4 illustrates experimental results and discussions. In Sect. 5 conclusions and future directions of this work are presented. Relevant references are listed at the end of the paper.

2 Literature Review

We organize the literature review into two parts. In the first part we present a brief literature review on WSO using artificial intelligence techniques and then we briefly introduce the Q-learning based RL algorithm related to WSO.

2.1 Welding Sequence Optimization

Several optimization methods are available in literature for welding sequence optimization. Among them, GA is one of the most popular methods available in the literature for welding sequence optimization. Mohammed et al. [12] presented GA based WSO where the distortion data computed by FEA has been used as a fitness function. Kadivar et al. [13] also presented GA based solution for WSO where only the distortion is used in the objective function and they completely neglect the effect of the welding sequence on the maximum residual stress. Damsbo and Ruboff [14] incorporated domain specific knowledge into a hybrid GA for welding sequence optimization. They minimized the robot path length to minimize the operation time but neglected the effect of welding sequence on deformation and residual stress. Islam et al. [15] coupled FEA approach with GA where the maximum structural deformation was used in the fitness function and other design variables such as welding direction and upper and lower bounds of welding process parameters were taken into effect in the model. Warmefjord et al. [16] discussed several alternative approaches to GA in spot welding sequence selection method where they suggested general simple guidelines, minimize variation in each step, sensitivity, and relative sensitivity. Kim et al. [17] proposed two types of heuristic algorithms called construction algorithm and an improvement algorithm where heuristics for the traveling salesman problem are tailored to the welding sequence optimization. However, they did not consider the inherent heat-caused deformation with the aim of minimizing the time required to process the task.

Romero-Hdz et al. [18] presented a literature overview of the artificial intelligence techniques used in WSO. The AI techniques reported include GA, Graph Search, Artificial Neural Networks (ANN) and Particle Swarm Optimization (PSO). Other popular methods are also described such as Joint Rigidity Method, Surrogate Models and the use of generalized guidelines. Some of the limitations of these studies are the lack of experimental validation in real components and ignoring some factors like residual stress and temperature which are important factors for the resulting welded quality.

Okumoto [19] presented an implementation of the Q-learning based RL algorithm to optimize the welding route of an automatic machine. The machine uses a simple truck system and it moves only in one direction until a force is detected. The fitness function in this work is based on the time, because, this type of machines are moved from one joint to another manually by the welder. As the amount of welding

seams increase, the total number of possible execution combinations grows exponentially. So, a bad decision can increase the labor hours that impacts on the cost and lead time. They used ε-greedy based selection method. This method stochastically adopts a lesser reward to avoid the local optima.

In this paper, we proposed a Q-Learning based Reinforcement learning algorithm where we use maximum structural deformation as the reward function that are described in the next section.

2.2 *Reinforcement Learning*

RL is a branch of machine learning which has been extensively used in different fields such as gaming [20], neuroscience [21], psychology [22], economics [23], engineering communications [24], engineering power systems [25], and robotics [26]. Some of the algorithms are inspired by stochastic dynamic programming like Q-learning algorithm which is the base of the proposed algorithm in this paper. RL techniques learn directly from empirical experiences of the environment. RL can be subdivided into two fundamental problems: learning and planning. While learning, the agent interacts with the real environment, by executing actions and observing their consequences. On the other hand, while planning the agent can interact with a model of the environment: by simulating actions and observing their consequences.

Figure 1 shows the basic framework of the RL algorithm. An RL task requires decisions to be made over many time steps. We assume that an agent exists in a world or environment, E, which can be summarized by a set of states, S. First, the agent receives observations from the environment E, then the agent solves the exploration-exploitation dilemma, whether to explore and get new information or

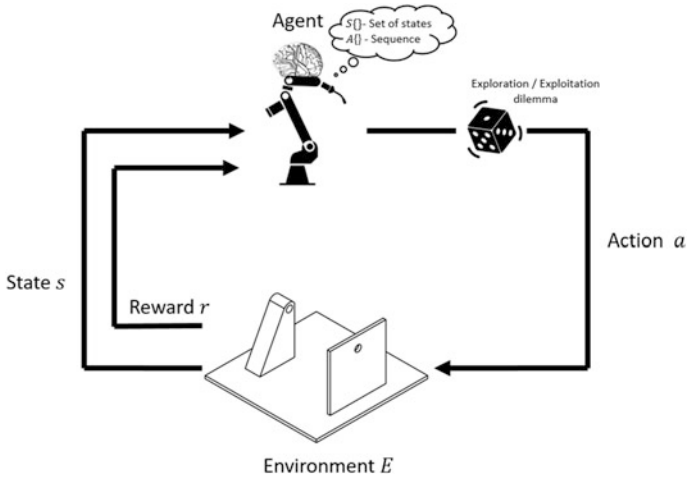

Fig. 1 Basic framework of RL

act with the information it knows and trust. Then selects an action a, and then it receives an immediate reward r and then go to next state. The agent again acts repeatedly so as to receive maximum reward from an initial state to a goal state. It is an optimization technique that can manage with moderate dynamic change in the environment through learning by repeating and evaluating the action.

In this paper, we applied Q-learning algorithm, one of the algorithms of RL for WSO. Q-learning algorithm estimates the value function $Q(s, a)$ which is obtained by the agent's repeating of the action by trial and error, for the environment. $Q(s, a)$ expresses the expectation of a gain when the agent takes the most suitable action after having chosen an action in a state s. The most suitable action is defined as the action a in state s, for which the value *of* $Q(s, a)$ becomes greatest among all the actions permissible in state s. The Q value is updated by the following Eq. (1) [19]:

$$Q(s,a) \leftarrow Q(s,a) + \alpha\{r(s,a) + \gamma \max_{a' \in A(s')} Q(s',a') - Q(s,a) \tag{1}$$

where $Q(s, a)$ is the value of action a in state s, $Q(s', a')$ is the value of action a' at state s' after transition, α is the learning rate ($0 < \alpha < 1$), and γ is the discount rate ($0 < \gamma < 1$). A number of selection methods have been proposed to solve the exploration-exploitation dilemma and choose one action executed among the many possible actions that exist. We used ε-greedy method in this study. This method stochastically adopts a lesser reward to avoid the local minima. The ε-greedy selects an action a in state s for which the value of $Q(s, a)$ is maximum at probability (1-ε), $0 < \varepsilon < 1$, as illustrated in the equation:

$$p(s,a) = \begin{cases} 1-\varepsilon, & \text{when } Q(s,a) \text{ is maximum} \\ \varepsilon, & \text{elsewhere} \end{cases} \tag{2}$$

3 Reinforcement Learning Based Welding Sequence Optimization

Figure 2 shows the flowchart and pseudo-code of the Q-learning based RL method on WSO respectively. We solve the exploration-exploitation dilemma by generating a random number between 0 and 1 and if it is less than or equal to 0.2 (the value of ε is taken as 0.2), exploration is executed, on the other hand, exploitation will be performed. For exploration, we choose the second best weld seam and for exploitation we choose the weld seam with a particular welding direction that gives the minimum of the maximum structural deformation. In this WSO experiment, the agent is considered as the robot or human, the actions of the agent are the weld seams that can be placed into the workpiece along with the direction of the welding, the state is defined as the set of actions already executed. The reward is defined as the inverse of the maximum structural deformation. The most suitable action is defined as the welding weld seam along a particular direction that provides minimum of the maximum structural deformation (Fig. 3).

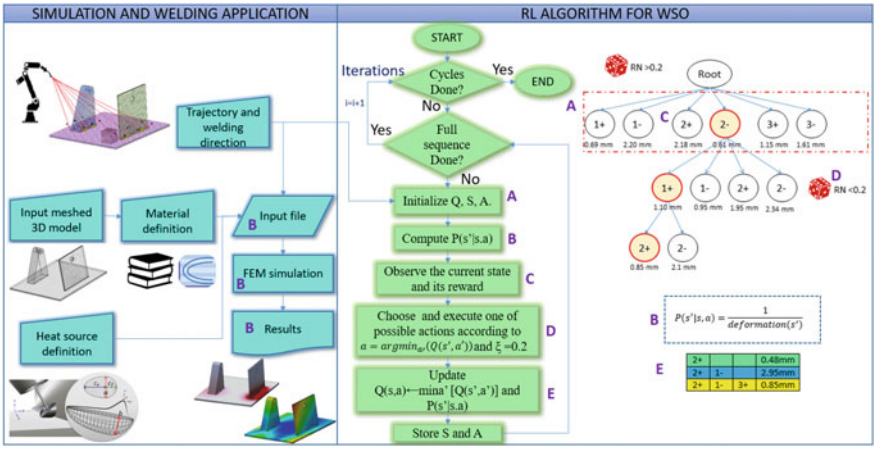

Fig. 2 Flowchart of Q-learning based reinforcement learning method on WSO

Initialize $Q(s,a) = 0$; $S = \{\}, A = \{\}, s = \{\}, A' = \{1+,1-,2+,2-,\ldots,8+,8-\}$;
Initialize a state-transition model $P(s'|s,a)$ $\quad P(s'|s,a) = 1/deformtion(s')$;
Do until learning end /*finish all the cycles or iterations*/
Do until we reach a goal /*all the seams are welded */
Observe a current state s,
Choose an action a from the set consisting of available welding seams along
all possible directions which are not welded yet which provides
minimum of the maximum structural deformation;
$a = argmin_{a' \in A'}[Q(s',a')]$ with $\varepsilon - greedy$ policy; $[Q(s',a') = minimum\ of\ the\ maximum\ structural\ deformation,\ \varepsilon = 0.2]$
Execute action a;
Update Q-value with $Q(s,a) \leftarrow min_a,[Q(s',a')]$ *and remove a and* $-a$ *from* A';
Update state-transition model $P(s'|s,a)$;
Store $S = \{s\}$ *and* $A = \{A,a\}$;
End
End

S, A: states and actions consisting of stochastic shortest paths.

Fig. 3 Pseudo-code of Q-learning based RL method on WSO

4 Experimental Results and Discussions

This section is organized as follows. First we describe the study case. Second, we mention the values of the parameters used in this study. Third, we illustrate the results of the FEA for the best and worst sequence found by the proposed RL method. Fourth, we demonstrate the effects of welding sequence on WSO. Finally, we show a comparative study among single objective GA [7], multi-objective GA [8] and Q-learning based RL method.

4.1 Study Case

Figure 4 illustrates some sample geometries of the mounting brackets available in the market. These geometries are typically used in heavy equipment, vehicles, and ships. Figure 5 demonstrates a mounting bracket which we chose as a study case in our experiment as well as the engineering drawing with all specifications.

Fig. 4 Mounting brackets available in the market as an example of welded parts

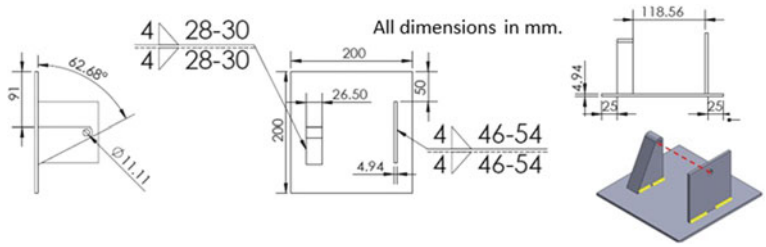

Fig. 5 Engineering drawing of the mounting bracket with 8 weld beads

4.2 Parameters Used

Table 1 illustrates values of the parameters of the Q-learning based RL algorithm used in the simulation experiment. We conduct the RL algorithm up to two iterations to find the pseudo optimal solution. Moreover, Table 2 shows the welding simulation and real experiment parameters.

4.3 Discussions About the FEA Results

The best sequence found was [−5, −8, +6, −7, −1, +3, +2, −4] with maximum structural deformation 0.93 mm. On the other hand, the worst sequence found is [−3, +4, −7, +6, +5, −1, +8, −2] and the corresponding maximum structural deformation is 2.76 mm as shown in Fig. 6. We conduct the RL experiment for two iterations. We select ε-greedy algorithm strategy where we choose the value of ε as 0.2. This indicates that the RL allows exploration 20% time and exploitation 80% time of the actions chosen. Since the value of our reward function at any stage in terms of maximum structural deformation cannot be computed by summing the value of the reward function of the previous stages, the value of the learning rate and discount factor are inapplicable in our application.

Table 1 RL parameters used in this experiment

Parameter	Value
Epochs (number of iterations)	2
Exploration rate	0.2
Exploitation rate	0.8
Learning rate	–
Discount factor	–
Selection method	ε-greedy method

Table 2 Welding simulation and real experiment parameters

Parameter	Value
Material	ASTM A36
Robot speed	50 cm/min
Current	234 A
Voltage	20.5 V

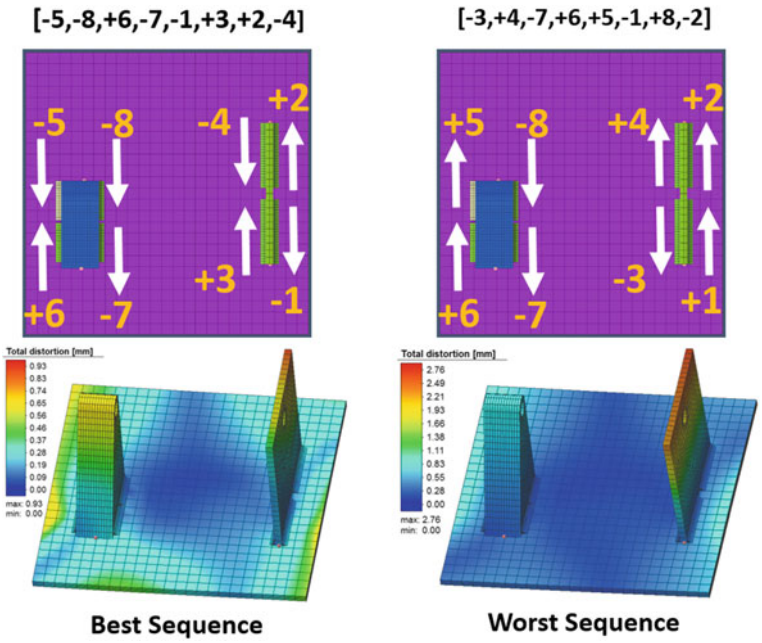

Fig. 6 Comparison between best (left column) and worst (right column) sequence and their deformation patterns

4.4 *Effects of Welding Sequence on Welding Process Optimization*

Normalized frequency of the structural deformation and effective stress values on the mounting bracket used in this study are shown in Fig. 7. If we consider the deformation value of the worst sequence as 100%, RL algorithm reduces about 66% maximum structural deformation over worst sequence (maximum structural deformation of best and worst sequence are 0.93 and 2.76 mm respectively). These results clearly demonstrate that welding sequence has significant effect on welding deformation. However, welding sequence has less effect on effective stress. These results are consistent with the results reported in the literature [7, 8].

4.5 *Comparative Analysis: Reinforcement Learning Versus Genetic Algorithm*

We compare the proposed RL method with the GA methods widely used in the WSO. In order to due this comparison, we have used the same parameters for GA reported in our previous work [7]. The structural deformation of the mounting

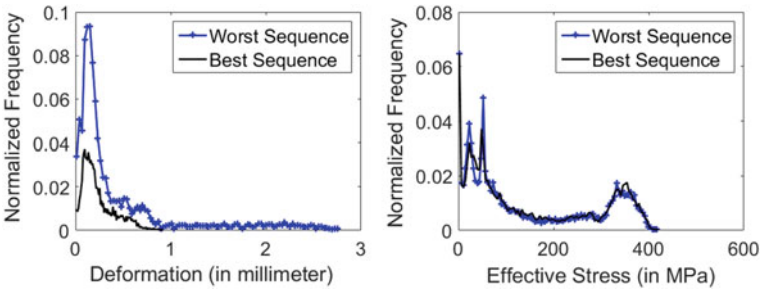

Fig. 7 Normal distribution of deformation and effective stress for best and worst sequence

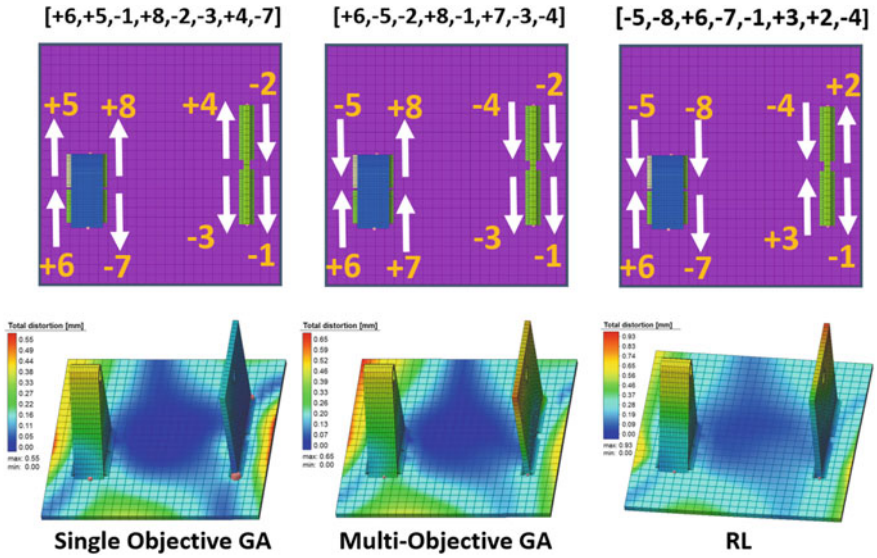

Fig. 8 From top to bottom: single objective GA, Multi-objective GA and RL algorithm

bracket for the best sequence found by the single objective, multi-objective and RL are demonstrated in Fig. 8. Table 3 illustrates the comparative analysis among single objective [7] and multi-objective GA [8] and RL method. Table 3 shows that though RL yields a bit more structural deformation, however, RL converges much faster than GA. RL finds a pseudo optimal solution in only two iterations whereas single objective and multi-objective GA require 115 and 81 simulations respectively. Since the average time required for each welding simulation experiment needs 30 min, RL method for our study case takes 30 h whereas single objective and multi-objective GA method take 57.5 and 40.5 h respectively to converge the algorithm. Figure 9 shows the search space (tree) for the best sequence explored by the RL algorithm.

Table 3 Comparative analysis among single objective genetic algorithm, multi-objective genetic algorithm and reinforcement learning

Method	Best sequence	Maximum structural deformation (mm)	# of sequences executed	Time (h)
Single objective GA	[+6, +5, −1, +8, −2, −3, +4, −7]	0.55	115	57.5
Multi-objective GA	[+ 6, −5, −2, +8, −1, +7, −3, −4]	0.66	81	40.5
Proposed RL	[−5, −8, +6, −7, −1, +3, +2, −4]	0.93	2	30

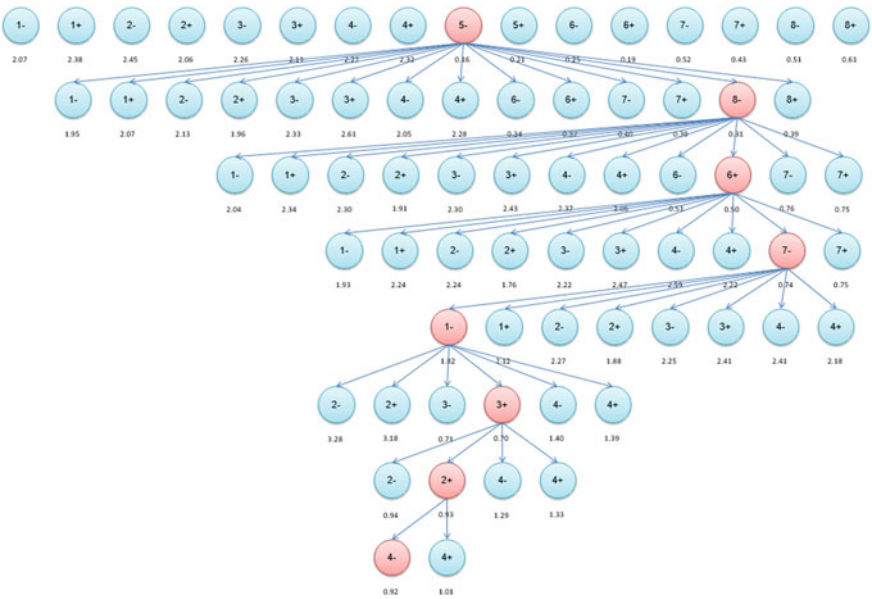

Fig. 9 Search space for the best sequence explored by Q-learning based RL algorithm

5 Conclusions and Future Works

Structural deformation plays an important role to measure the quality of the welded structures. Optimization of the welding sequence reduces the deformation of the welded structures. In this paper, the maximum structural deformation is exploited as the reward function of a proposed Q-learning based RL algorithm for WSO. RL is used to reduce significantly the search space of the exhaustive search. Structural deformation is computed using FEA. We conduct a simulation experiment on a mounting bracket which is typically used in vehicles and other applications. We

compare our RL based welding sequence optimization method with widely used single objective and multi-objective GA. Proposed RL based WSO method significantly reduces the search space over GA and thus RL finds the pseudo optimal welding sequence much faster than GA by slightly compromising the welding quality. Welding quality could be enhanced by incrementing the number of iterations of the RL method.

This work opens up different avenues for WSO research. In the near future, we would like to develop a more robust multivariate reward function including structural deformation, residual stress, temperature, and robot path time for welding sequence optimization. Information of the deformation, residual stress and temperature after welding each seam in a sequence needs to be investigated for achieving better reduction of welding deformation and residual stress.

Acknowledgements The authors gratefully acknowledge the support provided by CONACYT (The National Council of Science and Technology) and CIDESI (Center for Engineering and Industrial Development) as well as their personnel that helped to realize this work and the Basic Science Project (254801) supported by CONACYT, Mexico.

References

1. Goldak JA, Akhlaghi M (2005) Computational welding mechanics. http://www.worldcat.org/isbn/9780387232874. Accessed 21 May 2016
2. Masubuchi K (1980) Analysis of welded structures. Pergamon Press Ltd., Oxford
3. Islam M, Buijk A, Rais-Rohani M et al (2014) Simulation-based numerical optimization of arc welding process for reduced distortion in welded structures. Finite Elem Anal Des 84: 54–64
4. Kumar DA, Biswas P, Mandal NR et al (2011) A study on the effect of welding sequence in fabrication of large stiffened plate panels. J Mar Sci Appl 10:429–436
5. Jackson K, Darlington R (2011) Advanced engineering methods for assessing welding distortion in aero-engine assemblies. IOP Conf Ser Mater Sci Eng 26:12018
6. Sutton RS, Barto AG (1998) Reinforcement learning: an introduction. MIT press, Cambridge
7. Romero-Hdz J et al (2016) An elitism based genetic algorithm for welding sequence optimization to reduce deformation. Res Comput Sci 121:17–36
8. Romero-Hdz J et al (2016) Deformation and residual stress based multi-objective Genetic Algorithm (GA) for welding sequence optimization. In: Proceedings of the Mexican international conference on artificial intelligence, Cancun, Mexico, vol 1, pp 233–243
9. Derlukiewicz D, Przybyłek G (2008) Chosen aspects of FEM strength analysis of telescopic jib mounted on mobile platform. Autom Constr 17:278–283
10. Subbiah S, Singh OP, Mohan SK et al (2011) Effect of muffler mounting bracket designs on durability. Eng Fail Anal 18:1094–1107
11. Romeo ŞI et al (2015) Study of the dynamic behavior of a car body for mounting the rear axle. Proc Eur Automot Congr 25:782
12. Mohammed MB, Sun W, Hyde TH (2012) Welding sequence optimization of plasma arc for welded thin structures. WIT Trans Built Environ 125:231–242
13. Kadivar MH, Jafarpur K, Baradaran GH (2000) Optimizing welding sequence with genetic algorithm. Comput Mech 26:514–519
14. Damsbo M, Ruboff PT (1998) An evolutionary algorithm for welding task sequence ordering. Proc Artif Intell Symbolic Comput 1476:120–131

15. Islam M, Buijk A, Rais-Rohani M, Motoyama K (2014) Simulation-based numerical optimization of arc welding process for reduced distortion in welded structures. Finite Elem Anal Des 84:54–64
16. Warmefjord K, Soderberg R, Lindkvist L (2010) Strategies for optimization of spot welding sequence with respect to geometrical variation in sheet metal assemblies. Design and Manufacturing 3: 569–57
17. Kim HJ, Kim YD, Lee DH (2004) Scheduling for an arc-welding robot considering heat-caused distortion. J Oper Res Soc 56(1):39–50
18. Romero-Hdz J et al (2016) Welding sequence optimization using artificial intelligence techniques: an overview. Int J Comput Sci Eng 3(11):90–95
19. Okumoto Y (2008) Optimization of welding route by automatic machine using reinforcement learning method. J Ship Prod 24:135–138
20. Tesauro G (1994) TD-gammon, a self-teaching backgammon program, achieves master-level play. Neural Comput 6:215–219
21. Schultz W, Dayan P, Montague P (1997) A neural substrate of prediction and reward. Science 16:1936–1947
22. Sutton R (1990) Integrated architectures for learning, planning, and reacting based on approximating dynamic programming. In: Proceedings of 7th international conference on machine learning, vol 1, pp 216–224
23. Choi J, Laibson D, Madrian B et al (2007) Reinforcement learning and savings behavior. Yale Technical Report ICF Working Paper, 09–01
24. Singh S, Bertsekas D (1997) Reinforcement learning for dynamic channel allocation in cellular telephone systems. Adv Neural Inf Process Syst 9:974–982
25. Ernst D, Glavic M, Geurts P et al (2005) Approximate value iteration in the reinforcement learning context-application to electrical power system control. Int J Emerg Electr Power Syst 3(1):1066
26. Abbeel P, Coates A, Quigley M et al (2007) An application of reinforcement learning to aerobatic helicopter flight. Adv Neural Inf Process Syst 19:1–8

Time-Optimal Path Planning for Dual-Welding Robots Based on Intelligent Optimization Strategy

Xuewu Wang, Bin Tang, Yixin Yan and Xingsheng Gu

Abstract Dual-welding robots are widely used with the industry development, and dual-welding robots usually have to deal with a large number of weld joints. In this condition, traditional manual teaching method is time-consuming and inefficient. In this paper, an intelligent optimization strategy is proposed to realize time-optimal path planning for dual-welding robots. First, the welding robot path optimization problem is presented. Then, good diversity and convergence velocity of discrete group competition particle swarm optimization (GC-PSO) algorithm are tested. Compared with particle swarm optimization (PSO), genetic particle swarm optimization (GPSO) and chaos particle swarm optimization (CPSO) algorithms, GC-PSO algorithm shows its better optimization effectiveness. In addition, a method of collision detection and obstacle avoidance is given. At last, an intelligent optimization strategy is applied to time-optimal path planning for dual-welding robots, and the global optimal result can be obtained quickly. Simulation results show that the intelligent path planning strategy is effective and can be used for welding robot path optimization.

Keywords Particle swarm optimization (PSO) · Group competition
Welding robot · Path optimization · Obstacle avoidance

1 Introduction

Welding robot is widely used in industrial production process. Welding robot path planning mostly relies on the experience of engineers. This method is not only time-consuming and inefficient, but also difficult to find the desired welding path.

X. Wang (✉) · B. Tang · Y. Yan · X. Gu
Key Laboratory of Advanced Control and Optimization for Chemical Processes of Ministry of Education, East China University of Science and Technology, Shanghai, China
e-mail: wangxuew@ecust.edu.cn

S. Chen et al. (eds.), *Transactions on Intelligent Welding Manufacturing*,
Transactions on Intelligent Welding Manufacturing,
https://doi.org/10.1007/978-981-10-7043-3_3

Intelligent optimization algorithm provides a convenient and quick method for the welding robot path planning. Welding robot path optimization was simplified as the traveling salesman problem (TSP) problem and the path length was minimized based on double-global optimal particle swarm optimization (PSO) algorithm [1]. In [2], task sequencing and path planning in remote laser welding were studied based on TSP and meta-heuristic algorithm. The energy consumption and cycle time were optimized using restarted simulated annealing algorithm [3].

As widely used intelligent optimization algorithm, PSO is used to solve path planning problem. PSO [4] was first proposed by Kennedy and Eberhart in 1995. PSO algorithm has many advantages, such as simple structure, fast convergence speed and easy implementation. However, PSO has a disadvantage: when the optimized problem is complex, the dimension is high or there are a lot of local optimal values in the independent variables. In order to solve the premature problem of PSO algorithm and accelerate the convergence rate of the algorithm, many improvements were conducted. The first kind of improvement mostly aims at the PSO parameters, such as learning factor and inertia weight. In [5], a particle swarm algorithm with dynamic inertia weight adjustment was proposed to balance the global and local search ability of PSO. However, this improvement is largely dependent on the choice of random factors. The improvement of the position and velocity of PSO belongs to the second category. In [6], a position-weighted PSO algorithm was proposed to increase the determinacy and directionality of the particle searching for the optimal value. However, the improved method limits the search range and reduces the convergence rate of the particle. The third category is local search PSO algorithm based on the global optimal particle [7], such as chaos particle swarm optimization (CPSO) algorithm. In [8], the chaos was integrated into the motion of the particle, and the probability of falling into the local optimum was decreased. However, the algorithm complexity was increased and the convergence rate was reduced. The fourth category is based on the fusion of different intelligent optimization algorithms, such as genetic particle swarm optimization (GPSO) algorithm [9]. Incorporating the updating strategy into the PSO algorithm is the fifth category [10]. Improved PSO algorithm shows its advantages, such as fast rapid convergence and global optimization. Therefore, an improved PSO algorithm based on grouping and competition strategy is proposed to realize the welding robot path optimization.

Welding robot path optimization problem is described in Sect. 2. Group competition particle swarm optimization (GC-PSO) algorithm is presented in Sect. 3, and its discretization is also given. Then, the dual-robot obstacle avoidance strategy is presented in Sect. 4. Furthermore, time-optimal path planning for dual-welding robots is conducted based on GC-PSO in Sect. 5.

2 Optimization Problem Description

A part of the white body is selected as workpiece in this paper. The shape of the workpiece and the position of the weld joints are shown in Fig. 1. The robot is ABB R2400 robot and the welding tong is GTAW10. The welding pose will be presented in Sect. 3.3. For convenience, the pose of the welding tong is defined as "1" or "−1". When the longer part is in the upright position, the pose is defined as "1", otherwise it is defined as "−1". In view of the actual situation of the workpiece and fixture, both poses in welding process can be applied to some welding joints. Such a condition is defined as "0".

Efficiency is the critical goal for industrial production process, and welding time is the most direct efficiency indicator. In actual welding process, welding pose is related to welding time and obstacle avoidance. Therefore, welding pose is considered during conducting welding robot path planning.

In this paper, two robots are placed symmetrically and oppositely. The welding joints are assigned based on the following principles. First, the working space of the welding robots does not overlap. Next, welding joints with the same pose are assigned to the same robot. Besides, welding joints are divided to obtain the shortest welding time and the welding time for the two robots is nearly the same. If the welding time difference between the two robots is greater than the minimum difference, the welding joint with the farthest distance from the robot is assigned to the other robot until the two robots have nearly the same welding time and the shortest total time.

The time-optimal path planning for the dual-welding robots requires that the welding tong walks through all welding joints and the cost time is the shortest. Suppose that the number of weld joints is M, the number of transition points is N, and the weld joint order is $\pi(i)$ ($i = 1, 2, \ldots, n$). Then, the time-optimal path planning problem can be regarded as a constraint TSP problem. The welding robot global path planning problem can be described as

$$\min T = \sum_{i=1}^{N-1} L_{\pi(i),\pi(i+1)}/v, \tag{1}$$

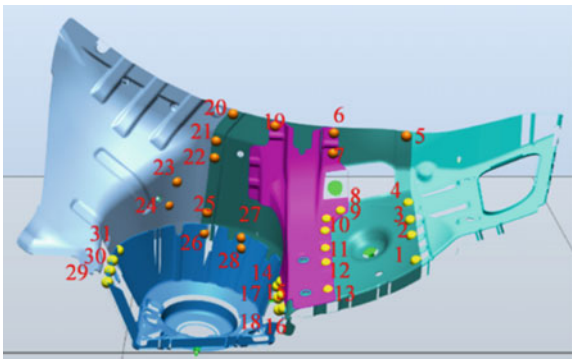

Fig. 1 Welding workpiece

$$\text{s.t. path } \pi(i)\ \pi(i+1) \text{ is safe path, } i = 1,\ 2,\ \ldots,\ n-1, \tag{2}$$

where $\sum_{i=1}^{N-1} L_{\pi(i),\,\pi(i+1)}$ is the sum of the distances between two welding joints, v is the welding speed which is set as 2 m/s, and path $\pi(i)\ \pi(i+1)$ is the path between two welding joints $\pi(i)$ and $\pi(i+1)$.

3 GC-PSO

3.1 Algorithm Introduction

Because traditional PSO algorithm slowly converges and easily falls into local optimum, GC-PSO algorithm is proposed in this paper. The algorithm divides the particle swarm into two parts according to the fitness value of each particle. Particles with fitness value in the top 20% of the total fitness value are regarded as leading particles, and the remaining particles are followers. After dividing all particles into two parts, all the particles are grouped randomly. Each group consists of a leading particle and some followers, where the followers are randomly assigned to the leading particles and the number of followers in each group is not unique. When iteration number satisfies $t = 10$, the fitness value of the particle is reordered. Then, the leading particle and followers are defined according to the fitness value. And all the particles are grouped randomly again.

GC-PSO algorithm adopts different speed updating strategies for different particles. In order to avoid the particle falling into local optimum, GC-PSO algorithm introduces intra-group competition and inter-group competition in the speed updating formula [11].

The velocity updating formulas for leading particles is described as

$$v_i^{t+1} = \omega v_i^t + v_i^t \,\text{Randn}\left(0, \sigma^2\right), \tag{3}$$

where

$$\sigma^2 = \begin{cases} 1, if_i < f_k \\ e^{\frac{-f_i + f_k}{|f_i + \epsilon|}}, \text{otherwise} \end{cases}, k \in [1, N_l], k \neq i. \tag{4}$$

The location updating formula for leading particles is described as

$$x_i^{k+1} = x_i^k + v_i^{k+1}, \tag{5}$$

where Randn(0, σ^2) is a Gaussian distribution function with mean 0 and variance σ^2. The parameter Randn(0, σ^2) expands the searching range of particle and avoids

the particle falling into local optimization. ε is an infinitely small number which promises the denominator is not zero. k denotes the number of the other leading particles which will increase the competition between the particles. This strategy can make the particle with poor fitness moves closer to the particle with better fitness. f is the corresponding fitness value of each particle. N_l is number of leading particles.

The speed updating formulas for follower are given as

$$v_1^{t+1} = \omega v_i^t + s_1 \,\mathrm{Rand}\,(v_{j1}^t - v_i^t) + s_2 \,\mathrm{Rand}\,(v_{j2}^t - v_i^t), \tag{6}$$

$$s_1 = \mathrm{e}^{\frac{f_i - f_{j1}}{|f_i| + \varepsilon}}, \tag{7}$$

$$s_2 = \mathrm{e}^{(f_{j2} - f_i)}. \tag{8}$$

The location updating formula for follower is given as

$$x_i^{k+1} = x_i^k + v_i^{k+1}. \tag{9}$$

The velocity updating formula for follower contains two parameters s_1 and s_2. s_1 is the intra-group competition coefficient, and j_1 is the number of leading particles in the group. Follower competes with the leading particle with probability s_1. s_2 is the inter-group competition coefficient, and j_2 is the number of the leading particles in other groups. Followers in this group compete with the leading particles in other groups with the probability s_2.

The detailed flow of the algorithm is presented as follows.

Step 1 Initialize the particle swarm, and define the related parameters: the number of leading particle, the number of following particle, and the particle size Popsize.

Step 2 Calculate the fitness value of the particles and determine the individual optimal position p_{best} and the global optimal position g_{best}; set t as 1.

Step 3 After iterating G times, the particles are reordered and grouped according to the fitness value. G = 10 denotes iteration time.

Step 4 Update the position, velocity and fitness values of the leading particles and followers according to Eqs. (3), (5), (6) and (9).

Step 5 Update the individual optimal position p_{best} and the global optimal position g_{best} of the current particle swarm.

Step 6 Set $t = t + 1$; stop if the iteration condition is satisfied; otherwise, return to Step 3.

The number of leading particles and the value of update coefficient have an important influence on the convergence precision and convergence speed of the algorithm. If N_l and G are set too large, the algorithm cannot converge quickly to the global optimal value. If N_l and G are set too small, the algorithm easily falls into local optimum. After tests, the following conclusions can be drawn. When N_l is set as 20% of the total number of particles, and G is set as 10, the convergence rate is improved obviously and the convergence precision is guaranteed. In addition, ω decreases exponentially from 0.9 to 0.4 with the increase of the iteration for the convergence accuracy, convergence rate and robustness of the algorithm.

3.2 Algorithm Discretization

Although the GC-PSO shows the ability of fast convergence and optimization, it can only solve the continuous problem. In order to solve the problem of dual-robot path planning, the GC-PSO algorithm needs to be discretized.

In discrete PSO algorithm, each particle represents a feasible solution, and the population is a set of feasible solutions. Like continuous PSO algorithm, x_i in discrete particle swarm algorithm also represents the ith sorting result, v_i represents the velocity of the ith particle, p_{best} represents the best individual, and g_{best} represents the best population sort. Among them, v_i is a set of directions the particle can search; x_i, p_{best} and g_{best} are the results of optimization. Equations (3), (5), (6) and (9) are updated as follows.

Velocity and position updating equations for leading particle are respectively presented as

$$v_i^{t+1} = \omega v_i^t + v_i^t \,\text{Randn}\left(0, \sigma^2\right), \tag{10}$$

$$x_i^{t+1} = x_i^t \oplus v_i^{t+1}. \tag{11}$$

Velocity and position updating equations for follower are respectively presented as

$$v_i^{t+1} = \omega v_i^t + s_1 \,\text{Rand}\left(v_{j1}^t - v_i^t\right) + s_2 \,\text{Rand}\left(v_{j2}^t - v_i^t\right), \tag{12}$$

$$x_i^{t+1} = x_i^t \oplus v_i^{t+1}. \tag{13}$$

In the above equations, the operators +, − and $\oplus$ have new definitions. The definitions include the rule of particle crossover and combination with individual and global, which is important to transfer continuous algorithm to the discrete algorithm. Subtraction operator "−" represents the difference set of individual optimal position and the current position. For the example of $x_i^t \oplus v_i^{t+1}$o, $\oplus$

operation refers to conduction exchange order v_i^{t+1} for x_i^t, where v_i^{t+1} is a set of particle exchange orders. Addition operator "+" represents the union of two edge sets. The above discretization method inherits the characteristics of continuous GC-PSO. The updating process of GC-PSO is the process moving to the global optimal solution.

3.3 Algorithm Validation

Convergence rate and accuracy among standard PSO, genetic algorithm (GA), GPSO and GC-PSO algorithms are compared based on four TSPs. Four algorithms independently run 30 times for each test function, the population size is set as 100, and the maximum number of iterations for each run is set as 500 ω decreases exponentially from 0.9 to 0.4 with the increase of the iteration. Other parameters for these algorithms are listed in Table 1.

The average convergence curves of four algorithms are shown in Fig. 2. It can be concluded that GC-PSO still shows excellent convergence speed and accuracy with the same parameters and discrete method. GC-PSO algorithm uses the intra-group and inter-group competitions by the speed updating formula to make each particle move toward the global optimal position. The group division strategy ensures that the algorithm does not fall into local optimum. The simulation results show that GC-PSO algorithm is still feasible and efficient after discretization.

4 Dual-Robot Obstacle Avoidance Strategy

4.1 Three-Dimensional Grid Method Modeling

Working environment model for robot obstacle avoidance is established first. Grid method can establish an intuitive working environment which is conducive to judge local environment. Hence, the three-dimensional grid method is selected in this

Table 1 Algorithms parameters

Algorithm	Parameter
PSO	$c_1 = 1.49445,\ c_2 = 1.49445,\ \omega_{\max} = 0.9,\ \omega_{\min} = 0.4$
GPSO [12]	$c_1 = 1.49445,\ c_2 = 1.49445,\ p_c = 0.7,\ p_{\mathrm{m}} = 0.05$ $\omega_{\max} = 0.9, \omega_{\min} = 0.4$
GA [13]	$p_c = 0.7,\ p_m = 0.05,\ \mathrm{GGAP} = 0.1$
GC-PSO	$c_1 = 1.49445,\ c_2 = 1.49445,\ \omega_{\max} = 0.9,\ \omega_{\min} = 0.4$ leading particle percent $= 0.2,$ follower percent $= 0.8$

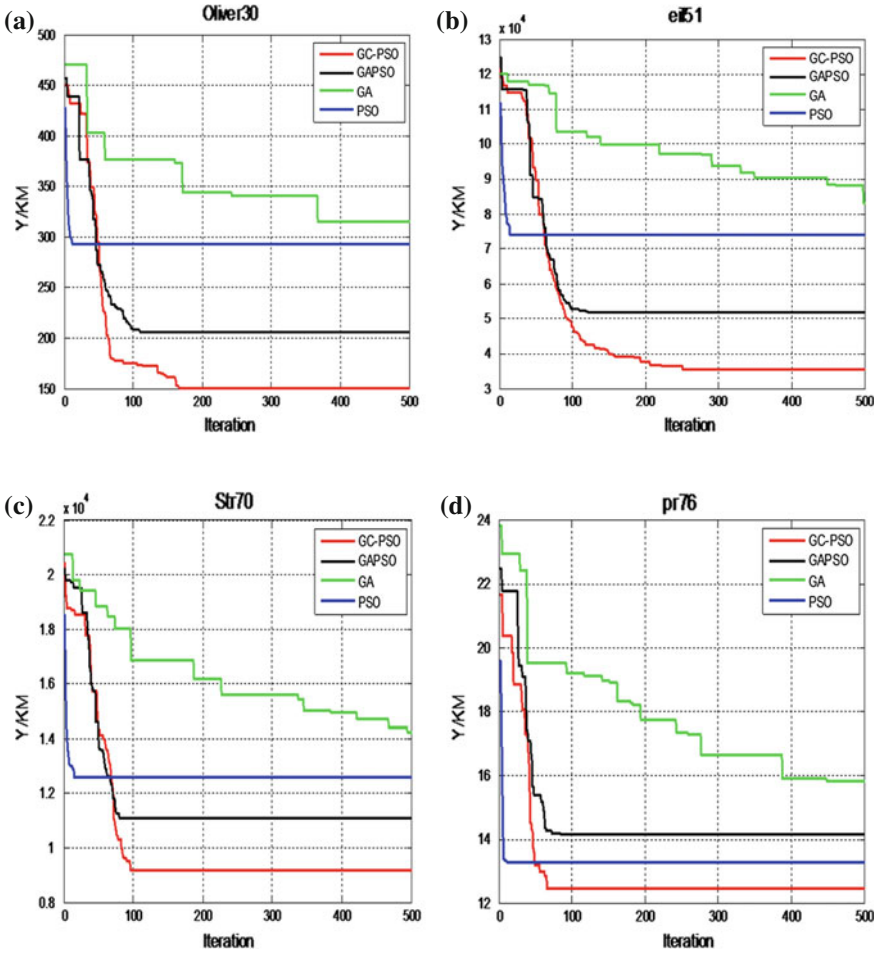

Fig. 2 The average convergence curves of four algorithms

paper to establish the working environmental model. And the steps are given as follows.

Step 1 Simplify the workpiece as a combination of some triangles. This is because free grid and obstacle grid are more easily identified through triangles.

Step 2 Create the grid matrix. Grid size affects the accuracy of path planning. The less the grid is, the better the accuracy of the path is, but this will take a long time to search the best path. The larger the grid is, the worse the accuracy of the path is, while the best path can be quickly found. In view of the searching time and accuracy, the whole space is divided into cubes

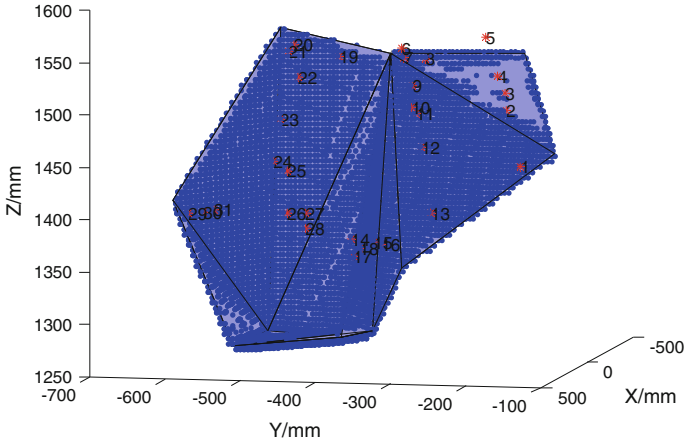

Fig. 3 Three-dimensional environment model using grid method

with a side length of 5 mm. The center of each cube is used as the starting point of the search path. Each center point is projected to a plane. If the projection point is outside the triangle, this triangle is not an obstacle at this point. If the projection point is inside the triangle and the length of the vertical line is less than 6 mm, the triangle is an obstacle.

Step 3 Identify the free grids and obstacle grids. If there is an obstacle for the center point, it means that the point is the obstacle point and the related grid is an obstacle grid; otherwise, the point is a free point and the related grid is a free grid. Obstacle points are indicated by *, as shown in Fig. 3.

4.2 Obstacle Avoidance Between Robot and Workpiece

Local searching starts from initial solution, and begins to search the vicinity field. If particle can find a better solution, then it replaces the initial solution. Ant colony algorithm is applied to realize local obstacle avoidance path planning [14].

The parameters of ant colony optimization (ACO) are initialized as follows. Based on the empirical value, the weight α of the pheromone is set as 1, the weight β of heuristic pheromone is set as 11, the evaporation coefficient ρ of pheromone is set as 0.9, and the pheromone quality coefficient Q is set as 5. The iteration number N is set as 50, and the population quantity M is set as 50. The coordinates of the starting point and the terminal point are initialized. The initialized pheromones for all points are set as 0.5. Iterator is defined as n. The number of ants is expressed as k.

The local obstacle avoidance path of two robots can be obtained by the local search algorithm. However, the path obtained by ant colony algorithm is not a

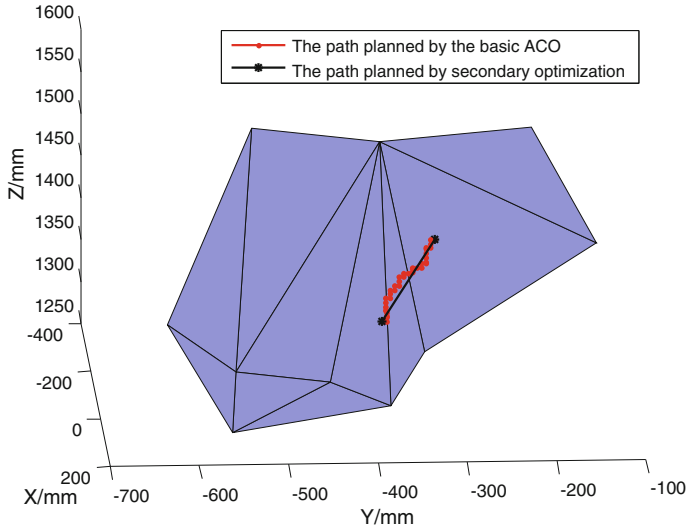

Fig. 4 Local obstacle avoidance path planning

straight line, so it cannot meet requirement of the shortest welding path. In order to achieve the shortest and collision free welding path, second optimization is conducted. Principles of the second optimization are presented as follows. Some nodes are canceled and leaved nodes are connected to obtain a shorter path. In the process, collision detection is always conducted to promise a collision free path. Welding joints 12 and 15 are taken as an example. The simulation results are shown in Fig. 4.

4.3 Obstacle Avoidance Between Robots and Fixture

The obstacle avoidance between robot and fixture needs to be studied. In this paper, the welding tong is regard as a point, and the distance between welding tong and fixture is calculated to conduct collision detection.

Collision detection between welding tong and fixture steps is given as follows. A welding path is obtained by optimization algorithm firstly. Then, the shortest distance between welding tong and fixture is calculated. If the shortest distance is less than the safety threshold, geometrical method [15] is used to obtain a transition point to avoid collision.

Figure 5 shows two welding joint positions in the adjacent region. Starting point and terminal point are connected in a line which is called Line 1. The intersection of two planes is called Line 2. Lines 1 and 2 locate on different surfaces. A transition point in Line 2 is obtained to make the path shortest, which moves from the starting

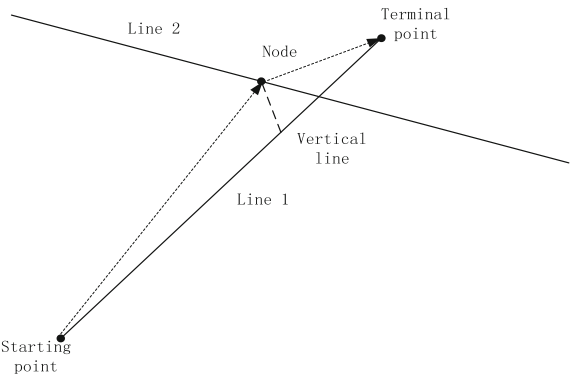

Fig. 5 Transition point solution

point, the transition point, and reaches the terminal point. This transition point is the intersection of the line 2 and the middle vertical line of the two lines.

5 Time-Optimal Path Planning for Dual-Welding Robots

Based on the environment modeling and the obstacle avoidance strategy, GC-PSO algorithm is used to optimize the robot welding time, and realizes the time-optimal obstacle avoidance path planning. Assume that the welding speed of the robot is 2 m/s, and the welding time of each weld joint is 0.5 s. The steps of time-optimal path planning are presented as follows.

Step 1 Set the position of two robots which are placed on the two sides of workpiece, and determine the weld joint coordinates.
Step 2 Initially assign all the welding joints for two robots according to the assignment principle.
Step 3 Establish weldment and robot workspace model according to the grid method.
Step 4 Obtain the local collision free path for robot and weldment by ant colony algorithm.
Step 5 Realize collision free path among the welding tong, tooling fixture and workpiece based on collision detection and geometry method.
Step 6 Based on the division result of the welding joints, calculate the welding time of each robot by discrete GC-PSO algorithm.
Step 7 If the welding time difference between two robots is greater than the set time difference, divide the weld joints again according to the division principle of weld joints, and return to Step 6. Otherwise, go to Step 8.
Step 8 Output the optimized welding joint order and the welding time of each robot.

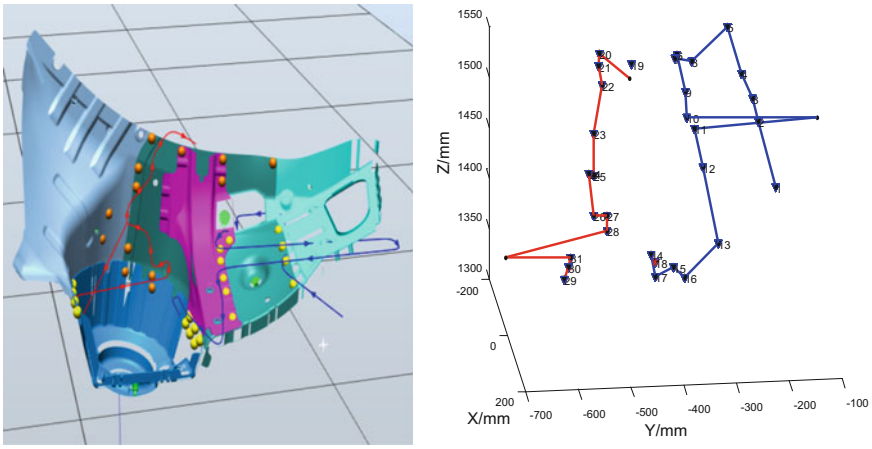

(a) Dual-robot welding path in RobotStudio (b) Dual-robot welding path in Matlab

Fig. 6 Optimization results of welding path

In this paper, in order to meet the requirement of the shortest welding time, welding joints are divided according to the welding pose. This principle can reduce the welding pose change in welding process. In order to facilitate the calculation, the welding tong reverses when it arrives at the transition point, and the reversing time is set as 2 s. For example, there is a pillar between the welding joints 10 and 11 for the robot 2. Hence, geometric method is used to avoid collision between the robot and fixture. A transition point is selected at the edge of the workpiece. When the robot 2 finishes the welding of the welding joint 10, it moves to the transition point. Then, it moves to the welding joint 12 and welds the welding joint 12.

Based on the optimization strategy, welding path lengths for two robots are 70.2914 and 109.29004 mm, respectively. The final optimal welding time is 94.259072s. Global path planning orders are: 19–20–21–22–23–25–24–26–27–28–31–30–29 and 1–2–3–4–5–8–7–6–9–10–11–12–13–16–15–17–14–18, respectively. The path planning results with obstacle avoidance for dual-welding robots is shown in Fig. 6.

6 Conclusion

Compared with traditional manual teaching method, intelligent robot path planning has a high industrial application value. In order to realize intelligent welding path planning for two robots, GC-PSO algorithm and obstacle avoidance strategy are studied after the optimization problem is described. Then, the dual-robot time-optimal path planning is conducted based on the mentioned optimization strategy. The optimized welding path can help welding engineering by shortening

the teaching time. As welding robot application and artificial intelligence technology increase rapidly, intelligent robot welding path planning will draw more attention, and will play an important role in welding automation in the future.

It can be seen that only simulation is performed in this paper. Detailed research works need to be done to improve the optimization strategy. And some experiments also need to be done to promise the strategy effectiveness.

Acknowledgements The work is founded by the Shanghai Nature Science Foundation (14ZR1409900), and the National Natural Science Foundation of China (61773165, 61573144).

References

1. Wang XW, Shi YP, Ding DY et al (2016) Double global optimum genetic algorithm-particle swarm optimization-based welding robot path planning. Eng Optim 48(2):299–316
2. Kovács A (2016) Integrated task sequencing and path planning for robotic remote laser welding. Int J Prod Res 54(4):1210–1224
3. Li Z, Tang Q, Zhang LP (2016) Minimizing energy consumption and cycle time in two-sided robotic assembly line systems using restarted simulated annealing algorithm. J Clean Prod 135:508–522
4. Kennedy J et al (1995) Particle swarm optimization. In: Proceedings of IEEE international conference on neural networks, vol 4, IEEE, Piscataway, pp 1942–1948
5. Amoshahy MJ, Shamsi M, Sedaaghi MH (2016) A novel flexible inertia weight particle swarm optimization algorithm. PLoS ONE 38:281–295
6. Guedria NB (2016) Improved accelerated PSO algorithm for mechanical engineering optimization problems. Appl Soft Comput 40(40):455–467
7. Ye Y, Yin CB, Gong Y et al (2016) Position control of nonlinear hydraulic system using an improved PSO based PID controller. Mech Syst Signal Process 83:241–259
8. Dong N, Fang X, Wu AG (2016) A novel chaotic particle swarm optimization algorithm for parking space guidance. Math Probl Eng 2016:1–14
9. Benvidi A, Abbasi S, Gharaghani S et al (2017) Spectrophotometric determination of synthetic colorants using PSO-GA-ANN. Food Chem 220:377–384
10. Wu DQ, Zheng JG (2013) Parallel particle swarm optimization algorithm based on hybrid strategy adaptive learning. Control Decis 28(7):1087–1093
11. Wu D, Xu S, Kong F (2016) Convergence analysis and improvement of chicken swarm optimization. IEEE Access 2016(99):1–1
12. Yan LM, Gu YC, Li JD (2011) Optimal strategy of searching FPD weights scanning matrix using GA-PSO. J Shanghai Univ 15(4):292–296
13. Jayalakshmi GA, Sathiamoorthy S, Rajaram R (2001) A hybrid genetic algorithm: a new approach to solve traveling salesman problem. Int J Comput Eng Sci 2(2):339
14. Wang XW, Xue LK, Yan YX et al (2017) Welding robot collision-free path optimization. Appl Sci 7(2):89
15. Wang XW, Yan YX, Ding DY et al (2016) Obstacle avoidance path planning of welding robot based on Lévy-PSO algorithm. J Shanghai Jiao Tong Univ 50(10):1517–1520

Improving Stability of Welding Model with ME-ELM

Jianxiong Ye, Han Ye, Zhigang Li, Xingling Peng, Jinlan Zhou and Bo Guo

Abstract Welding shape is important in evaluating welding quality, but accurate predictive model is hard to achieve, because welding is a complex nonlinear process, and the sampled data are inevitably contaminated. Extreme learning machine (ELM) is used to construct a single-hidden layer feedforward network (SLFN) in our study, for improving stability of welding model, M-estimation is combined with ELM and a new algorithm named ME-ELM is developed; researches indicate that it works more effective than BP and other variants of ELM in reducing influence, furthermore, it can improve the model's anti-disturbance and robustness performance even if the data are seriously contaminated. Real TIG welding models are constructed with ME-ELM, by comparing with BP, multiple nonlinear regression (MNR), and linear regression (LR), conclusions can be gotten that ME-ELM can resist the interference effectively and has the highest accuracy in predicting the welding shape.

Keywords Welding shape · Welding model · ME-ELM algorithm Stability

1 Introduction

There are many kinds of welding methods, such as resistance welding, braze welding, gas metal arc welding (GMAW), tungsten inert gas (TIG) welding, flux cored arc welding (FCAW), submerged arc welding (SAW), etc., as a kind of

J. Ye (✉) · X. Peng · J. Zhou · B. Guo
Jiangxi Province Key Laboratory of Precision Drive & Control, Nanchang Institute of Technology, Nanchang, China
e-mail: jxlpyjx@163.com

H. Ye
Jiangxi Aeronautical Institute, Nanchang, China

Z. Li
School of Mechanics Engineering, East China Jiao Tong University, Nanchang, China

S. Chen et al. (eds.), *Transactions on Intelligent Welding Manufacturing*, Transactions on Intelligent Welding Manufacturing,
https://doi.org/10.1007/978-981-10-7043-3_4

hot-working process, welding is widely used in building of marine engineering, railways, and electrical power plants etc., it is reported that more than 2/3 of the steel need welding before utilization [1].

The mechanical property after welding is not only determined by composition of metal, but also by the shape of welding joint [2, 3], the desired welding shape relies on many factors, such as welding speed, wire feeding speed, welding current, welding gas flow rate, so it is difficult to construct the model between the shape and so many welding parameters. Till now, there are at least four kinds of modeling methods: multi-nonlinear regression (MNR), response surface methodology (RSM), Taguchi method, and ANN nonlinear mapping [4–7]. Shi et al. [8] used MNR to predict the bead geometry in wet FCAW, and sensitive analysis is performed later, this method is also used on SAW to predict the pips bead shape and realize online control [3]; Palani and Morgan [9] used RSM to develop a model predicting welding joint shape in FCAW; Taguchi is popularly used and has various forms, Tarng et al. [10] and Biswas et al. [11] applied grey-Taguchi and PCA-Taguchi to predict the bead shape in SAW. However, because welding shape relates to many factors, all methods above can not work efficiently and effectively. ANN and other similar intelligent calculation methods are widely used now [12–15], but from the view of mathematics, ANN and its variants still have to face several issues like time-consuming, over-fitting, or local minima, it is meaningful to find out new measures to build welding model.

Based on ELM, some hybrid methods are supposed in our research. SA, GS, and GA are combined with normal ELM to find out better network structures, ME-ELM is suggested for reducing training data noise to enhancing the model stability and accuracy.

The rest of this paper is arranged as follows. Section 2 introduces the principle of basic ELM, points out relevant problems relating accuracy and stability; Sect. 3 focus on enhancing model stability, ME-ELM is introduced in detail, tests on specific complicated functions indicate that this algorithm has the ability to refrain the adverse effect of noise; Sect. 4 provides models on real TIG welding, besides the method proposed in this paper, BP and MNR are also used to create welding models, the residual errors are compared as well as that of LR(linear regression) which has been published in references [27] already; in the end, conclusions are presented in Sect. 5.

2 Introduction of Basic ELM

2.1 Principle of ELM

ELM is a kind of feedforward neural network, it has two types of structure, named as multilayer structure and single-layer structure. Single-layer structure is an SLFN, it has an input layer, an output layer, and only one hidden layer, each hidden neuron has an activation function, the functions may be same or different, just as shown in

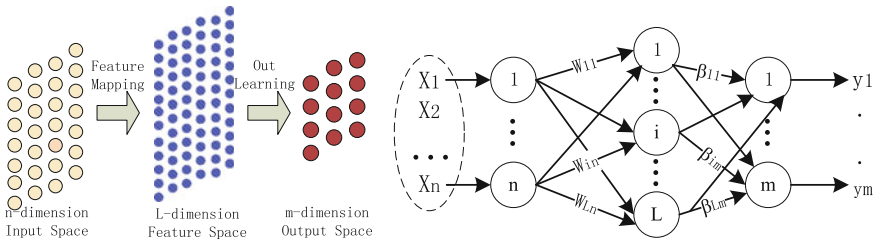

Fig. 1 Network structure of ELM

Fig. 1, $[x_1, x_2, \ldots, x_N]$ means input data, $[y_1, y_2, \ldots, y_N]$ means output data, $W = [W_1, W_2, \ldots, W_N]$ and $\beta = [\beta_1, \beta_2, \ldots, \beta_N]$ are input matrix and output matrix. Hidden layer maps data from input space to feature space with input matrix W, and then convert them into result space with output matrix β, it is clear that they play an important role in model performance.

The working process is as follows: Given training samples (x_i, t_i), input vector and output vector are $x_i = (x_{i1}, x_{i2}, \ldots, x_{in}) \in R^n$ and $y_i = (y_{i1}, y_{i2}, \ldots, y_{im}) \in R^m$, if the number of hidden neurons is L and activation function is $g(x_i)$, we may have:

$$y_j = \sum_{i=1}^{L} \beta_i g(w_i x_j + b_i),\ j = 1, \ldots, N \tag{1}$$

where $w_i = (w_{i1}, w_{i2}, \ldots, w_{in})$ indicates weights from input row to ith hidden neuron, $\beta_i = [\beta_{i1}, \beta_{i2}, \ldots, \beta_{im}]$ represents rights from ith hidden layer to output layer.

Equation (1) can be summarized as:

$$Y = H\beta \tag{2}$$

β means output matrix, H is input matrix and it can be expressed:

$$\begin{aligned} &H(w_1, \ldots, w_L, b_1, \ldots, b_L, x_1, \ldots, x_N) \\ &= \begin{bmatrix} g(w_1 \cdot x_1 + b_1) & \ldots & g(w_L \cdot x_1 + b_L) \\ \cdots & \cdots & \cdots \\ \cdots & \cdots & \cdots \\ g(w_1 \cdot x_N + b_1) & & g(w_L \cdot x_N + b_L) \end{bmatrix}_{N \times L} \end{aligned} \tag{3}$$

There is a conclusion in [16] that for a stand SLFNs which has n input neurons, m output neurons, and L hidden layer neurons, given N distinct observations $\{x_i, y_i\}$, if the activation function g: $R \rightarrow R$ is infinitely differentiable in any interval, then we can randomly get the w_i and b_i according to any continuous probability distribution and have the result that the input matrix H is definitely invertible and β can be analytically calculated out based on least square solution. So we have Eq. (4).

$$\hat{\beta} = H^{\dagger}T = \min_{\beta}((H\beta - Y) = 0) \tag{4}$$

Judgments can be obtained from Eq. (4) that different $H^{\dagger}$ leads to different network output, and more, different number of hidden neurons needs different methods of calculating $H^{\dagger}$ [17], such as singular value decomposition, orthogonal projection, and iterative methods [18, 19], so how to solve $H^{\dagger}$ is important, a popular and efficient closed-form solution is:

$$\hat{\beta} = \begin{cases} H^T(I/C + HH^T)^{-1}T, & if \quad N \leq L \\ (I/C + H^TH)^{-1}H^TT, & if \quad N > L \end{cases} \tag{5}$$

where C is a parameter used for controlling the trade-off between the training error and norm of output weights [20, 21], it can improve network accuracy significantly.

2.2 Main Problems in Modeling of ELM

Equation (4) discloses the reason why ELM has fast training speed, but reveals two problems with accuracy and stability. The first one is about the number L and the rights of input matrix W, if we can choose proper value of them, the model accuracy will be improved; the second problem is about matrix β, as the discussion above, β is essentially decided by H, different H results in different β, but random W and traditional solving of $H^{\dagger}$ can not guarantee a better β, especially when the training data is contaminated, so we need a new way for better β.

3 Methods for Improving Model Stability

3.1 Design of ME-ELM

Equations (4–5) illustrate that the simulation results are greatly affected by training data, noisy data will inevitably lead to poor performance. M-estimator is a kind of robust estimator which is good at drawing out a reliable conclusion from bad data, especially outliers. So, M-estimator is tried to combine with ELM to decrease the noise influence, by adopting estimation function and least square criterion, output matrix parameters are adjusted during iterations [22], this way is embedded into training algorithm of ELM and is called ME-ELM.

Considering the training target $(H\beta - Y) = 0$, formula (4) can be expressed as follows:

$$\hat{\beta} = (H^T PH)^{-1} H^T PT \tag{6}$$

where P is an adjusting matrix, it can reduce outliers influence by changing its values adaptively. If samples have no bias, all related coefficients in P will be 1, which implies ME-ELM works in the same way as ELM; if part of samples are moderately polluted, the corresponding coefficients in matrix P will be less than 1, to weaken the noise influence; for samples with gross errors, the relative coefficients tend to be zeros, therefore the bad impacts can be decreased greatly. So P plays an important role here, its values are regulated by estimation function ψ, for clear description, statistic function (x) is introduced as first.

$$Q(\beta) = \sum_{i=1}^{N} \rho(e_i) = \sum_{i=1}^{N} \rho(T_i - H_i\beta_i) \tag{7}$$

where $Q(x)$ is optimization objective function, solutions to Eq. (7) are called M-estimators:

$$\hat{\beta} = \arg\min_{\beta}(\sum_{i=1}^{N} \rho(T_i - H_i\beta_i)) \tag{8}$$

Define estimation function $\psi(x) = \frac{\partial \rho(x)}{\partial \beta}$, so the minimum β is:

$$\frac{\partial Q(\beta)}{\partial \beta} = 0 \Rightarrow \sum_{i=1}^{N} \psi(T_i - H_i\beta)H_i = 0 \tag{9}$$

There are several popular estimation functions ψ, similar results can be gotten in terms of efficiency and deviation with one of them [23], Hurb function is expressed as Eq. (10) [24].

$$\psi(x) = \begin{cases} x & |x| \le k \\ k & |x| > k \end{cases}, \quad \rho(x) = \begin{cases} x^2/2 & |x| \le k \\ k|x| - k^2/2 & |x| > k \end{cases}, \; k = 1.345 \tag{10}$$

Algorithm of ME-ELM can be designed as follows:

Step 1 Determine the network structure, acquire original value with normal ELM: $\beta_0 = H^{\dagger}T$ and $e_0 = T - H^{\dagger}\beta_0$

Step 2 Setting initial parameters, such as adjusting factor $k = 1.345$ and error variable $\varepsilon = 1$

Step 3 Iteration process:

```
while ((ε <1e04) or (N<100))
```

(a) `Standardizing` e_i `as` $e_i = e_i/s = 0.6745e_i/\mathrm{med}(|e_i|)$, `med(`$|e_i|$`)` `is the middle of` $|e_i|$.

(b) Adjusting $W_i = \frac{\psi(u_i)}{u_i}$ and calculate $\hat{\beta}^{(i)} = (H^T W_i H)^{-1} H^T W_i T$ with Huber function.

(c) Renewing variables: $e_i = T - H\hat{\beta}^{(i)}$, $N = N+1$, $\varepsilon = \left|\hat{\beta}^{(i)} - \hat{\beta}^{(i-1)}\right|$

$e_i = T - H\hat{\beta}^{(i)}$, $N = N+1$, $\varepsilon = \left|\hat{\beta}^{(i)} - \hat{\beta}^{(i-1)}\right|$

End while

3.2 Experiments for Stability

To verify the capability of ME-ELM in enhancing stability, some popular algorithms are used for comparison, including ELM, ELM-C, B_ELM, and BP, the networks are constructed based on noisy samples and tested with non-noise data, then stability performance can be distinguished by RMSE and DEV. SinC function is defined as follow:

$$y(x) = \begin{cases} \sin x/x & x \neq 0 \\ 1 & x = 0 \end{cases} \tag{11}$$

First, 5000 groups data are generated randomly, then white Gaussian noise is added to independent variables, by selecting different noise distribution range of [−0.2 0.2], [0 2], and [−2 2], three batches of 5000 training data are prepared, after network models are constructed by various algorithms, stability performance can be checked out with noise-free data. Comparisons are carried out between ME-ELM and some other algorithms, such as ELM-C, BP, the number of hidden neurons is fixed as 20, to examine the universal property of ME-ELM, several linear and nonlinear multivariable function are tested, results of $y = \exp(x_1/2)\, x_1 + \sin(x_2)$ are also listed in Table 1.

In addition, to avoid rank deficient problem in ME-ELM, random minor value can be added to the adjusted value on the base of Eq. (10), which is expressed as follows.

$$\psi(x) = \begin{cases} x & |x| < k (k > 0) \\ k + 0.1 * rank(0) & |x| > k (k > 0) \end{cases} \tag{12}$$

Obvious difference in stability performance can be seen from Fig. 2, where both ELM [16] and ME-ELM are used to model SinC function when the training data have been added Gaussian noise, and the noise distribution interval is [0 2].

It is clear from the comparison above that ME-ELM has good ability of noise reduction, it can produce a better model which has much better performance than ELM, ELM-C, and B-ELM.

Table 1 Testing error comparison between different models

Function	Testing error	ELM	ELM−C	B-ELM	BP	ME-ELM	Noise distribution
$y = \sin c(x)$	RMSE	0.002498	0.075118	0.365096	0.03426	**0.000121**	[−0.2 0.2]
	Dev	0.000044	−0.002815	0.105855	−0.000025	**−0.000001**	
	RMSE	0.102556	0.123228	0.329231	0.109186	**0.002475**	[0 2]
	Dev	−0.100852	−0.098573	0.005053	−0.102048	**0.000630**	
	RMSE	0.020395	0.074426	0.3352543	0.037857	**0.001051**	[−2 2]
	Dev	0.002487	0.004764	0.072820	0.002093	**−0.000035**	
$y = \exp(x_1/2)*$ $x_1 + \sin(x_2)$	RMSE	0.002307	0.056295	0.073086	0.006358	**0.000030**	[−0.2 0.2]
	Dev	0.0000078	0.000599	−0.033326	0.000113	**0**	
	RMSE	0.101063	0.115764	0.486288	0.111284	**0.000576**	[0 2]
	Dev	0.099678	−0.100685	−0.415225	−0.102691	**−0.000111**	
	RMSE	0.016717	0.057668	0.093592	0.045291	**0.000105**	[−2 2]
	Dev	−0.000287	−0.001082	0.074013	−0.000445	**0.000013**	

Bold numbers are the best ones with least errors in different trials

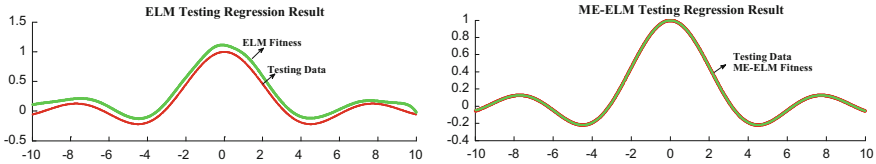

Fig. 2 Testing results of ELM and ME-ELM

4 Study of TIG Welding Modeling and Welding Shape Prediction

Welding is a complex time-variant process and welding joint shape relates to many variables [25, 26], furthermore, joint shape is susceptible to interference, even the fluctuation of electric grid may result in the changing of geometry, and all the training data will inevitably be contaminated, so how to guarantee the model performance is very important.

4.1 Experimental Design and Data Acquisition

To design experiments, the contributing factors and relative levels should be determined at first, and then experimental design matrix will be arranged in orthogonal method, the work is often planned as follows:

1. Identification of important process parameters.
2. Finding the upper and lower limits with different levels of the parameters.
3. Confirm design matrix according to orthogonal table
4. Conducting the experiments as per the design matrix, if needed, repeating the specific experiment.
5. Specimen preparation, if necessary, measuring the bead shape on different samples.
6. Treating data with filtering and recording these responses.

For convenient comparison, TIG welding data published in [27] are used, it is also used in [28] where the TIG welding variables include welding speed (S), wire speed (WS), cleaning percentage (CP), welding current (C) and arc gap (G), and weld bead shape parameters comprise front height (FH), front width (FW), back height (BH), and back width (BW), shown in Table 2.

Table 2 Experimental data [27]

Number	Input					Output			
	Speed/ (cm.min−1)	Wire speed/ (cm.min−1)	Cleaning/ (%)	Gap/ (mm)	Current/ (V)	Front height/ (mm)	Front width/ (mm)	Back height/ (mm)	Back width/ (mm)
1	24	1.5	30	2.4	80	−0.149	6.09	0.672	5.664
2	24	1.5	30	3.2	80	0.027	6.411	0.412	5.197
3	24	1.5	70	2.4	80	−0.179	7.432	0.593	7.058
4	24	1.5	70	3.2	80	−0.306	7.287	0.63	6.895
5	24	2.5	30	2.4	80	0.155	6.676	0.743	5.96
6	24	2.5	30	3.2	80	0.099	6.824	0.803	5.732
7	24	2.5	70	2.4	80	−0.129	7.009	0.878	6.989
8	24	2.5	70	3.2	80	−0.077	7.46	0.82	7.809
9	24	1.5	30	2.4	95	−0.017	8.664	0.437	8.75
10	24	1.5	30	3.2	95	−0.25	8.782	0.593	9.993
11	24	1.5	70	2.4	95	−0.553	9.757	0.852	9.993
12	24	1.5	70	3.2	95	−0.42	10.374	0.736	10.687
13	24	2.5	30	2.4	95	−0.345	9.783	0.965	10.237
14	24	2.5	30	3.2	95	−0.043	8.803	0.654	9.076
15	24	2.5	70	2.4	95	−0.134	9.75	0.798	9.465
16	24	2.5	70	3.2	95	−0.168	10.348	0.708	10.193
17	24	1.5	30	2.4	110	−0.599	11.348	0.805	11.679
18	24	1.5	30	3.2	110	−0.745	11.491	1.1	11.848
19	24	1.5	70	2.4	110	−0.254	11.237	0.47	12
20	24	1.5	70	3.2	110	−0.683	12.946	0.945	13.921
21	24	2.5	30	2.4	110	−0.232	9.338	0.866	10.611
22	24	2.5	30	3.2	110	−0.557	12.348	1.139	12.403
23	24	2.5	70	2.4	110	−0.623	11.767	1.128	12.86
24	24	2.5	70	3.2	110	−0.617	12.533	1.084	13.346
25	35	1.5	30	2.4	80	0.123	5.355	0.245	4.104

(continued)

Table 2 (continued)

Number	Input					Output			
	Speed/ (cm.min−1)	Wire speed/ (cm.min−1)	Cleaning/ (%)	Gap/ (mm)	Current/ (V)	Front height/ (mm)	Front width/ (mm)	Back height/ (mm)	Back width/ (mm)
26	35	1.5	30	3.2	80	0.108	5.173	0.34	3.418
27	35	1.5	70	2.4	80	−0.044	5.833	0.51	4.875
28	35	1.5	70	3.2	80	−0.09	5.831	0.502	5.082
29	35	2.5	30	2.4	80	0.251	5.656	0.557	4.37
30	35	2.5	30	3.2	80	0.23	5.562	0.593	3.948
31	35	2.5	70	2.4	80	0.18	5.711	0.45	5.085
32	35	2.5	70	3.2	80	0.12	5.85	0.626	4.989
33	35	1.5	30	2.4	95	−0.213	6.348	0.458	5.874
34	35	1.5	30	3.2	95	−0.19	6.992	0.447	6.74
35	35	1.5	70	2.4	95	−0.152	7.163	0.464	6.994
36	35	1.5	70	3.2	95	−0.213	7.25	0.504	7.019
37	35	2.5	30	2.4	95	−0.164	7.288	0.715	6.724
38	35	2.5	30	3.2	95	−0.113	6.966	0.746	6.433
39	35	2.5	70	2.4	95	−0.107	7.055	0.696	7.24
40	35	2.5	70	3.2	95	−0.018	7.549	0.591	7.166
41	35	1.5	30	2.4	110	−0.575	8.337	0.766	8.763
42	35	1.5	30	3.2	110	−0.267	8.605	0.506	8.58
43	35	1.5	70	2.4	110	−0.385	9.109	0.672	9.652
44	35	1.5	70	3.2	110	−0.564	9.67	0.743	9.952
45	35	2.5	30	2.4	110	−0.556	8.756	1.011	8.853
46	35	2.5	30	3.2	110	−0.188	9.442	0.666	9.614
47	35	2.5	70	2.4	110	−0.309	9.015	0.784	9.041
48	35	2.5	70	3.2	110	−0.318	9.297	0.785	9.47
49	46	1.5	30	2.4	80	0.357	4.982	0.001	2.255
50	46	1.5	30	3.2	80	0.168	4.898	0.277	2.998

(continued)

Table 2 (continued)

Number	Input					Output			
	Speed/ (cm.min−1)	Wire speed/ (cm.min−1)	Cleaning/ (%)	Gap/ (mm)	Current/ (V)	Front height/ (mm)	Front width/ (mm)	Back height/ (mm)	Back width/ (mm)
51	46	1.5	70	2.4	80	0.088	5.02	0.281	3.302
52	46	1.5	70	3.2	80	0.09	4.423	0.42	3.172
53	46	2.5	30	2.4	80	0.39	4.78	0.062	1.33
54	46	2.5	30	3.2	80	0.487	4.992	0.139	1.6
55	46	2.5	70	2.4	80	0.38	5.231	0.397	2.817
56	46	2.5	70	3.2	80	0.394	5.337	0.378	3.041
57	46	1.5	30	2.4	95	−0.321	5.847	0.44	5.332
58	46	1.5	30	3.2	95	−0.152	5.704	0.386	5.35
59	46	1.5	70	2.4	95	−0.155	5.967	0.445	5.415
60	46	1.5	70	3.2	95	−0.09	5.892	0.399	5.319
61	46	2.5	30	2.4	95	−0.236	5.984	0.696	5.531
62	46	2.5	30	3.2	95	0.067	6.03	0.575	5.636
63	46	2.5	70	2.4	95	−0.075	5.562	0.816	4.835
64	46	2.5	70	3.2	95	0.138	6.546	0.575	6.285
65	46	1.5	30	2.4	110	−0.217	6.092	0.359	6.419
66	46	1.5	30	3.2	110	−0.339	7.335	0.619	7.52
67	46	1.5	70	2.4	110	−0.249	7.719	0.492	7.706
68	46	1.5	70	3.2	110	−0.396	7.633	0.458	7.601
69	46	2.5	30	2.4	110	−0.01	6.396	0.536	6.197
70	46	2.5	30	3.2	110	0.074	6.863	0.484	6.072
71	46	2.5	70	2.4	110	−0.201	7.052	0.658	7.48
72	46	2.5	70	3.2	110	−0.358	7.759	0.798	7.917

4.2 Models Performance Comparison for TIG

For simplicity, only the comparison between ME-ELM and BP, MNR, and LR are given out. Welding data are normalized at first and then separated into two groups: 56 records are used for training and the rest 16 records for testing. To begin with ME-ELM, the number of middle neurons is set as 40 by SA at first, and then, GA is used to get proper input matrix, M-estimation is used at last to calculate the output matrix. BP network is created with 40 middle layer numbers and four output numbers, active function and output function are "tansig" and "purelin", the comparison is shown in Fig. 3.

The MNR model is always better than linear regression [29], suppose the input variables are $X1$, $X2$, $X3$, $X4$, $X5$, the output variables indicating the bead shape are denoted by FH, FW, BH, and BW, the nonlinear regression forms can be given out as:

$$\left.\begin{aligned} FH &= g_1 x_1^{a_1} x_2^{a_2} x_3^{a_3} x_4^{a_4} x_5^{a_5} \\ FW &= g_2 x_1^{b_1} x_2^{b_2} x_3^{b_3} x_4^{b_4} x_5^{b_5} \\ BH &= g_3 x_1^{c_1} x_2^{c_2} x_3^{c_3} x_4^{c_4} x_5^{c_5} \\ BW &= g_1 x_1^{d_1} x_2^{d_2} x_3^{d_3} x_4^{d_4} x_5^{d_5} \end{aligned}\right\} \tag{13}$$

By proper treating of original data, it can be converted to:

$$\left.\begin{aligned} \lg(FH) &= G_1 + a_1 \lg x_1 + a_2 \lg x_2 + a_3 \lg x_3 + a_4 \lg x_4 + a_5 \lg x_5 \\ \lg(FW) &= G_2 + b_1 \lg x_1 + b_2 \lg x_2 + b_3 \lg x_3 + b_4 \lg x_4 + b_5 \lg x_5 \\ \lg(BH) &= G_3 + c_1 \lg x_1 + c_2 \lg x_2 + c_3 \lg x_3 + c_4 \lg x_4 + c_5 \lg x_5 \\ \lg(BW) &= G_4 + d_1 \lg x_1 + d_2 \lg x_2 + d_3 \lg x_3 + d_4 \lg x_4 + d_5 \lg x_5 \end{aligned}\right\}, G_i = \lg(g_i), \quad i = 1, 2, 3, 4 \tag{14}$$

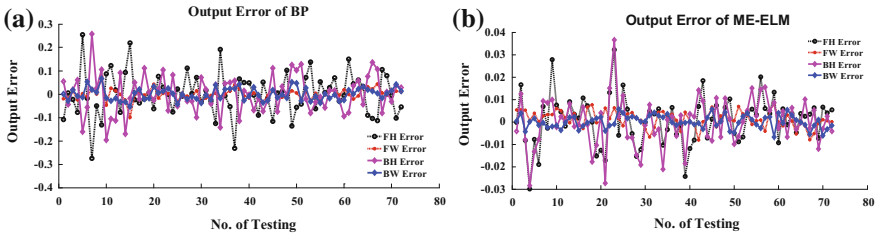

Fig. 3 Training errors of BP and ME-ELM

So the regression model can be achieved according to Least Square principle:

$$\left.\begin{aligned} FH &= 0.7341\left(\frac{x_1}{46}\right)^{0.5667}\left(\frac{x_2}{2.5}\right)^{0.3428}\left(\frac{x_3}{70}\right)^{-0.0874}\left(\frac{x_4}{3.2}\right)^{-0.0459}\left(\frac{x_5}{110}\right)^{-1.9754} - 1 \\ FW &= 7.8699\left(\frac{x_1}{46}\right)^{-0.6622}\left(\frac{x_2}{2.5}\right)^{0.0392}\left(\frac{x_3}{70}\right)^{0.0844}\left(\frac{x_4}{3.2}\right)^{0.1290}\left(\frac{x_5}{110}\right)^{1.4149} \\ BH &= 0.7949\left(\frac{x_1}{46}\right)^{-1.2730}\left(\frac{x_2}{2.5}\right)^{0.7392}\left(\frac{x_3}{70}\right)^{0.3809}\left(\frac{x_4}{3.2}\right)^{0.6715}\left(\frac{x_5}{110}\right)^{2.3903} \\ BW &= 7.6050\left(\frac{x_1}{46}\right)^{-1.0607}\left(\frac{x_2}{2.5}\right)^{-0.0473}\left(\frac{x_3}{70}\right)^{0.01877}\left(\frac{x_4}{3.2}\right)^{0.1341}\left(\frac{x_5}{110}\right)^{2.5845} \end{aligned}\right\} \quad (15)$$

Comparison results between MNR, LR, and ME-ELM are shown in Table 3, The better values are shown in bold font, it is clear that ME-ELM algorithm has much more better performance.

5 Discussion of ME-ELM in Underwater Welding

Studies of welding parameters optimization methods have been carried out for a long time, in which the welding model is very important, especially in underwater welding [30]. There are three kinds of welding methods for underwater welding, named as wet welding, dry welding, and semidry welding. Compared with other two methods, there are many bubbles and turbulent fluid accompany with the wet welding process, in the meantime, evaporation cooling has a great effect on the melt zone so as to lead to a bad welding performance, the horizontal resurfacing welding is shown in Fig. 4. So it is critical to refrain the noises for building the wet welding model, preliminary study suggested that ME-ELM can work its way effectively and detail results will be given out in further paper.

6 Conclusion

Methods for improving model accuracy and stability are studied in this paper, comparison results on benchmark problems, artificial functions, and real TIG welding process indicate that ME-ELM can work effectively. Further conclusions can be drawn as follows:

Table 3 Testing errors of MNR, LR [27] and ME-ELM for trials 1–16

Trial No.	Front height, FH /(mm)			Front width, FW /(mm)			Back height, BH/(mm)			Back width, BW/(mm)		
	MNR	LR [27]	ME-ELM	MNR	LR [27]	ME-ELM	MNR	LR [27]	ME-ELM	MNR	LR [27]	ME-ELM
1	−0.1624	**−0.0006**	0.0020	0.6293	−0.0415	**0.0019**	0.0099	**−0.0034**	0.00856	0.6206	0.1333	**0.0046**
2	−0.0903	0.0164	−0.0065	−0.5725	1.2334	**0.0003**	0.1509	**0**	−0.0027	0.5522	1.1617	**−0.0007**
3	−0.1112	0.0063	**0.0029**	0.2449	−0.1281	**0.0038**	−0.2356	**−0.0028**	0.0153	−0.496	0.2787	**0.0013**
4	**0.0023**	−0.0088	0.0158	−0.323	0.1066	**0.00130**	0.12986	**0.0056**	0.0130	1.2480	−0.2834	**0.0012**
5	−0.0074	0.0034	**0.0010**	−0.1452	−0.0647	**0.0003**	−0.1127	**−0.0033**	0.0070	−0.495	0.18	**−0.0010**
6	0.0708	−0.0121	**−0.0113**	0.4923	0.1534	**−0.0069**	−0.1654	0.0052	**−0.0030**	0.2487	−0.3809	**−0.0029**
7	0.0335	0.1452	**−0.0050**	0.2550	0.4801	**0.00163**	0.0299	**−0.1216**	−0.0024	−1.1512	0.5552	**−0.0040**
8	0.0214	**−0.0054**	−0.0299	−0.3990	0.0601	**−0.0055**	−0.0909	**0.0024**	−0.0248	0.3957	−0.1491	**−0.0063**
9	0.0660	**0.0015**	−0.0069	−0.7024	**0.0001**	−0.0066	−0.0604	**0.0044**	−0.0047	1.0689	−0.0704	**0.0027**
10	0.0053	**0.0041**	−0.0072	−0.1539	−0.0572	**−0.0007**	−0.2244	−0.0007	**−0.0002**	−0.8752	0.1368	**0.0023**
11	0.1061	−0.0118	**0.0075**	−1.0767	0.2149	**0.0006**	0.17868	0.0088	**−0.0015**	0.52997	−0.5185	**−0.0058**
12	−0.185	0.0077	**−0.0111**	0.6632	−0.2057	**−0.0047**	−0.06152	−0.013	**−0.0040**	0.04378	0.5619	**−0.0028**
13	0.1110	**0.0028**	−0.0103	−1.0788	−0.065	**0**	0.30235	−0.0058	**−0.0034**	1.61262	0.1894	**−0.0027**
14	−0.123	0.6169	**−0.0069**	−0.2866	−0.371	**−0.0030**	−0.0428	−0.0665	**0.0024**	−0.2102	−0.2039	**−0.0081**
15	0.1397	−0.0012	0.0207	−0.1012	−0.0114	**−0.0026**	0.37200	−0.002	**0.0086**	1.7290	0.0448	**0.0011**
16	0.0952	**−0.0014**	0.0023	0.1103	0.0397	**−0.0043**	−0.0031	0.0045	**0.0003**	−0.3124	−0.1223	**0.0006**

Bold numbers are the best ones with least errors in different trials

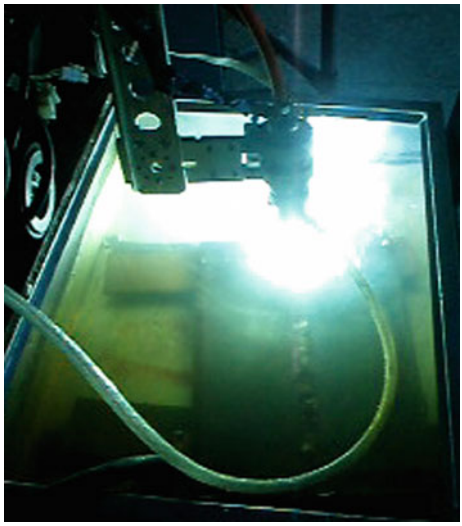

Fig. 4 Resurfacing of wet welding

- Regarding the ability of reducing data noise and improving the simulation accuracy, ME-ELM is better than BP, normal ELM and its corrective methods, such as ELM-C, B-ELM, it is suitable for constructing welding model.
- Parameter k of estimation functions in ME-ELM is very important. Small k lead to small rights for outliers, this will result in a strong suppression on influence. On the contrary, if k is set to be a big positive number, ME-ELM tends to be the normal ELM.
- MNR and LR are all prototype-based, their performance relies mainly on type assumption, generally speaking, and their simulation accuracy is inferior to that of ME-ELM.

Acknowledgements The work is partially founded by the Open Project Program of Jiangxi Province Key Laboratory of Precision Drive & Control (PLPDC-KFKT-201625), the National Natural Science Foundation of China (51665016), the JiangXi Province Science Foundation (20151BAB207047).

References

1. Du B, Cheng Y, Li CF (2012) Analysis of global welding market. Chin Mech Manuf Digest 2:1–7
2. American Welding Society (2016) Welding handbook. Welding Handbook committee, Miami, Florida
3. Murugana N, Gunaraj V (2015) Prediction and control of weld bead geometry and shape relationships in submerged arc welding of pipes. J Mater Process Technol 168(3):478–487
4. Kim IS, Basu A, Siores E (1996) Mathematical models for control of weld bead penetration in the GMAW process. Int J Adv Manuf Technol 12(6):393–401

5. Rao PS, Gupta OP, Murty SSN et al (2009) Effect of process parameters and mathematical model for the prediction of bead geometry in pulsed GMA welding. Int J Adv Manuf Technol 45(5–6):496–505
6. Pal K, Pla SK (2011) Soft computing methods used for the modeling and optimization of gas metal arc welding. Int J Manuf Res 6(1):15–29
7. Murugan N, Parmar RS (1994) Effects of MIG process parameters on the geometry of the bead in the automatic surfacing of stainless steel. J Mater Process 41(4):381–398
8. Shi YH, Zhang ZP, Huang J (2013) Sensitivity model for prediction of bead geometry in underwater wet flux cored arc welding. Trans Nonferrous Met Soc China 23(7):1977–1984
9. Palani PK, Murugan N (2006) Development of mathematical models for prediction of weld bead geometry in cladding by flux cored arc welding. Int J Adv Manuf Technol 30(7–8):669–676
10. Tarng YS, Juang SC, Chang CH (2002) The use of grey based Taguchi methods to determine submerged arc welding process parameters in hard facing. J Mater Process Technol 128(1):1–6
11. Biswas A, Bhaumik S, Majumdar G et al (2011) Bead geometry optimization of submerged arc weld: exploration of weighted principal component analysis (WPCA). Appl Mech Mater 110:790–798
12. Satheesh M, Dhas JER (2014) Multi objective optimization of weld parameters of boiler steel using fuzzy based desirability function. J Eng Sci Technol Rev 7(1):29–36
13. Mondal P, Bose D (2015) Optimization of the process parameters for MIG welding of AISI 304 and IS 1079 using fuzzy logic method. Int Res J Eng Technol 2(8):483–488
14. Katherasan D, Elias JV, Sathiya P et al (2014) Simulation and parameter optimization of flux cored arc welding using artificial neural network and particle swarm optimization algorithm. J Intell Manuf 25:67–76
15. Subashini L, Vasudevan M (2012) Adaptive neuro-fuzzy inference system (ANFIS)-based models for predicting the weld bead width and depth of penetration from the infrared thermal image of the weld pool. Metall Mater Trans 43(2):145–154
16. Huang GB, Zhu QY, Siew CK (2006) Extreme learning machine: theory and applications. Neuro Comput 70:489–501
17. Frénay B et al (2010) Using SVMs with randomized feature spaces: an extreme learning approach. In: 18th European symposium on artificial neural networks, vol 2010, D-side publication, Bruges, pp 315–320
18. Huang GB, Ding X, Zhou H (2010) Optimization method based extreme learning machine for classification. Neuro Comput 74(12):155–163
19. Widrow B, Greenblatt A, Kim Y et al (2013) The no-prop algorithm: a new learning algorithm for multilayer neural networks. Neural Networks 37(1):182–188
20. Huang GB, Bai Z, Kasun LLC (2015) Local receptive fields based extreme learning machine. IEEE Comput Intell Mag 10(2):18–29
21. Huang GB (2014) An insight into extreme learning machines: random neurons, random features and kernels. Cogn Comput 6(3):376–390
22. Hampel FR, Ronchetti EM, Rousseeuw PJ et al (2011) Robust statistics: the approach based on influence functions. Wiley, Hoboken, New Jersey
23. Stigler SM (2010) The changing history of robustness. Am Stat 64(4):277–281
24. Street JO, Carroll RJ, Ruppert D (1988) A note on computing robust regression estimates via iteratively reweighted least squares. Am Stat 42(2):152–154
25. Ye JX (2013) Wet welding platform design based on ultrasonic sensor. Int J Appl Crypt 5 (2):707–714
26. Ye JX, Zhang H (2008) Automatic underwater arc welding seam-tracking system based on flux-core wire and rotating arc sensor. Trans China Weld 29(3):141–144
27. Juang SC, Tarng YS, Lii HR (1998) A comparison between the back-propagation and counter-propagation networks in the modeling of the TIG welding process. J Mater Process Technol 75(1–3):54–62

28. Nagesha DS, Datta GL (2010) Genetic algorithm for optimization of welding variables for height to width ratio and application of ANN for prediction of bead geometry for TIG welding process. Appl Soft Comput 10(3):897–907
29. Du JH (2010) A study on underwater welding seam forming and tracking based on rotating arc sensor. Dissertation, South China University of Technology
30. Ye JX, Zhang H (2009) Research of intellectual calculation in welding parameters optimization. Mater Rev 23(12):69–72

Study on the Cracks of NiTiNb/TC4 Lap Joints Welded by Micro Laser Welding

Yuhua Chen, Zilin Zhan, Yuqing Mao, Yangyang Yu and Weiwei Lu

Abstract Dissimilar metal sheets of $Ni_{47}Ti_{44}Nb_9$ (at.%, short for NiTiNb) shape memory alloy and Ti6Al4V (TC4) alloy with the same thickness of 0.2 mm are joined by using micro laser welding technology. The microstructure and crack in the weld are studied by optical microscope (OM) and scanning electron microscope (SEM). The results show that the cracks are easy to generate during the laser lap welding of NiTiNb alloy and TC4 alloy due to plenty of brittle intermetallic compound of Ti_2Ni. However, the welding cracks can significantly reduce or disappear by adding filler metal of Ni foil. No-defect joint is obtained when NiTiNb alloy is located on the upper and 50 μm thick Ni foil is added during the lap welding process. The crack sensitivity can be decreased because of finer grains and elliptic boundaries. The shear load of the joint can reach 162 N.

Keywords NiTiNb/TC4 dissimilar metals · Micro laser welding
Filler metal of Ni · Crack control

1 Introduction

The joining of dissimilar materials is of great significance to the modern industry since single material is unable to meet the needs of a variety of functions for composite structures, so different materials need to be welded to satisfy the multiple uses [1–3]. However, it is easy to produce many cracks during welding dissimilar materials due to the differences in their physical and chemical properties, and the cracks can severely reduce the weld quality such as strength and plasticity.

Y. Chen (✉) · Z. Zhan · Y. Mao (✉) · Y. Yu · W. Lu
School of Aerospace Manufacturing Engineering, Nanchang Hangkong University, Nanchang 330063, China
e-mail: ch.yu.hu@163.com

Y. Mao
e-mail: maoyuqing-8888@163.com

S. Chen et al. (eds.), *Transactions on Intelligent Welding Manufacturing*,
Transactions on Intelligent Welding Manufacturing,
https://doi.org/10.1007/978-981-10-7043-3_5

Therefore, the further application of this welded joint with dissimilar materials is limited [4, 5].

$Ni_{47}Ti_{44}Nb_9$ (at.%, short for NiTiNb) is one of the Ti–Ni shape memory alloys, and it is widely used in aerospace, nuclear industry, offshore oil, household appliances, and daily necessities for its excellent specific strength, corrosion resistance, wear resistance, shape memory effect, and damping properties [6, 7]. Ti6Al4V (TC4) is a kind of titanium alloy that owns both of α and β phases, and it is widely used in biomedical, aerospace, ships and so on for good strength, corrosion resistance, and high temperature resistant performance [8]. The dissimilar material welding of ultra-thin NiTiNb to TC4 could be used for reducing the noise in sound attenuation of aircraft engine components [9]. However, it is easy to produce plenty of brittle intermetallic compound like Ti_2Ni, Ni_3Ti, etc. during the welding process [10, 11]. In addition, Ti alloy can absorb hydrogen from 250 °C, oxygen from 400 °C, and nitrogen from 600 °C [12], which makes it easy to get the brittle joint and generate the welding crack. Therefore, the traditional welding method is difficult to meet the requirements of the TC4 and NiTiNb alloy welding.

Laser welding is one of the important processing methods for the characteristics of high energy density, high precision and so on. Because the power is lower, micro laser welding as one of laser welding technologies commonly used in welding metal sheet, metal wire, and small electronic precision part connection, and it plays an important role in the field of the micro connection field [13, 14]. Li et al. [15, 16] studied the welding of NiTi alloy to stainless steel by adding the metal wire of Ni and Co, and they found that the welding cracks were eliminated. Zoeram and Mousavi [17] found that the transverse cracks were controlled when 1 mm thick NiTi alloy and TC4 alloy were welded by adding filler metal of Cu. Moreover, some high temperature materials such as pure Nb, Ta, and V may also be added to remove the cracks during the welding of TiNi alloy to TC4 alloy [18–20]. However, these materials are rare as well as expensive, so their use is limited.

Therefore in the experiment, micro pulse laser equipment is applied to the lap welding of NiTiNb and TC4 alloy sheets with the same thickness of 0.2 mm, and Ni sheet as a filler metal is used to control the cracks during the welding. The microstructure, crack, and fracture surface of the joint is investigated, and the data can provide the theoretical support for the dissimilar welding of NiTiNb toTC4 alloys.

2 Materials and Methods

In the experiment, 0.3 mm thick NiTiNb hot rolled sheet and 0.2 mm thick TC4 sheet are adopted as a base material. Filler metal of pure Ni foil with a thickness of 50 μm is added in the middle of two alloys during the welding process. Their main chemical components and physical properties are shown in Tables 1 and 2, respectively.

Table 1 Chemical compositions of materials

Element	Mass fraction (%)	
	NiTiNb	TC4
Al	–	5.5
V	–	4.37
Ti	29	90.13
Ni	60	–
Nb	11	–

Table 2 Physical properties of materials

Material	Melting point (°C)	Coefficient of linear expansion × 10^6 ($°C^{-1}$)	Thermal conductivity (W m^{-1} $°C^{-1}$)	Specific heat capacity (J g^{-1} K^{-1})
NiTiNb	1250	11.43	9.8	0.461
TC4	1630	9.1	6.8	0.611
Ni	1453	13.3	5.9	0.456

According to ASTM G1-90, NiTiNb alloy sheets are put in a mixed solution (volume ratio, HF:HNO_3:H_2O = 1:3:5) to remove the oxide film before the welding, and then are washed and dried by acetone. The welded NiTiNb alloy sheets must be controlled within 200 ± 10 μm thickness to keep the same thickness as TC4 alloy sheet.

SL-80 type Nd:YAG pulsed laser welding machine is used in the experiment. The laser wavelength is 1.06 μm and the largest laser power is 80 W. The gas protection device is designed in the experiment to prevent the weld from being oxidized. The pure argon gas is filled in the gas box and the gas flow rate is 8 L/min. The process parameters were selected as follows: the laser power is 20 W, the laser spot diameter is 0.3 mm, the pulse width is 6.0 ms, the laser frequency is 5 Hz, and the welding speed is 300 mm/min.

After welding, the microstructure is observed by an optical microscope (OM), and the crack morphologies and fracture surfaces are analyzed by scanning electron microscope (SEM) and energy dispersive spectrometry (EDS).

3 Results and Discussion

3.1 Crack Sensitivity for Different Lap Position

Figure 1 shows the cross section of the joint produced by adding the filler metal of 100 μm thick Ni when NiTiNb alloy is placed on the upper. The macrostructure of the weld presents an onion ring shape which is related to thermal agitation of the laser. In the bottom of the weld, lots of cracks appear near the side of TC4 alloy,

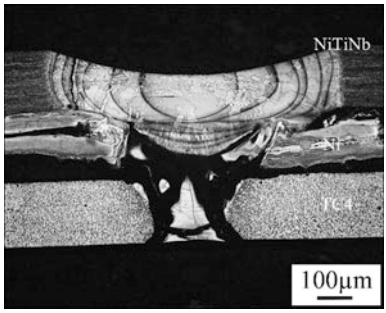

Fig. 1 Cross section of the joint when NiTiNb alloy is placed on the upper and 100 μm thick Ni foil is added

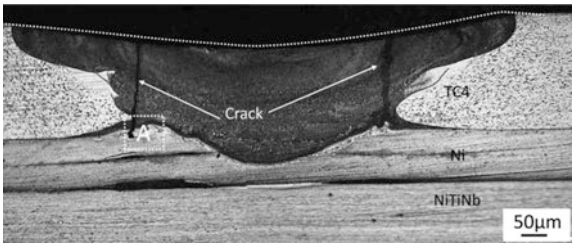

Fig. 2 Cross section of the joint when TC4 alloy is placed on the upper and 100 μm thick Ni foil is added

and the cracking distance is larger. The main reason is that it is easy to generate a large number of brittle intermetallic compounds such as Ti_2Ni and Ni_3Ti in the weld when NiTiNb alloy and TC4 alloy are welded [21]. What is more, the difference of the linear expansion coefficients between NiTiNb alloy and TC4 alloy is large, which makes the weld suffer from large stress concentration. The cracks are easy to generate because of the effect of residual stress during welding. The physical properties of Ni are between those of NiTiNb and TC4 alloys, so it can form metallurgical combination with base material since it can play a buffer action to the welding crack. During welding, this can change the type and number of brittle intermetallic compounds by controlling the melting-mixing ratio of Ni to Ti element according to the Ti–Ni binary phase diagram. Thus, Ni as filler metal can reduce or eliminate the welding cracks during laser welding.

Figure 2 shows the cross section of the joint when TC4 alloy is located on the top during welding. It is clearly seen that two cracks expand upwards from the weld center, the number of cracks significantly decrease and the cracking distance becomes smaller. Figure 3 shows a magnified graph of the crack in the zone A of Fig. 2. It is found that the crack originates from the interface of Ni, fusion zone, and TC4 alloy, and then expands through the grains along the vertical direction. The analysis is that the solidification shrinkage and thermal contraction increase during the cooling process due to the difference in thermal expansion coefficients (the difference of thermal expansion coefficients between TC4 and Ni is bigger than that of TC4 and NiTiNb). The crack produces along the columnar crystal which can urge the inhomogeneous deformation of grains, and add the brittleness and crack sensitivity of the weld.

Fig. 3 Magnified graph in the region A of Fig. 2

3.2 *Crack Morphology for Adding Filler Metal*

Figure 4 shows the macro cross section when TC4 alloy is placed on the upper and the filler metal of Ni with 50 μm thickness is added during welding. The number of cracks reduces and the cracking distance of the crack is only about 5 μm. Figure 5 shows the local position of the crack. It is seen that the crack originates from the bottom of the weld, different phase structures are layered, and the thickness of compound layers is between 3 and 15 μm in the weld bottom. Lots of shrinkage pores exist near the area of the zone in Fig. 5. The reason is that there is no enough liquid metal supplying from the surrounding of the crack. The EDS result shows that the element proportion of Ti and Ni is 0.83:1 in the zone. However, the element proportion of Ni and Ti in the area is 65.27:28.71, which is close to the ratio of brittle phase of Ti_2Ni. The crack is easy to generate and expand during the process of energy release, and the brittleness of the weld increases.

The cracks can be prevented by reducing the generation of brittle compound [22]. Figure 6a shows the surface morphology of the joint when TC4 alloy is placed on the upper and 50 μm thick Ni filler metal is added during welding. The longitudinal crack occurs on the surface of the joint. However, a no-defect weld is produced when NiTiNb alloy is placed on the upper and 50 μm thick Ni foil is added, as shown in Fig. 6b. Figure 6c shows the cross section of the joint in Fig. 6b when 50 μm thick Ni foil is added. The local cross section of the weld presents chrysanthemum shape which may be related to the thermal agitation of laser during

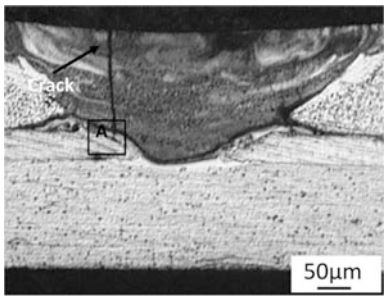

Fig. 4 Cross section of the joint when TC4 alloy is placed on the upper and 50 μm thick Ni foil is added

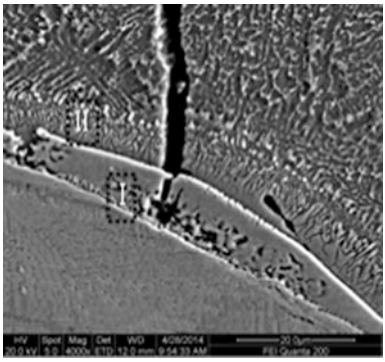

Fig. 5 Magnified graph in the region A of Fig. 4

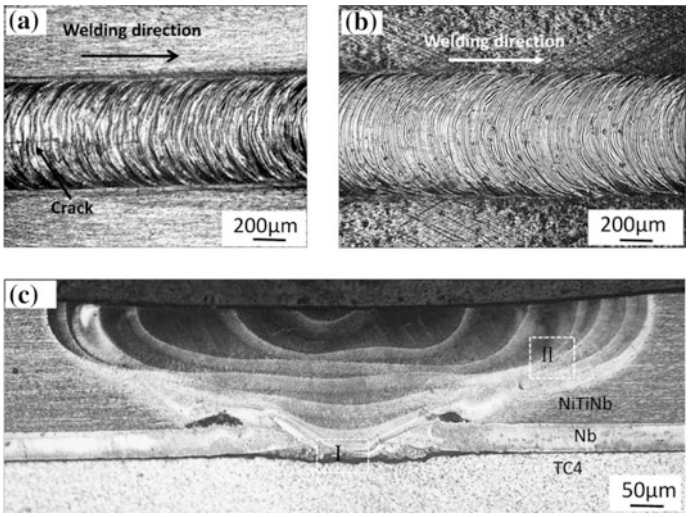

Fig. 6 Surface morphology when TC4 alloy: **a** or NiTiNb alloy; **b** is placed on the upper and cross-sectional morphology; **c** of the joint in Fig. 6b

the welding process. Also, the width of the upper molten pool is wider than that in the bottom. However, it is similar to the "bowl" shape for the whole weld due to heat transfer. High temperature is produced by laser focusing which can cause the loss of alloy elements, so the top shape of the weld is concave. The closed metallurgical combination is formed, and the defects such as blowholes and cracks are not found in the weld. Different organizations can be seen in the weld, which suggests that the macro segregation is coming.

3.3 Distribution of Element

Figure 7 shows an enlarged map of the area I in Fig. 6c. The layered microstructure is obvious in the bottom of the melted pool that presents different phase structures. A transition layer with a width of 10 μm is adjacent to the base material. Table 3 shows the result of EDS analysis in the area in Fig. 6c. The content of Ni in the area of Point C is the highest, and then reduces with the increase of the distance from Point C. However, the content of Ti element becomes higher with the increase of the distance from Point C, and it is close to that of TC4 at Point A and that of TiNiNb at Point E, respectively. The content of Nb gradually decreases from Point E to Point A. The reason is that Point C is in the area of Ni sheet. Al and V elements gradually reduce in the fusion zone along the vertical direction to the weld surface. The result in Table 4 shows that the black area lacks V element while the white area contains V element. The content of Al near weld surface reduces and it is about 0.14% in the area of in Fig. 6c. Point B mainly contains Ni element and Ti element; the ratio of Ni to Ti is about 31.26:60.21. It is proved that this area is Ti_2Ni phase according to the studies of Song et al. [23] and Chen et al. [24] and Ti–Ni binary phase diagram. The existence of brittle Ti_2Ni phase can increase the crack sensitivity and reduce the toughness of the weld.

Figure 8 shows a magnified map of the area II in Fig. 6c. In the weld center, the heat dissipation is slower than that far from this area, which can form the dendrite in bar shape. However, the supercooling degree of the right area far from the weld center is larger than that of the weld center because of faster heat dissipation, so like

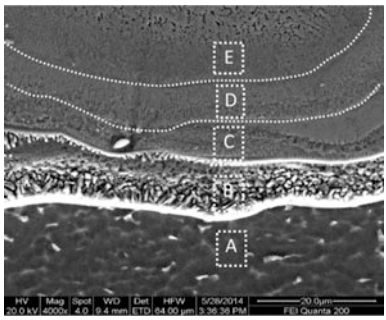

Fig. 7 Microstructure in the bottom of the weld

Table 3 EDS analysis in the bottom of the weld when NiTiNb alloy is placed on the upper and 50 μm thick Ni foil is added

Point	Element content (at.%)				
	Ni	Ti	Nb	V	Al
A	–	88.89	–	3.81	7.30
B	31.26	60.21	0.48	4.57	3.48
C	59.58	33.68	2.57	1.54	2.63
D	55.04	38.84	6.12	–	–
E	40.89	47.30	11.25	–	0.56

Table 4 EDS analysis when NiTiNb alloy is placed on the upper

Point	Element content (at.%)				
	Ni	Ti	Nb	V	Al
F	47.45	46.56	5.85	–	0.14
G	43.03	46.59	9.57	0.67	0.14

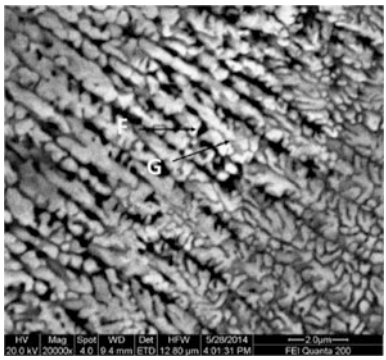

Fig. 8 SEM image in the area of Fig. 6c

the parent metal on the right, the grain size is finer. Little V element is found at Point G from Table 4, but Point F lacks V element. The content of Nb element at Point F is higher than that at Point G. The content of Nb element in the white area is higher than that in the black area. In general, the black areas are low-melting eutectic zones, and the gap can be filled by crystal grains, so the crystallization crack is prevented [25]. The compositions in these regions are uniformly distributed and the small grain and elliptic boundaries are formed in the weld. These conditions are very helpful for avoiding the stress concentration. Therefore, the cracks in the weld obviously decrease even disappear.

3.4 Fracture Surface

When NiTiNb alloy is placed on the upper and 50 μm thick filler metal of Ni is added during welding, the tensile test of the joint is carried out and the fracture surface is analyzed. Figure 9 shows the load-displacement curve of the tensile sample. It is seen that the shear load is about 162 N. Figure 10 shows the SEM image of the fracture surface of the tensile sample. The macro fracture is flat and the cleavage stage is found in local region of fracture surface. Also, few micro-cracks are observed. The main reason is that large stress concentration occurs due to brittle compounds generated by composition segregation. During the testing process, the cracks rapidly expand to the surrounding when the load is greater than the yield strength of the weld and the brittle fracture occurs.

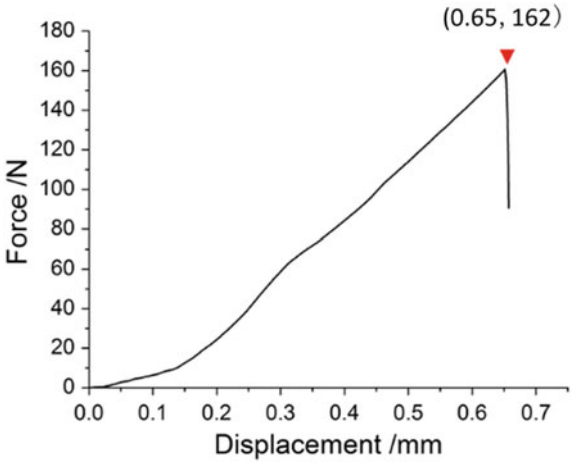

Fig. 9 Load-displacement curve when NiTiNb alloy is placed on the upper and 50 μm thick Ni foil is added

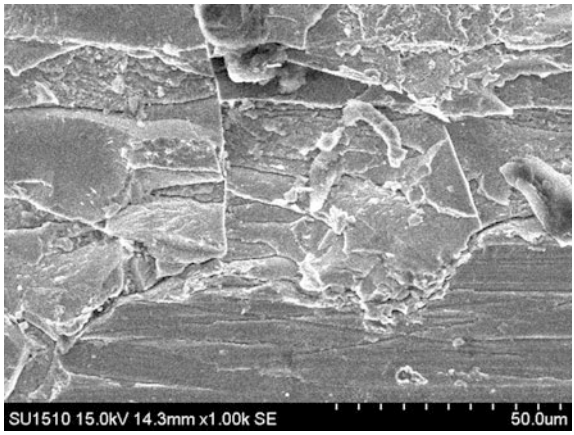

Fig. 10 SEM image of fracture surface

4 Conclusion

(1) Lots of cracks are generated when NiTiNb alloy and TC4 alloy are joined by laser welding due to brittle intermetallic compounds. The decrease and elimination of the cracks in the joint can be controlled by adding filler metal of Ni with different thicknesses and a no-defect joint can be obtained.

(2) The crack sensitivity of the joint increases due to the formation of Ti_2Ni brittle compounds. The finer grains and elliptic boundaries are formed when filler metal of Ni is added during the welding process, which can prevent the crack from the formation and reduce the crack sensitivity.

(3) When NiTiNb alloy is placed on the upper and 50 μm thick filler metal of Ni is added, no crack is found on the surface and the cross section of the weld. The shear load of the joint can reach 162 N and the fracture mechanism presents a brittle fracture.

Acknowledgements The research is supported by the National Natural Science Foundation of China (51565040), the Aviation Science Funds (2014ZE56016), the Jiangxi Science and Technology Plan Projects (20151BBE50034), and the State Key Laboratory of Advanced Welding and Connection Open Topics (AWJ-M15-03).

References

1. Sonato M, Piccolroaz A, Miszuris W et al (2015) General transmission conditions for thin elasto-plastic pressure-dependent interphase between dissimilar materials. Int J Solids Struct 64:9–21
2. Volkov SS, Kholopov YV (1998) Technology and equipment for ultrasonic welding of polymer based composite structures. Russ Ultrason 28(4):145–155
3. Wei YN, Li JL, Xiong JT et al (2015) Research status on friction stir welding of aluminum/steel dissimilar metals. J Netshape Form Eng 7(5):34–40
4. Miranda RM, Assuncao E, Silva RJC et al (2015) Fiber laser welding of NiTi to Ti-6Al-4V. Int J Adv Manuf Technol 81(9):1533–1538
5. Zoeram AS, Mousavi SAAA (2014) Laser welding of Ti-6Al-4V to Nitinol. Mater Des 61:185–190
6. Zhou JB, Wang KL, Chen Q et al (2014) Calculation of the pull-out force of $Ni_{47}Ti_{44}Nb_9$ shape memory ally pipe coupling. Appl Mech Mater 697:360–364
7. Piotrowski B, Zineb TB, Ebehardt A et al (2011) Experimental analysis of $Ni_{47}Ti_{44}Nb_9$ shape memory alloy behavior for tightening application numerical design. Proc Int Symp Steel Struct 258:331–338
8. Li GR, Li YM, Wang FF et al (2015) Microstructure and performance of solid TC4 titanium alloy subjected to the high pulsed magnetic field treatment. J Alloy Compd 644:750–756
9. Mabe J (2008) Variable area jet nozzle for noise reduction using shape memory alloy actuators. J Acoust Soc Am 123:3871–3876
10. Fokin VN, Fokina EE, Korobov II et al (2014) Hydriding of intermetallic compound Ti_2Ni. Russ J Inorg Chem 59:1073–1076
11. Mullner P (1999) Shape memory alloys. Mater Sci Eng 268:246–247
12. Montanari R, Costanza G, Tata ME et al (2008) Lattice expansion of Ti-6Al-4V by nitrogen and oxygen absorption. Mater Charact 59(3):334–337
13. Zhang C, Sun X (2013) Susceptibility to stress corrosion of laser-welded composite arch wire in acid artificial saliva. Adv Mater Sci Eng 46(13):171–177
14. Shelyagin VD, Orishich AM, Khaskin V et al (2014) Technological peculiarities of laser, microplasma and hybrid laser-microplasma welding of aluminium alloys. Paton Weld J 5:33–39
15. Li HM, Sun DQ, Dong P et al (2012) Analysis and prevention of cracks in laser-welded joint of TiNi shape memory alloy and stainless steel. Trans China Weld Inst 33(12):41–44
16. Li HM, Sun DQ, Dong P et al (2011) Study on Laser welding of dissimilar materials between TiNi shape memory alloy/stainless steel. J Mater Eng 1(10):47–51
17. Zoeram AS, Mousavi SAAA (2014) Effect of interlayer thickness on microstructure and mechanical properties of as welded Ti6Al4V/Cu/NiTi joints. Mater Lett 133:5–8

18. Oliveira JP, Panton B, Zeng Z et al (2016) Laser joining of NiTi to Ti6Al4V using a niobium interlayer. Acta Mater 105:9–15
19. Haas T, Schuessler A (1999) Welding and joining of TiNi shape memory alloys: engineering aspects and medical applications. In: Proceedings of the 1st European conference on shape memory and superelastic technologies, SMST, Paris, pp 103–114
20. Lu L (2012) Research on electron beam welding of TC4 titanium alloy and 304 stainless steel. Dissertation, Nanjing University of Technology, China
21. Oliveira JP, Panton B, Zeng Z et al (2016) Laser joining of NiTi to Ti-6Al-4V using a niobium interlayer. Acta Mater 105:9–15
22. Hu P, Zhang H, Zhang XZ et al (2014) Application of a corner chamfer to steel billets to reduce risk of internal cracking during casting with soft reduction. ISIJ Int 54(10):2283–2287
23. Song P, Zhu Y, Guo W et al (2013) Mechanism of crack formation in the laser welded joint between NiTi shape memory alloy and TC4. Rare Metal Mater Eng 4:6–9
24. Chen YH, Mao YQ, Lu WW et al (2017) Investigation of welding crack in micro laser welded NiTiNb shape memory alloy and Ti6Al4V alloy dissimilar metals joints. Opt Laser Technol 91:197–202
25. Min P, Shuichi M, Kazuhiro O et al (1992) Effects of Nb addition on the microstructure of Ti-Ni alloys. Mater Trans, JIM 33(4):337–345

Research on the Ultrasonic Welding of Titanium Alloy After Embedding Fiber Bragg Grating Sensor

Zhengqiang Zhu and Qiankun Xiao

Abstract Fiber Bragg grating (FBG) sensor is a preferred carrier for information transmission and sensing of smart metal structures. The electroplated nickel FBG is embedded in a direct or indirect way and welded by ultrasonic welding to research the rapid prototyping and sensing properties of the titanium alloy intelligent structural parts. The experiment of embedding electroplated nickel FBG into titanium alloy in the direct way shows that titanium alloy is not suitable for embedding matrix. The experiment of embedding electroplated nickel FBG in the indirect way shows that the figure of FBG temperature sensitivity is 2.13 times larger than that of original bare fiber grating, and is 1.11 times larger than that of direct way. This fact means that embedding metallized FBG into the titanium alloy structure in the indirect way is an effective way.

Keywords Metal intelligent structure · Embedded metal
Fiber Bragg grating (FBG)

1 Introduction

Owing to the unique properties, fiber Bragg grating (FBG) has been widely used in civil engineering, aerospace, shipbuilding, petrochemical and other fields [1]. In view of the advantages of energy conservation, environmental protection, easy operation and fast welding of ultrasonic welding [2], embedding FBG sensor into titanium alloy has a great research value to realize intelligent structure which can perceive the external environment [3]. Considering that the main component of ordinary fiber is quartz, and the strength especially the shear stress is poor, it becomes more fragile after coupling of the fiber grating sensor which is likely to cause damage to the fracture under the ultrasonic vibration [4, 5]. Therefore, it must

Z. Zhu (✉) · Q. Xiao
School of Mechanical & Electrical Engineering, Nanchang University, Nanchang, China
e-mail: zhuzhq01@163.com

S. Chen et al. (eds.), *Transactions on Intelligent Welding Manufacturing*,
Transactions on Intelligent Welding Manufacturing,
https://doi.org/10.1007/978-981-10-7043-3_6

be effectively protected before being embedded into titanium alloy. This paper introduces the metal protection method of FBG sensor in detail. Finally, the FBG is embedded according to the optimized process parameters of ultrasonic welding of titanium alloy, and the FBG embedded into titanium alloy is tested to determine whether it loses efficacy after being embedded [6].

2 Related Work on FBG

FBG is the most common fiber grating which belongs to the typical wavelength modulation type optical fiber sensor [7]. It uses the optical fiber writing technology to form a space phase grating with the core refractive index periodically changed along the fiber axes. The schematic diagram of the FBG sensor is shown in Fig. 1. When the broadband light wave transmits in the raster, the reflection of the light that satisfies the Prague phase matching conditions is strong, and the light that does not satisfy the Prague phase matching conditions is reflected back, while light transmission is not affected [8]. This is the choice of fiber grating light. Bragg was the first one to explain this tuning wavelength reflection phenomenon [9], so this kind of grating is named as Bragg grating, and the reflection condition is called Prague condition.

Due to the high melting point of the metal, the embedded fiber grating sensor has a lot of difficulties. The methods used are casting, shape deposition manufacturing, brazing and ultrasonic welding. In the casting method, Hamid et al. [10] cast a tin–lead alloy with a tin content of 65% (melting point of about 190 °C) in a square low carbon steel hollow model as a protective layer for optical fibers, and then used the laser free molding to deposit WC–Co alloy layer on the outer surface of the low carbon steel model. A high hardness outer cutting tool was obtained to monitor the temperature and stress of the tool during cutting. Figure 2 shows the FBG embedded cutting tool in the physical model. In the shape deposition manufacturing technology, a nickel-plated optical fiber sensor was successfully built into the stainless steel by laser-assisted shape deposition on the surface of the stainless steel

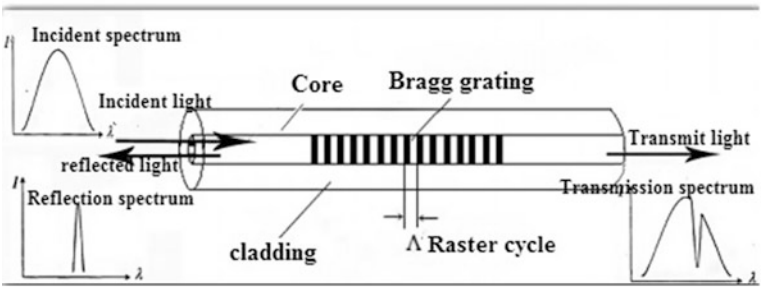

Fig. 1 Schematic diagram of FBG sensor

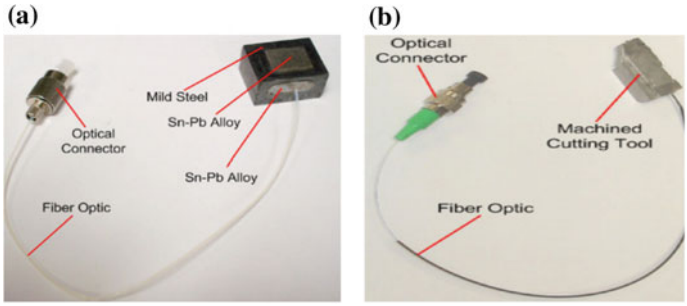

Fig. 2 The embedded FBG cutting tool in **a** the physical model by casting method and **b** laser free molding manufacturing method

substrate [11]. The FBG temperature sensitivity after the embedding was improved. In the brazing method, an electroplated nickel FBG was successfully buried into the low carbon steel, and the buried FBG temperature sensitivity increased by 1 times. In addition, a metal FBG was successfully crushed and embedded into the nickel-chromium alloy material by means of vacuum brazing, and the FBG temperature sensitivity increased by 1.1 times.

3 Experiments

3.1 Pretreatment

Fiber is a nonmetal. To coat the metal on its surface, it is necessary to make the fiber form a clean catalytic transition surface. The specific steps of the pretreatment are generally to remove the coating and then degrease and sensitize the final activation. After the pretreatment, it must plate nickel in the fiber to achieve further protection. Fiber grating plating nickel includes two steps: the first is chemical plating, and the second is electroplating.

Chemical plating refers to the catalytic reduction of metal ions in the bath on the substrate of the clean catalytic transition surface, and the reduced metal atoms are deposited on the surface of the substrate to form a continuous metal coating reaction process [12]. It has a lot of advantages, including uniform coating, beautiful appearance, a wide application of substrates (conductors, semiconductors and non-conductor), no-load current, and so on. The purpose of chemical plating nickel is to form a thin layer of conductive nickel-phosphorus alloy on the surface of the non-conductive fiber grating, and it is ready for electroplating nickel. Chemical plating experiment device is shown in Fig. 3.

Because of the nickel–phosphorus alloy layer is very thin after chemical plating, it is difficult to protect the fiber under high-frequency vibration grating. Therefore, it is necessary to electroplate a layer of dense nickel so as to improve the FBG's

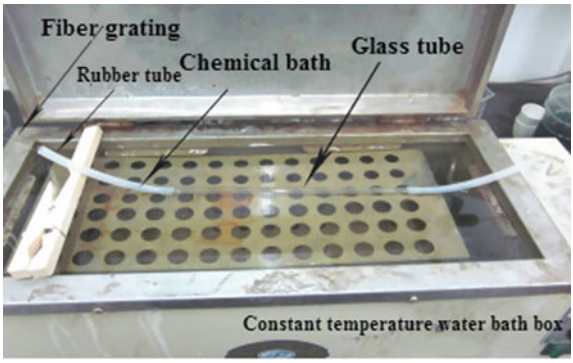

Fig. 3 Chemical plating device

anti-pressure and bending ability [13, 14]. Electroplating is an electro-chemical process that uses an electrolysis process to reduce the metal ions to metal and deposit them on the surface. Figure 4 shows the schematic diagram of fiber grating electroplating nickel.

Besides ultrasonic vibration, the welding temperature and welding pressure are also the key to embed FBG into titanium alloy under ultrasonic welding [15]. Therefore, it is important to design FBG sensor embedding method. We have designed two ways, named "direct embedding" and "indirect embedding". Figure 5 shows three kinds of direct embedding. Figure 6 shows a schematic diagram of indirect embedding scheme.

Considering that the thickness of the titanium alloy is 0.3 mm, the upper and lower titanium alloy is 0.6 mm totally. Therefore, the diameter of the FBG after the direct embedding method should be controlled within 0.6 mm. The FBG diameter of the nickel after plating is 300–550 μm (the diameter of the bare fiber is 125 μm).

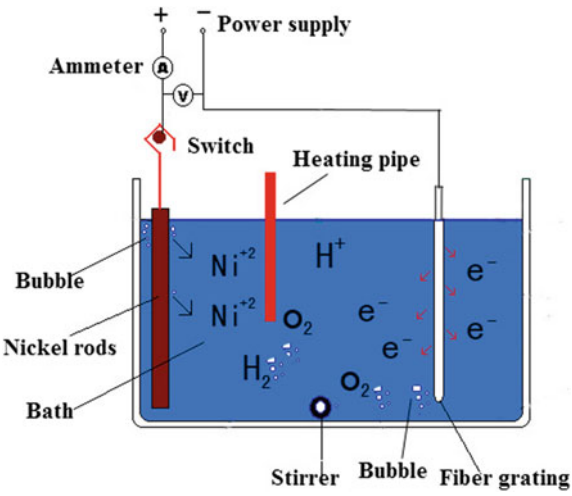

Fig. 4 Fiber grating electroplating nickel

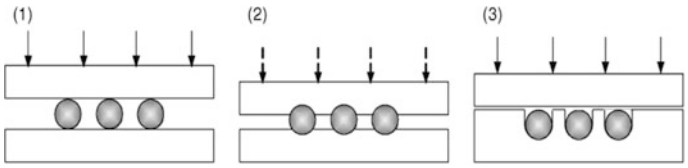

Fig. 5 Direct embedding FBG

Fig. 6 Indirect embedding FBG

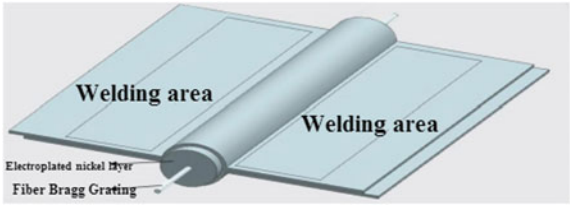

The indirect embedding method is not limited by the FBG diameter, and the thickness of the plating layer can be increased appropriately. The FBG embedded in the indirect way has a diameter of 841 μm after nickel plating. In three kinds of direct embedding, analysis shows that the second is more suitable for this experiment, as shown in Fig. 5.

3.2 Direct Embedding

Interception of Ti6Al4V titanium alloy sheet is completed by using the metal cutting equipment. The sheet is 150 mm × 40 mm × 0.3 mm. Three upper and lower grooves are machined into two titanium alloy sheets, as shown in Fig. 5. After the grooves are machined, alcohol is used to wipe the weld zone and groove to achieve a cleaner bonding surface and a better bonding strength. Adjust the ultrasonic welding equipment parameters. The use of ultrasonic welding parameters is: the operating frequency is 20 kHz, the maximum output power is 4 kW, the welding time is 45–125 ms, the vibration amplitude is 35 μm, the welding head area is 4 mm × 4 mm, and the welding pressure is 801.17, 1144.53 and 1487.89 N respectively. Some low hardness materials are used to position the weld before welding. The so-called positioning refers to no welding and no ultrasonic vibration, but the welding head under the welding pressure is in welding test. The purpose is to ensure the correct location of the welding [16]. Observe the indentation to determine whether the welding head plane is parallel to the base. Put the electroplated FBG into the groove between two flakes, and start pre-welding with a lower welding time. The purpose is to gradually bury FBG in the titanium alloy matrix, and to complete the final welding with the increase of the welding time.

3.3 Indirect Embedding

Interception of Ti6Al4V titanium alloy sheet is also completed by using the metal cutting equipment. The Ti6Al4V titanium alloy sheet is 150 mm × 20 mm 0.3 mm. With the machining method, the middle part of titanium alloy sheet is processed into the arc form that needs the plating of a good FBG arc and is processed into the arc close to coincidence to improve the FBG and titanium contact area. Then, the titanium alloy and FBG form an organic whole to protect the fiber grating. Figure 7 shows the arc area diagram. After processing of a good arc is completed, alcohol is used to wipe the welding area and arc area to obtain a cleaner surface and a better combination of bonding strength. The ultrasonic welding equipment parameters need to be adjusted. The optimization process parameters of the titanium alloy ultrasonic welding are: the operating frequency is 20 kHz, the maximum output power is 4 kW, the welding time is 125 ms, the vibration amplitude is 35 μm, the welding head area is 4 mm × 4 mm, and the welding pressure is 1144.53 N.

After pre-welding, put the plated FBG into the arc between two sheets. Weld one side of the arc first to reduce a subsequent welding impact on the previous welding area, and use mechanical method to clamp the welded area. Then, weld the other side. Welding should be careful to prevent the welding head from felling in the arc area.

3.4 Ultrasonic Welding

Ultrasonic metal welding [17, 18] as a special connection technology has lots of advantages, such as energy saving, environmental protection and easy operation. It has been widely used in the industrial field, especially in the electronics industry and nuclear energy industry for the preparation of new materials, body welding and parts packaging.

Ultrasonic metal welding principle is not transmitting the current to the material, and not applying the flame or arc and other high-temperature heat source to the material. It uses the ultrasonic high-frequency vibration and static pressure of the combined effect to clean the oxide film in the surface of material welding area. The ultrasonic high-frequency vibration energy enters into the material interface and brings the friction work, deformation energy and limited temperature rise to achieve the same metal or dissimilar metal connection in a special method [19, 20]. The schematic diagram of welding principle is shown in Fig. 8.

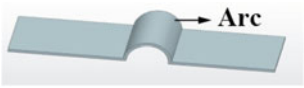

Fig. 7 Schematic diagram of arc area

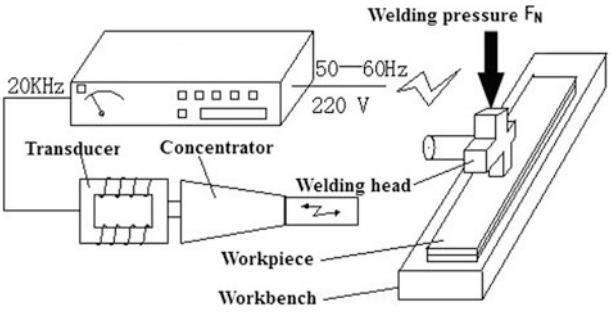

Fig. 8 Ultrasonic welding principle diagram

4 Results and Discussion

Embed the FBG sensor after metal protection into the titanium alloy structure directly, under the optimum welding process parameters (welding pressure is 1144.53 N and welding time is 125 ms). We accidentally find that FBG on both sides in the edge of the welding head is instantly cut into two sections at the end of welding [21]. By observing the cross-section and surface of the welded joints, we find that the joints of the upper and lower surfaces are smooth, and FBG embedding does not cause bulging. There is no pinhole on the cross-section due to the FBG embedded. The cross section is repeatedly observed by the metallographic microscope (magnification to 1000 times). Pinhole still cannot be found.

The welding time is gradually reduced. FBG still fails to be embedded. With the welding time at 105 ms and the welding pressure at 1144.53 N, the welding spot is peeled off. It is found that there is little black charred powder between the interfaces. Adjust the welding time at 85 ms or so. The titanium alloy ultrasonic welding is not reliable, so there is no need to further reduce the welding time. Figure 9 shows a cross-sectional view of the electroplated nickel fiber which is cut off at the edge of the weld with the welding pressure at 1144.53 N and the welding time at 85 and 95 ms respectively. When the welding pressure is reduced to 801.17 N, the

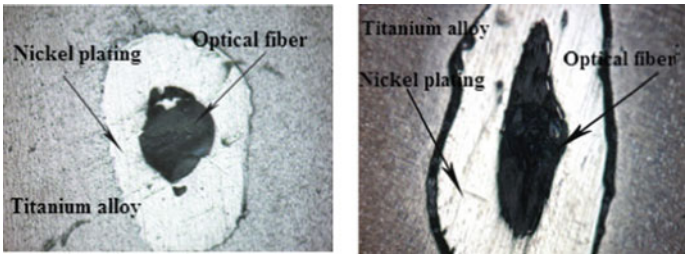

Fig. 9 A cross-sectional view of the nickel-plated fiber cut at the edge of the welding head

situation is similar as the welding pressure 1144.53 N. With lower welding time, electroplated nickel FBG is still flattened and the solder interface is not bonded. The main reason is that the titanium alloy has a high hardness, it is difficult to instantly press nickel plating FBG into the titanium alloy matrix, and the FBG is flattened by the welding pressure. Under the optimum welding process parameters, the interfacial temperature is as high as 1172.4 °C, while the nickel layer is too softened to protect the FBG at this temperature, and the yield strength is very low [22].

Considering the above reasons, the titanium alloy sheet is heated to 300 °C by incubator, and then the FBG is embedded, but the test indicates that there is no effect. Perhaps, the temperature needs to be heated to above 1000 °C, the titanium is completely softened, and then low welding energy FBG welding embedding may be successful. Due to the test equipment problems and considering that the FBG is not in the best welding process parameters, the welding embedding will lose the significance of the experiment, so the test stops.

After electroplated nickel FBG is embedded into the titanium alloy, its sensing performance is tested to determine whether the indirect embedding method is effective. Fiber grating sensing experiment equipment and fiber grating are produced by Shanghai Purple Light Photoelectric Technology Co., Ltd. The grating length is 32 mm, and the fiber grating Bragg center wavelength is 1550.103 nm at 20 °C.

Firstly, the temperature sensing test is taken for naked grating. Fiber coating stripping plier is used to strip the coating bare side layer of grating at a length of 15–20 mm. After stripping, wipe the fiber with cotton, put the fiber into the fiber adapter, then connect the light adapter in the fiber grating sensor network analyzer, and finally put the bare fiber grating into the constant temperature water bath box. Initial temperature is 20 °C and heated to 90 °C. The interval is 10 °C and stays 10 min. Record 15 reflection wavelengths when the wavelength becomes stable and take the average. The measured mean wavelength of the reflection is linearly fitted with Origin 8.5 software. Figure 10 shows the naked grating temperature sensor test data. We can see that the naked grating temperature sensor linearity is good from

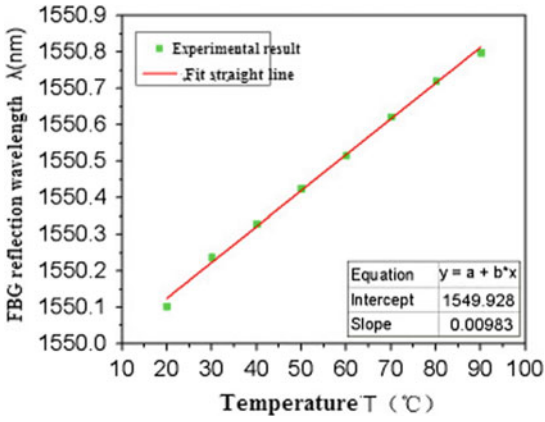

Fig. 10 Temperature measurement test data for bare fiber gratings

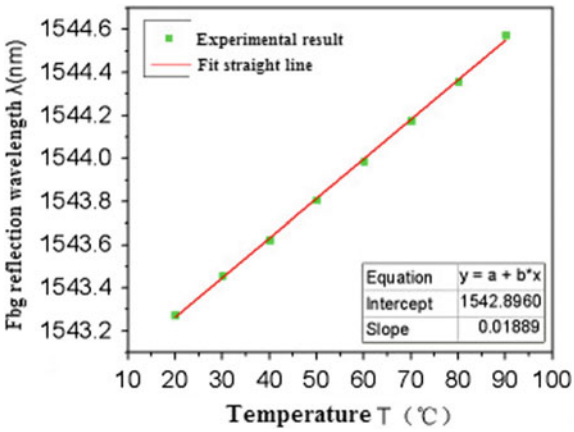

Fig. 11 Temperature sensing test data of electroplated fiber grating

the figure, and the intelligent metal structure of the information transmission is the ideal sensor. The fitting results show the temperature of the bare grating.

Metallize the bare fiber grating after the temperature sensing test, and test its temperature sensing. The purpose is to analyze the temperature sensitivity changes after the fiber grating embedded. The steps of the test are the same as those of the bare grating temperature sensing test. Figure 11 shows the temperature sensing test data of the electroplated fiber grating. It can be seen from the figure that the electroplated fiber grating maintains a good linearity. The temperature sensitivity of the electroplated fiber grating is 18.89 pm/°C. The temperature sensitivity has greatly improved than that of the original bare fiber grating.

Finally, make a temperature sensing test for the FBG embedded into titanium alloy in the indirect way. The test steps are the same as those of the bare grating temperature sensing test. Considering that the buried FBG has hysteresis phenomenon, so a set of temperature sensing tests for cooling down is added. Figure 12 shows the indirect embedded fiber grating temperature sensing test data. It can be seen from the figure that FBG reflection wavelength and temperature changes still maintain a good linear relationship, and there exists hysteresis phenomenon but it is not obvious. From the results of the fitting, it is found that the FBG temperature sensitivity coefficient in the titanium alloy structure is 20.92 pm/°C (during the temperature rise) and 20.71 pm/°C (during the cooling process). The temperature sensitivity has been improved before the fiber grating being embedded.

Due to the electroplated FBG or embedded FBG into the titanium alloy structure, the temperature sensitivity is improved. The reason is that the fiber grating is metallized or encapsulated, though the thermal coefficient of the fiber grating is not changed, but the metallized material or encapsulated FBG material thermal expansion coefficient is greater than the thermal expansion coefficient of fiber grating. The temperature changes play the role of thermal stress on the fiber grating, the grating center wavelength drift is exacerbated, so the fiber grating metallization or packaging increases the temperature sensitivity.

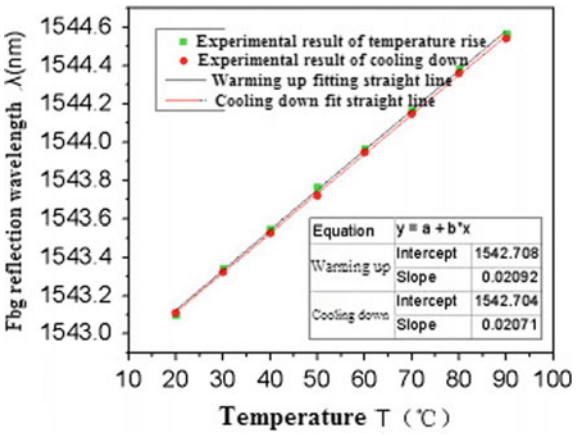

Fig. 12 Temperature measurement test data for FBG indirect embedding

The main parameters of FBG are provided by Shanghai Purple Light Photoelectric Technology Co., Ltd. The specific parameters are: Poisson's ratio is 0.17, thermal expansion coefficient is 0.55×10^{-6} °C^{-1}, elastic modulus is 7.474 kPa, thermal coefficient is 667.8 °C^{-1}, center wavelength is 1550.103 nm, elastic coefficient is 0.121 and 0.27, and fiber grating diameter is 125 μm. The nickel plating layer parameters are: thermal expansion coefficient is 1.42×10^{-5} °C^{-1}, Poisson's ratio is 0.31, and elastic modulus is 1981.56 Pa.

$$\frac{\Delta\lambda_B}{\Delta T} = (a_0 + \zeta)\lambda_B + \left\{ D - \frac{n_{eff}^2}{2}\left[(P_{11} + P_{12})C + P_{12}D\right] \right\}\lambda_B \tag{1}$$

$$D = \frac{(a_1 - a_0)E_1[B - 2v_0]}{B\left(E_0\frac{S_0}{S_1} + E_1\right) - 2E_1v_0 - 2E_0v_1\frac{S_0}{S_1}} \tag{2}$$

$$C = \frac{(a_1 - a_0)E_1[(1 - v_0) - Bv_0]}{B\left(E_0\frac{S_0}{S_1} + E_1\right) - 2E_1v_0 - 2E_0v_1\frac{S_0}{S_1}} \tag{3}$$

$$B = 1 + \frac{(S_1 + S_0)(1 + v_1)E_0}{E_1(1 + v_0)S_1 + E_0(1 + v_1)S_0} \tag{4}$$

where a_0 is the thermal expansion coefficient of optical fiber, a_1 is the thermal expansion coefficient of Nickel plating, ζ is the optical fiber thermal coefficient, v_0 is the fiber Poisson ratio, v_1 is the Poisson's ratio of the nickel-plated layer, S_0 and S_1 are fiber grating cross-sectional area, E_0 is the elastic modulus of the fiber, E_1 is the elastic modulus of the nickel plating layer, P_{11} and P_{12} are shelling coefficients, λ_B is the center wavelength of the grating, and n_{eff} is the effective refractive index of the fiber. The thickness of the coating 358 μm and above parameters are taken into Eq. (1). The theoretical value of FBG temperature sensitivity is 20.91 pm/°C, while

the measured value is 18.89 pm/°C. There is no big difference between the theoretical value and the actual value. The main reason is that there is deviation in the calculated parameters and the actual parameters used.

5 Conclusion

The test of embedding electroplated nickel FBG into the titanium alloy in the direct way means that the titanium alloy is not suitable for embedding matrix. The temperature sensitivity coefficient of the bare fiber grating is 9.83 pm/°C, and the sensitivity of FBG is 18.89 pm/°C after nickel plating. The FBG temperature sensitivity coefficient of the indirect embedding into titanium alloy structure is 20.92 pm/°C (during the temperature rise) and 20.71 pm/°C (during cooling). The temperature sensitivity of the FBG embedded into the titanium alloy in the indirect way is 2.13 times larger than that of the original bare fiber grating, and is 1.11 times larger than that of the FBG sensor after electroplating nickel. It indicates that indirect embedding is an effective method to embed FBG into the titanium alloy structure. FBG is not damaged by indirect embedding into the titanium alloy, and the temperature sensitivity has been improved.

References

1. Othonos A, Kalli K, Pureur D et al (2006) Fibre Bragg gratings. Springer, Berlin, pp 189–269
2. Hill KO, Meltz G (1997) Fiber Bragg grating technology fundamentals and overview. J Lightwave Technol 15(8):1263–1276
3. Studer M, Peters KJ (2017) Embedded optical fiber Bragg grating sensors for the measurement of crack-bridging forces in composites. Proc SPIE Int Soc Opt Eng 4694:284–295
4. Peng PC, Tseng HY, Chi S (2014) Long-distance FBG sensor system using a linear-cavity fiber Raman laser scheme. IEEE Photonics Technol Lett 16(2):575–577
5. Jin L, Zhang W, Zhang H et al (2005) An embedded FBG sensor for simultaneous measurement of stress and temperature. IEEE Photonics Technol Lett 18(1):154–156
6. Wang X, Matsushima K, Nishiki A et al (2004) High reflectivity superstructured FBG for coherent optical code generation and recognition. Opt Express 12(22):5457–5468
7. Lau KT, Yuan L, Zhou LM et al (2011) Strain monitoring in FRP laminates and concrete beams using FBG sensors. Compos Struct 51(1):9–20
8. Leng J, Asundi A (2003) Structural health monitoring of smart composite materials by using EFPI and FBG sensors. Sens Actuators, A 103(3):330–340
9. Lancet T (1942) Sir William Bragg. Lancet 239:360
10. Hamid RK, Mauricio Z, Ningsu L (2010) Application of adaptive wavelet networks for vibration control of base isolated structures. Int J Wavelets Multiresolut Inf Process 08 (05):773–791
11. Yu X, Yu Y, Liao Y et al (2005) Strain measurement of steel structure using a novel FBG sensor packaged by titanium alloy slice. Proc SPIE 6019:448–453
12. Jing W, Hou W (1996) Chemical plating. J Yanbei Teach Coll 12(4):32–34
13. Bladon JJ (1995) Electroplating process. US Patent 5425873 A

14. Liang W, Huang Y, Xu Y et al (2005) Highly sensitive fiber Bragg grating refractive index sensors. Appl Phys Lett 86(15):151122
15. Pospori A, Marques CAF, Sáez-Rodríguez D et al (2017) Thermal and chemical treatment of polymer optical fiber Bragg grating sensors for enhanced mechanical sensitivity. Opt Fiber Technol 36:68–74
16. Takeda S, Minakuchi S, Okabe Y et al (2015) Delamination monitoring of laminated composites subjected to low-velocity impact using small-diameter FBG sensors. Compos A Appl Sci Manuf 36(7):903–908
17. Zhang CQ, Robson JD, Prangnell PB (2016) Dissimilar ultrasonic spot welding of aerospace aluminum alloy AA2139 to titanium alloy TiAl6V4. J Mater Process Technol 231:382–388
18. Lipari CP (1983) Ultrasonic welding. US Patent 4410383 A
19. Watanabe T, Sakuyama H, Yanagisawa A (2009) Ultrasonic welding between mild steel sheet and Al-Mg alloy sheet. J Mater Process Tech 209(15–16):5475–5480
20. Harman G, Albers J (2003) The ultrasonic welding mechanism as applied to aluminum-and gold-wire bonding in microelectronics. IEEE Trans Parts Hybrids Packag 13(4):406–412
21. Matsuoka SI (1998) Ultrasonic welding of ceramics/metals using inserts. J Mater Process Technol 75(1–3):259–265
22. Panteli A, Robson JD, Brough I et al (2012) The effect of high strain rate deformation on intermetallic reaction during ultrasonic welding aluminium to magnesium. Mater Sci Eng, A 556:31–42

Analysis of Vacuum Chamber Structure Based on Visual Finite Element Modeling

Yanhu Wang and Xizhang Chen

Abstract The feasibility of improving the vacuum chamber structure of vacuum packaging machine is discussed. The finite element software, Visual Environment, is used to simulate the structures of prime vacuum chamber and improved vacuum chamber which is built most through weld process. The results show that the maximum weld residual stress of the improved vacuum chamber changes and the stress concentration is greatly reduced with finite element analysis (FEA). At the same time, a path for a particular site is created and the range of stress changes is found from the original 270–340 to 240–310 MPa. The improved method not only saves resources but also improves product quality, which is verified by the actual product.

Keywords Vacuum chamber · Finite element analysis (FEA)
Welding residual stress · Structure

1 Introduction

With the improvement of modern consumption concept, product packaging and texture gradually arouse people's attention. The vacuum packaging compared to other packaging has the advantage to maintain the color and keep fresh in prolonged shelf-life items, especially for the packaging of active substances [1]. It promotes the evolution of the packaging machine. However, the vacuum packaging machine structure and the process designed by many enterprises are not much reasonable. Most of them lead the vacuum chamber to crack. A well-known packaging company named Hualian Machinery Group is good at producing the vacuum packaging machine. These years it also meets similar quality problem. In order to advance the vacuum packaging machine, it improves the structure of

Y. Wang · X. Chen (✉)
School of Mechanical and Electrical Engineering, Wenzhou University, Wenzhou, China
e-mail: kernel.chen@gmail.com

S. Chen et al. (eds.), *Transactions on Intelligent Welding Manufacturing*,
Transactions on Intelligent Welding Manufacturing,
https://doi.org/10.1007/978-981-10-7043-3_7

vacuum packaging machine. Consumers very satisfy the improvement vacuum packaging machine during the use of the product.

With the development of finite element technology, the product structure is constructed by the simulation to predict product defects and provide important information for structure optimization [2]. In this work, finite element analysis (FEA) software Visual Environment is used to analyze two different structures of vacuum chamber, and provides theoretical basis for the improvement on the vacuum chamber structure.

2 Vacuum Packaging Machine

2.1 Composition of the Vacuum Packaging Machine

The vacuum packaging machine is shown in Fig. 1. The vacuum packaging machine consists of handle, vacuum cover, link, seal assembly, vacuum chamber, chassis, control panels, vacuum pumps and caster. Eight main parts are shown in Table 1.

2.2 Working Principle

When the bag is in the vacuum chamber, the vacuum cover is closed, and the machine starts to build an airtight vacuum space. After vacuuming is completed, it

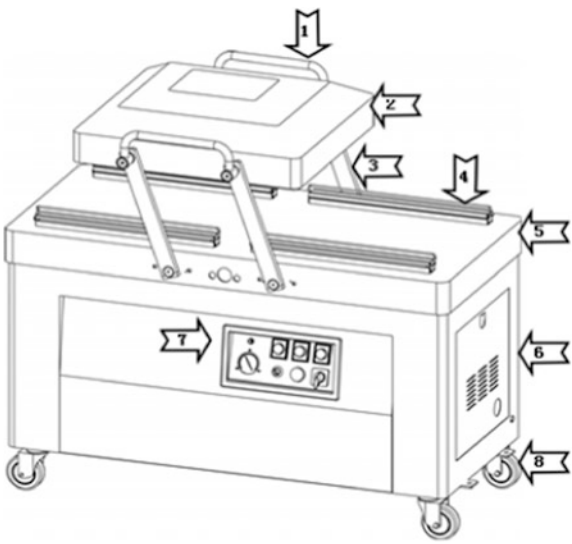

Fig. 1 Vacuum packaging machine

should fill with inert gas firstly if needed. Different pressure is used between the vacuum chamber and the outside atmosphere to overcome spring force. Let the heat sealing plate drop with the air bag. The heat sealing plate is installed with an electric hot flat. When there is a large low-voltage through the flat, heat is generated to seal the bag. The vacuum cover is cooled and then opened. At last, vacuum packaging process is completed.

3 FEA of Vacuum Chamber Model

3.1 Prime Machine's Vacuum Chamber

Material of vacuum chamber is 0Cr18Ni9 alloy. The composition is Cr18.09%, Ni8.15%, Si0.35%, C0.0344%, S0.003%, Mn1.03% and P0.039%, in addition to Fe. Table 2 shows some mechanical properties of 0Cr18Ni9 material. There are many studies on 0Cr18Ni9 stainless steel in stress corrosion, stress fatigue and fracture [3, 4]. When the material plastic deformation occurs, it is also prone to deformation which induces martensitic phase transformation. The formation of martensitic phase improves the strength and hardness of the material but reduces the ductility and toughness. Therefore, plastic deformation must be limited for this kind of austenitic stainless steel product to ensure that the products during the service still have enough plasticity and toughness [5].

The stress and strain parameters of 0Cr18Ni9 materials are obtained by tensile test. The stress and strain obtained by the experiment are called nominal stress and nominal strain. True stress and strain are needed during simulating the material plasticity parameter. Nominal stress σ_{nom} and strain ε_{nom} are transformed into true stress σ_{true} and strain ε_{true} by

Table 1 The main parts of vacuum packaging machine

Number	Part name
1	Handle
2	Vacuum cover
3	Link
4	Seal assemble
5	Vacuum chamber
6	Chassis
7	Control panels
8	Caster

Table 2 Some characteristics of 0Cr18Ni9 material

Material	Elastic modulus/GPa	Poisson's ratio	Yield strength/MPa
0Cr18Ni9	204	0.285	205

$$\varepsilon_{\text{nom}} = \frac{\Delta l}{l_0}, \tag{1}$$

$$\sigma_{\text{nom}} = \frac{F}{A_0}, \tag{2}$$

$$\varepsilon_{\text{true}} = \int_{l_0}^{l} \frac{\mathrm{d}l}{l} = \ln\left(\frac{l}{l_0}\right) = \ln(1+\varepsilon_{\text{nom}}), \tag{3}$$

$$\sigma_{\text{true}} = \frac{F}{A} = \frac{F}{A_0 \frac{l}{l_0}} = \sigma_{\text{nom}}(1+\varepsilon_{\text{nom}}). \tag{4}$$

The relationship between true stress and strain is shown in Fig. 2.

The vacuum chamber manufacturing process consists of laser cutting, bending and welding. Of course, there is another way to build the vacuum chamber through the stud welding technology which is more advanced and high efficiency [7]. As the vacuum chamber is the center of the symmetrical pattern and most of the vacuum chamber manufacturing process are welding, 1/4 model for simulation that can get the same accuracy on the simulation result is constructed to save time and improve efficiency, as shown in the Fig. 3.

When one dimension scale is much smaller than other components, FEA can be carried out using shell element to simplify the calculation. At present, the solid shell

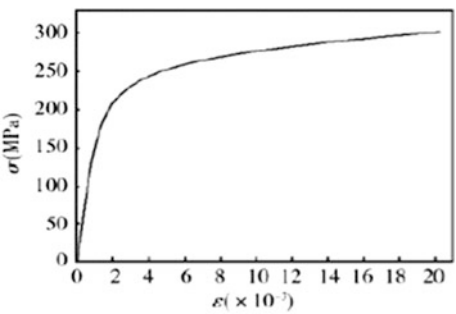

Fig. 2 The stress strain curve [6]

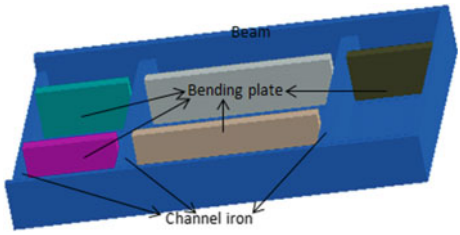

Fig. 3 The 1/4 model of vacuum chamber

element has aroused widespread concern [8]. The shell element is divided into three categories: general shell, thin shell and thick shell. It is generally considered that if the ratio of thickness to span of the shell which is made of a single material is between 1/20 and 1/10, it is thick shell. Because the vacuum chamber thickness is only 4 mm, much smaller than 1/10 of global size belongs to the typical shell element. So it is necessary to extract the thin shell of the vacuum chamber. The features of the suction holes, threaded holes and so on are ignored to reduce the calculation. The Visual Mesh software is used to clean up the geometry and repair the surface, as well as to complete the surface modeling. The replanting size is 10 which is greater than thickness. The fine meshes are adopted in the diagonal to improve the accuracy of computation and the coarse meshes are used in less important regions where they don't have problems to reduce the solution time. The density of mesh has little impact on the mechanical response of crystal plastic deformation and the mesh quality can be used to analyze three-dimensional elasticity problems [9, 10]. The meshing model is shown in Fig. 4.

The appropriate thickness and assignment material for various parts of the shell is set according to the thickness of the plate and ribs [11]. The purpose of applying the boundary constraint is to prevent the rigid displacement during calculation [12]. Boundary conditions are based on the actual working conditions. The vacuum chamber is fixed at four sides as a fixed constraint. There are 13 welds, the welding wizard is set according to the number on the grid model. All of the pretreatments are processed by Visual Weld. The corresponding stress results are shown in Fig. 5.

The stress result with a maximum stress of 350.5 MPa is shown in Fig. 5. The stress level is high and it exceeds the yield strength of the material. It is seen that stress concentrates in the bending plate and the channel junction. The stress concentration is the main factor affecting the fracture and maybe microstructure [13, 14]. The test machine shows the location of the crack. A path is built on the first weld to research the relationship between residual stress and yield strength. The red line is residual stress line and the green line is yield strength line. The result is shown in Fig. 6.

It is seen that there is a large fluctuation in residual stress and yield strength at each channel from Fig. 6. Especially, when there is a large increase in yield strength

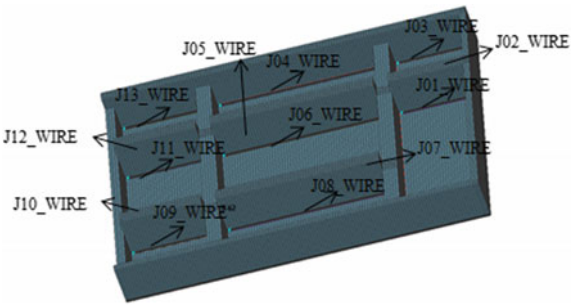

Fig. 4 The 1/4 model of the original vacuum chamber grid

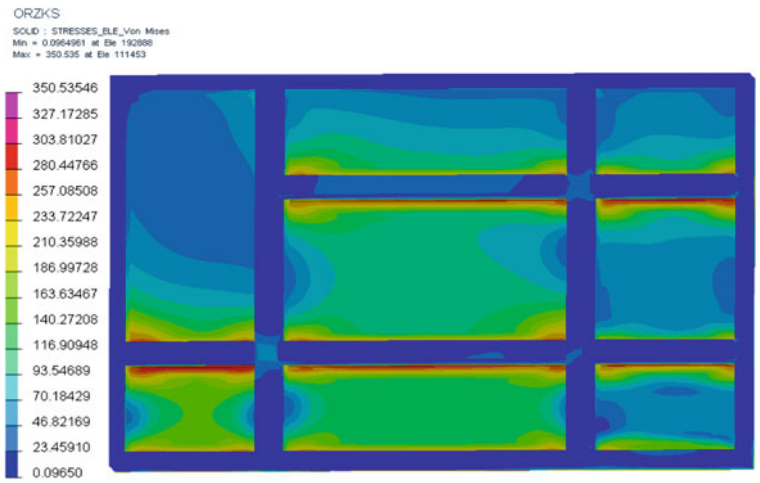

Fig. 5 The stress cloud of the vacuum chamber

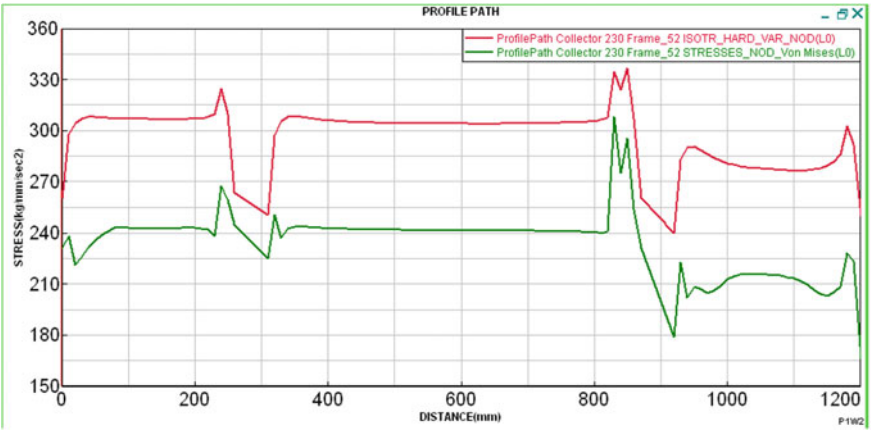

Fig. 6 The relationship between residual stress and yield strength for the vacuum chamber

at each channel and then there is a low fast drop, the residual stress changes slowly. There is no yield point but the residual stress and yield strength are very close. It is possible to cause material failure especially in the vacuum chamber of the studio because the vacuum state is easy to cause greater stress damage. As the number of welds increases, the much more residual stress is accumulated at the first weld. The load on the junction between channel iron and bending plate is mainly shared by the bending plate. Large stress is concentrated in their junction and it easily causes weld cracks.

The cause of junction stress for channel iron and bending plate is considered: in commissioning model, the bending plate height is improved to improve the vacuum chamber stiffness in design. However, the increase of the bending plate height leads to fluctuation in the junction, which produces stress non-uniform and causes stress concentration and plastic deformation. The more the welds are, the worse the condition will be. As the number of welds increases, the much more stress is concentrated at the first weld.

3.2 Improved Vacuum Chamber

The test machine model is constructed and the possible cracking of the issues are proposed to improve the vacuum packaging machine program. The improved program especially aims at bending plate and reducing the welds. It is not by the use of welding but the mechanical methods for the vacuum chamber of the central beam. The bending plate height is reduced through 45° treating at the end of bending plate so that the junction channel iron has uniform stress. The improved model is shown in Fig. 7. The same way is used to mesh the improved vacuum chamber and the grid model is shown in Fig. 8.

The same method is used to analyze the improved vacuum chamber. Because it is not by the use of welding but the mechanical methods for the vacuum chamber of the central beam, the number of welds reduces to 10. Compared with the previous model, this model has decreased three welds. The overall model will reduce 12 welds due to only a 1/4 of the present model. The less welds will shorten the product completion time and improve the efficiency for the enterprises. The same method is used to make all pretreatments, and then the file is put to simulate. The corresponding result is shown in Fig. 9.

The stress is shown on the border of improved model and significant improvement is got. There is a slight decrease in the maximum stress and the maximum value is decreased from previous 350.5 to 312.9 MPa. The position of the maximum stress has changed and the maximum stress concentration area

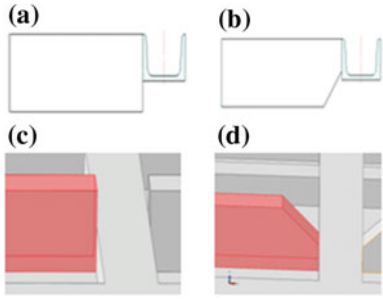

Fig. 7 The comparison chart of bending plate before and after improvements: the original bending plate (**a**); the improved bending plate (**b**); the original three-dimensional model (**c**); the improved three-dimensional model (**d**)

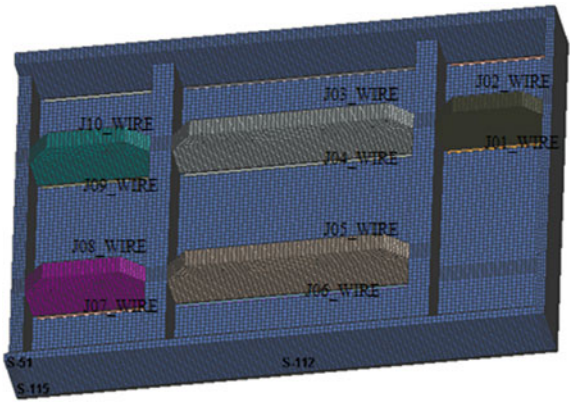

Fig. 8 The 1/4 model of the advanced vacuum chamber grid

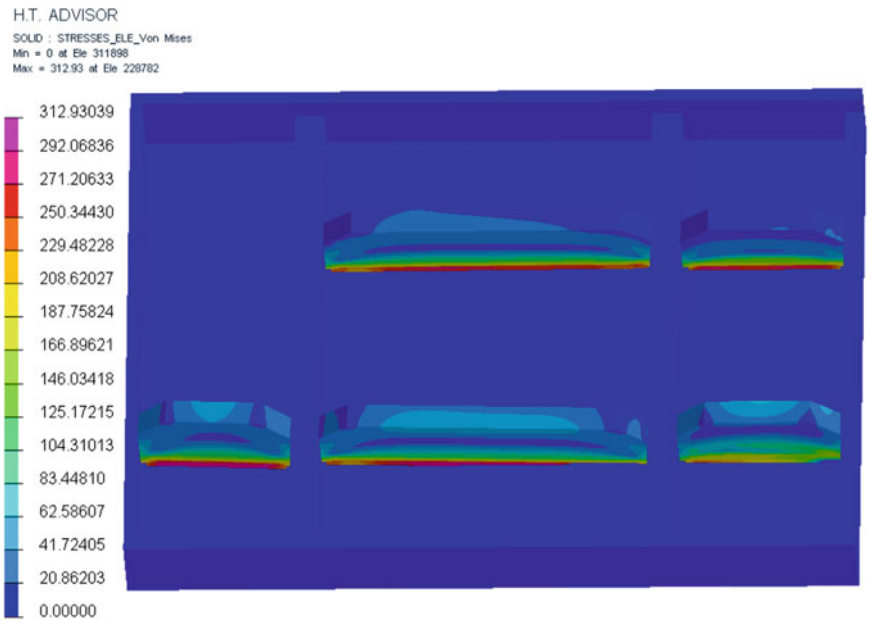

Fig. 9 The stress cloud of the improved vacuum chamber

decreases significantly while the stress distribution has improved a lot. The same path from top to bottom is built on the first weld to research the path change relationship between residual stress and yield strength. The location of the path is the same as that of the test machine's vacuum chamber, as shown in Fig. 10.

The overall variation curve is consistent with the previous model. The stress is improved and the maximum value is reduced from previous 340 to 310 MPa, about

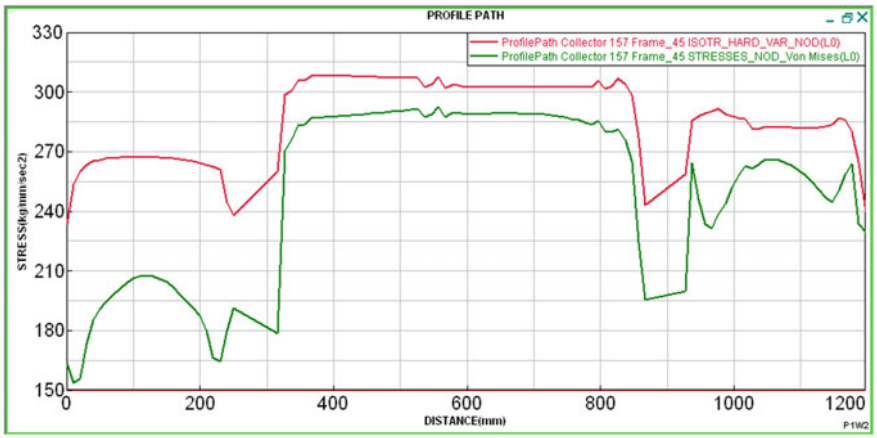

Fig. 10 The relationship between residual stress and yield strength for the improved vacuum chamber

9%. It can be known that the method of reducing welds is working. Compared with those of the vacuum chamber of tested machine, the residual stress and yield strength change slowly. It can be deduced from Fig. 10 that the stress of each channel just decreases, not increases. There is a certain stress reduction at the junction and the amplitude of fluctuation is relatively small. In each junction, the stress value is reduced. It shows that the improved channel iron can play a better supporting role. Bending plate can share the load better.

It is also known that the stress value at the junction of the channel and the bending plate in the previous stress analysis is the greatest. It is also possible to infer from Fig. 11. Although the stress value is the largest here in the improved model, the stress is much large in the yield curve from the yield strength. So the modified model to improve the stress of this position plays an important role.

In order to research the relationship between stress and yield strength at the original and improved models, a path in the channel and the first weld at the bending plate are established. The result is shown in Fig. 11. It can be seen that the residual stress of the original model is fluctuant. While the residual stress of the improved model steadily reduces. The residual stress and yield strength are obviously lower than those of original model. So the improved model is less likely to yield and has better performance.

4 Conclusion

FEA of the 1/4 vacuum chamber is used to distinguish the positions where stress is large and relatively concentrated and the stress amplitude changes greatly. These areas can produce plastic deformation which influences the quality of products

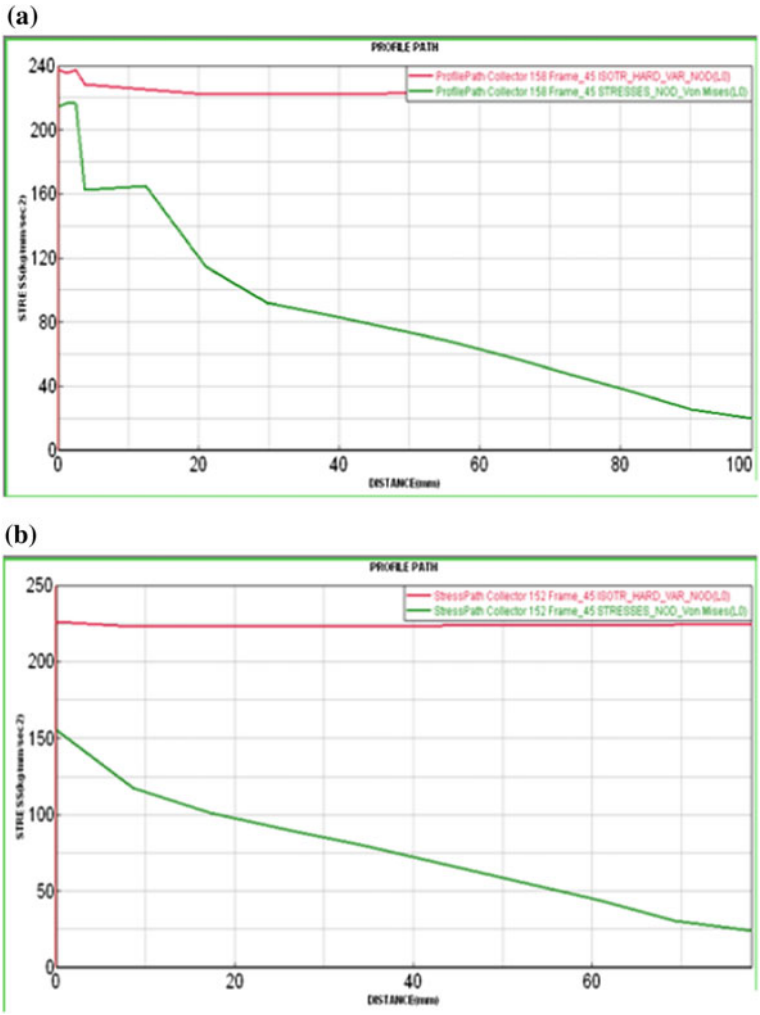

Fig. 11 The relationship between residual stress and yield strength at the position of channel and bend plate junction: original model (**a**) and advanced model (**b**)

seriously. In order to improve the bending plate with 45° treat at the end of bending plate and to reduce the welds, it is not by the use of welding but the mechanical methods for the vacuum chamber of the central beam. It can be deduced that the stress of the improved vacuum chamber has decreased by FEA. At the same time, a path for a particular site is constructed where the range of stress changes from the original 270–340 to 240–310 MPa and the stress is greatly improved. The actual effect will be more obvious if the simulation model is overall. The results of the simulation provide theoretical basis for improving the vacuum chamber structure.

Acknowledgements This work is supported by the National Natural Science Foundation of China (51575401) and the Zhejiang Provincial Natural Science Foundation (LY16E050007).

References

1. Sun JM, Li Z (2014) Design and study on the deoxidizing system in antioxidant packaging equipment. Packag Eng 35(7):6–10
2. Wang YH, Chen XZ, Huang L et al (2016) Finite element analysis and improvement of vacuum cover for packing machine. J Shanghai Jiao Tong Univ 50(12):1925–1928
3. Han C, Kim KS (2001) Time-dependent crack growth in stainless steel 304 in the plasticity-dominant field. Eng Fract Mech 68(1):39–52
4. Baik YM, Kim KS (2001) The combined effect of frequency and load level on fatigue crack growth in stainless steel 304. Int J Fatigue 23(5):417–425
5. Ling L, Li XX, Wang XL et al (2012) Constitutive model of stainless steel OCr18Ni9 and its influence on cutting force prediction. China Mech Eng 23(18):2243–2247
6. Li XM (2012) Study on plastic deformation behavior of stainless steel 0Crl8Ni9Ti under uniaxial stress. CFHI Technol 2:46–49
7. Wang YH, Chen XZ, Jiang Q (2016) Pull arc stud welding process of the vacuum chamber of the double chamber vacuum packaging machine. Weld Technol 45(5):119–122
8. Hauptmann R, Doll S, Harnau M et al (2001) "Solid-shell" elements with linear and quadratic shape functions at large deformations with nearly incompressible materials. Comput Struct 79(18):1671–1685
9. Kanber B, Bozkurt OY (2006) Finite element analysis of elasto-plastic plate bending problems using transition rectangular plate elements. Acta Mech Sin 22(4):355–365
10. Guzelbey IH, Kanber B (2000) A practical rule for the derivation of transition finite elements. Int J Numer Meth Eng 47(5):1029–1056
11. Yang L, Kong FY, Wang W (2014) Numerical simulation for temperature effect of external thermal insulation system with XPS board. J Shenyang Univ Technol 36(6):701–705
12. Wang YH, Chen XZ, Konovalov S (2016) Strain-stress simulation and comparison of different welding sequences during manufacturing of packing vacuum cover. Series Mater Sci Eng 150(1):012036
13. Li QF (2004) Fracture mechanics and engineering applications. Harbin Engineering University Press, Harbin, China
14. Fang YY, Chen XZ, Bruce M et al (2016) Effects of strain rate on the hot deformation behavior and dynamic recrystallization in China low activation martensitic steel. Fusion Eng Des 103:21–30

Single-Channel Blind Source Separation and Its Application on Arc Sound Signal Processing

Wenjing Ren, Guangrui Wen, Riwei Luan, Zhe Yang and Zhifen Zhang

Abstract Welding arc sound signal is an important signal in intelligent welding diagnosis, due to its informative, noncontact, easy collected. However, due to the interference of ambient noise, the arc sound signal is highly complex and noisy, which seriously limits the application of arc sound signals. In this paper, a single-channel blind source separation (BSS) algorithm based on the ensemble empirical mode decomposition (EEMD) is proposed to purify and denoise the arc sound signals. First, EEMD is used to decompose one channel signal to several intrinsic mode functions (IMFs). Second, principal component analysis (PCA) is used to reduce the multidimension IMFs to low-dimension IMFs, which are regarded as the virtual multichannels signals. Finally, independent component analysis (ICA) separates the virtual multichannels signals into target sources. The approach was tested by simulation and experiments. The simulated results show that signals separated from mixed signal using this approach highly match the source signals that make up the mixed signal. Moreover, experimental results indicated that the source signals of arc sound were effectively separated with the environmental noise signals. The statistical characteristics of the spectrum in 5–6.5 kHz band extracted from the arc sound source signals can accurately identify the two types of weld penetrations.

Keywords Single-channel blind source separation · EEMD
Arc sound signal · Intelligent welding diagnosis

W. Ren · G. Wen · R. Luan · Z. Yang · Z. Zhang (✉)
The Research Institute of Diagnosis and Cybernetics, Xi'an Jiao Tong University, Xi'an, China
e-mail: zzf919@xjtu.edu.cn

S. Chen et al. (eds.), *Transactions on Intelligent Welding Manufacturing*,
Transactions on Intelligent Welding Manufacturing,
https://doi.org/10.1007/978-981-10-7043-3_8

1 Introduction

As an accompanying signal of welding process, arc sound signal carries abundant information of welding physical parameters. Experienced manual welders can obtain higher welding quality through the feedback of arc sound [1]. Welding arc sound signal is the interaction of energy change, arc volume fluctuation, protective gas flow, molten pool shape, and so on [2–5], thus creating a tight correspondence between arc sound signals and those parameters. Recently, acoustic signals are widely used in welding process defect detection and welding dynamic monitoring. Emad [6] reveals the relationship between arc sound signal and such penetration states as partial penetration, full penetration, and burn through. Power spectrum density (PSD) features were extracted from arc sound signals, and three welding states were effectively identified by means of neural network. Lv [7–9] realizes the recognition of welding arc length and penetration state, using time and frequency domain characteristics extracted from the sound signals of gas tungsten arc welding (GTAW). Zhang [10] using support vector machine (SVM-CA) estimate the different weld penetrations, local caving, and porosity of GTAW, based on the fusion of voltage, sound, and spectral signals. And a set of multi-signals preprocessing, feature extraction, dimensionality reduction, and fusion defect pattern recognition methods were put forward.

The key to the accuracy of welding defect detection is the quality of the original signal. As for the complex working environment, the original arc sound signal is usually a superposition of many source signals such as arc, welding machine, and environment. As a result, the original arc sound signals are complex and have low signal-to-noise ratio. Therefore, effective noise reduction is greatly important to improve the accuracy of welding defect detection. At present, the widely used methods for denoising are noise filtering, time domain average, etc. [11]. But these methods cannot remove the environmental noise whose frequencies are low and overlapping with arc sound signal. Blind source separation (BSS) is a dominant technique for separating the multivariate signals into different source independent components. The independent component analysis (ICA) is the main method for BSS. ICA separates useful signals from noises and concentrates them into the corresponding independent components. Then the noises can be easily reduced. It has been applied in various fields such as rotors fault diagnosis, electroencephalography (EEG), etc. [12, 13], but few literatures report the application on welding audio signal. The biggest limit of ICA is that if there are fewer channel signals than sources signals, ICA cannot guarantee efficient separations and useful information may be lost.

In this paper, a novel approach of single-channel BSS based on EEMD is presented. To overcome the limitation of the ICA, EEMD has been proposed to assist ICA for improving the performance of denoising. The single-channel mixed signal is decomposed first by EEMD to IMFs. Then PCA is used to reduce the IMFs to principal components (PCs). Finally, ICA separated the PCs into the target source signals. The effectiveness of the approach is verified by simulation and

actual arc sound signals. The results proved that the proposed approach is conducive to the characteristics extraction of arc sound signals. Eight statistical characteristics extracted from the spectrum of separated signal u_1 can distinguish the partial penetration from the full penetration effectively.

2 Single-Channel Blind Source Separation

2.1 Blind Source Separation

BSS is used to separate source signals from one or more observations with an unknown mixture process of sources. ICA is a common method for BSS and is widely used in many disciplines [14]. In this method, source signals are separated from observations based on the statistical independence hypothesis of sources, without any prior knowledge. The ICA mathematical model is shown in Fig. 1.

Where $s(t)$ ($s(t) = [s_1, s_2, \ldots, s_m]^{\mathrm{T}}$) is source signals. $x(t)$ ($x(t) = [x_1, x_2, \ldots, x_n]^{\mathrm{T}}$) is original signals, which is linearly combined from $s(t)$ by a mixing matrix, expressed as $x(t) = A_{n\times m}{\cdot}s(t)$.

Under the condition that $x(t)$ is known, $A_{n\times m}$ and $s(t)$ are unknown, ICA is the approximate estimation of separating source signals $s(t)$ by optimizing the separation matrix $W_{n\times m}$. The optimal $W_{n\times m}$ should make sure the separated signals have strongest independence.

Therefore, ICA is essentially an optimization problem, which mainly includes two aspects: the one is to establish the optimal objective function to determine the independence standard; the other one is to select the appropriate algorithm to optimize the objective function. According to these two aspects, a variety of ICA methods can be derived. Among them, fast independent component analysis (FastICA) is a widely used and mature algorithm. In this method, the negative entropy maximization standard is used to obtain the most optimal separation matrix [15]. The calculation steps are listed in Fig. 2.

2.2 Single-Channel BSS Based on EEMD

Because of the complex environment in engineering practice, the number of signal sources is difficult to predict. Meanwhile, the multisensors are high cost and hard to

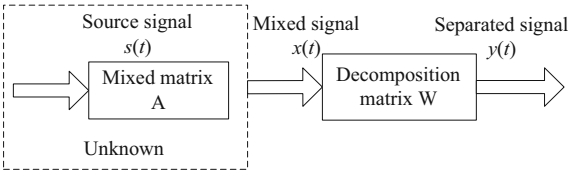

Fig. 1 Mathematical model of ICA

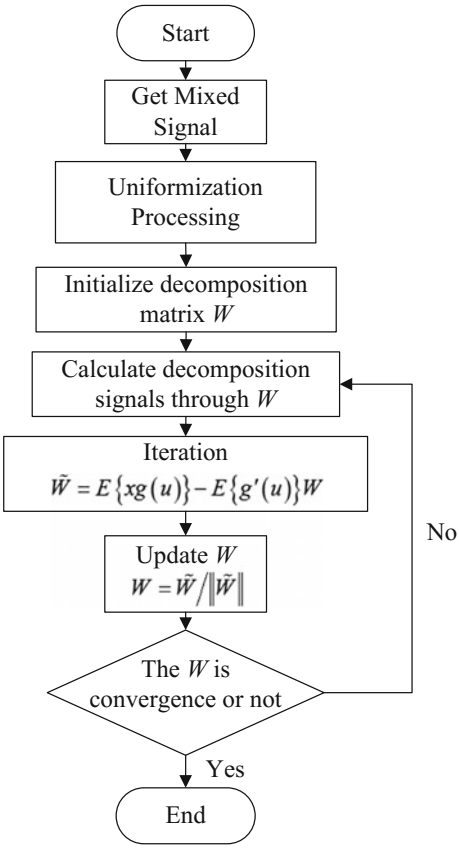

Fig. 2 Block diagram of FastICA

assembly. So the number of sensors is often less than that of signal sources, and even only single-channel signal is collected. In order to realize the single-channel BSS, the single-channel signal should be decomposed to virtual multichannel signals.

Empirical Mode Decomposition (EMD) is a time-frequency analysis method proposed by Huang in 1998 [16]. It decomposes the signal into a series of Intrinsic Mode Functions (IMFs) based on the local time characteristics of signals. Thus, the complex signal is reformed into multiple single components whose instantaneous frequencies are meaningful. EMD can adaptively decompose the signals, so it is quite suitable for decomposing the nonlinear and nonstationary signals. A significant drawback of EMD is that the decomposed signals have aliasing in frequency.

EEMD is an improved EMD algorithm [17]. The aliasing is restrained by adding white noises to original signal before decomposing. The decomposed results, which have added different white noise, are averaged to eliminate the white noises in IMFs. Because of the uniform distribution of white noise scale, it can not only

smooth the abnormal disturbances such as pulse interference but also can provide evenly distributed random scale for signals, and effectively suppress the frequency aliasing. The steps of the EEMD algorithm are described as follows.

(a) Adding Gaussian white noise $\omega(t)$ to $x(t)$,

$$X(t) = x(t) + \omega(t) \tag{1}$$

(b) Decompose $x(t)$ to IMFs by using EMD,

$$X(t) = \sum_{n=1}^{N} c_n(t) + r_N(t) \tag{2}$$

where, $c_{\mathrm{n}}(t)$ the nth IMF; N is the number of IMFs in each decomposition; $r_N(t)$ is the residual volume after decomposing.

(c) Repeat steps a and b M times, but adding different Gaussian white noise each time. The final IMFs are the average of M times IMFs:

$$c_n(t) = \frac{1}{M} \sum_{i=1}^{M} c_{in}(t) \tag{3}$$

where, $c_{in}(t)$ is the nth IMF decomposed by the ith times EMD. As the final IMFs decomposed by EEMD are usually multiple, which will cause high iteration numbers and slow convergence when multiple IMFs are directly used for ICA. To solve this problem, PCA is used to reduce the number of the IMFs. The principal components which contribute most are selected and regarded as the virtual multi-channel signals. Then FastICA is processed on them to obtain the separated source signals. Then the single-channel BSS is proposed and its total principle is as follows (Fig. 3):

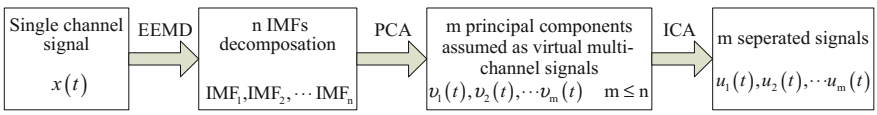

Fig. 3 Total block diagram of single-channel BSS

3 Simulation Analysis

In order to verify the effectiveness of this proposed method, simulations are carried out. First, three source signals, labeled $s_1(t)$, $s_2(t)$, $s_3(t)$, are established and mixed into a single-channel mixed signal $x(t)$.

$$s_1(t) = 5 \times \sin(2 \times \pi \times 450 \times t) \cdot \mathrm{e}^{-5000\left((t-\mathrm{round}(t\times 15)/15)^2\right)} \tag{4}$$

$$s_2(t) = \sin(2 \times \pi \times 100 \times t) \tag{5}$$

$$s_3(t) = \sin(2 \times \pi \times 50 \times t) \tag{6}$$

$$x(t) = 1.1s_1(t) + 0.7s_2(t) + 0.85s_3(t) + 0.1n(t) \tag{7}$$

where $n(t)$ is a noise signal. The signals are simulated at a sampling rate of 2048 Hz. Their time domain and spectrum graphs are shown in Fig. 4.

According to the process scheme showed in Fig. 3, the mixed signal $x(t)$ is decomposed to nine IMFs by EEMD, in which the variance of the white noise is half the variance of $x(t)$, and the decomposed times (M) is 100. The nine IMFs are reduced to three principal components by PCA, and the cumulative contribution rate of the three principal components is 98.47%. The three principal components are used as the virtual multichannel mixed signals to be processed by ICA. And finally, three separations are obtained, whose time domain and spectrum graphs are shown in Fig. 5.

Comparing the results in Figs. 4 and 5, the separation signals are basically consistent with the source signals. It is proved that the newly proposed method can effectively realize the blind source separating of single-channel mixed signals. The differences of the amplitudes and orders between the separated signals and the source signals are also consistent with the uncertainty of the results separated by BSS.

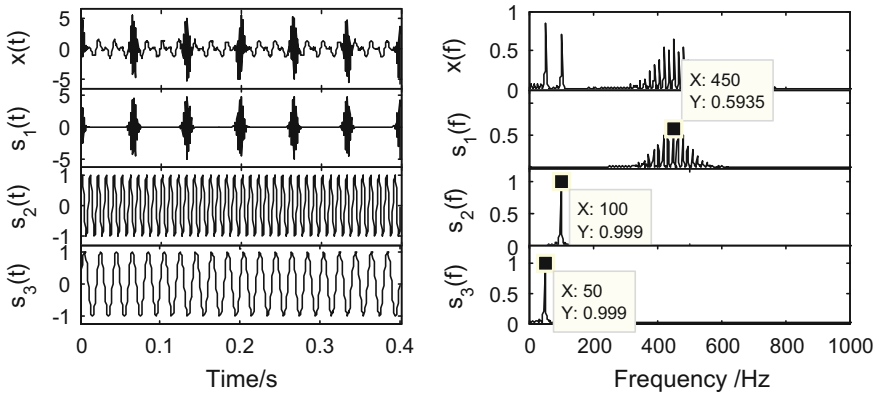

(a) Time domain (b) Frequency spectrum

Fig. 4 The time and frequency domain graphs of source signals and mixed signal

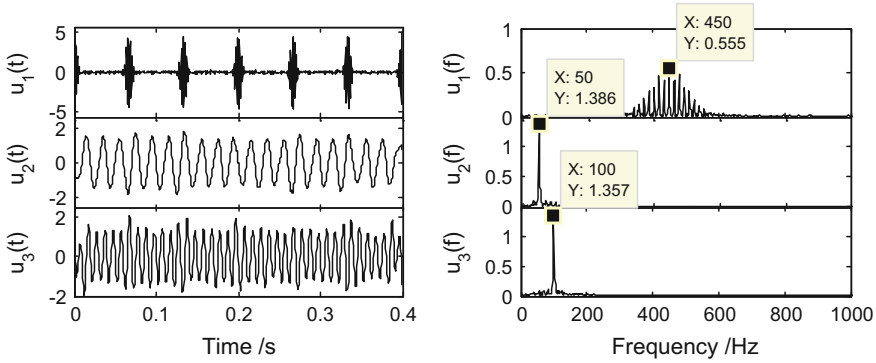

(a) Time domain (b) Frequency spectrum

Fig. 5 The time domain and spectrum graphs of separated signals

4 The Welding Arc Sound Signal Processing

4.1 Experimental Data Acquisition

The arc sound signal used in this paper is the single-channel arc sound signals collected during the welding process of aluminum alloy pulsed GTAW. The experimental conditions are shown in Table 1.

The audio sensing system includes an omnidirectional capacitance microphone (MP201) to pick audio signals, and a signal conditioner (MC104) to filter and amplify the signals. The microphone has the frequency response from 20 to 20 kHz. The sound signals are collected with the sampling rate of 40 kHz by a data acquisition card in the computer.

In order to verify the influence of single-channel BSS on welding quality diagnosis, arc sound signals in two states of welding, including partial penetration and full penetration, were collected and processed respectively. Because the base welding current parts are mainly used to maintain the welding arc and contain little welding information. The base level signals are discarded and only peak signals are

Table 1 Experiment conditions and welding parameters

Welding parameters	Value
Pulse frequency (Hz)	2
Peak current (A)	260
Base current (A)	50
Ar flow (L/min)	15
Welding speed (mm/s)	3
Feed speed (L/min)	7
Electrode diameter (mm)	3.2
Duty ratio (%)	50
Material type	LF6 Al alloy

reserved for further processing. To meet the requirement of processing efficiency and accuracy, the signals are divided into several data blocks whose size are 3000 sampling points.

4.2 Arc Sound Signal Processing and Analysis

The time domain graph and spectrum graph of arc sound signals of partial penetration and full penetration are shown in Fig. 6. The frequency spectrum comparison between different penetration states show that the arc sound signal spectrum is mainly concentrated at 0–15 kHz, and the frequency distributions are complex. The frequency characteristics under different penetration states are different, but not significant.

The proposed method of single-channel BSS was used to deal with the welding audio signals. First, the single data block was decomposed to 12 IMFs by EEMD. Then PCA was used to reduce the 12 IMFs to three principal components, whose sum contribution rate was more than 90%. The three principal components were treated as the virtual multichannel signals. The separated signals are separated from those three virtual channel signals through FastICA algorithm. The results are shown in Fig. 7.

Figure 7a, b are spectrums of three separated signals obtained from partial penetration and full penetration welding acoustic signals, respectively. Due to the

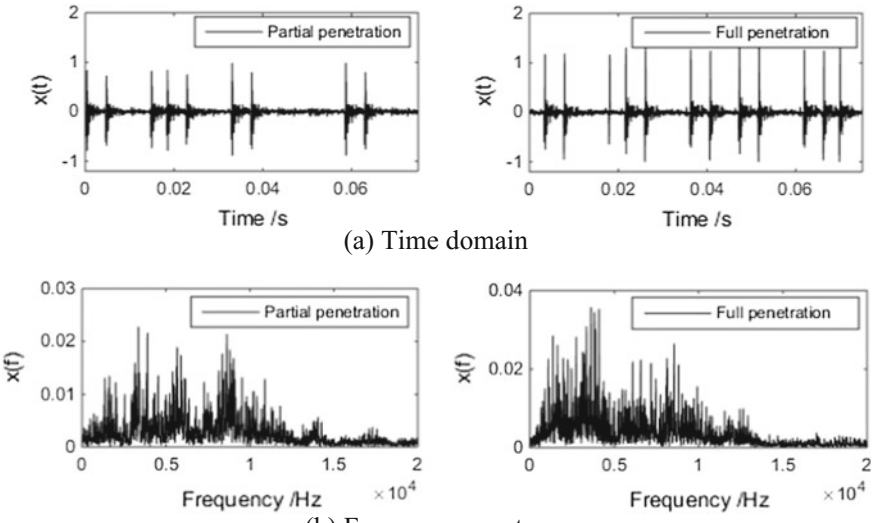

Fig. 6 The time domain and spectrum graphs of the partial penetration and full penetration arc sound signals

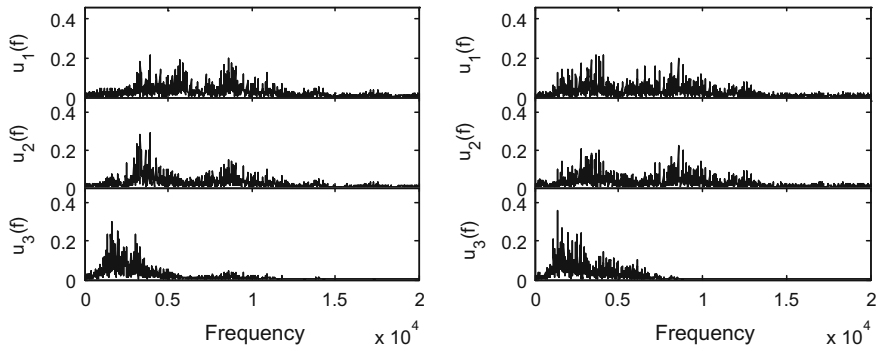

(a) Partial penetration (b) Full penetration

Fig. 7 The spectrum of partial penetration and full penetration

Table 2 The correlation coefficients between each separation and source signals

	u_1(t)	u_2(t)	u_3(t)
Partial penetration	0.926	0.022	0.322
Full penetration	0.977	0.123	0.014

uncertainty of the amplitude and the order of signals separated by BSS, a method is proposed to identify and order each separation according to their characteristics. The correlation coefficients between the each separation signal and the original signal are calculated, and the separation with maximum correlation coefficient is selected as u_1. The remaining two separations are ordered by the frequency of spectral peaks. The separation with higher peak frequency is selected as u_2, and the other is u_3. The separations in Fig. 7 have been sorted. The correlation coefficients between each separation signal in Fig. 7 and the original mixed signal are shown in Table 2.

It can be seen from Table 2 that the separation signal u_1 has a high correlation with the original signal, while the separation signal u_2 and u_3 have very small correlation with the original signal. In Fig. 7, the spectrum of the separated signal u_1 is similar to that of the original signal, while u_2 and u_3 greatly differ from the original signal. These indicate that the separated signal u_1 contains the main welding arc sound information, while u_2 and u_3 are isolated signals other than the audio signal. It is obvious that the spectrum in the middle frequency band (5–6.5 kHz) is remarkable.

Thirty groups of full penetration and partial penetration samples were processed as mentioned above, 15 common statistical characteristics were extracted from the frequency spectrum in the 5–6.5 kHz band of signal separation u_1 to identify different penetration states. The identification results of characteristics extracted from the separated signals were compared with that from the original signals. The results show that the 15 characteristic values extracted from the original signals cannot

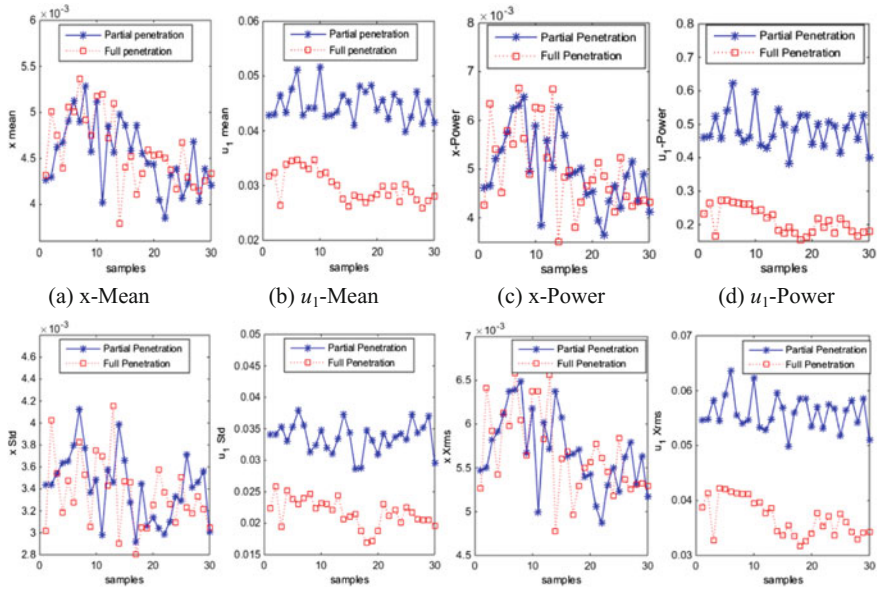

Fig. 8 Statistical characteristics of partial penetration and full penetration arc sound signal

distinguish the partial penetration from full penetration. However, for the characteristics exacted from the separation signals u_1, there are eight characteristics can effectively distinguish the two welding penetration status, including the mean, amplitude, energy, variance, root mean square, waveform factor, covariance, and peak value of the spectrum. The identification results of first four characteristics are shown in Fig. 8.

Figure 8 shows that the characteristics extracted from the original signals are irregularly distributed and cannot distinguish the two penetration states. The statistical characteristics of u_1 can effectively distinguish two kinds of welding penetration states. The main reason can be analyzed as follow: As is known, sources of sound emission are ordinarily from the vibration caused by plasma, metal vapor, and cracking in weld zone. This vibration usually has a higher frequency corresponding to the high-frequency component of the arc sound. When the weld penetration changes, the vibration's intensity and features change accordingly, which cause an obvious change of high frequency in the spectrum of arc sound. However, the original audio sound signals contain noises produced by environment, equipment, and so on. The frequency domain information of the welding states is masked by noise frequency. The separation signal u_1 obtained by single-channel BSS is the source signal of arc. Other source signals of environment and equipment are filtered out. So the characteristics of high frequency (around 6 kHz) in the

spectrum are highlighted. The statistical characteristic parameters, such as mean and variance, etc. can well reflect the spectral intensity and characteristics. That is why the characteristics mentioned above can be used to effectively identify the welding penetration states as shown in Fig. 8.

5 Conclusion

The single-channel BSS method based on EEMD is proposed for arc sound signal to reduce the environmental noises. In the proposed method, the single-channel signal is decomposed into IMFs by EEMD. Then PCA is used to reduce the IMFs to PCs. Finally, source signals can be separated from the principal components using FastICA. The method's efficiency was verified by simulation as well as real welding arc sound signals. The main conclusions are summarized as follows.

(a) The simulated results show that the separated signals are basically consistent with the source signals making up the mixed single-channel signal, but the order and amplitude of separations are uncertain. Three separated source signals are obtained from the collected single-channel arc sound signals. The sorted separation signal u_1 which has the largest correlation with the original arc sound signal is the source signal of arc sound.
(b) Thirty groups of full penetration and partial penetration arc sound signals were separated by this proposed method, the statistical characteristics of the spectrum in the 5–6.5 kHz band were extracted from the separated signal u_1. Eight statistical characteristics such as the mean amplitude, energy, and so on, can effectively distinguish the partial penetration from the full penetration. But, the characteristics extracted from original signal are irregularly distributed, and cannot distinguish the different penetrations.
(c) The source signal of arc sound can be effectively separated from single-channel signal by the single-channel BSS. After that, the frequency domain characteristics indicating welding conditions become more obviously. High-quality welding arc sound signals are provided for state detection.

Acknowledgements This work was supported by National Natural Science Foundation of China (51605372), China Postdoctoral Science Foundation Funding (2016M602805), the National Natural Science Foundation of China (51365051, 51421004), and the Program for New Century Excellent Talents in University (NCET-13-0461).

References

1. Tam J et al (2005) Developing psycho-acoustic experiments in gas metal arc welding. In: IEEE International Conference on Mechatronics and Automations, vol 1–4, Niagara Falls, pp 1112–1117

2. Cayo EH, Alfaro SCA (2009) A non-intrusive GMA welding process quality monitoring system using acoustic sensing. Sensors 9(9):7150–7166
3. Chen CM, Kovacevic R, Jandgric D (2003) Wavelet transform analysis of acoustic emission in monitoring friction stir welding of 6061 aluminum. Int J Mach Tools Manuf 43(13): 1383–1390
4. Grad L, Grum J, Polajnar I et al (2004) Feasibility study of acoustic signals for on-line monitoring in short circuit gas metal arc welding. Int J Mach Tools Manuf 44(5):555–561
5. Saini D, Floyd S (1998) An investigation of gas metal arc welding sound signature for on-line quality control. Weld J 77(4):172S–179S
6. Saad E, Wang H, Kovacevic R (2006) Classification of molten pool modes in variable polarity plasma arc welding based on acoustic signature. J Mater Process Technol 174 (1–3):127–136
7. Lv N, Xu Y, Zhong J et al (2013) Research on detection of welding penetration state during robotic GTAW process based on arc arc sound. Ind Robot 40(5):474–493
8. Lv N, Xu Y, Zhang Z et al (2013) Audio sensing and modeling of arc dynamic characteristic during pulsed Al alloy GTAW process. Sens Rev 33(2):141–156
9. Lv N, Zhong J, Wang J et al (2014) Automatic measuring and processing system of audio sensing for real-time arc height control of pulsed GTAW. Sens Rev 34(1):51–66
10. Zhang Z, Chen H, Xu Y et al (2015) Multisensor-based real-time quality monitoring by means of feature extraction, selection and modeling for Al alloy in arc welding. Mech Syst Signal Process 60–61:151–165
11. Chen ZW (2010) MIG welding arc sound signal de-noising technique research. Dissertation, Harbin University of Science and Technology, China
12. Zeng K et al (2016) An EEMD-ICA approach to enhancing artifact rejection for noisy multivariate neural data. IEEE Trans Neural Syst Rehabil Eng Publ IEEE Eng Med Biol Soc 24:630–638
13. Zvokelj M, Zupan S, Prebil I (2016) EEMD-based multiscale ICA method for slewing bearing fault detection and diagnosis. J Sound Vib 370:394–423
14. Hyvarinen A, Oja E (2000) Independent component analysis: algorithms and applications. Neural Netw 13(4–5):411–430
15. Gu YN (2016) The research of blind source separation algorithm for single channel linear mixed signal. Publishing House of Electronics Industry, China, pp 29–38
16. Huang NE, Shen Z, Long SR et al (1998) The empirical mode decomposition and the Hilbert spectrum for nonlinear and non-stationary time series analysis. Proc Roy Soc Math Phys Eng Sci 454(1971):903–995
17. Wu Z, Huang NE (2009) Ensemble empirical mode decomposition: a noise-assisted data analysis method. Adv Adapt Data Anal Theor Appl 1(1):1–41

Investigation on Surface Quality in a Hybrid Manufacturing System Combining Wire and Arc Additive Manufacturing and Machining

Fang Li, Shujun Chen, Junbiao Shi and Hongyu Tian

Abstract Wire and arc additive manufacturing (WAAM) has gained popularity in recent years due to its unique efficiency and cost advantages. Nevertheless, due to the stair-stepping effect and the liquidity of molten metal, the achieved geometric accuracy and surface quality are still very limited. The combination of WAAM and machining, namely hybrid manufacturing, provides a fundamental solution to the above problem. Because machining is performed after depositing several layers, the deposition width, deposition height, and surface waviness have great effects on the machined surface quality, in addition to the machining parameters including spindle speed and feedrate. In this paper, the dependence of the machined surface quality (characterized by surface roughness) on the influencing factors mentioned above is investigated based on quadratic general rotary unitized design (QGRUD). To reduce the number of experiments, a comprehensive factor, namely material removal area (MRA), is introduced to characterize the deposition width, deposition height, and surface waviness. The analysis results show that spindle speed is the most influential factor, followed by MRA and feedrate. Furthermore, a high spindle speed and a moderate feedrate are preferred, which contribute to not only improving the surface quality and the efficiency but also reducing the demand of geometric accuracy for WAAM.

Keywords Hybrid manufacturing · Wire and arc additive manufacturing Machining · Surface roughness · Parametric optimization

F. Li · S. Chen (✉) · J. Shi · H. Tian
College of Mechanical Engineering and Applied Electronics Technology,
Beijing University of Technology, Beijing, China
e-mail: sjchen@bjut.edu.cn

S. Chen et al. (eds.), *Transactions on Intelligent Welding Manufacturing*,
Transactions on Intelligent Welding Manufacturing,
https://doi.org/10.1007/978-981-10-7043-3_9

1 Introduction

Metallic additive manufacturing (AM) techniques can be broadly categorized depending on how the feedstock is supplied (powder bed, powder feeding and wire feeding) and which energy source is selected (electron beam, laser, and arc) [1, 2]. Among them, wire and arc additive manufacturing (WAAM) [3, 4], employing metal wire as the feedstock and welding arc as the heat source, has drawn increasing research interest in recent years. It offers various advantages such as high productivity, low cost, high material utilization, high energy efficiency, and safe operation. These advantages make WAAM highly competitive in fabricating medium to large-scale metal parts. Nevertheless, its inherent drawbacks, i.e., low geometric accuracy and poor surface quality due to the stair-stepping effect and the liquidity of molten metal, greatly limit its application in high-precision occasions. The combination of WAAM and machining, namely hybrid manufacturing, provides a fundamental solution to the above problem [5]. It enables material depositing and surface finishing to be achieved in a single setup, thereby making the best use of the strengths of both processes while avoiding their limitations. Several effects have been made to develop hybrid manufacturing systems in recent years [6–10].

The hybrid manufacturing system studied in this paper is illustrated in Fig. 1. Both the side and the top surfaces are machined after depositing several layers, followed by subsequent addition and subtraction steps until the final part is created. Only the quality of the side surface is concerned in this paper because the top surface will be covered by the subsequent layers. It can be observed from Fig. 1 that the axial cutting depth during machining is determined by the product of the layer thickness and the number of layers, i.e., deposition height, whereas the radial cutting depth is determined by the deposition width minus the target width as well as the surface waviness. Specifically, the surface waviness is in the form of peaks

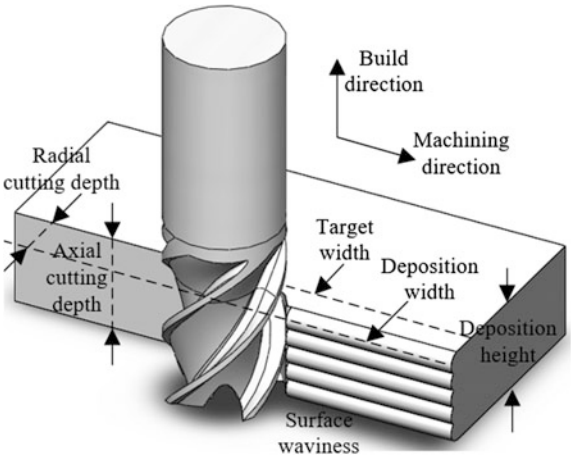

Fig. 1 Schematic diagram of a hybrid manufacturing system

and valleys resulting from the stair-stepping effect. Therefore, all of the deposition width, deposition height, and surface waviness have great effects on the machined surface quality. In addition, the machining parameters such as spindle speed and federate also have effects on the machined surface quality. As a consequence, it is more challenging to assess surface quality in a hybrid manufacturing system compared with individual machining systems.

Surface roughness (R_a) is commonly used to indicate surface quality, which is related to the part functional performance in terms of fatigue, corrosion resistance, creep life, etc. Generally, surface roughness depends on several factors, such as spindle speed, feedrate, radial and axial cutting depths, tool material and geometry, tool wear, etc. [11]. There have been numerous studies conducted on the prediction of surface roughness and the optimization of process parameters. Oktem et al. [12] applied a Taguchi optimization method to find the optimal process parameters which minimize surface roughness when milling the mold surfaces of 7075-T6 aluminum material. Kilickap et al. studied the influence of machining parameters on the surface roughness obtained in drilling of AISI 1045 and developed a mathematical prediction model using response surface methodology (RSM) [13]. Oktem et al. [14] developed an artificial neural network (ANN) to predict the surface roughness and applied the genetic algorithm to determine optimum cutting parameter leading to minimum surface roughness.

This paper aims to investigate the dependence of the machined surface quality, characterized by surface roughness, on the main influencing factors including deposition width, deposition height, surface waviness, spindle speed, and feedrate mentioned above, and provide a guide to optimize these process parameters in the hybrid manufacturing system. The quadratic general rotary unitized design (QGRUD) is adopted, which is a regression method with rotation and versatility, thus enabling one to reduce the number of experiments and get more accurate results [15]. Besides, a comprehensive factor, namely material removal area (MRA), is introduced to characterize the deposition width, deposition height, and surface waviness. Thus, the influencing factors involved reduced from five to three, i.e., spindle speed, feedrate and MRA, and thereby the required number of experiments is much less.

2 System Description

A hybrid manufacturing system combining WAAM and machining has been developed at Beijing University of Technology (BJUT), as shown in Fig. 2. It is based on a two-robot cooperative platform. One robot is IGM RTI2000, equipped with two Fronius Synergic 5000 welding machines to implement Tandem GMAW (gas metal arc welding)-based WAAM. In Tandem GMAW, two welding wires are passed through the same welding torch, thus providing much higher productivity than conventional GMAW. The other robot is KUKA KR500, which is a heavy-duty robot that is suitable for milling applications. It is equipped with a

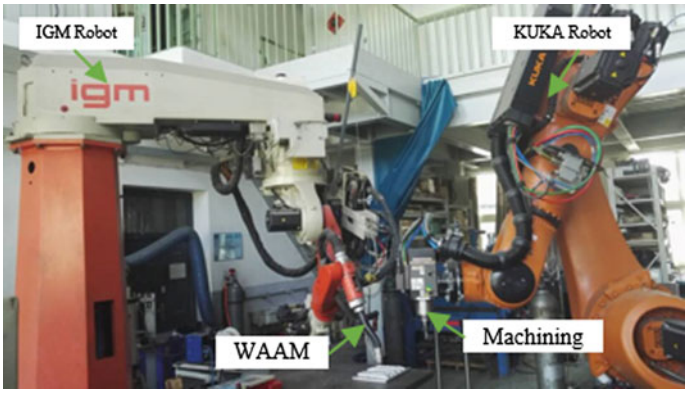

Fig. 2 Hybrid manufacturing system based on a two-robot cooperative platform

high-speed electric spindle ES779 with a maximum spindle speed of 22,000 rpm. The wire material used is Al2325 alloy with the chemical composition of Cu 3.9–4.8%, Mn 0.1–1.0%, Ti 0.15%, Mg 0.4–0.8%, Zn 0.3%, etc., in addition to Al. The substrate material is Al2219 alloy. Aluminum alloy has wide applications in civil aviation and automobile industry due to light weight and favorable properties.

3 Methods

3.1 Definition of Material Removal Area (MRA)

As mentioned above, five factors affecting the surface roughness, i.e., deposition width, deposition height, surface waviness, spindle speed, and feedrate, are considered. If the QGRUD is applied directly, 64 sets of experiments are required, which are extremely time-consuming. In this paper, a comprehensive factor, namely MRA, is introduced to characterize the deposition width, deposition height, and surface waviness. Thus, the factors involved reduced from five to three and the required number of experiments is reduced to 20 according to QGRUD. MRA is defined as the sectional area of the region that needs to be removed, as illustrated in Fig. 3. The effects of the three factors on the surface roughness can be reflected through MRA. It is also known that MRA is an indicator of the geometric accuracy of the WAAM process. The higher the geometric accuracy, the lower the MRA.

From Fig. 3, we know that MRA can be calculated as follows:

$$\mathrm{MRA} = N \times (W_0 \times H_0 + \partial \times W_1 \times H_0) \tag{1}$$

where N denotes the number of layers, H_0 denotes the layer thickness, W_0 denotes the deposition width minus the target width and W_1 denotes the maximum distance

between the peaks and the valleys on the surface. The coefficient ∂ is determined to 0.7 based on preliminary experiments. Generally, N is fixed in practice, i.e., the WAAM process and the machining process are alternated every N layers. In this paper, N is set to 6.

3.2 Design of Experiments

To apply QGRUD, the predominant factors affecting the response should be identified and their upper and lower limits should be determined first. In this paper, spindle speed (A), feedrate (B), and MRA (C) are identified as the predominant factors and surface roughness (R_a) is the response. The lower and upper limits of these factors are determined as seen in Table 1, which are divided into five levels coded by −1.6817, −1, 0, +1 and +1.6817 according to QGRUD.

The 3-factor-5-level QGRUD requires 20 sets of experiments in total, 8 as factorial points, 6 as star points, and 6 as center points. The resulting design matrix is generated, as given in Table 2.

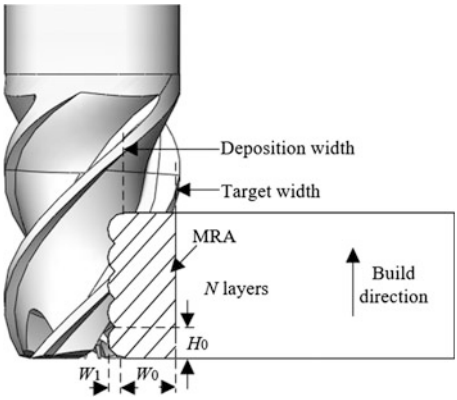

Fig. 3 Illustration of MRA

Table 1 Coding for factor and level

Symbol	Parameter	Level				
		−1.68	−1	0	1	1.68
A	Spindle speed (rpm)	1000	2400	4500	6600	8000
B	Feedrate (mm/s)	1	1.8	3	4.2	5
C	MRA (mm^2)	10	14	20	26	30

Table 2 Experimental design matrix and the response

Exp. No.	Coding (*A B C*)	Roughness (μm)	Exp. No.	Coding (*A B C*)	Roughness (μm)
1	(−1−1 −1)	1.75	11	(0 − 1.682 0)	1.76
2	(1 − 1 −1)	1.36	12	(0 1.682 0)	1.86
3	(−1 1 − 1)	1.95	13	(0 0 − 1.682)	1.65
4	(1 1 − 1)	1.52	14	(0 0 1.682)	1.78
5	(−1−1 1)	1.99	15	(0 0 0)	1.59
6	(1 − 1 1)	1.51	16	(0 0 0)	1.65
7	(−1 1 1)	2.11	17	(0 0 0)	1.52
8	(1 1 1)	1.81	18	(0 0 0)	1.53
9	(−1.682 0 0)	2.46	19	(0 0 0)	1.67
10	(1.682 0 0)	1.55	20	(0 0 0)	1.63

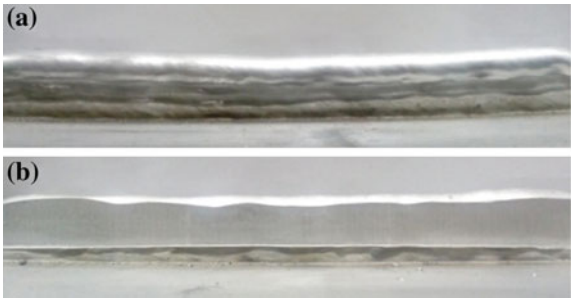

Fig. 4 Surface: **a** Surface of original wall structures (6 layers). **b** Surface after machining

3.3 Experiments

The experiments went through two phases. First, the WAAM experiments were carried out using the IGM RTI2000 robot to produce wall structures with 6 layers (i.e., $N = 6$), as shown in Fig. 4a. The material of the wire and the substrate has been given in Sect. 2. The travel speed was set to 0.48 m/min, the wire feedrate was set to 4.3 m/min and the welding voltage was set to 18.4 V. The shielding gas was Ar at a flow rate of 22 L/min. With the wall structures produced by WAAM, 20 sets of machining experiments were conducted then using the KUKA KR500 robot according to the experimental design matrix in Table 2, as shown in Fig. 4b. The machining tool, made of uncoated carbide alloy, had a diameter of 14 mm with a helix angle of 55°. The working mode was down milling. No cooling and lubricating agent were used. After each experiment, the surface roughness in the tool feed direction was measured using a portable roughmeter TR200 with a sensitivity of 0.01 μm. Specifically, the surface roughness was measured five times at different locations and repeated twice at each location. The average value was recorded, as given in Table 2.

4 Results

4.1 Regression Model

According to the experimental results given in Table 2, the quadratic regression model that describes the dependence of the surface roughness on the spindle speed (A), the feedrate (B), and the MRA (C) was obtained with the aid of the software Design-Expert 6.0 as follows.

$$R_a = 1.61 - 0.23A + 0.069B + 0.078C + 0.018AB + 0.005AC + 0.0075BC + 0.12A^2 + 0.054B^2 + 0.02C^2 \quad (2)$$

Then the variance analysis and F value testing were undertaken to validate the obtained regression model, as given in Table 3.

The F value of Lack of Fit was 4.56, lower than $F_{0.05}(5, 5) = 5.05$, indicating that Lack of Fit was not significant. The F value of the regression equation was 11.2, higher than $F_{0.05}(9, 10) = 3.137$, indicating that the regression model was significant and therefore fitted the actual system closely. Thus, we can conclude that the regression model was accurate and credible. At the level of 0.05, P values of A, B, C, and A^2 term were all lower than 0.05, which indicated that their effects on the surface roughness were significant. In contrast, P values of AB, AC, BC, and B^2 and C^2 were higher than 0.05, which indicated that their effects on the surface roughness were not significant and could be neglected. It is interesting that for any two factors, their interaction effects were not significant. After omitting the insignificant factors, the quadratic regression model was simplified to

Table 3 Variance analysis and F value testing results

Source	Sum of squares	df	Mean square	F value	P value
A	0.72	1	0.72	65.57	< 0.0001
B	0.066	1	0.066	6.02	0.0341
C	0.082	1	0.082	7.50	0.0209
AB	0.00245	1	0.00245	0.22	0.6462
AC	0.0002	1	0.0002	0.018	0.8951
BC	0.00045	1	0.00045	0.041	0.8434
A^2	0.21	1	0.21	19.27	0.0014
B^2	0.040	1	0.040	3.56	0.0885
C^2	0.004888	1	0.004888	0.45	0.5190
Model	1.10	9	0.12	11.2	0.0010
Residual	0.11	10	0.012		
Lack of fit	0.090	5	0.018	4.56	0.0607
Pure error	0.020	5	0.003937		
Total	1.21	19			

$$R_a \approx 1.61 - 0.23A + 0.069B + 0.078C + 0.12A^2 \quad (3)$$

4.2 Single Factor Effect Analysis

Based on the obtained quadratic regression model (Eq. 3), the effects of single factor on the surface roughness were analyzed, as shown in Fig. 5. It was obtained by varying one factor while keeping the other factors at zero level. It is clearly obtained that spindle speed is the dominant factor affecting the surface roughness, followed by MRA and feedrate. It is also observed the surface roughness increases with the increasing of feedrate and MRA. This is easy to understand because the material removal rate (MRR) is equal to the product of the feedrate and MRA. Higher MRR means higher cutting force and therefore higher surface roughness. On the other hand, the surface roughness decreases with increasing spindle speed because the corresponding cutting force is much lower.

4.3 Optimization

The reduction of the surface roughness can be achieved either by optimizing the MRA, i.e., the WAAM parameters or by optimizing the machining parameters. Figure 6 presents the surface roughness as a function of the spindle speed and the feedrate when the MRA is 10, 17, 24, and 30 respectively. We can conclude that

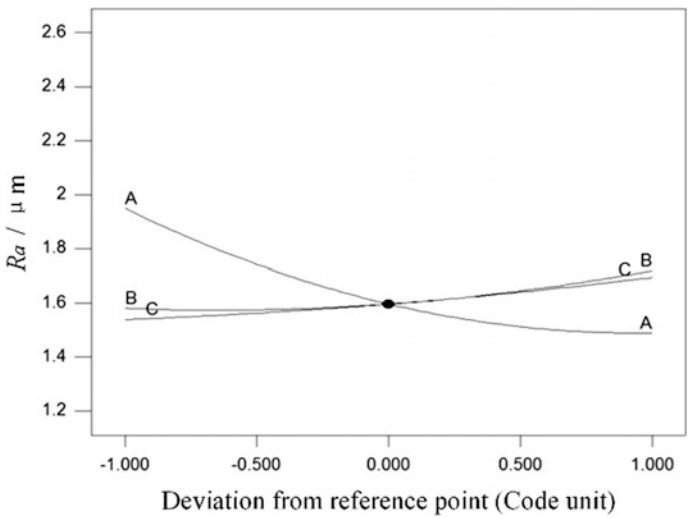

Fig. 5 Single factor effect analysis

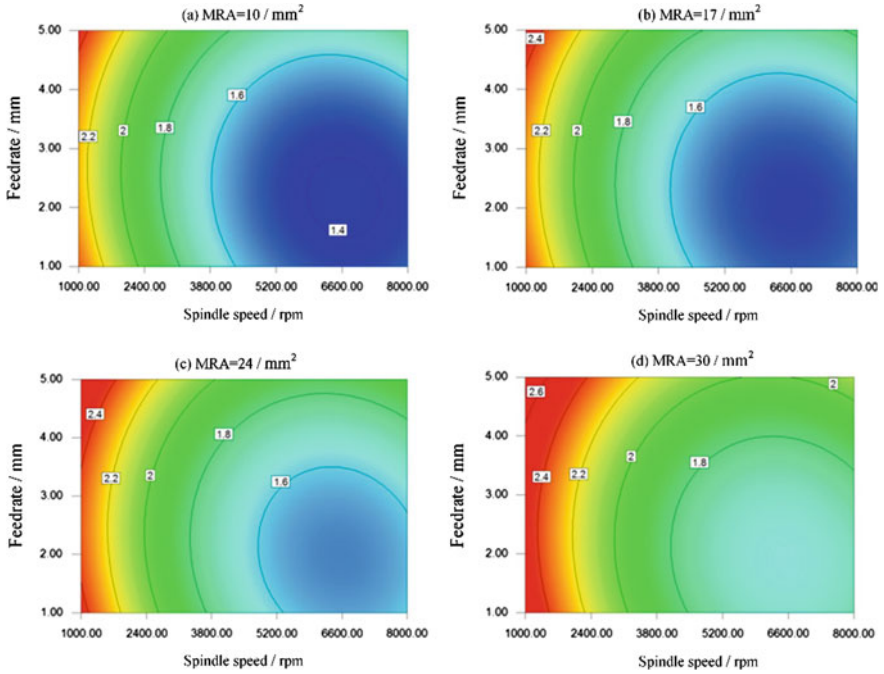

Fig. 6 Surface roughness as a function of spindle speed and feedrate when the MRA is 10, 17, 24, and 30 respectively

when the spindle speed is low, e.g., 1000 rpm, the MRA should be small enough to reduce the surface roughness. In contrast, when the spindle speed is high, e.g., 8000 rpm, no matter how large the MRA is, the surface roughness is still very small. As it is more difficult to accurately control the MRA than the other process parameters due to the liquidity of molten metal, employing a high spindle speed is very essential. It helps reduce the demand of geometric accuracy (i.e., MRA) for WAAM. Namely, if the spindle speed is quite low, the demand of geometric accuracy for WAAM is much higher. With regard to the feedrate, though lower feedrate leads to lower surface roughness, its effect is less significant than other factors. On the other hand, lower feedrate also means lower efficiency. Therefore, in order to achieve a good balance between surface quality and efficiency, a moderate feedrate is preferred. In conclusion, in order to minimize the surface roughness, increase the efficiency and reduce demand of geometric accuracy for WAAM, we expect a high spindle speed and a moderate feedrate in the hybrid manufacturing system.

5 Conclusion

A hybrid manufacturing system combining WAAM and machining has been introduced in this paper. The dependence of surface quality on deposition width, deposition height, surface waviness, spindle speed, and feedrate has been investigated based on QGRUD. From the experimental and the analysis results, the following conclusions are obtained:

1. By introducing a comprehensive factor, namely MRA, to characterize the deposition width, deposition height and surface waviness, the required number of experiments is greatly reduced.
2. Spindle speed is the most influential factor on the surface roughness, followed by MRA and feedrate. For any two factors, their interaction effects are not significant.
3. A high spindle speed is very essential for the hybrid manufacturing system, which contributes to not only improving the surface quality, but also reducing the demand of geometric accuracy for WAAM.
4. A moderate feedrate is preferred in order to achieve a good balance between the surface quality and the efficiency.

Acknowledgements This paper is supported by the National Natural Science Foundation of China (51475009) and the China Postdoctoral Science Foundation Funded Project (2017M610726).

References

1. Frazier WE (2014) Metal additive manufacturing: a review. J Mater Eng Perform 23(6): 1917–1928
2. Karunakaran KP, Bernard A, Suryakumar S et al (2012) Rapid manufacturing of metallic objects. Rapid Prototyping J 18(4):264–280
3. Ding D, Pan Z, Cuiuri D et al (2015) Wire-feed additive manufacturing of metal components: technologies, developments and future interests. Int J Adv Manuf Tech 81(1):465–481
4. Xiong J, Zhang G, Zhang W (2015) Forming appearance analysis in multi-layer single-pass GMAW-based additive manufacturing. Int J Adv Manuf Tech 80(9–12):1767–1776
5. Flynn JM, Shokrani A, Newman ST et al (2016) Hybrid additive and subtractive machine tools—research and industrial developments. Int J Mach Tool Manuf 101:79–101
6. Song YA, Park S, Choi D et al (2005) 3D welding and milling: part I—a direct approach for freeform fabrication of metallic prototypes. Int J Mach Tool Manuf 45(9):1057–1062
7. Song YA, Park S (2006) Experimental investigations into rapid prototyping of composites by novel hybrid deposition process. J Mater Process Tech 171(1):35–40
8. Karunakaran KP, Suryakumar S, Pushpa V et al (2010) Low cost integration of additive and subtractive processes for hybrid layered manufacturing. Robot Comput Integr Manf 26 (5):490–499
9. Xiong X, Zhang H, Wang G et al (2010) Hybrid plasma deposition and milling for an aeroengine double helix integral impeller made of superalloy. Robot Comput Integr Manf 26 (4):291–295

10. Zhu Z, Dhokia V, Newman ST et al (2014) Application of a hybrid process for high precision manufacture of difficult to machine prismatic parts. Int J Adv Manuf Tech 74(5–8): 1115–1132
11. Yang D, Liu Z (2015) Surface topography analysis and cutting parameters optimization for peripheral milling titanium alloy Ti–6Al–4V. Int J Refract Met Hard Mater 51:192–200
12. Oktem H, Erzurumlu T, Col M (2006) A study of the Taguchi optimization method for surface roughness in finish milling of mold surfaces. Int J Adv Manuf Tech 28(7):694–700
13. Kilickap E, Huseyinoglu M, Yardimeden A (2011) Optimization of drilling parameters on surface roughness in drilling of AISI 1045 using response surface methodology and genetic algorithm. Int J Adv Manuf Tech 52(1):79–88
14. Oktem H, Erzurumlu T, Erzincanli F (2006) Prediction of minimum surface roughness in end milling mold parts using neural network and genetic algorithm. Mater Des 27(9):735–744
15. Akankwasa NT, Wang J, Zhang Y (2015) Study of optimum spinning parameters for production of t-400/cotton core spun yarn by ring spinning. J Text Inst 107(4):1–8

Preliminary Research on Intelligent Mobile Tool Cart for Industrial Manufacturing in a Factory Environment

Shengnan Gai, Qiang Luo and Shujun Chen

Abstract Intellectualization of manufacturing is a general trend due to the development of technology and science. This paper presents a preliminary research on intelligent mobile tool cart (IMTC) for working alongside workers in manufacturing process. Tool cart problem is considered as an exemplary intelligent mobile tool cart service system. A type of differential-driven mobile cart with a tool basket which is mounted on the top of the mobile cart compose the intelligent mobile tool cart. The IMTC is designed to provide workers with remote motion control and tools positioning services. Daily used instructions are exercised as commands to control the IMTC in the factory environment by using Leap Motion sensor for finger/hand position detection. The IMTC provides its real-time position information to the worker. To fulfill estimating the location of IMTC, QR localization method is proposed. We verified the features of the IMTC and feasibility of the proposed localization method through experimental trials.

Keywords Service robot · Intelligent mobile tool cart · Position detection Gesture command

1 Introduction

In recent decades, we realize that the robot helps general public and plays a large role in our life. It is worth mentioning that the application of mobile robot has drawn much attention. Till now, researchers designed and implemented many successful mobile robot systems. Duan et al. [1] proposed a miniature wheel-track-legged mobile robot to carry out military and civilian missions. Thrun et al. [2] described an interactive four-guide robot for museum guidance. Engelberger [3] demonstrate a healthcare robot for convenience of hospital

S. Gai · Q. Luo · S. Chen (✉)
College of Mechanical Engineering and Applied Electronics Technology, Beijing University of Technology, Beijing, China
e-mail: sjchen@bjut.edu.cn

S. Chen et al. (eds.), *Transactions on Intelligent Welding Manufacturing*,
Transactions on Intelligent Welding Manufacturing,
https://doi.org/10.1007/978-981-10-7043-3_10

assistance. Garingo et al. [4] developed a wireless, mobile, robotic telemedicine system in the Neonatal Intensive Care Unit (NICU). In service robot area, researchers always choose human body, face, voice, arm, or leg as the research objective. Lee et al. [5] implemented human tracking by legs scanning from a moving robot to monitor a moving target person. Jung et al. [6] set human torso as research objective to allow a mobile robot track a desired human in front. Gai et al. [7] introduced daily used instructions as commands through a Kinect to control mobile shopping cart and provide consumer intelligent shopping services. Chen et al. [8] presented an interactive mobile robot only based on visual information to support face-to-face interaction between human and robot. Otsuka et al. [9] utilized voice for controlling robot head movements to guarantee robot behave the way human expect it to and offer natural spoken communication between human and robot. It is probably fair to say that the diversification of information to the mobile cart makes applicability of the mobile cart more extensive. However, the two legs in [5], the torso part in [6], the arm in [7] and face and arm combined in [8] provide relatively sweeping gesture commands to the mobile cart which is not suitable for an industry application. Besides, noisy industry environment might give rise to voice control invalidation.

This paper proposes a novel method for workers to control IMTC by employing hand/finger gestures commands. We attempt to use hands or fingers to express emotion and give orders. The commercialized Leap Motion sensor mounted on the operation platform is utilized to achieve the goal. The Leap Motion is able to detect two hands and ten fingers at once. It is used to provide position information of the hands and fingers with high precision in real-time and receive hand/finger gesture commands. Based on customs and understandable of human beings, we defined seven hand/finger gesture commands using the right hand to control the Intelligent Mobile Tool Cart (IMTC). Besides, a camera is installed on the bottom of the cart to detect the QR code from a QR marker streaks labeled on the ground. By decoding the stored position information from the QR code, the exact location of the cart can be realized accordingly. The QR localization method is proposed to provide stable location information to the IMTC. The feasibility of the QR localization method is verified through experiments.

This paper is organized as follows. The Intelligent Mobile Tool Cart and usage of Leap Motion sensor are introduced in Sects. 2 and 3, respectively. Section 4 presents and verifies QR localization method based on Wi-Fi network. Section 5 evaluates the performance of the proposed IMTC through experiment trials. Finally, the conclusion is organized in the last section.

2 Overview of Intelligent Mobile Tool Cart Service System

2.1 Introduction to Intelligent Mobile Tool Cart Service System

The Intelligent Mobile Tool Cart Service System is demonstrated in Fig. 1. Several devices including a Wi-Fi box, a Leap Motion, cart appliances, and QR marker streaks are interconnected to realize the intelligent service to the worker. The two major functions of the IMTC are cart remote motion sensing control and cart location-recognition services. The cart remote sensing motion control is realized by employing Leap Motion sensor. The Leap Motion provides an interface between the worker and the IMTC. Commands include Go Forward, Draw Back, Turn Left, Turn Right, Start/Stop, Acceleration, and Deceleration, which will be executed by IMTC in the experiment apart. Besides, during this process, IMTC speed adjustment could be achieved by employing Acceleration command and Deceleration command.

The location information is provided by QR code. A camera installed on the bottom of the cart attempts to detect the QR code when the cart passes through a QR code marker streak, and the QR position information will be decoded by employing ZBar. By implementing hybrid localization algorithm which will be described in Sect. 4, the worker will receive a real-time location of the IMTC.

2.2 Mechanism and Hardware

A tool basket often refers to a kind of storage to hold tools. The first tool basket was built in the early nineteenth century made of wool material. Noffsinger [10] developed a foldable tool cart. Mccauley et al. [11] designed a tool storage and bolt organizer device. Lately, Lin et al. [12] proposed a cart, which can store tools and parts in 2016. Nonetheless, those designs applied on the factory can only provide

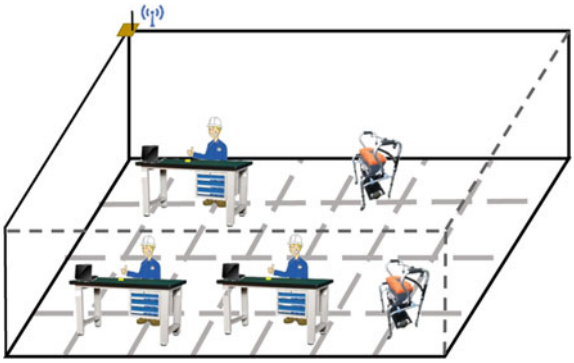

Fig. 1 Demonstration of IMTC service system in a factory environment

workers with convenience to some extent. Workers still need to interrupt working and leave the operation platform to take tools from a tool holder located apart from the operation platform.

To solve the problem, a novel intelligent mobile tool cart is developed as shown in Fig. 2. In a factory environment, the operation platform is equipped with a Leap Motion. And IMTC which is comprised of a tool basket, a camera, a LED lights, and a differential-driven mobile cart will be used in the factory environment to assist worker with providing intelligent service for industry manufacturing. Two motors drive the differential-driven wheels and provide the momentum to the IMTC. The tools, for example, chisels, screwdrivers, pliers, and so on, are hold in the tool basket which is installed on the top of the cart as shown in Fig. 2. A camera is installed at the bottom of the cart to detect QR marker and LED lights are fixed on the differential-driven mobile cart for better illumination. In this paper, the mounting position of the camera is higher than the LED lights. It will guarantee capturing at least one integrated QR code that could be detected by the camera in the range of the LED lights. Besides, a DSP controller for motor control, and two lead-acid DC batteries for power supply. The parameters of the IMTC are summarized in Table 1.

3 Sensor System

3.1 Description of Leap Motion

The proposed system using Leap Motion could detect the position of the hand/finger and receive gesture commands. Leap Motion is a motion sensing input device commercialized by Leap Company. The Leap Motion recognizes and tracks hands and fingers. The effective range of the Leap Motion extends from 0.025 to 0.6 m in distance above the device along *Y* axis and the angle of vision covers 150 degrees in default. Figure 3 shows the effective range of the Leap Motion.

Generally speaking, the Leap Motion has a webcam-like structure and allows users to interact with it through a natural user interface by applying hand/finger

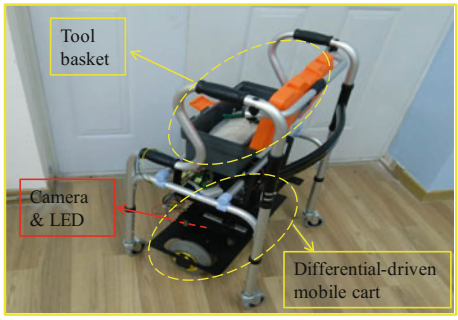

Fig. 2 Intelligent mobile tool cart

Table 1 Main specification of the tool cart

	Specification	Quantity
Motor	DC motor, 90 W, 18:1, Maxon (for driving shopping cart)	2
	DC motor, 25 W, 66:1, Faulhaver (for lifting DDTM)	1
DSP controller	dsPIC33FJ128 M	1
Motion controller	Leap motion, USB 2.0	1
Battery	Lead-acid, DC, 12 V	2
Camera	C270, USB 2.0, Logitech	1
Illumination light	LED lights	1
$W \times L \times H$	0.58 m × 0.9 m × 0.86 m	
Wheel radius	0.15 m	
Max speed	1.2 m/s	

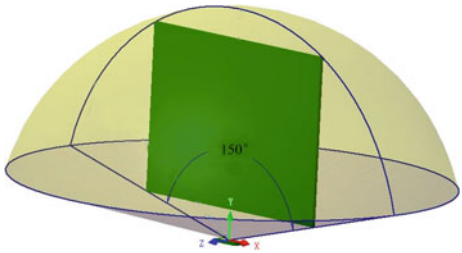

Fig. 3 Effective range of the leap motion

gesture commands detection. The novel control method of MTC using Leap Motion depends on advances in entities tracking, such as hands and fingers. If all or part of a finger is not visible, the finger characteristics will be estimated based on recent observations and the anatomical model of the hand. The natural user interface could be done by using kinds of programming language, such as C++, C#, Unity, Objective-C, Java, Python, JavaScript, and so on. And C++ was adopted in this paper.

3.2 Commands to Leap Motion

In this paper, the Leap Motion installed on the operation platform is used to detect hand/finger gesture commands of the worker. To read gesture commands, hand/finger detection should be set. In our experiment, we use right hand and its three fingers (index finger, middle finger, and ring finger) to recognize gesture commands. Depending on the effective range of Leap Motion we define seven commands, Go Forward, Draw Back, Turn Left, Turn Right, Start/Stop, Acceleration, and Deceleration. When the worker places his right hand with three fingers on seven different regions, shown in Fig. 4, within effective range, the corresponding

gesture command will be recognized and sent to the MTC through Wi-Fi connection. The Mobile Tool Cart responding to Go Forward, Draw Back, Turn Left, Turn Right, Start/Stop, Acceleration, and Deceleration will be tested in Sect. 5.

4 QR Localization Method

The Quick Response Code (QR Code) is a machine-readable optical label that contains information about the item to which it is attached. Due to its fast readability and greater storage capacity, the QR code gained more and more popularity. The famous applications of QR code include product tracking, item identification, mobile operating, code payment, website login, document management, and general marketing. In this work, we use QR code to locate the cart in the given environment. As described in Sect. 2, a camera is installed on the cart to detect the QR code from a QR marker streaks labeled on the ground. By decoding the stored position information from the QR code, exact location of the cart can be realized accordingly.

Success read and read time should be taken into consideration when we use camera to detect QR code. During the test trip when the cart passes through QR marker streaks, the success read is defined as the QR code number that is accurately scanned. The read time is defined as the total time that is cost to scan a QR code marker and decode the scanned QR code. Only when a QR code is detected by a camera successfully and gets precise decoding information at the same time, it is possible to get effective position information of the shopping cart. However, it is noted that camera is sensitive to light. In our research, the QR marker streaks are statically labeled on the ground and the camera is moving with the cart. The cart velocity affects both the success read and the read time. In order to determine the influence of lights and shopping cart velocity on the success read and read time, we performed experiments in the following.

The light condition of experimental environment is set as four cases; adequate illumination with using LED lights, adequate illumination without using LED lights, inadequate illumination with using LED lights, and inadequate illumination

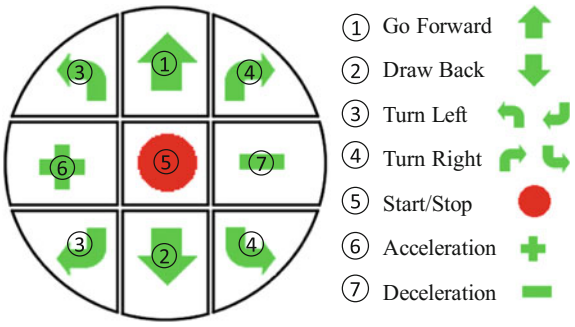

Fig. 4 Hang/finger gesture commands within leap motion effective range

without using LED lights. The experiment was carried out under these four different light cases, respectively. As shown in Fig. 5, there are ten QR marker streaks labeled on the ground. The distance between two neighbor steaks is 0.5 m and the position of the first steak is (0, 0.5). The cart is initially located at the origin position (0, 0) marked by green dot in Fig. 5. The cart starts from the origin position and passes through ten QR marker streaks.

When the cart passes through each QR marker streak, we decode the QR position value P_{QR} and odometry position value P_{odo} at the same time. However, it is noted that the odometry position value is greater than the absolute position of the QR marker streak. This is because camera detection and QR code decoding take some time which is demonstrated in Fig. 6. Their total time (i.e., time latency) is defined as read time given by

$$T_{rt} = T_{odo} - T_{QR} = \frac{P_{odo} - P_{QR}}{v},$$

where P_{odo} is the measured odometry value when QR code position is received, and P_{QR} is the corresponding QR code position value. v is a constant value at the desired velocity of the cart for one test trial. In this experiment, five specific velocities ranging from 0.4 to 1.2 m/s were tested. Each test trial was executed ten times by setting the same cart velocity under the same illumination case. The experiment results of success read average under four different illumination cases in different velocity is shown in Table 2.

From Table 2, adequate illumination condition gives rise to outstanding QR code success read under the same cart velocity by comparing adequate illumination condition with inadequate illumination condition. And by using LED lights the success read is improved by 3–7.6% comparing with without using LED lights.

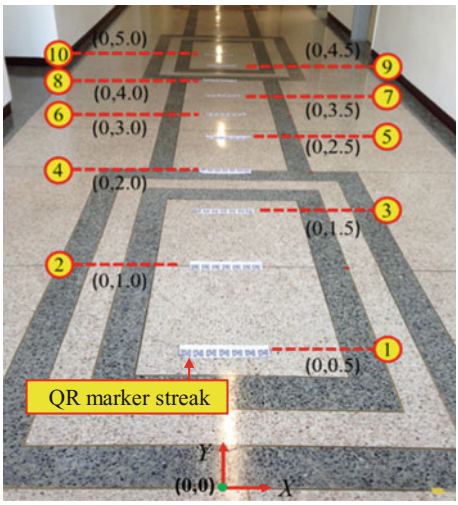

Fig. 5 Test environment of QR code

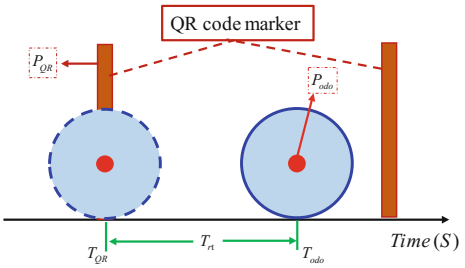

Fig. 6 Demonstration of QR localization method

Table 2 Success read test for different illumination case

	Adequate illumination		Inadequate illumination	
	LED (%)	Without LED (%)	LED (%)	Without LED (%)
0.4 m/s	100	100	60	35.46
0.6 m/s	100	100	36.52	0
0.8 m/s	100	100	0	0
1.0 m/s	100	97	0	0
1.2 m/s	100	92.4	0	0

The IMTC will be applied to an adequate illumination environment, so in this paper, we just take adequate illumination case into consideration. By employing LED lights to improve the performance of QR code detection, the corresponding read time is summarized in Table 3.

From Table 3, we can see that the read time is relatively stable under the same velocity of the cart. And as the velocity of the cart increases, the read time grows slightly as well. All read time in Table 3 are less than 0.4 s in all speeds under consideration and the cart velocity limitation is low (1.2 m/s), so it is reasonable to using QR positioning information to provide cart location in real application.

Table 3 Read time test for different velocities

	0.4 m/s	0.6 m/s	0.8 m/s	1.0 m/s	1.2 m/s
1	0.338	0.338	0.325	0.324	0.332
2	0.348	0.295	0.299	0.345	0.372
3	0.353	0.337	0.305	0.347	0.355
4	0.253	0.363	0.326	0.345	0.363
5	0.313	0.358	0.331	0.35	0.39
6	0.32	0.312	0.37	0.356	0.355
7	0.33	0.342	0.346	0.348	0.34
8	0.28	0.335	0.34	0.334	0.361
9	0.288	0.308	0.323	0.327	0.342
10	0.313	0.332	0.329	0.342	0.353
M	0.314	0.332	0.329	0.342	0.356

5 Experiment

In order to evaluate the effectiveness of the proposed control method of Intelligent Mobile Tool Cart, two experiment trials are conducted. The first experiment was in a factory similarly environment and the second experiment was in a real factory environment. Both of the two environments were Wi-Fi enabled.

5.1 Experiment 1 (Leap Motion Based Control Method Performance Test in a Factory Similarly Environment)

Initially, the tester stood in front of the operation platform and the Intelligent Mobile Tool Cart located beside the operation platform. The tester put his right hand within the effective range of the Leap Motion and gave commands to IMTC through Wi-Fi communication. We tested each command 50 times. If the tester put his right hand with three fingers in region 2 of the Leap Motion, the IMTC executed Draw Back command as shown in Fig. 7. If the tester put his right hand with three fingers in region 4, the IMTC executed Turn Right command as shown in Fig. 8. Repeated the experiment procedures mentioned above in the other 5 regions and recorded the experiment results. The Start/Stop command is used to initialize the system when it appears at the first time, and call for stop action when the Start/Stop command appears after the other commands.

The upper three figures of Figs. 7 and 8 demonstrate the reaction of MTC when the MTC executes Draw Back command and Turn Right command, respectively. In the bottom three figures, the first figure shows the specific command gesture, the second figure shows corresponding command region with respect to the Leap Motion and the third figure shows the interface window. The frame rate of three

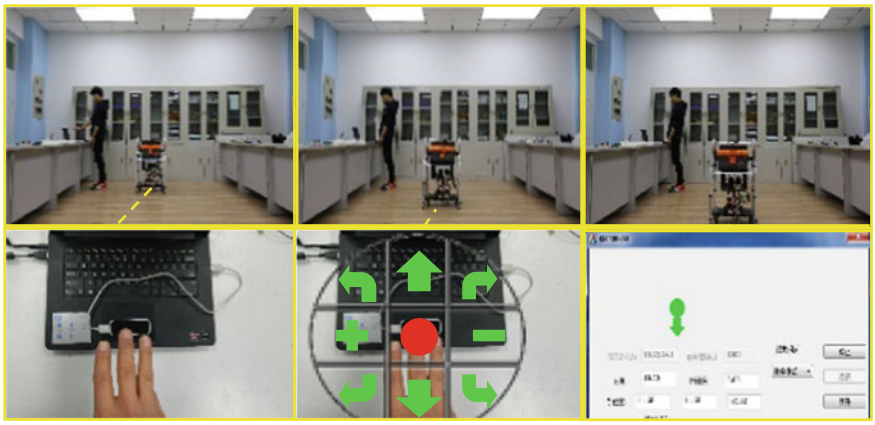

Fig. 7 Draw back command of MTC

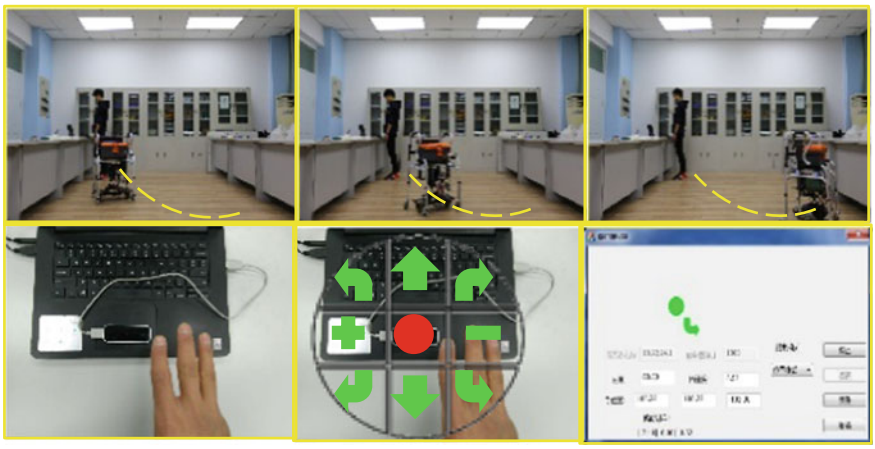

Fig. 8 Turn right command of MTC

cameras of Leap Motion is 290 FPS, the IMTC reaction speed due to the time of completing the gesture and information transmission through Wi-Fi. A single commend could be detected and transmitted within 0.5 s which was also confirmed in the experiment. And the experiment result is summarized in Table 4.

As shown in Table 4, the tester gave IMTC Draw Back command 50 times, the IMTC executed correct operation command 46 times, incorrect operation 2 times and no action 2 times. The accuracy of the Draw Back command is 92%. The tester gave IMTC Turn Right command 50 times, the MTC executed correct operation command 46 times, incorrect operation 3 times and no action 1 time. The accuracy of the Turn Right command is 92%. As demonstrated in Table 2, the IMTC executed correct operation above 90% among seven commands. Based on the experiment results, we can say that IMTC makes responses effectively when receive different commands.

Table 4 Experiment result

No.	Command	Correct	Incorrect	No action	Accuracy (%)
1	Go Forward	47	1	2	94
2	Draw Back	46	2	2	92
3	Turn Left	45	2	3	90
4	Turn Right	46	3	1	92
5	Start/Stop	46	1	3	92
6	Acceleration	46	3	1	92
7	Deceleration	47	2	1	94

5.2 *Experiment 2 (Leap Motion Based Intelligent Mobile Tool Cart Movement Performance Test in a Real Factory Environment)*

Based on the Leap Motion, the performance of the developed Intelligent Mobile Tool Cart was tested in Engineering Research Center of Advanced Manufacturing Technology for Automotive Components, Ministry of Education which is located in Beijing University of Technology. The experiment environment is demonstrated in Fig. 9.

The tester stood in front of the operation platform and the Intelligent Mobile Tool Cart was set at initial position beside the operation platform as shown in Fig. 9. Tester using the proposed hand/finger gesture commands to control IMTC. The IMTC started to move from initial position and arrived at A, B, C, and D position in sequence. When IMTC passed through A, B, C, and D, trajectory of the IMTC was a "S" shape curve which is known as complex path shown in yellow dashed line in Fig. 9. And all the seven hand/finger gesture commands designed in this paper were employed during this trajectory. Figure 10 shows experimentation process in detail. In Fig. 10a–d demonstrate the movement of IMTC from initial position to A position, from A position to B position, from B position to C position, and from C position to D position, respectively. During whole experiment process, the designed hand/finger gesture commands worked sensitively and reliably. And IMTC could accomplish the desired path from initial position to D position steadily. From experiment 2, it is marked that the proposed hand/finger gesture commands could achieve desired function and provide worker with a simple and new working experience.

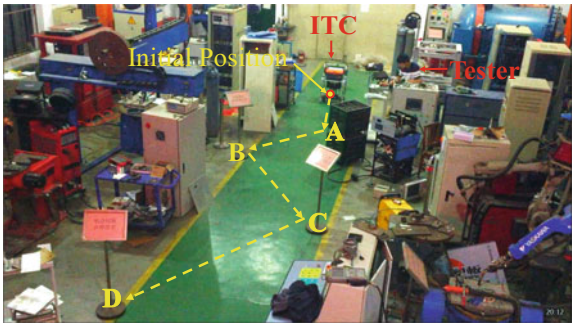

Fig. 9 Experiment 2 environment

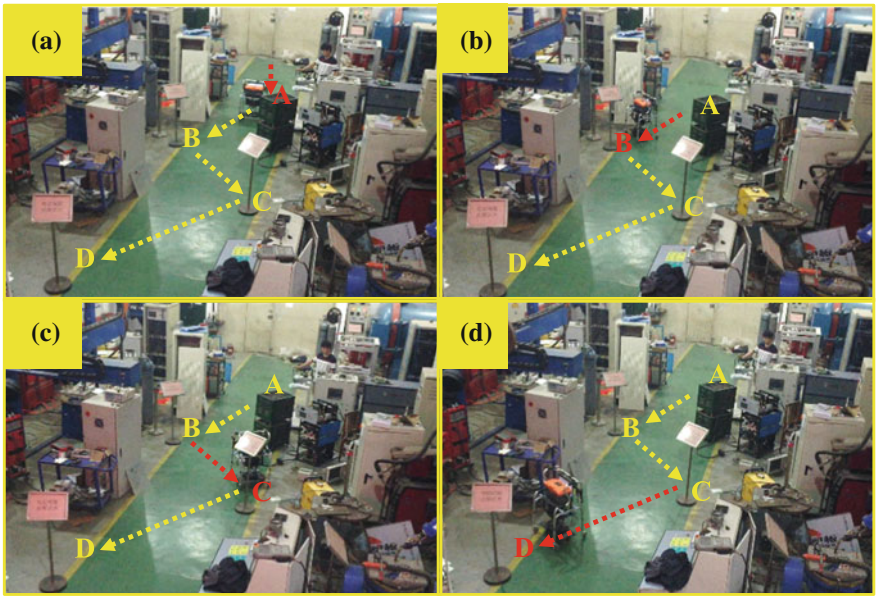

Fig. 10 Demonstration of experiment 2

6 Conclusion

The paper developed a novel intelligent mobile tool cart (IMTC) to move to an advance stage in providing assistance to workers. The worker would be serviced by remote motion control and cart location-recognition services. In this paper, a novel method for reading hand/finger gesture commands using Leap Motion to control a mobile tool cart is proposed and implemented. We achieved the task that IMTC responded to the defined seven gesture commands, such as Go Forward, Draw Back, Turn Left, Turn Right, Start/Stop, Acceleration, and Deceleration successfully. Real industry environment experiment verified stability of the developed IMTC, reliability and sensitivity of the proposed control method. Besides, a QR localization method is proposed and verified to provide real-time location information of the IMTC to the worker. The response time is controlled within 0.5 s. As a conclusion, the proposed IMTC with the proposed remote sensing motion control method and QR localization method achieved anticipated goal of simplifying the working process and providing intelligent service to workers.

References

1. Duan X et al (2007) Development and analysis of miniature wheel-track-legged mobile robot. Chin J Mech Eng 20:24–28
2. Thrun S et al (1999) MINERVA: a second generation mobile tour-guide robot. In: Proceedings of the IEEE international conference on robotics and automation IEEE, vol 3, pp 1999–2005
3. Engelberger JF (1999) Health-care robotics goes commercial: the helpmate experience. Robotica 11:517–523
4. Garingo A, Friedlich P, Tesoriero L et al (2012) The use of mobile robotic tele-medicine technology in the neonatal intensive care unit. J Perinatol 32(1):55–63
5. Lee JH et al (2006) People tracking using a robot in motion with laser range finder. In: Proceedings of IEEE/RSJ conference on intelligent robots and systems, pp 2936–2942
6. Jung EJ et al (2012) Control algorithms for a mobile robot tracking a human in front. In: Proceedings of IEEE/RSJ conference on intelligent robots and systems, pp 2411–2416
7. Gai S et al (2013) Mobile shopping cart application using Kinect. In: Proceedings of IEEE international conference on ubiquitous robots and ambient intelligence, pp 289–291
8. Chen L et al (2014) Stereovision-only based interactive mobile robot for Hu-man-Robot Face-to-Face interaction. In: Proceedings of international conference on pattern recognition, pp 1840–1845
9. Otsuka T, Nakadai K, Takahashi T (2010) Voice-awareness control for a humanoid robot consistent with its body posture and movements. Paladyn 1(1):80–88
10. Noffsinger AA (2004) Foldable tool cart. US Patent 10217225, Aug 2004
11. Mccauley KG (2014) Tool storage and bolt organizer device. US patent 13755679, Feb 2014
12. Lin YH (2016) Cart for storage of tools and parts. US Patent 15144796, Dec 2016

Microstructure and Mechanical Properties of Friction Stir Weld of Dissimilar Ti6Al4V Titanium Alloy to AA2024 Aluminum Alloy

Yuhua Chen, Wenming Cao, Shuhan Li, Chao Chen and Jilin Xie

Abstract Dissimilar Ti6Al4V titanium alloy and AA2024 aluminum alloy sheets with a thickness of 3 mm were friction stir welded successfully, and the microstructure and mechanical properties of the butt joints were investigated. The results show that: the stirred zone (SZ) exhibits a mixture structure, which is characterized by fine recrystallized grains of aluminum alloy and titanium particles. Unfilled defects are observed among titanium particles in SZ. Moreover, at the aluminum side the thermal-mechanically affected zone (TMAZ) and the heat affected zone (HAZ) appeared like in the traditional FSW-joints. But, at the titanium side, a recrystallization band with a width of 6–10 μm and a layer with fibrous structures are found at the joint interface. Also, the Ti–Al compounds layer with some micro-cracks is presented in the fibrous structure. The hardness distribution of the joint along the cross-section centerline varies significantly due to the existence of different broken titanium particles. The ultimate tensile strength (UTS) of the joint reached 83% of aluminum base metal and the joint failed with a ductile–brittle fracture mode.

Keywords Ti/Al dissimilar metals · FSW · Microstructure
Mechanical properties

1 Introduction

Compared with other materials, titanium alloys have many advantages such as low density, high specific strength, and excellent corrosion-resistance, so they are widely used in automotive, aerospace, and ship industries. Aluminum alloys are also attractive in these fields due to their low density and good economic features. In order to meet the special performance requirements for aviation materials,

Y. Chen (✉) · W. Cao · S. Li · C. Chen · J. Xie
School of Aeronautical Manufacturing Engineering, Nanchang Hangkong University, Nanchang, China
e-mail: ch.yu.hu@163.com

S. Chen et al. (eds.), *Transactions on Intelligent Welding Manufacturing*,
Transactions on Intelligent Welding Manufacturing,
https://doi.org/10.1007/978-981-10-7043-3_11

structures with high strength and low weight are widely used. The joining of titanium alloy with aluminum alloy could have a major application in aerospace and automobile industries where high strength and low weight are desirable. However, it is difficult to weld these two alloys because of the great differences in physical, chemical, and metallurgical properties [1–4]. Some welding methods for joining these two materials such as laser and hybrid laser welding [5–8], solid-state diffusion bonding [9, 10], ultrasonic welding [11, 12], as well as explosive welding [13, 14] have been reported.

These studies show that the key issue encountered in welding Al alloys to Ti alloys is the formation of intermetallic compounds in joints. Friction stir welding (FSW) is a novel solid-state welding technology [15]. It is suitable for welding Al alloys to Ti alloys due to the lower temperature and shorter time (compared to the fusion welding process) during the process [16–20].

Although there are a few studies about friction stir welding of Ti/Al dissimilar alloys, the details of the microstructural evolution of dissimilar joints have not been fully understood and the ultimate tensile strength of the joint still cannot meet the industry demand.

In this paper, AA2024 alloy and Ti6Al4V alloy, which are widely used in industries, are welded by FSW. To make a comprehensive analysis of the joining mechanism, the microstructure, intermetallic compounds, hardness distribution, and tensile strength of the dissimilar joints are investigated.

2 Experiment Details

The experiment materials are 3 mm thick of AA2024 alloy and Ti6Al4V alloy plates with the chemical compositions shown in Tables 1 and 2, respectively.

The butt joints were welded using an FSW tool consisting of a threaded pin of 6 mm diameter and a concave shoulder of 18 mm diameter. The welding tool was made from nickel base superalloy. The processing parameters were selected as 700 rpm for tool rotation speed and 60 mm/min for travel speed based on the large number of experiments. A schematic illustration of the dissimilar FSW experiment was shown in Fig. 1. During FSW process, Ti6Al4V and AA2024 were placed at the advancing side (AS) and the retreating side (RS) of the tool pin, respectively. The pin was inserted into the AA2024 aluminum sheet with 2.5 mm offset to the welding line. The weld sections taken perpendicular to the welding direction were polished and etched using different kind of etchant (1% HF + 3% HNO_3 + 5% H_2O to Al and 3% HF + 10% HNO_3 + 87% H_2O to Ti). Polished metallographic cross sections were examined by optical microscopy (OM) and scanning electron

Table 1 Chemical composition of AA2024

Cu	Si	Mn	Mg	Fe	Zn	Ni	Ti	Al
4.3	1.0	0.73	0.55	0.3	0.08	0.02	0.02	Balance

Table 2 Chemical composition of Ti6Al4V

Al	V	Fe	C	N	H	O	Ti
6.0	4.0	0.026	0.015	0.008	0.007	0.06	Balance

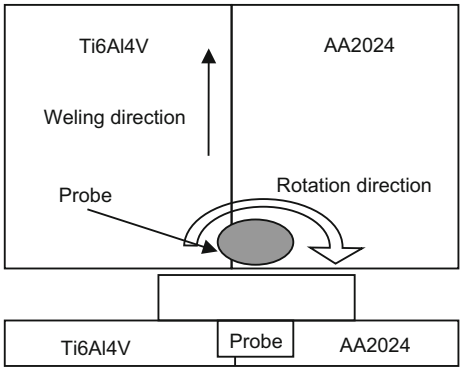

Fig. 1 Schematic illustration showing setup of dissimilar FSW

microscope (SEM) equipped with an EDX system. Hardness tests were done every 500 μm at the center of the section using a Vickers indenter at a load of 0.2 kg. Tensile tests were conducted at a crosshead speed of 1 mm/min.

3 Results and Discussions

3.1 Macrostructure and Microstructure of Dissimilar Joint

Since the hardness and melting point of the Ti6Al4V alloy are higher than those of the AA2024 alloy. In dissimilar FSW, the alumina alloys should have better plastic flowability due to the welding temperature is not enough to plasticizing the Ti6Al4V alloy. By in terms of the pin offset technique, Al–Ti dissimilar joints can be formed. However, it is hard to join the two metals if the pin totally inserted to the alumina with an offset of 3 mm in this study. Figure 2 shows the surface morphology of the dissimilar welded specimen. The surface of the joint is very smooth and covered by a layer of aluminum alloy. Curved key sheaths produced by tool shoulder were not very clear. Figure 3 shows the cross-sectional macrostructure of the dissimilar weld. Because the welding tool was shifted toward the Al alloy, the stir zone (SZ) occurs mainly on the Al side of the joint. The stir zone is composed by Al and Ti, and an onion ring like structure was formed at the bottom of the joint. The interface between the nugget zone and the Ti base metal is not very straight, two hook structures are observed at the top and the bottom of the joint, respectively. They were believed to enhance the joints tensile strength capacity. No pore or other defect can be found in Figs. 2 and 3, indicating that sound joint could be produced with the designated experimental parameters.

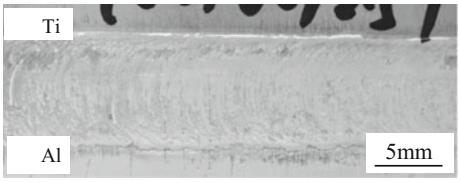

Fig. 2 Appearances of dissimilar joint

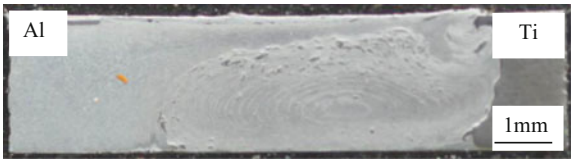

Fig. 3 Cross-section structure of dissimilar joint prepared by FSW

Figure 4 shows the optical microstructures of the dissimilar joint. On the retreating side, there are SZ, TMAZ, and HAZ. While at the advancing side of the joint, there are no obvious SZ, TMAZ, and HAZ, because the melting point of titanium alloy is higher than that of the aluminum alloy. As shown in Fig. 4a, the microstructure of aluminum BM is a typical quenching and nature aging structure which is mainly composed of aluminum matrix and precipitation strengthening phases. Figure 4b shows the microstructure of titanium BM, which is a mixture of α and β phases. Figure 4c shows the microstructures of HAZ and TMAZ in the Al side. No plastic deformation occurred in HAZ, but the grains in HAZ were heated to growing up during FSW. Compared with the microstructures of the BM, it could be seen that the grain shape in HAZ does not change, but the size becomes coarse due to the thermal cycle in the welding process. Meanwhile, grains in the TMAZ show a curved shape, indicating that these grains undergo notable plastic deformation caused by the welding tool. Figure 4d shows the interface between the aluminum alloy and titanium alloy; also it is the interface of stir zone and advancing side. There is a hook structure inserting into the SZ firmly hooking the aluminum substrate. During the welding process, titanium alloy was strongly scratched by the rotation tool. And parts of titanium were separated from the substrate turn to titanium particles flowing with the plastic aluminum; hook structure was the titanium that not separated completely. All means that the titanium at the interface undergoes intensively plastic deformation by the tool. Figure 4e and f show the SZ of the dissimilar joint. Figure 4e is the weld nugget besides the TMAZ in aluminum side. Due to the dynamic recrystallization caused by welding tool, grains in this zone are fine grains and obviously streamlined organization; also part of titanium particles was observed in this area. Figure 4f shows large number of different forms titanium particles embedded in the aluminum alloy matrix, and also with many unfilled flaws between the adjoining titanium particles. The reason for the defects formed is that the gap formed by two particles is too small to be filled by the plastic aluminum alloys during the weld processing. Microstructures in the SZ are very complicated and aluminum grains size in this region is not even, grains besides the particle are smaller than those of far from it. However, they are all smaller than those of the region where no titanium particles exist.

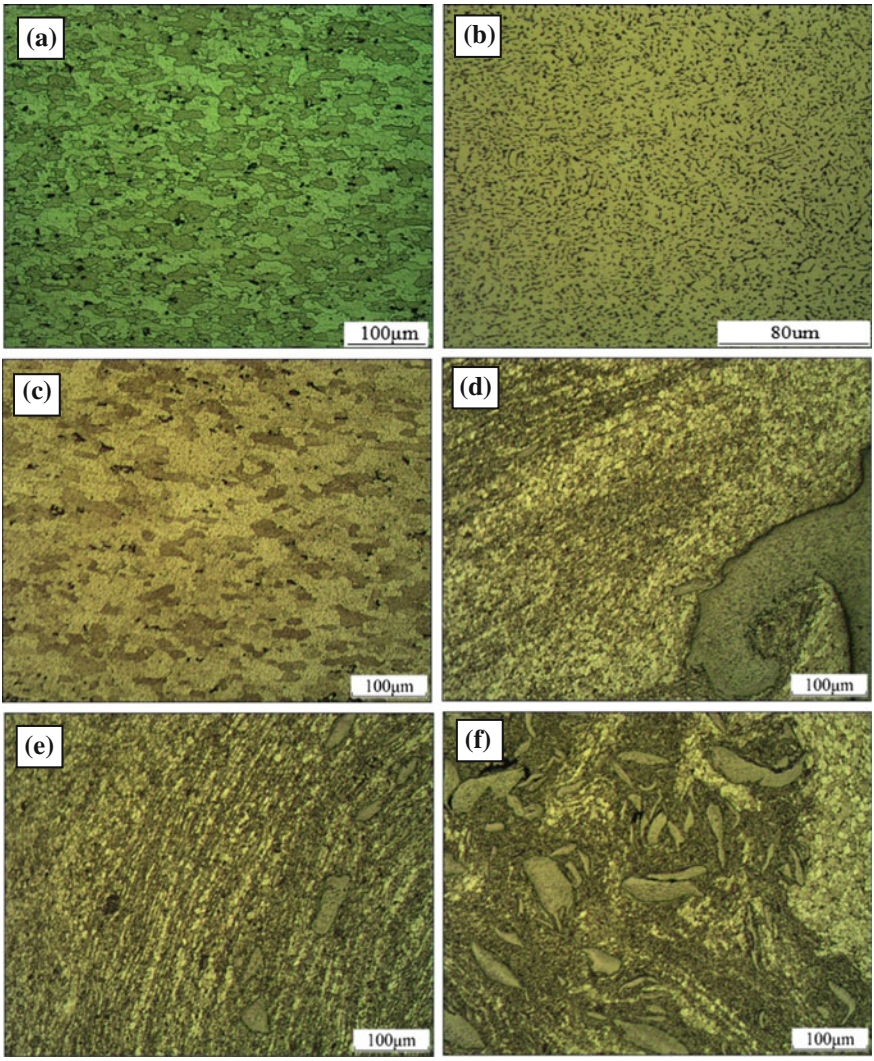

Fig. 4 Optical microstructures of the dissimilar joint: **a** Aluminum base metal; **b** Titanium base metal; **c** HAZ and TMAZ in Al side; **d** interface of Al/Ti; **e** SZ near the Al side; **f** SZ near the Ti side

3.2 Interface Characteristic of Dissimilar Joints

Figures 5a–d is the interface between the stir zone (SZ) and the Ti alloy side. Figure 5e is the EDS test result of area M in Fig. 5c and f is micro-XRD test result. It can be clearly seen from Fig. 5a that there are some titanium particles in the figure, embedded in the aluminum matrix, the dark part, with different size and

shapes. Moreover, the titanium particles present flow patterns with the aluminum alloy matrix. Nevertheless, in Fig. 5a layer of fibrous structure that is not the same as the two parent materials is observed.

This layer is considered to be the diffusion area because the EDS test result and the micro-XRD test result show that Ti–Al components were formed in this area. The EDS test result shows that elements in Ti alloy and elements in Al alloy are

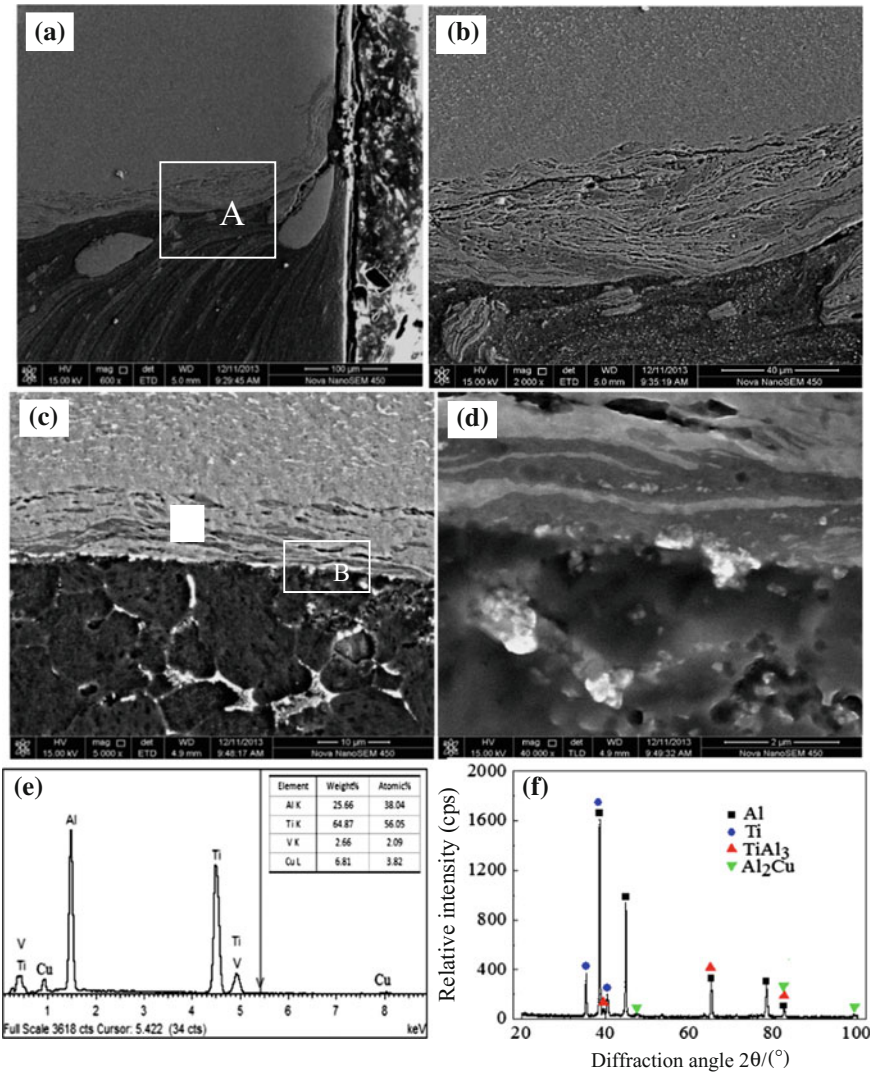

Fig. 5 SEM picture of the joint interface: **a** Upper area of the interface; **b** amplification of zone A in (a); **c** middle area of the interface; **d** amplification of zone B in figure (c); **e** EDS test of zone M in (c); **f** micro-XRD test of interface

diffusion to each other in this area formed intermetallic compounds (IMC) $TiAl_3$ as shown in the micro-XRD test result. Further, amplification of the interface as shown in Fig. 5c, a narrow band adjacent to the fibrous structure is observed in the titanium parent, where the equiaxed primary α and β grains have been elongated.

The width of this band is about 6–10 μm. Disappearance of remaining lamellar structures that have been found in the titanium alloy corroborates recrystallization in the small affected band. The fibrous structure shown in Fig. 5d is a very complicated structure that the titanium alloy and IMC layers appear alternately as lamellar-structure. Besides, some micro-cracks are found in the IMC layers.

3.3 Mechanical Properties of Dissimilar Joints

As shown in Fig. 6, the hardness level continuously amounts to 120 HV0.2 on the aluminum side. A sharp increase to approximately 330 HV0.2 occurs at the Ti/Al transition. Hardness values dramatic changes in the SZ. In spite of the high FSW process temperature, hardness values in the center of the SZ reach 150 HV0.2. Probably, this is a result of grain boundary hardening. Individual higher hardness values (shown point P) occurred in the SZ near the HAZ which occurred when the indenter hit a titanium particle. On that level, the hardness profile is proceeding on the retreating side in principle like in conventional FSW-joints, except, the loss in hardness to aluminum of 90 HV0.2 is caused by the relatively high heat input, which leads to an over-aging effect. The ultimate tensile strength (UTS) of the dissimilar joint is 347 MPa that is representing 83% of the UTS of 2024 base material. Figure 7 shows the fracture location of the dissimilar joint. It can be seen that the fracture location is between the SZ and the aluminum alloy side.

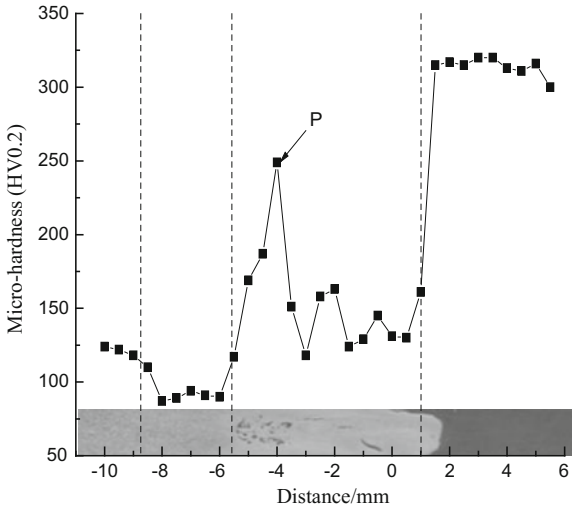

Fig. 6 Micro-hardness distribution of titanium/aluminum FSW joint

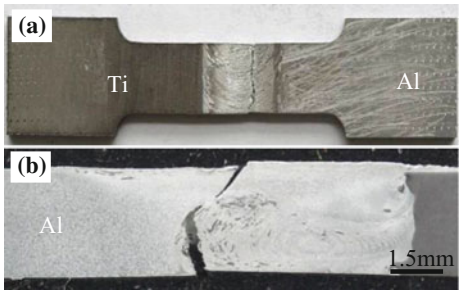

Fig. 7 Specimen after the tensile test: **a** Top surface of tensile specimen; **b** optical image of a cross-section of joint

Furthermore, the failed location was along the 45° direction with respect to the weld specimen surface at the crown, then, turn to about 90° at the bottom. The unfilled defects between the titanium particles as mentioned above were the main reason to explain the fracture direction turned.

Figure 8 illustrates the SEM images of the tensile fracture surface. Figure 8a shows the appearance of tensile fracture and the fracture features vary appreciably with the locations across the weld due to the complex microstructures of the nugget. Figures 8b–d show the magnified micrographs of the fracture surfaces marked in Fig. 8a. As shown in Fig. 8b, flat surface and small dimples can be observed in this region. Intergranular fracture patterns exist in some regions, as shown in Fig. 8c and some cleavage planes can be seen clearly in the region. A large number of dimples with different depth are observed in Fig. 8d, indicating that a ductile fracture has taken place in these regions. Therefore, the fracture mode of the dissimilar joints can be defined as a ductile–brittle mixed fracture.

4 Conclusion

Friction stir welding of Ti6Al4V alloy and AA2024 alloy with a thickness of 3 mm was conducted. The macro/microstructure, the interface characteristic, and the mechanical properties of the dissimilar joint were investigated. The results can be summarized as follows.

1. AA2024 aluminum alloy and Ti6Al4V titanium alloy are joined successfully through FSW with pin offset technique under a rotation speed of 700 r/min and a welding speed of 60 mm/min.
2. TMAZ and HAZ occurred at the aluminum side like in the conventional FSW-joints. Unfilled defects are observed at the SZ. Grains near the titanium particle are smaller than those of far from it. However, they are all smaller than those of the zone where no titanium particles exist.
3. At the titanium side, a recrystallization band with a width of 6–10 μm and a layer of fibrous structure are observed. The Ti–Al compounds layer, including $TiAl_3$, are formed in the fibrous structure, and also some micro-cracks are found in the IMC layers.

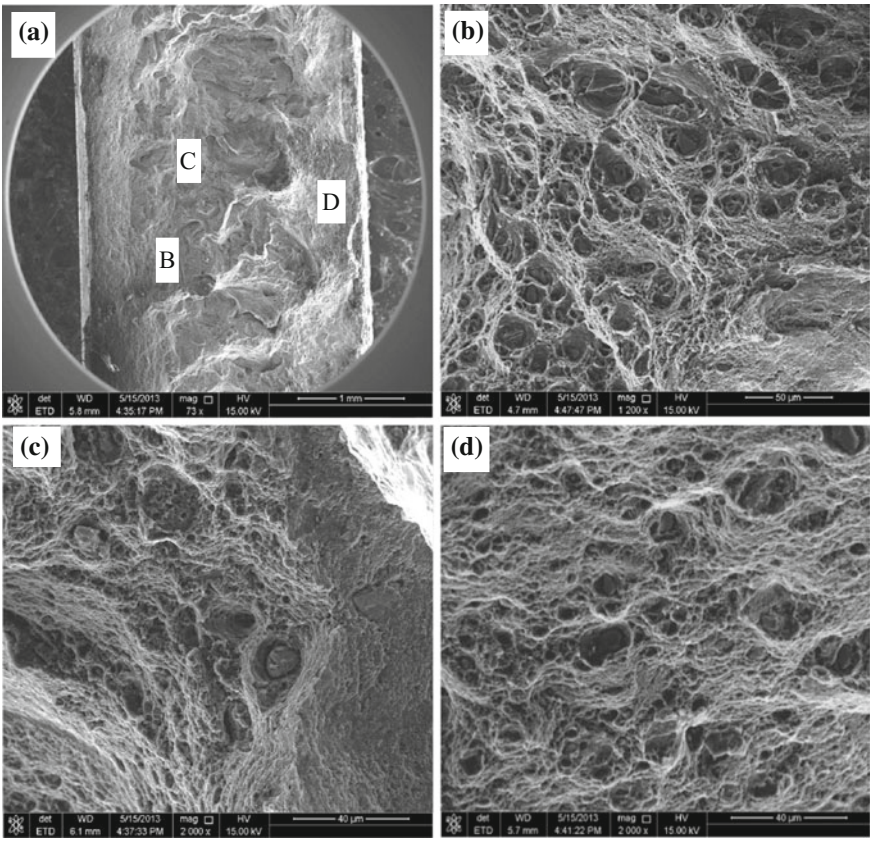

Fig. 8 Fracture surface from titanium alloy side of the joint: **a** Overview of the surface; **b** zone B; **c** zone C; **d** zone D

4. The hardness of the joint is sharply changed. Sudden drop from average hardness of 330 HV at titanium alloy to average hardness of 120 HV at aluminum side. The hardness of the forging organization in the SZ was higher than that of the base metal by 150 HV and the enriched titanium particles regional owns a hardness level peak during the SZ. The average hardness of 90 HV occurred at HAZ. The UTS of the joint is 347 MPa which is 83% of the AA2024 alloy and the joints failed with a ductile–brittle fracture mode.

Acknowledgements The National Natural Science Foundation of China (51265042), the Science and Technology Planning Project of Jiangxi Province (20171BCB24007), and the Natural Science Foundation of Jiangxi Province (20114BAB206006).

References

1. Mishrar RS, Ma ZY (2005) Friction stir welding and processing. Mater Sci Eng R 50:1–78
2. Kenevisi MS, Khoie SMM, Alaei M (2013) Microstructural evaluation and mechanical properties of the diffusion bonded Al/Ti alloys joint. Mech Mater 64(1):69–75
3. Samavatian M, Khodabandeh A, Halvaee A et al (2015) Transient liquid phase bonding of Al 2024 to Ti-6Al-4V alloy using Cu-Zn interlayer. Trans Nonferrous Met Soc China 25(3): 770–775
4. Tomashchuk I, Sallamand P, Cicala E et al (2015) Direct keyhole laser welding of aluminum alloy AA5754 to titanium alloy Ti6Al4V. J Mater Process Technol 217:96–104
5. Chen SH, Li LQ, Chen YB et al (2010) Si diffusion behavior during laser welding-brazing of Al alloy and Ti alloy with Al-12Si filler wire. Trans Nonferrous Met Soc China 20(1):64–70
6. Vaidya WV, Horstmann M, Ventzke V et al (2010) Improving interfacial properties of a laser beam welded dissimilar joint of aluminum AA6056 and titanium Ti6Al4V for aeronautical applications. J Mater Sci 45:6242–6254
7. Song ZH, Kazuhiro N, Wu AP et al (2013) Interfacial microstructure and mechanical property of Ti6Al4V/A6061 dissimilar joint by direct laser brazing without filler metal and groove. Mater Sci Eng A 60:111–120
8. Casalino G, Mortello M, Peyre P (2015) Yb–YAG laser offset welding of AA5754 and T40 butt joint. J Mater Process Technol 223:139–149
9. Yao W, Wu AP, Zou GS (2007) Structure and forming process of the Ti/A1 diffusion bonding joints. Rare Metal Mater Eng 36(4):700–704
10. Chen SH, Li LQ, Chen YB et al (2011) Joining mechanism of Ti/Al dissimilar alloys during laser welding-brazing process. J Alloy Compd 509(3):891–898
11. Zhang CQ, Robson JD, Ciuca O et al (2014) Microstructural characterization and mechanical properties of high power ultrasonic spot welded aluminum alloy AA6111-TiAl6V4 dissimilar joints. Mater Charact 97:83–91
12. Zhu Z, Kang YL, Wang X (2012) Ultrasonic welding of dissimilar metals AA6061 and Ti6Al4V. Int J Adv Manuf Technol 59(5):569–574
13. Xia HB, Wang SG, Ben HF (2014) Microstructure and mechanical properties of Ti/Al explosive cladding. Mater Des 56:1014–1019
14. Samavatian M, Halvaee A, Amadeh AA et al (2014) An investigation on microstructure evolution and mechanical properties during liquid state diffusion bonding of Al2024 to Ti-6Al-4V. Mater Charact 98(13):113–118
15. Thomas WM, Nicholas ED, Needham JC, et al (1991) GB Patent 9125978, 8 December 1991
16. Wu AP, Song ZH, Kazuhiro N et al (2015) Interface and properties of the friction stir welded joints of titanium alloy Ti6Al4V with aluminum alloy 6061. Mater Des 71:85–92
17. Bang HS, Song HJ et al (2013) Joint properties of dissimilar Al6061-T6 aluminum alloy/Ti6%Al4%V titanium alloy by gas tungsten arc welding assisted hybrid friction stir welding. Mater Des 51:544–551
18. Li B, Zhang ZH, Shen YF et al (2014) Dissimilar friction stir welding of Ti–6Al–4V alloy and aluminum alloy employing a modified butt joint configuration: influences of process variables on the weld interfaces and tensile properties. Mater Des 53:838–848
19. Aonuma M, Nakata K (2011) Dissimilar metal joining of 2024 and 7075 aluminum alloys to titanium alloys by friction stir welding. Mater Trans 52(5):948–952
20. Chen YH, Ni Q, Ke LM (2012) Interface characteristic of friction stir welding lap joints of Ti/Al dissimilar alloys. Trans Nonferrous Met Soc China 22(2):299–304

Control of Current Waveform for Pulsed MIG Welding of Aluminum Alloy Sheets

Min Xu and Jiaxiang Xue

Abstract In this chapter, a simplified model of pulsed MIG welding is established and simulated using MATLAB. In addition, the anti-interference of a current waveform is simulated using the adaptive neural network feedforward control. Depending on the "one droplet per pulse" relationship in pulse frequency modulation, faster adjustment of the arc length, compared with the adjustment of the constant current characteristic, is achieved by increasing or decreasing the base time of the average current.

Keywords Aluminum alloy · Power supply for pulsed MIG welding
Adaptive neural network · One droplet per pulse

1 Introduction

The base current is the primary factor for maintaining an arc in the welding process, especially in the control of the low energy input of thin aluminum alloy pulsed MIG welding. To obtain the ideal base current and time, PID control is employed to achieve a steady arc and to not burn through the aluminum alloy sheet [1–3]. The required base current of pulsed welding is the object of this PID control.

M. Xu · J. Xue (✉)
School of Mechanical and Automotive Engineering,
South China University of Technology, Guangzhou, China
e-mail: mejiaxue@scut.edu.cn

S. Chen et al. (eds.), *Transactions on Intelligent Welding Manufacturing*,
Transactions on Intelligent Welding Manufacturing,
https://doi.org/10.1007/978-981-10-7043-3_12

2 PID Modeling and Control Simulation

2.1 Principle of PID Control

In 1922, the use of proportional integral derivative (PID) control [1] in the position control system was proposed by Nicholas Minorsky. The system block diagram is shown in Fig. 1.

The incremental PID control algorithm satisfies the DSP programming requirements and causes less error due to misoperation [2]. Therefore, in this chapter, the control algorithm is adopted; the subroutine flow chart is shown in Fig. 2. The formula is developed according to the following recursive principle:

$$u(k-1) = k_p\left(\text{error}(k-1) + T_I\sum_{j=0}^{k-1}\text{error}(j) + T_D(\text{error}(k-1) - \text{error}(k-2))\right)$$

The incremental PID control algorithm is as follows:

$$\begin{aligned}\Delta u(k) &= u(k) - u(k-1)\\ \Delta u(k) &= k_p(\text{error}(k) - \text{error}(k-1)) + T_I\text{error}(k)\\ &\quad + T_D(\text{error}(k) - 2\text{error}(k-1) + \text{error}(k-2))\end{aligned}$$

Taking into account the limits on word length and the operating speed of the program, the PID control algorithm is combined with the integer operation, but the operation results in error due to a half adjustment. To reduce the rounding error, the method of reducing the value of the coefficient k is proposed. It is worth noting that due to the reluctance of the k value within a certain range in an actual process, appropriate compensation for the remainder of k is needed. The operation process is shown in Fig. 3.

2.2 PID Controller Parameters

To obtain the ideal control effect, the optimal values of k_p, T_I, and T_D in the PID controller algorithm are determined based on a simulation; the simulation waveform

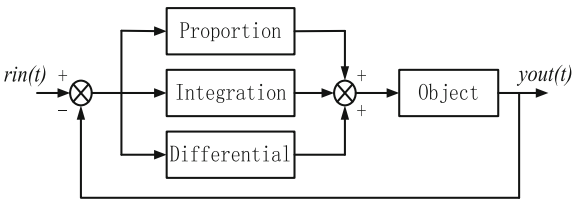

Fig. 1 Schematic diagram of PID control system

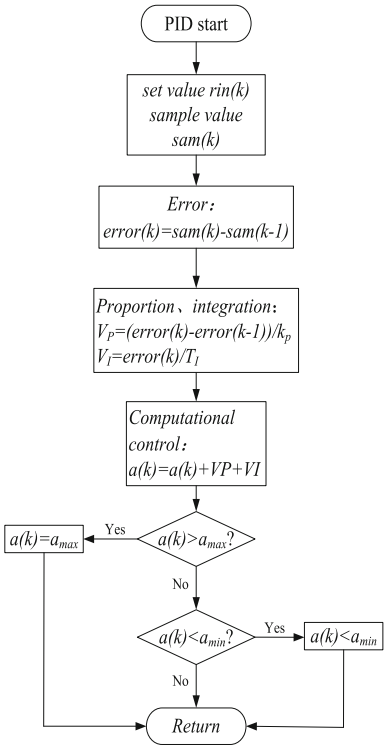

Fig. 2 Flow chart of PID control subroutine

of the pulse is shown in Fig. 4. The transfer function of the aluminum alloy pulsed MIG welding power supply is as follows [3]:

$$G(s) = \frac{1}{s^3 + 6s^2 + 5s}$$

While adjusting k_p, it is found, by comparing (a) and (b) in Fig. 5, that the smaller the value of k_p is, the less the number of shock waves is; hence, the best value of k_p to achieve the maximum output current is 2.2.

Mere adjustment of the k_p cannot lead to the desired outcome; therefore, the T_I value must be regulated after the k_p is determined. Figure 6 shows that the greater the value of T_I is, the smoother the waveform is and that the overshoot phenomenon eased significantly when k_p = 2.2, T_I = 3.

Finally, after the k_p and T_I values settle, the differential time T_D is employed to avoid the overshoot. Comparing the different results, T_D = 20 is determined to be the best T_D parameter, as shown in Fig. 7. To sum up, the best PID parameters suitable for this chapter are k_p = 2.2, T_I = 3, and T_D = 20.

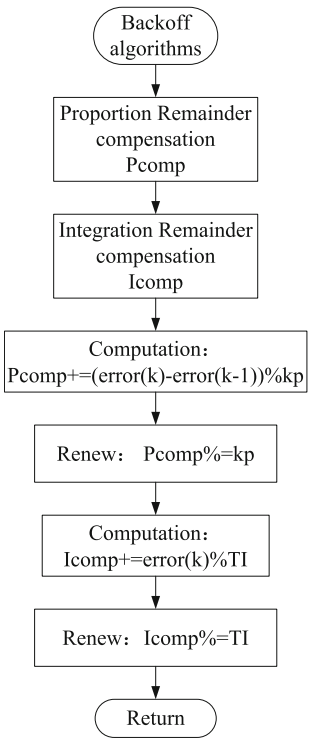

Fig. 3 Proportional and integral remainder error complement

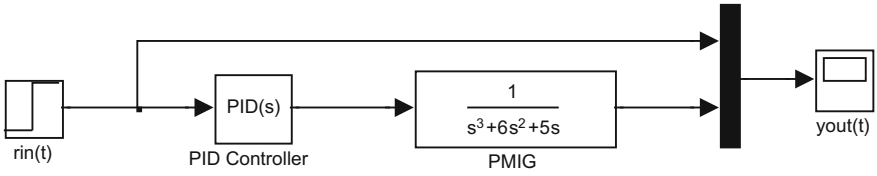

Fig. 4 PID controller parameter regulation simulation model

3 Anti-disturbance Control

The aluminum alloy pulsed MIG welding power supply is a piece of electrical equipment that combines strong and weak current; hence, there are multiple sources of interference, including the electromagnetic fields, the power grids, and the chip itself. The disturbance of the current signal, which is the foundation of the control, can be caused by the above sources of interference. Therefore, the suppression of interference signals is necessary in thin aluminum alloy pulsed MIG welding [4].

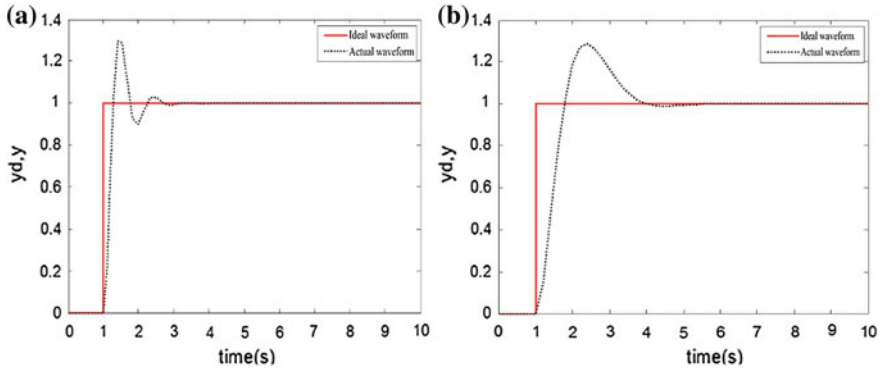

Fig. 5 k_p simulation diagram: **a** $k_p = 10$; **b** $k_p = 3$

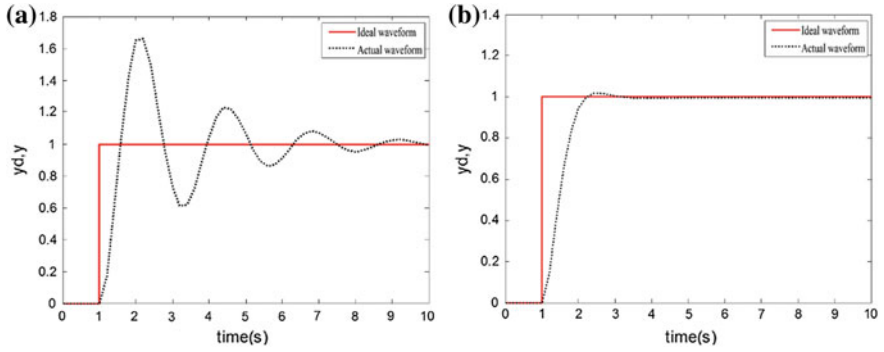

Fig. 6 T_I simulation diagram: **a** $T_I = 10$; **b** $T_I = 4$

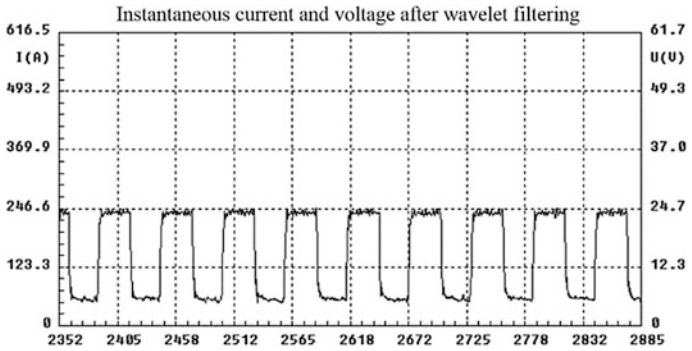

Fig. 7 Current output waveform corresponding to the best PID parameters

The traditional feedforward controller is based on the size and direction of the interference and is controlled by the interference so that the original object does not deviate [5].

According to Hecht Nielsen, the artificial neural network (ANN) is a large-scale nonlinear adaptive system composed of a number of processing units through a certain interconnection [6]. The artificial neural network can be used to address questions in cases with unknown background knowledge and inference rules because an ANN can offer distributed storage, parallel processing, self-learning, self-organizing, and adaptive nonlinear dynamic systems [7]. Therefore, in this chapter, the artificial neural network is used to replace the traditional feedforward compensator for feedforward control. The control structure model is shown in Fig. 8.

The pulsed MIG welding power supply of an alloy sheet [8] is equivalent to

$$M\dot{q} + F(q, \dot{q}) = u, \quad y = q + d$$

where M is the unknown system inertia, Q is the ideal output, that is, the external factors caused by the interference, D is the interference of the output of the system, u is the input of the system, and y is the output of the system.

The tracking error is expressed as $e_v = \dot{e} + \lambda_c e$ ($\lambda_c > 0$, a scalar), and the formulation can be expressed as:

$$\begin{aligned} M\dot{e}_v &= M\ddot{e} + M\lambda_c\dot{e} \\ &= F(q, \dot{q}) - u + M\ddot{q}_d + M\lambda_c\dot{e} - M\ddot{d} \end{aligned}$$

Hypothesis 1: Nominal control can guarantee the asymptotic convergence of the tracking error e_v, that is, the Lyapunov function

$$V_1(e_v) = \frac{1}{2}Me_v^2$$

Hypothesis 2: The optimal weight W_1 is specified on the compact set and is calculated by solving

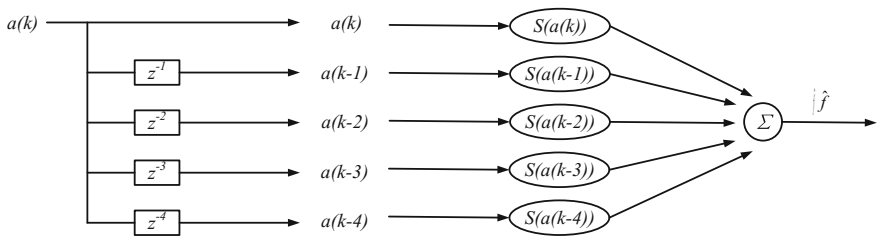

Fig. 8 Neural network compensation structure

$$\begin{aligned} M\dot{e}_v &= F(q,\dot{q}) - u_{\text{nominal}} + \hat{w}^T\Phi(x) + M\ddot{q}_d + M\lambda_c\dot{e} - H(x) - \Delta\phi_1 \\ &= F(q,\dot{q}) - u_{\text{nominal}} + M\ddot{q}_d + M\lambda_c\dot{e} - \bar{w}^T\Phi(x) - \Delta\phi_1 - \Delta\phi_2 \end{aligned}$$

The weight estimation error is $\bar{w} = w - \hat{w}$. The corrected adaptive law [9–12], based on the parameter w, is as follows:

$$\dot{\hat{w}} = -\Gamma\Phi(x)e_v - \sigma\Gamma|e_v|\hat{w}$$

where $\Gamma > 0$ is the gain matrix; $\sigma > 0$ is a scalar parameter.

Theorem *Considering the control law, the parameter update method, and the tracking error, and taking the Lyapunov equation into account, the following calculation can be obtained:*

$$V = \frac{1}{2}Me_v^2 + \frac{1}{2}\bar{w}^T\Gamma^{-1}\bar{w}$$

$$|e| \le \frac{\varepsilon_1 + \varepsilon_2 + \frac{\sigma}{4}M^{*2}}{Q\lambda_c}$$

It can be seen that the system is stable.

4 Simulation Results and Analysis

The external disturbance transfer function is as follows:

$$D(s) = \frac{3.757 \times 10^{-6}s^3 + 0.3077s^2 + 1.381 \times 10^4 s + 8.374 \times 10^8}{s^3 + 1885s^2 + 1.777 \times 10^6 s + 8.374 \times 10^8}$$

The ideal waveform is selected as $q_d = 0, \dot{q}_d = 0, \ddot{q}_d = 0$. The external vibration ω = 0.2sin500t is introduced at t = 0. The simulation uses the integral step t_s = 1, and its initial condition is that the nominal controller is PID controller 2. The structure of the controller is as follows:

$$u = u_{\text{nominal}} - w^{\text{T}}\Phi(a(k), a(k-1), a(k-2), a(k-3), a(k-4))$$

Among them, $w = [\,w_1 \quad w_2 \quad w_3 \quad w_4 \quad w_5\,]^{\text{T}}$, the basis function is $S(x)$ = 1.18/(1 + e − x), and the network basis function is

$$\begin{aligned} &\Phi(a(k), a(k-1), a(k-2), a(k-3), a(k-4)) \\ &= [S(a(k), a(k-1), a(k-2), a(k-3), a(k-4))]^{\text{T}} \end{aligned}$$

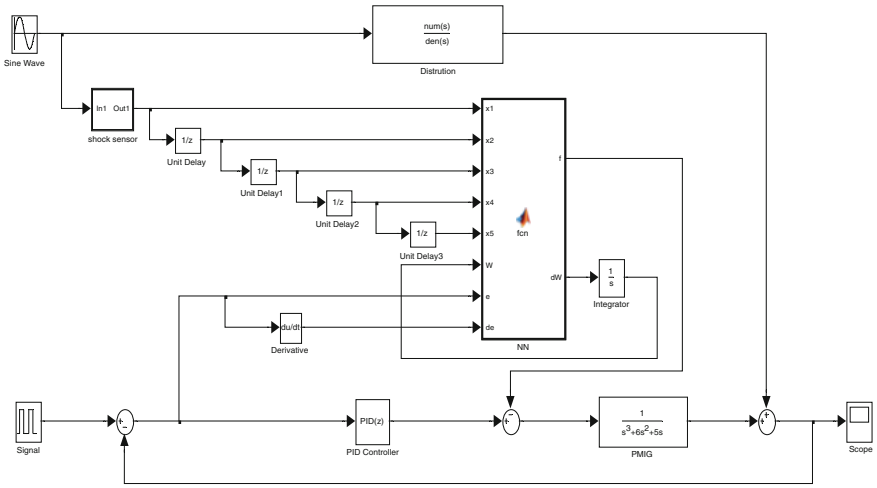

Fig. 9 Simulation of adaptive neural network feedforward control based on e correction

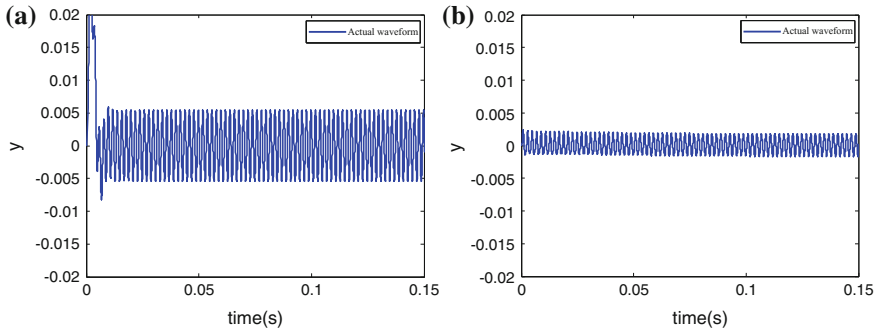

Fig. 10 Comparison of simulation waveforms: **a** Waveform with external disturbance. **b** Waveform diagram of adaptive neural network feedforward control based on e correction method

The tracking error expression $e_v = \dot{e} + \lambda_c e$, the feedforward input $f = w^{\mathrm{T}}\Phi(x)$ and the modified adaptive law are all included in the function module. The algorithm is built within the Simulink environment, as shown in Fig. 9.

According to the simulation model established above and the data in Fig. 9, the comparison diagram of the waveform in Fig. 10 can be obtained. The results show that the feedforward control method of the adaptive neural network based on e correction can effectively suppress the interference by more than 50%.

To facilitate the simulation and description, the current value of the DSP is compared after A/D conversion, as shown in Fig. 11. Figure 11a shows that the high-frequency fluctuation waveform is similar to a sawtooth wave, while Fig. 11b

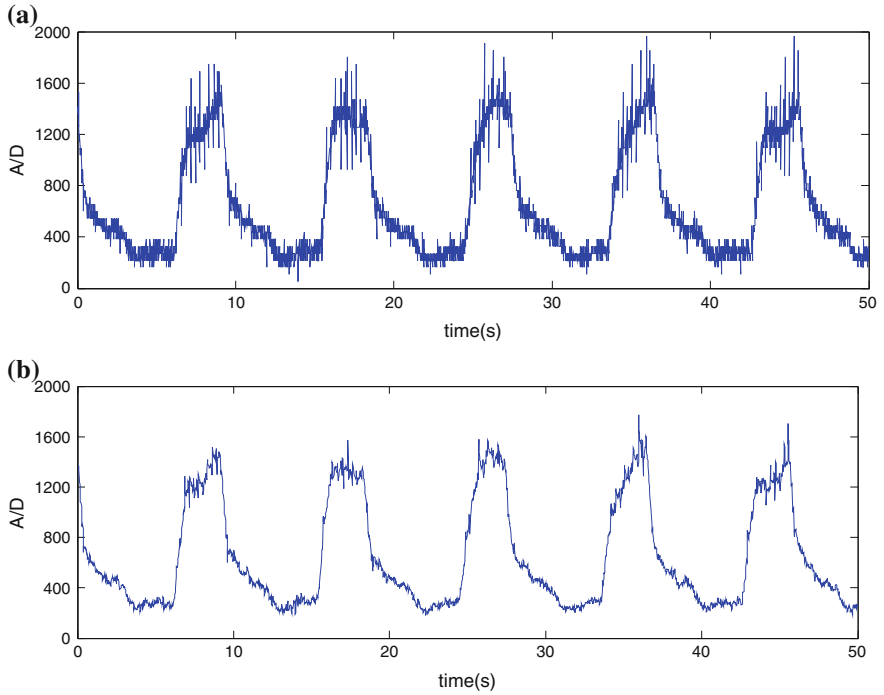

Fig. 11 Comparison of current waveform: **a** Actual waveform. **b** Waveform of adaptive neural network feedforward control based on modified *e* method

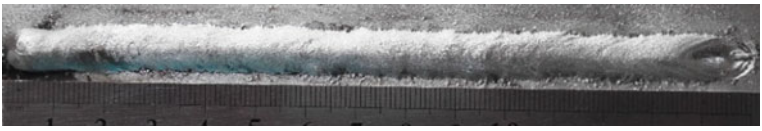

Fig. 12 Single pulse welding experiment

shows the anti-jamming waveform with adaptive neural network feedforward control based on modified *e* method. Results indicates that the feedforward control method of the adaptive neural network based on e correction can effectively suppress the interference.

The single pulse welding experiment was carried out using the above anti-interference control. The experimental parameters were as follows: the pulse peak current I_p = 240 A, the peak time t_p = 3 ms, the pulse base current I_b = 53 A, the base value time t_b = 12 ms, and a welding speed of 0.5 m/min. Figure 12 shows the weld appearance by single pulsed welding with the proposed control algorithm. Results indicates that the proposed control algorithm can be used to obtain high quality welds.

5 Conclusion

1. Based on the modeling and simulation of PID control, the optimal parameters are determined to be $k_p = 2.2$, integral time constant $T_I = 3$, and differential time constant $T_D = 20$. Furthermore, the current value of the DSP is processed for anti-jamming using a combination of the optimal PID controller and the adaptive neural network e correction method of feedforward control.
2. Pulse frequency modulation is employed in the process of welding arc length adjustment, which returns the arc length back to its original length faster than controlled variation of the external characteristics of the constant current.

References

1. Morimoto K, Doi T, Manabe H et al (2006) Advanced high power DC-DC converter using a novel type voltage source full-bridge soft-switching PWM inverter with high frequency transformer link for arc welding applications. IEEE Trans Ind Appl 126(3):237–247
2. Liu JK (2016) Advanced PID control MATLAB simulation, 4th edn. Publishing House of Electronics Industry, Beijing
3. Liao TF (2016) Study on waveform modulation method and process mechanism of double pulse MIG welding of aluminum alloy. Dissertation, South China University of Technology
4. Wei ZH (2012) Research on current waveform regulation of sinusoid modulated pulse MIG welding in aluminum alloy and expert system. Dissertation, South China University of Technology
5. Yao P (2012) Intelligent control strategy and process performance evaluation method for integrated twin wire arc welding power source. Dissertation, South China University of Technology
6. Wen D, Dong L (2009) MATLAB simulation of process control system. China Machine Press, Beijing
7. Zhao L (2015) Artificial neural network technology and its application. Electron Technol Softw Eng 2015(2):29–29
8. Liu XY, Liu H (2008) Artificial neural network and particle swarm optimization. Beijing University of Posts and Telecommunications Press, Beijing
9. Ren X, Lewis FL, Zhang J et al (2009) Feedforward control based on neural networks for hard disk drives. IEEE Trans Magn 45(7):3025–3030
10. Huang Y, Na J, Wu X et al (2015) Adaptive control of nonlinear uncertain active suspension systems with prescribed performance. ISA Trans 54:145–155
11. Li G, Na J, Stoten DP et al (2014) Adaptive feedforward control for dynamically substructured systems based on neural network compensation. IEEE Trans Control Syst Technol 22(3):944–954
12. Na J, Chen Q, Ren X et al (2014) Adaptive prescribed performance motion control of servo mechanisms with friction compensation. IEEE Trans Industr Electron 61(1):486–494

Part III
Short Papers and Technical Notes

Study of Ultrasonic Phased Array in Underwater Welding

Jianxiong Ye, Zhigang Li, Xingling Peng, Jinlan Zhou and Bo Guo

Abstract The popular sensors used in water have a lot of difficulties when compared with those used in land welding automation. It is meaningful to find a new kind of sensor which is suitable to work in underwater welding. Ultrasonic phased array (PA) can work in water conveniently and send out required sound beam. Compared with single-ultrasonic sensor, PA works faster and effectively. In this chapter, interference principle of acoustic beam is analyzed first. Then, the relationship of focusing precision, PA shape, gap distance between adjacent units, sensor element number, and time resolution is revealed with simulation. Proper physical parameters of PA are determined. At last, high time resolution circuit based on complex programmable logic device (CPLD) is given out. It works together with sound-emitting and -receiving circuits to realize fast scan on welding workpiece, so that the seam line can be deduced with underwater distance detection.

Keywords Underwater welding · Ultrasonic phased array · Sound interference Circuit design

1 Introduction

Ocean plays a significant role in keeping sustainable development of our world, so wet welding technology is becoming more and more important with the continuous increase of marine engineering. The wet welding studies are mainly focused on welding method, welding stability, and welding material, Gao et al. [1] studied underwater friction stud welding. Mori et al. [2] studied underwater explosive welding of tungsten. Hu et al. [3] studied the arc stability of wet manual welding.

J. Ye (✉) · X. Peng · J. Zhou · B. Guo
Jiangxi Province Key Laboratory of Precision Drive & Control,
Nanchang Institute of Technology, Nanchang, China
e-mail: jxlpyjx@163.com

Z. Li
School of Mechanics Engineering, East China Jiao Tong University, Nanchang, China

S. Chen et al. (eds.), *Transactions on Intelligent Welding Manufacturing*,
Transactions on Intelligent Welding Manufacturing,
https://doi.org/10.1007/978-981-10-7043-3_13

Mazzaferro and Machado [4] studied arc stability in underwater shielded metal arc welding at shallow depths. Guo et al. [5, 6] studied metal transfer at shallow water. As for wet welding automation, the biggest problem lies in that almost all the sensors are hard to work in water. It is well known that the popular welding sensors are charge-coupled device (CCD) cameras and rotating arc sensors [7, 8], but both are unsuitable for wet welding. For the cameras, they must be sealed in a transparent box to prevent water, and auxiliary illuminator is always needed for intensifying illumination. Besides these, images are influenced inevitably by arc lights, vapor bubbles, and substance suspending in water. Regarding the rotating arc sensors, they cannot work directly in water either. How to confirm the electric motor to run reliably in water is a big problem to be solved first. Another problem is that the length of welding arc is affected by water pressure markedly. The arc length shortens and the arc width attenuates while the water pressure increases. If the pressure becomes big enough, the welding arc may be extinguished.

Because welding automation is based on high-performance sensor, it is imperative to look for a new one for wet welding. Previous research indicates that ultrasonic sensor can work directly in water, and sound beam is insensitive to arc light and steam vapor [9]. In addition, precise distance detection between workpiece and sensor has been fulfilled in water with ultrasonic sensor by means of cross-correlation [10–12]. Based on these, ultrasonic phased array (PA) is introduced in our work. PA consists of tens or even hundreds small units. These tiny parts may also be called transducers or units, and often be arranged in line, in circle, or other specific shapes. All the units can be driven separately, so the sound beam may be focused on the expected positions quickly and conveniently without any mechanical movements. The form of workpiece can be obtained by way of distance detection. It is clear that PA is much more flexible and effective than single-ultrasonic sensor in wet welding.

The rest of this chapter is arranged as follows. Section 2 introduces Huygens' principle which points out the requirements of how to get steady sound wave interference, and then, by help of software simulation, the proper physical parameters of PA sensor are determined, including the shape, the number of units, and the gap distance between adjacent elements. Section 3 introduces electric circuits which are designed for producing high-resolution time sequence, generating excitation signal, sending sound wave, and receiving sound wave.

2 Physical Parameter Determination of PA

PA is constructed by a set of small transducers with different shape and size. Acoustic waves are emitted from these small units and interact with each other in water. To confirm multi-waves focused on a specific point (generally speaking, this point is on the surface of workpiece), the beams must meet some conditions. According to Huygens' principle, the waves should have the same frequency and stable phase difference. The synthetic wave has the biggest amplitude when the

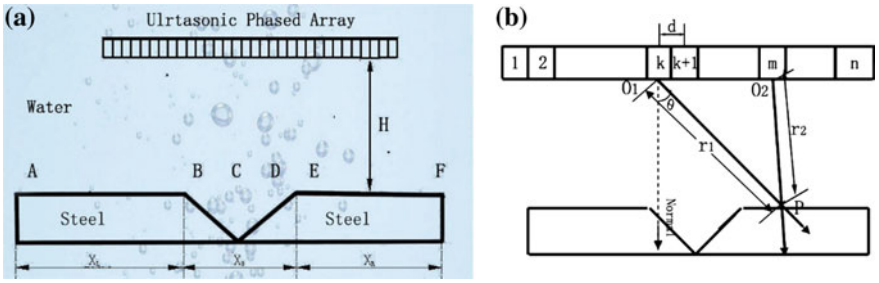

Fig. 1 Ultrasonic PA working method in wet welding

phase difference is an even multiple of π(180°), whereas it has the smallest amplitude when the phase difference is an odd multiple of π(180°). Then, the magnitude of the displacement of the summed waves is between the minimum and maximum values. As shown in Fig. 1a, PA is fixed above the welding material about 30 cm in water. Acoustic beams are sent out from the selected units with the same frequency at different moments according to the designed programs, so as to be focused exactly on the surface of workpiece in a line which is perpendicular to welding seam. By way of distance detection between PA and these convergences, material topography can be figured out and welding center for V-groove can be derived out. Compared with those of single-ultrasonic sensor, the detection speed and accuracy of PA can be improved greatly due to high working frequency and mechanical movement elimination.

The physical size of PA, the number of transducers, and the clearance between units have great effects on the focusing result. As described in Fig. 1b, let the beam be focused on the point P. The time interval between the elements O_1 and O_2 can be calculated out according to Cosine Theorem:

$$\begin{aligned} r_2^2 &= r_1^2 + [(m-k)d]^2 - 2r_1(m-k)d\,\cos\left(\frac{\pi}{2} - \theta\right) \\ &= r_1^2 + (id)^2 - 2r_1 id\,\sin\theta. \end{aligned} \tag{1}$$

From Eq. (1), time delay can be reasoned out as follows:

$$\Delta T_i = \Delta s/C = (r_1 - r_2)/C = \frac{r_1}{C}\left\{1 - \left[1 + \left(\frac{id}{r_1}\right)^2 - \frac{2id\,\sin\theta}{r_1}\right]^{\frac{1}{2}}\right\}, \tag{2}$$

where Δs is the difference of r_1 and r_2, C means the sound travel speed in water, and d is the interval spacing of adjacent units.

On the basis of Eq. (2), ArrayCalc is used to compute the interference patterns with a graphical method. In this software, individual array elements can be placed in 3D locations and orientations using a global coordinate system. A sphere centered on the global axis origin is the surface over which the array patterns are

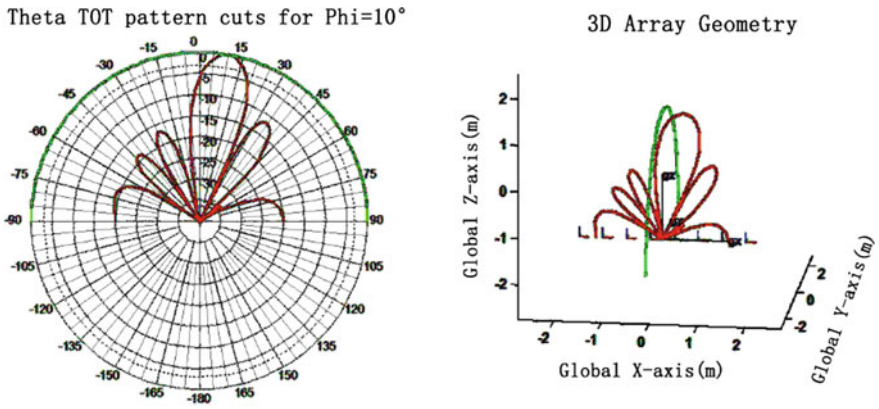

Fig. 2 PA focusing and deflection results

calculated. For a linear PA with eight elements, Fig. 2 gives out the interference results in 2D and 3D array geometry when the main lobe has a flexion of 10°.

Linear PA is selected here for wet welding, because this kind of PA is convenient to form a series of linear focusing points on workpiece surface than other shapes. Comparison tests are conducted to reveal the relationship between focusing precision and unit number with ArrayCalc which calculates the distance and direction from each element to the appropriate points on the surface and sums the field contributions to the interference patterns. For two different linear PAs with eight elements and 16 elements, besides 0.2 μs time resolution, other parameters are set as $b = 2$ mm and $d = 3$ mm. The focusing results are shown in Fig. 3.

More tests are carried out and some results are given out in Table 1. It is clear that more elements lead to better focusing accuracy, result in more converging strength, so concentrate more energy in main lobe. But in the meantime, more elements mean more channels, which can make circuits complicated and PCB board large.

At last, further research is carried out on relationship of time resolution and focusing accuracy. Beam deflection and focalization depend on time delay sequence. Erhard et al. [13] have pointed out that time quantizing error leads to discrete side lobe, which means energy expansion. The percentage of side lobe to main lobe can be expressed as [13]

$$S = \left(\frac{1 - \sin\frac{c}{\mu}}{N \sin\frac{c}{\mu}}\right)^{1/2} \approx \frac{\pi}{\mu(6N)^{1/2}}, \quad \mu \gg 1, \tag{3}$$

where N stands for the number of elements and μ is the ratio of pulse period time to minus quantized delay time. Small S value means better power concentration and high focusing precision. For a certain N, desired S can be achieved by increasing μ. In our study, the time delay is realized by hardware; that is to say, complex devices

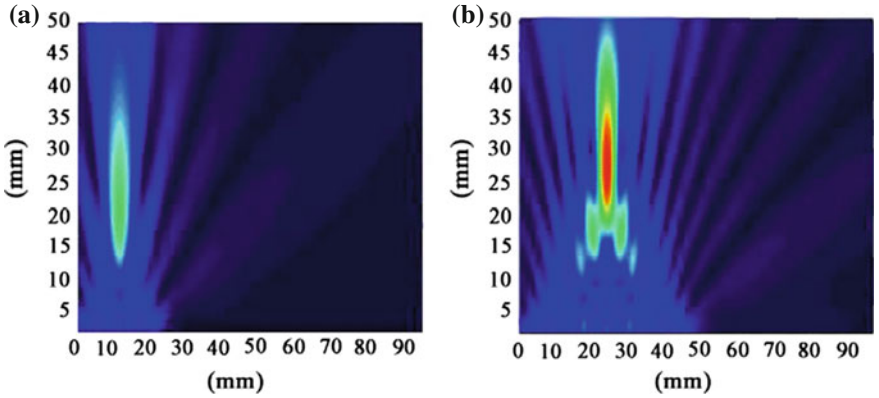

Fig. 3 Relationship between the number of PA units and the focusing precision eight elements, 16 elements

Table 1 Focusing accuracy under various number of elements

Element number	Ideal focusing point (mm, mm)	Real focusing point (mm, mm)	Mean square error (mm^2)
4	(5.5, 30)	(5.2, 16)	98.045
8	(11.5, 30)	(11.1, 20)	50.080
16	(23.5, 30)	(23.3, 27)	4.520
24	(32, 30)	(31.8, 28)	2.020
32	(47.5, 30)	(47.5, 29)	0.500

Table 2 Working parameters of PA

Number of elements	Center frequency (MHz)	Excitation voltage (V)	Gap of elements (mm)	Width of elements (mm)	Thickness of elements (mm)	Height of elements (mm)
16	2	120	1.7	1.5	1.1	10

are needed for high time resolution. Therefore, it is important to get the balance between circuit performance and focusing precision.

As for the working parameters of PA, sound propagation speed in water is roughly 1340 m/s, focal length is no more than 50 cm, and the minimum time interval is about 40 ns. It is proper to use a linear ultrasonic PA with parameters shown in Table 2.

3 Design of Electric Circuit

Besides generating and amplifying actuating signals, electric circuit is used to drive transducers according to specific time sequence, so that the sound beam can be sent out and echo can be sampled. The distance between PA and welding piece can be figured out by way of cross-correlation. The circuit used here can be divided into several parts, including control circuit, time delay sequence generator, stimulating signal amplifier, data acquisition unit, band-pass filter, wave sender and receiver, etc. It can be seen from Fig. 4 that control circuit contains 16 separate channels. Each channel has a triple-input control gate implemented by 74HCT11, which works in "AND" logic. Only when start, excitation signal and sequential signal are all in effective state simultaneously, the driven channel can become active, and the sound wave is emitted out.

Complex programmable logic device (CPLD), EPM1270144C5, provides high time resolution with a high-speed timer. It integrates 1270 logic units, 980 macro units, 212 users defined I/O pin, and 8192 bytes of flash memory in a single chip [14]. The steps for triggering each channel can be described as follows.

- Time values are sent to serial communication input buffer of CPLD from computer. The buffer is 8-bit long, and will be saved in turn to the registers of 16 transducers.
- A hardware accumulator starts to operate and compare the sum value with stored time. Time delay signal is sent out once the value matches.
- 74HCT11 is a high-speed controller with three input gates, i.e., sync signal ("start"), time delay signal (out1, out2, …), and actuating signal. Only when all the input signals are effective, the transducers can be driven.

PA is about 30 cm high above the welding piece. According to Eq. (2), the needed least delay time is 26.97 ns, and the max time is 1799.69 ns. By selecting

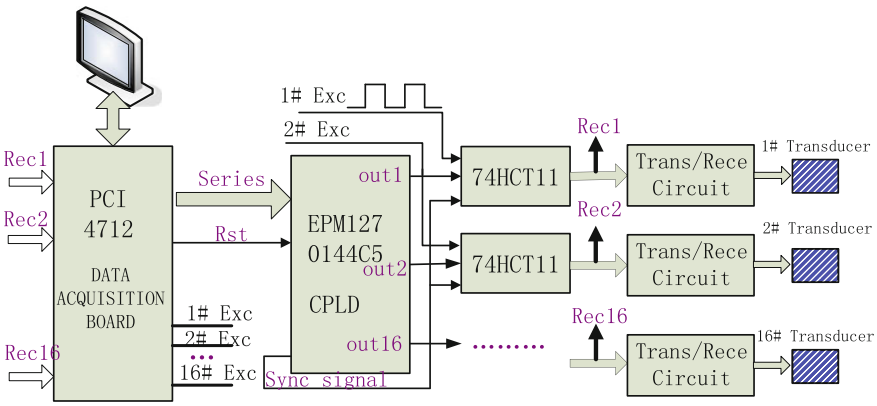

Fig. 4 Structure of control circuit

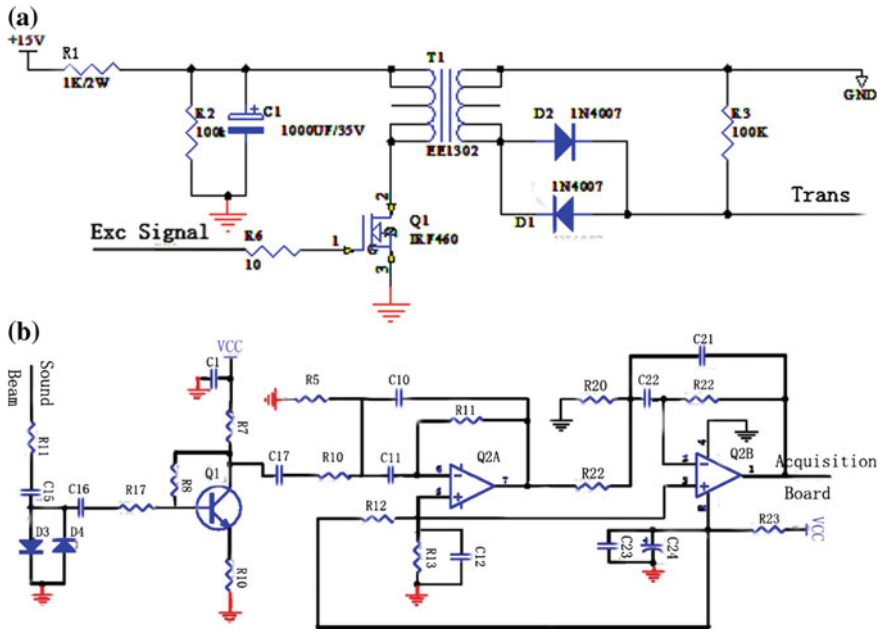

Fig. 5 Sound wave-emitting and receiving circuit

an 8-bit accumulator working at 100 MHz clock frequency, minimum 10 ns time delay and 2550 ns max delay can be attained with CPLD device, so this circuit can meet the resolution demand completely. But it should be mentioned that the initial time for each channel should be exactly same, and the wave frequency and original phase should be equal. To fulfill these requirements, high-frequency synchronization pulses are sent out from CPLD to ensure all the channels having the same original moment. Owing to the same inherent lag characteristic of channels, it can be guaranteed that the initial time for all the channels is entirely simultaneous.

Figure 5a is an emitting circuit. The exciting signal is amplified by the high-frequency transfer EE1302. The voltage can be risen to 130 V. The receiving circuit is shown in Fig. 5b. Echo waves are picked up by transducers, and then be enlarged by NPN9013. After that, they are adjusted by a band-pass filter which is constructed mainly by M33078. At last, the treated signal is provided to the data acquisition board PCI4712 for further processing.

4 Conclusion

In all, PA detects the distance by way of sound beam focusing. Its precision is mainly influenced by element number, element gap, and time resolution. Some conclusions can be drawn according to our study.

The focusing precision is closely related to the PA physical parameters and the number of elements. More elements lead to high accuracy.

The interferometry phase relies on the accuracy of delay time which is determined by time resolution, so the focusing precision is also related to time resolution.

High working frequency is useful for improving time resolution, which can be achieved with circuit based on CPLD in our research.

Further studies have carried out for PA to work as a sensor in wet welding. Results indicate that it can work in water conveniently, and the advantage of this sensor is remarkable.

Acknowledgements This work is supported by Science & Technology Project of Jiangxi Department of Education (GJJ151129), the National Natural Science Foundation of China (51665016), the Jiangxi Province Science Foundation (20151BAB207047), and the Open Project Program of Jiangxi Province Key Laboratory of Precision Drive & Control (PLPDC-KFKT-201625).

References

1. Gao H, Jiao XD, Zhou CF et al (2014) Study on simulation of underwater friction stud welding process based on Abaqus. Trans China Weld Inst 35(12):50–54
2. Mori D, Kasada R, Konishia S et al (2014) Underwater explosive welding of tungsten to reduced-activation ferritic steel F82H. Fusion Eng Des 89(7–8):1086–1090
3. Hu JK, Wu CS, Jia CB (2013) Welding process stability evaluation of underwater wet manual metal arc welding. Trans China Weld Inst 34(5):99–102
4. Mazzaferro JA, Machado IG (2009) Study of arc stability in underwater shielded metal arc welding at shallow depths. J Mech Eng Sci 233(3):699–709
5. Guo N, Guo W, Du YP et al (2015) Effect of boric acid on metal transfer mode of underwater flux-cored wire wet welding. J Mater Process Technol 223(9):124–128
6. Guo N, Wang MR, Du YP et al (2015) Metal transfer in underwater flux-cored wire wet welding at shallow water depth. Mater Lett 144(4):90–92
7. Zhang CS, Ye JX, Yin Y (2014) Application of sensors in welding automation. J Nanchang Inst Technol 31(6):58–62
8. Jia JP, Peng L, Liu YL et al (2014) Numerical simulation of metal transfer in GMAW based on rotating arc sensor. Hot Working Technol 43(3):142–146
9. Zhang CS, Ye JX (2009) Application of ultrasonic sensor in weld tracking. Weld Technol 38 (4):1–3
10. Liu ZY, Zhang CS, Ye JX et al (2013) Measurement of welding range using ultrasonic sensor in underwater based on correlation. Hot Working Technol 42(1):183–185
11. ArrayCalc. Simulation Soft of ultrasonic sensor. http://www.dbaudio.com/cn/systems/details/arraycalc.html. Accessed 11 June 2017
12. Yang B (2007) Research on high-precision phased ultrasonic transmission in phased array ultrasonic system. Dissertation, North University of China
13. Erhard A, Bertus N, Montag HJ et al (2003) Ultrasonic phased array system for railroad axle examination. Nondestr Test 8(3):274–277
14. Altera Corporation. CPLDs vs FPGAs comparing high-capacity programmable logic. http://pdf1.alldatasheet.com/datasheet-pdf/view/273777/ALTERA/EPM1270144C5.html. Accessed 11 June 2017

Type Identification and Feature Extraction of Weld Joint for Adaptive Robotic Welding

Ran Li, Manshu Dong, Xiaochao Zhang and Hongming Gao

Abstract In recent years, intelligent robotic welding has been an active research area. Vision sensors have been widely used in robotic welding systems for information collection and processing. For better welding quality and efficiency, it is necessary to achieve accurate and fast information processing and intelligent decision-making for welding robot. For weld joint information processing, most of the reported works focus on the feature extraction of weld joint concerning a specific type or a regular shape. In this chapter, an algorithm is proposed to identify joint type and extract relevant feature values by extracting three feature lines and two key turning points. Three types of weld joints are inspected and the results indicate that the algorithm is of high efficiency and robustness.

Keywords Laser vision sensor · Type identification · Feature extraction
Adaptive robotic welding

1 Introduction

Nowadays, with the development of modern manufacturing technologies and shortage of skilled manual welders, automatic welding becomes an inevitable trend. However, most of the welding robots applied in the automatic manufacturing are still primary teaching-playback robots. Their welding path and parameters are set in advance. The use of welding robots requires sufficient preparation of working conditions. But in practice, the positions and shapes of weld joint usually vary due to the workpiece distortion, changing misalignment and changing gap which are mainly caused by production error, assembly error and welding heat respectively.

R. Li · M. Dong · X. Zhang · H. Gao (✉)
State Key Laboratory of Advanced Welding and Joining,
Harbin Institute of Technology, Harbin, China
e-mail: gaaohm@hit.edu.cn

M. Dong
Ningxia Tiandi Benniu Industrial Group Co., Ltd, Shizuishan, China

S. Chen et al. (eds.), *Transactions on Intelligent Welding Manufacturing*,
Transactions on Intelligent Welding Manufacturing,
https://doi.org/10.1007/978-981-10-7043-3_14

Therefore, this type of welding robots cannot meet the enterprises' requirements on high quality and efficiency [1]. In order to address these issues, new welding robot should have the functions of real-time seam tracking and welding parameter adjustment to achieve adaptive robotic welding [2]. In an adaptive robotic welding system, the sensor system gets the information of the weld joint in advance and then extracts relevant feature values so as to determine the welding path and parameters [3].

Laser vision sensors are the most widely used sensors in welding manufacturing because such sensors are insensitive to electrical and magnetic interferences and robust even in the presence of extreme noise [4]. The principle of laser vision sensors is primarily based on triangulation technique. The camera captures the image of target weld joint with the projection of structured light. Then, the captured stripe is processed to extract the geometrical information of the weld joint.

Although feature extraction has been researched extensively [5–9], most of the works focus on the specific joint type with horizontal surfaces. The surface unevenness and misalignment are not considered, while they are inevitable in practice. The conventional feature values extracted are the trace coordinates used for path correction and the welding area used for parameter adjustment. These methods are exclusively applied to specific and well-assembled weld joint, so there is a need for an intelligent algorithm that can identify joint type (butt, lap or fillet joint) and extract relevant features even with big noise.

An algorithm for information processing of laser sensors in adaptive robotic welding is described in this chapter, and it can be used to identify the joint type and then calculate the relevant feature values in real time for most plate welding.

2 Experimental System

The experimental system (see Fig. 1a) consists of a six-axis industrial robot (Motoman, HP20D), a smart laser system (META, 50V1), a three-axis motion platform and a computer. All the components are interconnected by a hub. The sensor head fixed at the end effector of the robot, in front of the welding torch (see Fig. 1b), is 65 mm away from the workpiece surface with a 50 mm field of view. The built-in camera gets an image with a laser stripe projected on the surface. This image indicates the shape of joint. After interior operation, the joint information in the form of a series of relative coordinate values is sent to the computer.

3 The Proposed Method

The traditional methods extract feature points through calculating derivative [6] or turning angle [8]. The number and type of the turning points extracted determine the type of weld joint [10]. These methods depend highly on the precision of

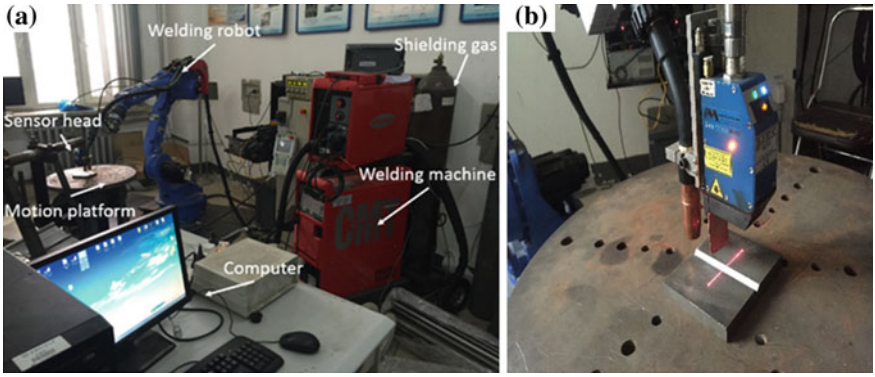

Fig. 1 Experimental system (**a**) and sensor head (**b**)

extraction of laser stripe, and most of them are applicable to a specific or regular joint. When the weld joint is irregular or the laser stripe is noisy, these methods may be not suitable. In order to adjust the welding parameters more sensitively, the adaptive welding robot system needs to extract feature values as soon as possible. Therefore, there is a need for an algorithm to quickly identify joint type and extract relevant feature values.

In practice, the surface of workpiece except the joint is usually flat. Due to the continuity of seam, the joint part is usually in the middle of the laser stripe. Therefore, two feature lines which indicate the surfaces of two workpieces can be extracted from the points at two ends of the laser stripe. Then, the two key turning points are extracted by calculating the deviation values from points to each line in the y-axis. The third feature line is extracted by connecting the two key turning points. The angle values among three feature lines and the distance between two key turning points determine the joint type, and the relevant feature values are then calculated according to the joint type. The detailed steps are shown below.

3.1 Type Identification

There is some noise in raw data sent from the laser sensor system due to specular reflection and arc light. These noise points should be removed first. The laser sensor system sends 1024 points in order of x-axis, so the valid data (X_i, Y_i) should meet this criterion: (1) $X_{i-1} < X_i < X_{i+1}$; (2) $-40 < Y_i < 40$, if $Y_{i-1} < Y_i > Y_{i+1}$ or $Y_{i-1} > Y_i < Y_{i+1}$, $|Y_i - Y_{i-1}| < 3$ and $|Y_i - Y_{i+1}| < 3$. The relevant thresholds are obtained through test. Because of edge distortion, the points at two ends are usually invalid. Therefore, the former ten points and the last ten points are removed.

The valid data contain nearly 1000 points. Two feature lines L_1 and L_2 are extracted from 200 points of both ends first by least square method. K_1 and K_2 are the slope values of L_1 and L_2 in y-axis respectively. D_1 and D_2 are the max

deviation values of L_1 and L_2 in y-axis respectively. Let L_1 be the feature line indicating the surface of left workpiece and L_2 be the feature line indicating the surface of right workpiece. Then, the deviation values in y-axis are consecutively calculated from the point 201 to the point 800. When the deviation values of ten consecutive points are beyond D_1, the last point close to these points in the left is regarded as the key turning point A. The point B is got by the same method. L_3 is then extracted by connecting A and B. The slope of L_3 is K_3. Through K_1, K_2 and K_3 and the distance between A and B, the type of weld joint can be identified.

Basically, there are three types of weld joints: butt joint, lap joint and fillet joint (see Fig. 2). For butt joint with groove, L_1, L_2 and L_3 are almost parallel. So, the angle values θ_{12}, θ_{13} and θ_{23} should be less than a certain value which is 30° in this chapter. For butt joint without groove, if L_1 and L_2 are almost coincident or the turning points are very close to each other, it is hard to find the accurate turning points. In this case, the turning points can be got by calculating the max deviation value in x-axis of consecutive points. If the max deviation value is more than a certain value which is 1 mm in this chapter, the two consecutive points are regarded as the turning points. If the max deviation value is less than 1 mm and the two feature lines are almost coincident, the joint is regarded as flat. If L_1 and L_2 are not coincident, the identification criterion is the same as that of butt joint with groove. For lap joint, L_1 and L_2 are almost parallel and L_3 is almost vertical to L_1 and L_2. So, the angle values θ_{13} and θ_{23} should be more than a certain value which is 60° in this paper. The angle value θ_{12} should be less than a certain value which is 30° in this paper. For fillet joint, L_1 and L_2 are almost vertical and the points A and B are almost coincident. So, the angle value θ_{12} should be more than a certain value which is 60° in this paper. And the distance between A and B should be less than a certain value which is 1 mm in this chapter. As the turning points A and B are almost coincident, θ_{12}, θ_{12} and L_3 are not considered. Figure 3 shows the block diagram of the whole algorithm.

3.2 Feature Extraction

As the joint type is identified, a series of feature values are then calculated according to actual demand. For lap joint and fillet joint, the main feature values are tracepoint and torch direction. The key turning point located at a low position is the

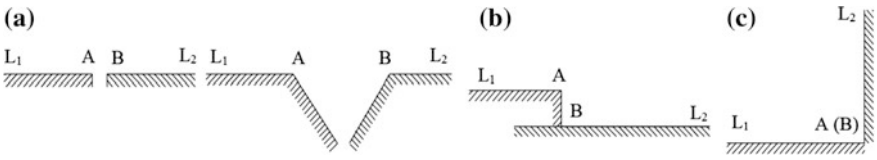

Fig. 2 Three main types of weld joint: **a** butt joint; **b** lap joint; and **c** fillet joint

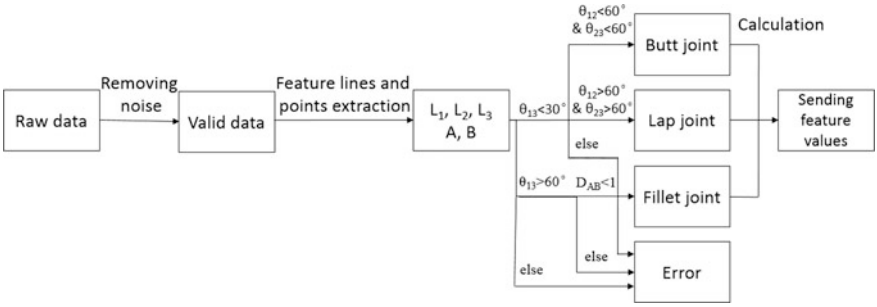

Fig. 3 Block diagram of the algorithm

tracepoint, and the relevant feature line which the tracepoint belongs to is the baseline. For lap joint, the torch vector is between baseline and L_3. For fillet joint, the torch vector is between L_1 and L_3. For butt joint, the tracepoint is the midpoint of gap. And the welding area is calculated by summing up the area of the trapezium composed by every two consecutive points between A and B and their vertical intersection points with L_3. The misalignment value is got by calculating the distance from the higher turning point to the line through the lower point.

4 Results and Discussion

Three types of weld joints are inspected to examine the performance of this algorithm.

A butt joint is tested and the raw data are plotted (see Fig. 4a). It is obvious that there are some distortion points at two ends. After data filtering, valid data are obtained (see Fig. 4b). Two feature lines are then calculated from 200 points at two ends by least square method, i.e. L_1 ($y = -0.1240x - 2.6884$) and L_2 ($y = -0.0360x - 2.0666$) which are the green and yellow lines in Fig. 4c respectively. The max deviation values are got: $D_1 = 0.0662$ and $D_2 = 0.0808$. By calculating the deviation values from other points to these two feature lines in sequence, the turning points A and B are extracted: A (−4.117, −2.265) and B (8.462, −2.46) shown in Figs. 4d and e. Then, the feature line L_3 is got: L_3 ($y = -0.0155x - 2.3288$). The angle values are calculated: $\theta_{12} = 5.0063°$, $\theta_{23} = 1.4035°$ and $\theta_{13} = 6.4075°$. According to the above block diagram, this joint is identified as a butt joint.

A lap joint is tested (see Fig. 5). The feature lines and feature points are got: L_1 ($y = -0.1223x - 4.9181$), L_2 ($y = -0.1279x + 1.4444$), L_3 ($y = 26.7265x - 112.4126$), A (4.005, −5.373) and B (4.239, 0.881). The max deviation values and angle values are: $D_1 = 0.1804$, $D_2 = 0.4259$, $\theta_{12} = 0.3159°$, $\theta_{13} = 85.17°$ and $\theta_{23} = 84.854°$. According to the above block diagram, this joint is identified as a lap joint.

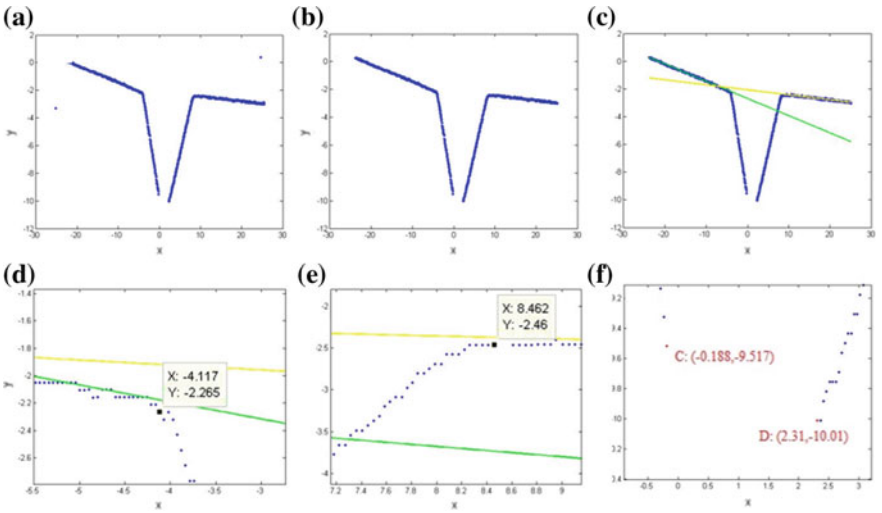

Fig. 4 Feature extraction of butt joint: **a** raw data; **b** valid data; **c** feature lines; **d** the point *A*; **e** the point *B*; and **f** gap points

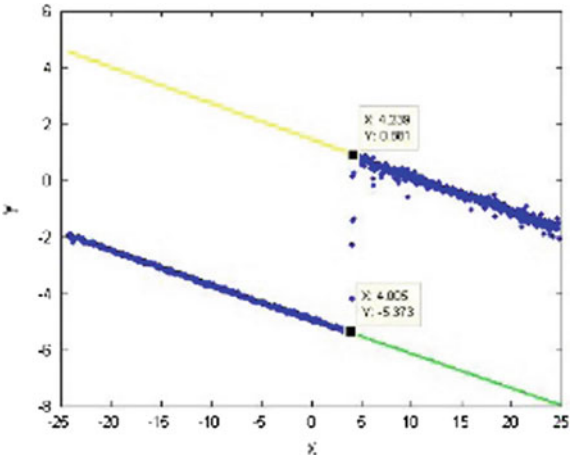

Fig. 5 Feature extraction of lap joint

A fillet joint is tested (see Fig. 6). The feature lines and feature points are got: L_1 ($y = -0.3988x - 11.0133$), L_2 ($y = 2.6580x - 45.5687$), A (11.17, −15.34) and B (11.404, −14.919). So, the angle value of L_1 and L_2 and the distance between A and B are got: $\theta_{12} = 88.875°$ and $D_{AB} = 0.482$. According to the above block diagram, this joint is identified as a fillet joint.

The results indicate that all three types of weld joints are successfully identified. As shown in Fig. 6, even if the data have some big noise, this algorithm can still find the appropriate key turning points according to the max deviation values.

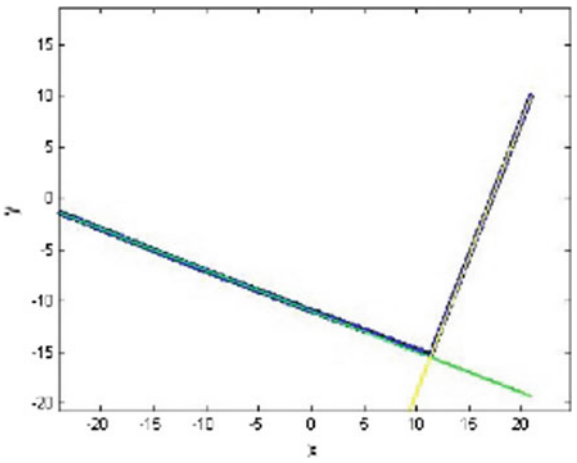

Fig. 6 Feature extraction of fillet joint

In order to test the accuracy of this algorithm, a standard V-groove is tested with given dimension (see Fig. 2). The groove is 10 mm wide and 5 mm deep after machine work. The algorithm identifies the joint type and then gives the feature values as follows: the groove width is 10.076 mm, the groove depth is 4.932 mm, the welding area is 25.696 mm^2, the misalignment value is 0.02 mm and the angle value of workpiece is 0.22. In consideration of the lateral resolution of the laser system, which is 0.05 mm, the errors of these values are acceptable.

5 Conclusion

An algorithm for type identification and feature extraction of irregular weld joints is presented in a practical and reliable way. The following conclusions can be made. The proposed algorithm can quickly identify the joint type according to the extracted three feature lines and two key turning points and the amount of computation is comparatively small due to the simple criterion. Even if the data noise is big, the set of max deviation value and consecutive deviation point number ensures the reliability and robustness of the algorithm. This algorithm can give fairly accurate feature values. And the error is within one-half of the lateral resolution of the laser system.

Acknowledgements This work is supported by the National Key Technology R&D Program of China (2015BAF01B01).

References

1. Xu YL (2013) Research on real-time tracking and control technology of three-dimension welding seam during welding robot GTAW process based on vision sensor and arc sensor. Dissertation, Shanghai Jiao Tong University, China
2. Chen SB, Lv N (2014) Research evolution on intelligentized technologies for arc welding process. J Manufact Process 16(1):109–122
3. He YS, Chen YX, Xu YL et al (2016) Autonomous detection of weld seam profiles via a model of saliency-based visual attention for robotic arc welding. J Intell Rob Syst 81 (3–4):395–406
4. Wu J, Smith JS, Lucas J (1996) Weld bead placement system for multi-pass welding. IEE Proc Sci Measur Technol 143(2):85–90
5. Shi YH et al (2007) Adaptive robotic welding system using laser vision sensing for underwater engineering. In: Proceedings of IEEE International Conference on Control and Automation. IEEE, Guangzhou, pp 1213–1217
6. Manorathna RP, et al (2014) Feature extraction and tracking of a weld joint for adaptive robotic welding. In: Proceedings of 13th international conference on control automation robotics & vision. IEEE, Singapore, pp 1368–1372
7. Zhang LG, Ye QX, Yang W et al (2014) Weld line detection and tracking via spatial-temporal cascaded hidden Markov models and cross structured light. IEEE Trans Instrum Meas 63 (4):742–753
8. Sung K, Lee H, Choi YS et al (2009) Development of a multiline laser vision sensor for joint tracking in welding. Weld J 88(4):79–85
9. Lei ZL, Lv T, Chen YB et al (2013) Features extraction for weld image of scanning laser sensing. Trans China Weld Inst 34(5):54–58
10. Muhammad J, Altun H, Abo-Serie E (2017) Welding seam profiling techniques based on active vision sensing for intelligent robotic welding. Int J Adv Manuf Technol 88 (1–4):127–145

Kinematic Model Analysis of an 8-DOF Photographic Robot

Xiaowei Xie, Xingang Miao, Su Wang and Feng Zhang

Abstract The photographic robot studied in this chapter is an 8-DOF PRRPR-S type. In order to obtain a stable and repeatable lens shooting trajectory, it is necessary to balance the robot's own weight and structural rigidity. First, based on the structural analysis of the photographic robot, the main parameters of the mechanism design are extracted. Then, with the help of the photographic robot calibration, the kinematics model of the robot is established. The DH model is applied on the first seven axes of the photographic robot. The 6-parameter model is used on the end actuator attitude adjustment rotation axis. Finally, the motion of each axis is simulated in MATLAB, which verifies the kinematic model.

Keywords Photographic robot · Kinematics analysis · DH model
6-parameter model

1 Introduction

The photographic robot can accurately reproduce the graphics and export the shooting trach at the same time, which cannot be realized by the manual operation. It is an important tool, used for shooting source material, for digital image synthesis technology, which provides the foundation for the creation of visual effects. At present, the use of photographic robots requires professional operators to participate. This approach has been approved to be time-consuming, which is less efficient. The purpose of this chapter is to establish the kinematic model of the 8-DOF photographic robot. This allows the operator to specify the target position of the end actuator and simplify the operation mode. The photographic robot controls the

X. Xie · X. Miao (✉) · S. Wang
Beijing Key Laboratory of Robot Bionics and Function Research,
Beijing University of Civil Engineering and Architecture, Beijing, China
e-mail: miaoxingang@bucea.edu.cn

F. Zhang
China Petroleum Pipeline Research Institute, Langfang, Hebei, China

S. Chen et al. (eds.), *Transactions on Intelligent Welding Manufacturing*,
Transactions on Intelligent Welding Manufacturing,
https://doi.org/10.1007/978-981-10-7043-3_15

movement of cameras and can monitor the welding process at a specified location in real time. This will make photographic robots widely used in welding manufacturing. While modeling is the key process of robot kinematics analysis, the DH modeling method is one of the most commonly used modeling methods [1, 2]. In this chapter, the first seven axes of the photographic robot are developed by this modeling method. However, this model acts singularly when the adjacent two joint axes of the robot are parallel or nearly parallel. Therefore, when parallel axes occur, the rotation of one y axis will be increased to avoid the singularity problem [3]. The rotation axis, which is performed by the actuator at the end for attitude adjustment, uses a 6-parameter S-model [4]. According to the kinematic model established by this method, the pose matrix of the end actuator can be obtained more accurately, which in practice has a great application value.

2 Schematics and Zero Status Parameter Tables

In this chapter, the type of photography robot is an 8-DOF PRRPR-S type, with complete spatial positioning capability. It belongs to the double redundant freedom robot. Physical prototype and key components are named as in Fig. 1. Compared with the traditional industrial robots, the arm can be elongated, and the robot body structure can be moved in a linear orbit. The kinematics model of the robot is established depending on each link as a rigid body. Kinematics model research mainly solves the problem of robot positioning, especially for describing the positional relationship between one connecting rod and another.

In this chapter, the DH method is used to model the photographic robot, while the 6-parameter model method is used for the end actuator transformation matrix. The above statement has already taken the calibration requirements into account. DH modeling methods in different literature are slightly different. The coordinate system $\{i\}$ in this chapter is attached to the connecting rod i at the origin of the joint axis of the connecting rod. The specification of the additional coordinate system of the connecting rod is summarized as follows:

(1) For the coordinate system $\{i\}$ of the connecting rod i, the Z axis is pointing in the axial direction of the joint axis, and for the linear motion axis, the axial direction is the direction of the motion axis;
(2) The X axis of the coordinate system $\{i\}$ is the vertical direction of the coordinate system $\{i-1\}$ Z axis and the coordinate system $\{i\}$ Z axis. The Y axis of the coordinate system $\{i\}$ is determined by the right-hand rule according to the X axis and Z axis.

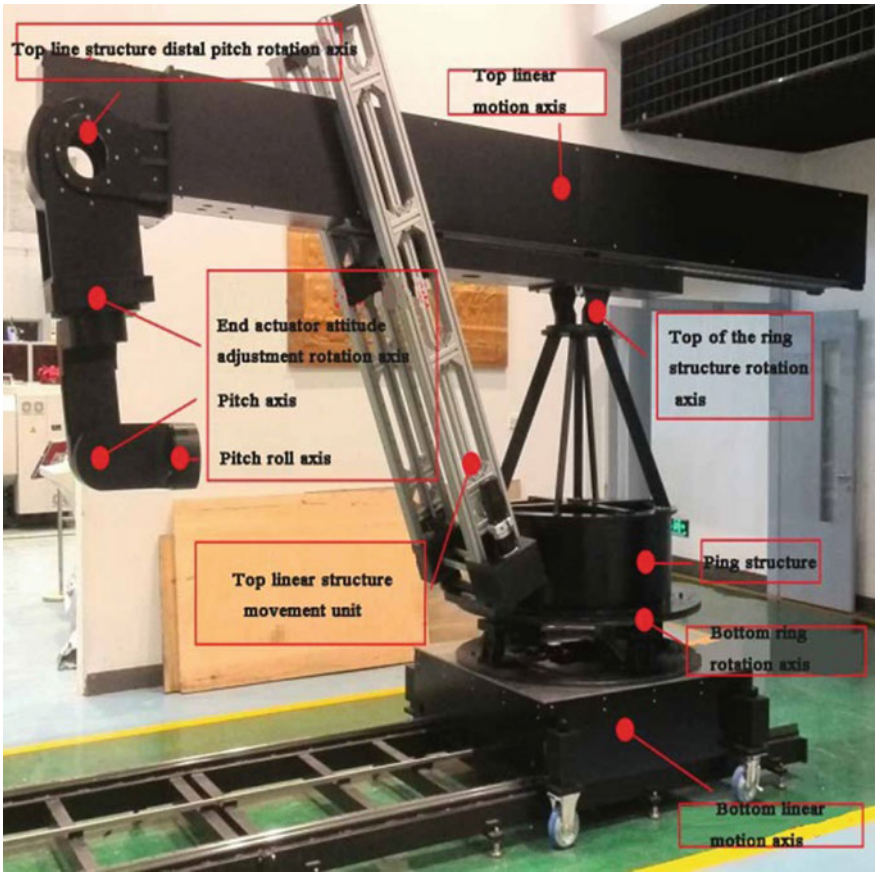

Fig. 1 Photographic robot movement axes and key parts named

Thus, the establishment of the photographic robot connecting rod coordinate system is shown in Fig. 2.

There are eight motion axes in the photographic robot, respectively, the bottom linear motion axis r_1, the bottom ring rotation axis θ_2, the top of the ring structure rotation axis θ_3, the top linear motion axis r_4, the top line structure distal pitch rotation axis θ_5, the end actuator attitude adjustment rotation axis θ_6, pitch axis θ_7 and roll axis θ_{ee}. Considering the zero state of the photographic robot, based on the DH and 6-parameter models, the kinematic link parameters of the photographic robot are obtained, as shown in Table 1. When the photographic robot is located in the zero state, the movement amount of each motor shaft is 0. The position and attitude of the photographic robot are shown in Table 1.

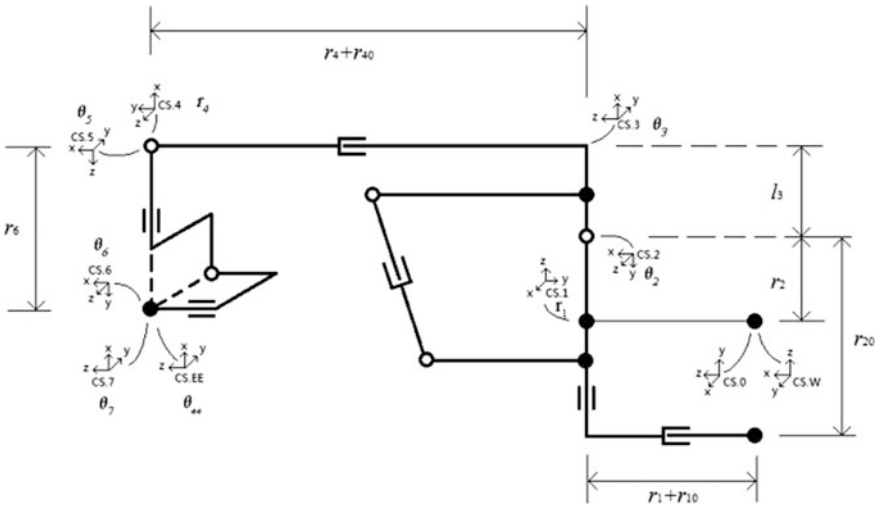

Fig. 2 Connecting rod coordinate system

Table 1 Photographic robot kinematic link parameters table

Parameter								
Vary	Type	i	1	2	3	4	5	6
W–0	1	0	π/2	0	0	π/2	–	–
0–1	1	1	0	$r_1 + r_{10}$	0	−π/2	–	–
1–2	1	2	−π/2	r_2	0	−π/2	–	–
2–3	1	3	−π/2	0	l_3	−π/2	–	–
3–4	1	4	0	$r_4 + r_{40}$	0	π/2	–	–
4–5	1	5	π/2	0	0	−π/2	–	–
5–6	1	6	0	r_6	0	π/2	–	–
6–7	1	7	−π/2	0	0	−π/2	–	–
7−EE	2	EE	0	0	0	0	0	0

3 Transformation Matrix

3.1 Transformation Matrix Type 1—DH (θ r l α)

The DH transformation matrix means that in the coordinate system $\{i\}$, it rotates θ around the current Z axis, then moves r along the Z axis, next moves l along the X axis, afterward rotates a around the X axis. The formula of the transformation matrix of DH modeling is

$$\mathbf{A}_{\mathrm{DH}} = \begin{bmatrix} \cos\theta & -\cos\alpha\cdot\sin\theta & \sin\theta\cdot\sin\alpha & l\cdot\cos\theta \\ \sin\theta & \cos\alpha\cdot\sin\theta & -\cos\theta\cdot\sin\alpha & l\cdot\sin\theta \\ 0 & \sin\alpha & \cos\alpha & r \\ 0 & 0 & 0 & 1 \end{bmatrix} \tag{1}$$

3.2 Transformation Matrix Type 2—EE (6-Parameter Transformation Matrix)

The 6-parameter transformation matrix means that, in the coordinate system $\{i\}$, the following transformation is performed in the new coordinate system after the transformation, it rotates θ around the Z axis, rotates β around the Y axis, rotates α around the X axis, then moves x along the X axis, moves y along the Y axis and finally moves z along the Z axis. The EE modeling transformation matrix formula is

$$\mathbf{A}_{\mathrm{ee}} = \begin{bmatrix} \cos\beta\cdot\cos\theta & \cos\theta\cdot\sin\alpha\cdot\sin\beta-\cos\alpha\cdot\sin\theta & \sin\alpha\cdot\sin\theta+\cos\alpha\cdot\sin\beta\cdot\cos\theta & \\ \cos\beta\cdot\sin\theta & \sin\theta\cdot\sin\alpha\cdot\sin\beta+\cos\alpha\cdot\cos\theta & -\sin\alpha\cdot\cos\theta+\cos\alpha\cdot\sin\beta\cdot\sin\theta & \\ -\sin\beta & \cos\beta\cdot\sin\alpha & \cos\alpha\cdot\cos\beta & \\ 0 & 0 & 0 & \\ z\cdot(\sin\alpha\cdot\sin\theta+\cos\alpha\cdot\sin\beta\cdot\cos\theta)-y\cdot(\cos\alpha\cdot\sin\theta-\cos\theta\cdot\sin\alpha\cdot\sin\beta)+x\cdot\cos\beta\cdot\cos\theta & \\ -z\cdot(\sin\alpha\cdot\cos\theta-\cos\alpha\cdot\sin\beta\cdot\sin\theta)+y\cdot(\cos\alpha\cdot\cos\theta+\sin\theta\cdot\sin\alpha\cdot\sin\beta)+x\cdot\cos\beta\cdot\sin\theta & \\ z\cdot\cos\alpha\cdot\cos\beta-x\cdot\sin\beta+y\cdot\cos\beta\cdot\sin\alpha & \\ 1 & \end{bmatrix} \tag{2}$$

From the above analysis, the photographic robot transformation matrix is obtained

$$\mathbf{A}_0 = \begin{bmatrix} 0 & 0 & 1 & 0 \\ 1 & 0 & 0 & 0 \\ 0 & 1 & 0 & 0 \\ 0 & 0 & 0 & 1 \end{bmatrix} \tag{3}$$

$$\mathbf{A}_1 = \begin{bmatrix} 1 & 0 & 0 & 0 \\ 0 & 0 & 1 & 0 \\ 0 & -1 & 0 & r_1+r_{10} \\ 0 & 0 & 0 & 1 \end{bmatrix} \tag{4}$$

$$\mathbf{A}_2 = \begin{bmatrix} \cos(\theta_2-\pi/2) & 0 & -\sin(\theta_2-\pi/2) & 0 \\ \sin(\theta_2-\pi/2) & 0 & \cos(\theta_2-\pi/2) & 0 \\ 0 & -1 & 0 & r_2 \\ 0 & 0 & 0 & 1 \end{bmatrix} \tag{5}$$

$$\mathbf{A}_3 = \begin{bmatrix} \cos(\theta_3 - \pi/2) & 0 & -\sin(\theta_3 - \pi/2) & l_3 \cdot \cos(\theta_3 - \pi/2) \\ \sin(\theta_3 - \pi/2) & 0 & \cos(\theta_3 - \pi/2) & l_3 \cdot \sin(\theta_3 - \pi/2) \\ 0 & -1 & 0 & 0 \\ 0 & 0 & 0 & 1 \end{bmatrix} \tag{6}$$

$$\mathbf{A}_4 = \begin{bmatrix} 1 & 0 & 0 & 0 \\ 0 & 0 & -1 & 0 \\ 0 & 1 & 0 & r_4 + r_{40} \\ 0 & 0 & 0 & 1 \end{bmatrix} \tag{7}$$

$$\mathbf{A}_5 = \begin{bmatrix} \cos(\theta_5 + \pi/2) & 0 & -\sin(\theta_5 + \pi/2) & 0 \\ \sin(\theta_5 + \pi/2) & 0 & \cos(\theta_5 + \pi/2) & 0 \\ 0 & -1 & 0 & 0 \\ 0 & 0 & 0 & 1 \end{bmatrix} \tag{8}$$

$$\mathbf{A}_6 = \begin{bmatrix} \cos\theta_6 & 0 & \sin\theta_6 & 0 \\ \sin\theta_6 & 0 & -\cos\theta_6 & 0 \\ 0 & 1 & 0 & r_6 \\ 0 & 0 & 0 & 1 \end{bmatrix} \tag{9}$$

$$\mathbf{A}_7 = \begin{bmatrix} \cos(\theta_7 - \pi/2) & 0 & -\sin(\theta_7 - \pi/2) & 0 \\ \sin(\theta_7 - \pi/2) & 0 & \cos(\theta_7 - \pi/2) & 0 \\ 0 & -1 & 0 & 0 \\ 0 & 0 & 0 & 1 \end{bmatrix} \tag{10}$$

$$\mathbf{A}_{ee} = \begin{bmatrix} \cos\theta_{ee} & \sin\theta_{ee} & 0 & 0 \\ -\sin\theta_{ee} & \cos\theta_{ee} & 0 & 0 \\ 0 & 0 & 1 & 0 \\ 0 & 0 & 0 & 1 \end{bmatrix} \tag{11}$$

The position of the end actuator coordinate system in the world coordinate system is

$$T_{ee} = \mathbf{A}_1 \cdot \mathbf{A}_2 \cdot \mathbf{A}_3 \cdot \mathbf{A}_4 \cdot \mathbf{A}_5 \cdot \mathbf{A}_6 \cdot \mathbf{A}_7 \cdot \mathbf{A}_{ee} \tag{12}$$

Among them, $r_1 = 0$, $r_4 = 0$, $r_{10} = 1000$, $r_2 = 300$, $l_3 = 333$, $r_{40} = 333$, $r_6 = 963$, $r_1 = 0$.

In Fig. 2, $r_{20} = 1969$. r_{20} is the distance from the upper surface of the bottom linear track to the top of the ring structure rotation axis. It is assumed that the height of the upper surface of the bottom linear track is used as the origin height of the world coordinate system. However, under the consideration that the positional expression of the photographic robot contains interrelated link parameters, the world coordinate system is placed in the middle of the two tracks, which makes the height lower than the height of the ring structure's top.

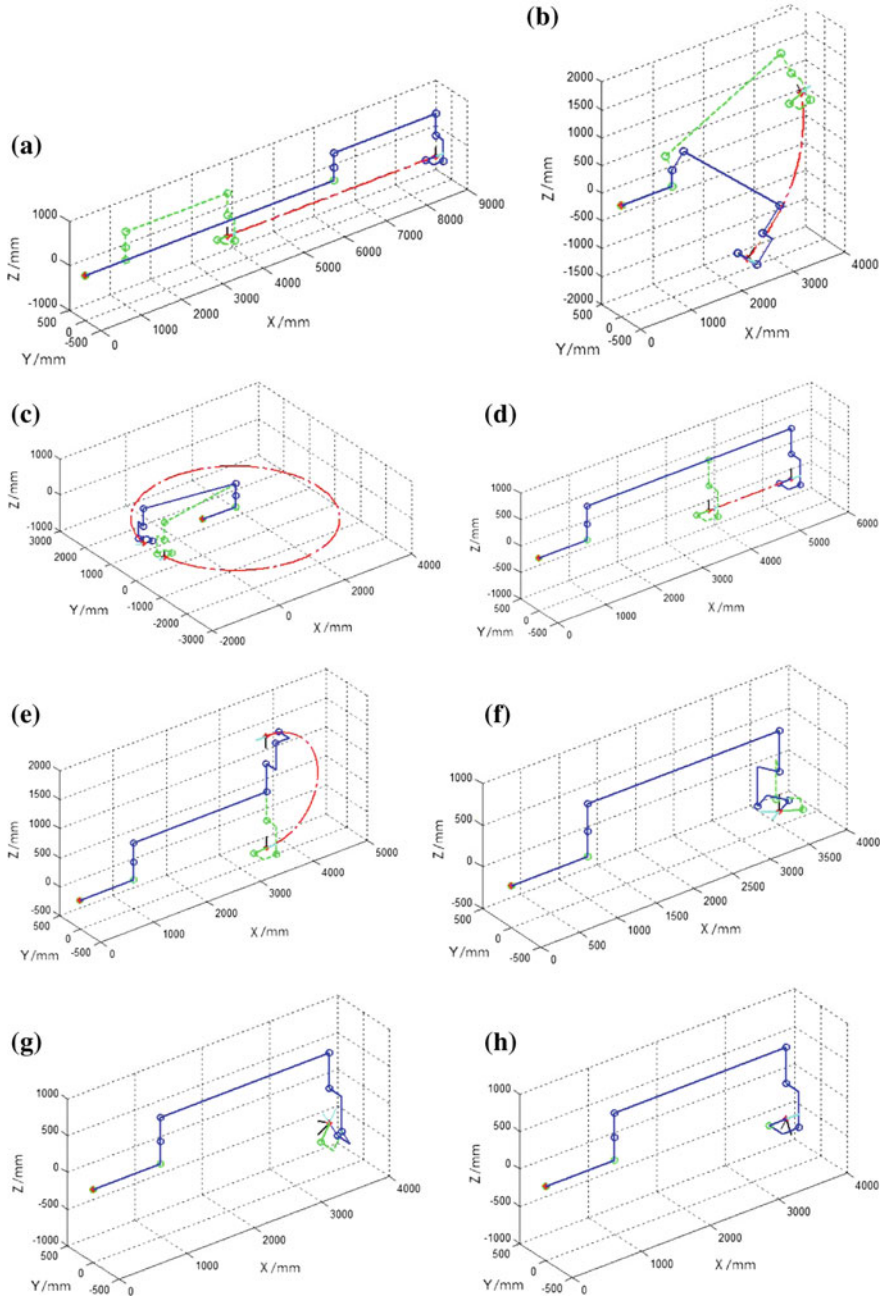

Fig. 3 Rotating platform model: **a** bottom linear motion axis; **b** top of the ring structure rotation axis; **c** bottom ring rotation axis; **d** top linear motion axis; **e** top line structure distal pitch rotation axis; **f** end actuator attitude adjustment rotation axis; **g** end actuator attitude adjustment pitch axis; **h** end actuator attitude adjustment pitch roll axis

4 Verification of Kinematics Model

In this chapter, the kinematics model of the photographic robot is displayed graphically with MATLAB software. It moves as much as possible within the motion range of each joint of the photographic robot [5]. As shown in Fig. 3, the green dotted line is the initial zero position of the photographic robot, the blue solid line is the end state of the motion of the photographic robot, the sky and black is the posture of the end actuator, and the red dotted line is the end actuator motion trajectory of the photographic robot. Among them, some photographers at the end of the kinetic model of movement state and the initial zero state coincidence, resulting in green dotted line is blocked by a blue solid line.

The figure shows the initial zero state, the motion end state and the end actuator motion trajectory of each axis of an 8-DOF robot. It can be seen from the figure that the end actuator of the photographic robot moves continuously from the initial zero position of the photographic robot to the end state of the motion of the photographic robot along the trajectory, and it is possible to visually see the eight axes of the photographic robot during the simulation animation passes through the continuous points of the trajectory, which fully complies with the requirements of the photographic robot design.

5 Conclusion

According to the calibration requirements of the 8-DOF photographic robot, both the DH model and the 6-parameter model has been purposed to establish the coordinate system and model. Through MATLAB simulation, it is shown that the kinematics simulation of the photographic robot can be realized by MATLAB software, which proves that the photographic robot can accurately move along with the desired trajectory on the computer. Overall, the discussed method has been proved to be complete, continuous and practical.

References

1. Sanler JP (1983) Kinematics and dynamics of machinery. Harper & Row, New York, pp 75–102
2. Whitney DE (2004) Mechanical assemblies: their design manufacture and role in product development. Oxford University Press, New York, pp 35–51
3. Nubiola A, Bonev IA (2013) Absolute calibration of an ABB IRB 1600 robot using a laser tracker. Robot Comput Integr Manuf 29(1):236–245
4. Stone HW et al (1988) Statistical performance evaluation of the S-model arm signature identification technique. In: IEEE ICRA. IEEE, Philadelphia, pp 939–946
5. Feng F, Zhang LP, Zhang B (2008) Simulator of four-degree-of-freedom robot simulation. J Henan Univ of Sci Technol 29(3):24–26

Author Index

S. Chen et al. (eds.), *Transactions on Intelligent Welding Manufacturing*,
Transactions on Intelligent Welding Manufacturing,
https://doi.org/10.1007/978-981-10-7043-3